AERODYNAMIC DRAG AND LIFT CHARACTERISTICS OF A NEWLY DEVELOPED ELLIPTICAL-BLADED SAVONIUS WIND TURBINE ROTOR

A Thesis
Submitted in Partial Fulfillment of the Requirements for
the Award of the Degree of

DOCTOR OF PHILOSOPHY

By

MD. NUR ALOM
(Regn No: 166103030)

DEPARTMENT OF MECHANICAL ENGINEERING
INDIAN INSTITUTE OF TECHNOLOGY GUWAHATI
GUWAHATI - 781039, INDIA

Declaration

I hereby certify that the work compiled in this dissertation entitled '**Aerodynamic drag and lift characteristics of a newly developed elliptical-bladed Savonius wind turbine rotor'** is the outcome of my research work under the guidance of Professor Ujjwal K. Saha in the Department of Mechanical Engineering, Indian Institute of Technology Guwahati, India.

Any part of this work has not earlier been submitted for the award of any degree, diploma, associate-ship, fellowship or its equivalent to any University or Institution.

Date: October 04, 2019

(Md. Nur Alom)
Registration No. 166103030
Department of Mechanical Engineering
Indian Institute of Technology Guwahati

Department of Mechanical Engineering
Indian Institute of Technology Guwahati
Guwahati-781039, India

Certificate

It is certified that the work contained in the thesis entitled '**Aerodynamic drag and lift characteristics of a newly developed elliptical-bladed Savonius wind turbine rotor'** submitted by **Md. Nur Alom** to the Indian Institute of Technology Guwahati for the award of the degree of Doctor of Philosophy has been carried out under my supervision in the Department of Mechanical Engineering, Indian Institute of Technology Guwahati. This work has not been submitted elsewhere for the award of any other degree or diploma.

Date: October 04, 2019

(Ujjwal K. Saha)
Professor
Department of Mechanical Engineering
Indian Institute of Technology Guwahati
Guwahati-781039, India

Acknowledgement

I express my deep sense of gratitude and indebtedness to Prof. U. K. Saha, but for that illustrious guidance this project would not have seen light. His illustrious guidance and effusive co-operation, co-ordination, encouraging interaction is great driving force for me in this project. His affectionate concern for students and his in-depth appreciation of the problem and valuable guidance for its solving keeps him on a unique pedestal as an outstanding guide.

I owe my deepest gratitude to my doctoral committee members Dr. Amaresh Dalal, Dr. Dipankar N. Basu and Dr. Pankaj Tiwari for their productive suggestions and advises towards my research findings. My sincere acknowledgement goes to Prof. Santosha K. Dwivedy (HOD, Mechanical Engineering Department) and Prof. Gopal Das (Dean, R & D) for providing all the research facilities and financial support.

I would like to thank all the faculty members, staffs, and research scholars of Mechanical Engineering Department, IIT Guwahati, for rendering their whole-hearted cooperation and pleasurable support in the entire course of work. A word of appreciation goes to the senior technicians of Mechanical Engineering Department Mr. Bijoy k. Choudhury, Mr. Dilip Chetri, Mr. Mrinal Sarma, Mr. Monoj K. Baishya, and Mr. Dhaneswar Khaklary for their assistance in the fabrication of wind turbine blades. I am also thankful to my seniors, friends and co-workers Dr. Bhaskor J. Bora, Dr. Achinta Sarkar, Mr. P. Mukherjee, Dr. Parag K. Talukdar, Mr. Avilash Sahoo, Mr. Sambit Majumder, Ms. Rubi Chakraborty, Mr. Suman Kumar, Mr. Supratim Kaushik, Ms. Ramyani Chakrabarty, Mr. Nitish Kumar and Mr. Bastav Borah for their friendship and unforgettable moments.

I would like to express my sincere thanks to the Director, Registrar and Deans of National Institute of Technology Meghalaya for giving me the opportunity to pursue PhD at IIT Guwahati and also for providing financial assistance to meet various professional expenses. I would also like to thank all the faculty and staff members of Mechanical Engineering Department of National Institute of Technology Meghalaya for their pleasant support in the entire course of work.

I would like to gratefully acknowledge the ASME for offering me the prestigious YETEP (Young Engineers Turbo Expo Participation) award which made me possible to attend and present my work at the ASME Turbo Expo 2017 conference held at Charlotte, NC, USA, during June 26 – 30, 2017. I am also grateful to DST-SERB, Govt. of India and ASME Outreach to Engineers for providing me the financial support for attending the ASME 39th International Conference on Ocean, Offshore and Arctic Engineering (OMAE 2019) held at Glasgow, Scotland, UK during June 9-14, 2019.

Acknowledgement would be incomplete without giving credit to the authors of many articles/proceedings/reports/theses, whose works have formed the framework of the present investigation.

Finally, I would like to express my gratitude to my beloved parents, wife, brothers and sister for their continuous encouragement and blessings.

October 04, 2019
Guwahati, India

Md. Nur Alom

ABSTRACT

The utilization of wind turbine is increasing throughout the world to provide electricity without contributing to the increase in global warming. The Savonius rotor is the simplest type of vertical-axis wind turbine that has a relatively low efficiency. A high negative torque produced by the returning blade is a major drawback of this rotor, and the designers have always attempted to reduce it for improving the performance. A considerable amount of research and development has been invested over the past few decades with various influencing parameters of this rotor to arrive at a suitable design configuration.

Besides using the conventional semicircular blades, other blade configurations have been evolved during the past two decades to improve the performance of the Savonius rotor. At the same time, various augmentation techniques have also been used to improve the rotor performance. Such augmentation techniques reduce the negative torque while maintaining a high rotational speed so that such a rotor system can be used for electricity generation.

The elliptical-bladed rotor that has shown its potential to harness wind energy more efficiently is considered for the present numerical and experimental studies. Upon optimizing its various influencing parameters, the vent augmentation technique is implemented on the rotor blades. The coefficients of drag, lift, torque and power (C_D, C_L, C_T and C_P) of the elliptical-bladed rotor have been evaluated to assess the rotor performance. Clearly, a higher C_D indicates a higher rotational speed and hence a higher C_T and C_P of the rotor.

In view of this, initially 2D unsteady simulations have been conducted for the elliptical, modified Bach, Benesh and semicircular profiles of the Savonius rotor. This is to check and corroborate the past research findings. The geometric parameters such as overlap ratio, number of rotor blades and effect of shaft are then considerd. The unsteady simulations are also carried out to analyze the influence of Reynolds number on the rotor performance. Thereafter, unsteady simulations are carried out by implementing the vent-augmenters.

The C_D and C_L of the elliptical-bladed rotor is evaluated and compared with that of a semicircular-bladed rotor. The average C_D for a complete rotation of elliptical and semicircular profiles are found to be 1.43 and 1.35, respectively. Hence, there is higher average C_D by 6% in the elliptical profile than the semicircular profile. Further, the C_L and C_D are also estimated for the modified Bach and Benesh profile to have a comparison in a common platform. The 3D unsteady simulations are then conducted to estimate the performance coefficents (C_T and C_P) and aerodynamic coefficients (C_D and C_L) of vented elliptical-bladed rotor.

Subsequently, the wind tunnel experiments are conducted to validate the numerical results. The wind tunnel tests show the peak C_P to be 0.19 and 0.15 for the elliptical-bladed and semicircular-bladed rotors, respectively at TSR = 0.7 and *AR* = 1.09. Hence, there is an improvement of C_P by 27% in elliptical-bladed rotor than the conventional semicircular-bladed rotor.

Finally, the multi-objective genetic algorithm (MOGA) has been applied to the optimized elliptical profile to minimize the incoming velocity and to obtain the maximum torque and lift coefficients. From the MOGA, the elliptical profile shows the C_P to be 0.35 at $V = 5.91$ m/s (at $TSR = 0.80$). At the same *TSR*, the semicircular profile shows the C_P to be 0.28 at $V = 6.06$ m/s. On the other hand, the unsteady numerical simulation at $V = 6.2$ m/s shows $C_P = 0.34$ and 0.27 for the elliptical- and semicircular profiles, respectively.

CONTENTS

NOMENCLATURE

Notations

A	Swept area (m^2)
AR	Aspect ratio
C_D	Drag coefficient
C_L	Lift coefficient
C_P	Power coefficient
C_T	Dynamic torque coefficient
C_{TS}	Static torque co-efficient
D	Rotor diameter (m)
D_f	Drag force (N)
D_O	End plate diameter of the rotor (m)
d	Chord length of the blade (m)
e	Overlap distance between rotor blades (m)
H	Rotor height (m)
k	Turbulence kinetic energy (m^2/s^2)
L	Characteristics length of the rotor (m)
L_f	Lift force (N)
l_1, l_2	Length of the curtain plate (m)
N	Rotor rotational speed (rpm)
n	Number of time step
P	Rotor power (W)
Re	Reynolds number
R	Rotational radius of the rotor
r_p	Radius of the rope
T	Torque (N-m)
T_S	Static torque (N-m)
u	Rotor tip speed (m/s)
V	Wind velocity (m/s)
X_1, X_2	x-distance of curtain plate from rotor center (m)
Y_1, Y_2	y-distance of curtain plate from rotor center (m)

Greek symbols

α	Angle of attack (^{0})
δ	Overlap ratio
ε	Energy dissipation rate (m^2/s^3)
θ	Sectional cut of ellipse (^{0})
λ	Tip speed ratio
μ	Dynamic viscosity (N-s/m^2)
ν	Kinematic viscosity (m^2/s)
ρ	Density of air (kg/m^3)
ω	Specific dissipation rate (1/s)

Abbreviations

ANFIS	Adaptive Neuro-Fuzzy Inference System
ANN	Artificial Neural Network
BR	Blockage Ratio
CFD	Computational Fluid Dynamics
DDM	Domain Decomposition Method
DES	Detached Eddy Simulation
DNS	Direct Numerical Simulation
DVM	Discrete Vortex Method
FDM	Finite Difference Method
FEM	Finite Element Method
FIS	Fuzzy Inference System
FVM	Finite Volume Method
HAWT	Horizontal Axis Wind Turbine
LES	Large Eddy Simulation
MAC	Marker-And-Cell
MOGA	Multi-objective Genetic Algorithm
OPAL	Optimization Library
OR	Overlap Ratio
PEHD	Polyethylene High Density
PV	Photovoltaic
PVC	Polyvinyl Chloride
RANS	Reynolds Averaged Navier-Stokes
RPM	Revolution Per Minute
RBF	Radial Basis Function
RNG	Renormalized
SB	Semicircular-bladed
SC	Semicircular
SIMPLE	Semi-Implicit Method for Pressure Linked Equations
SIMPLEC	SIMPLE Consistent
SST	Shear Stress Transport
TSR	Tip Speed Ratio
VAWT	Vertical Axis Wind Turbine
WTT	Wind Tunnel Test

LIST OF FIGURES

LIST OF TABLES

CHAPTER –1

Introduction

Chapter Outline

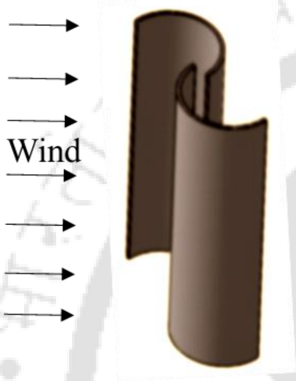

Overview

The wind energy is developing as one of the most cost-effective forms of clean and easily available renewable energies having a larger share in global annual installed capacity. Though wind energy conversion systems involving horizontal axis wind turbines (HAWTs) are leading the large scale and offshore wind market with their relatively higher efficiency, it is still equally important to advance the small-scale systems with vertical axis wind turbines (VAWTs) which can efficiently be exploited to provide easy and safe installation in limited spaces for grid-independent power production. In view of this, the Savonius wind turbines, a class of drag-based VAWTs, can be a feasible selection for off grid energy conversion in certain cases of limited space and low wind speed regions. This chapter gives an outline of the existing energy scenario, and the motivation behind the present study. This chapter also gives the objective of the present investigation and a detailed roadmap to attain the intended objective along with the layout of the thesis.

1.1 Motivation

In the past century, it has been seen that the utilization of non-renewable sources of energy has caused an environmental destruction greater than any other human activity. Electricity generated from fossil fuels such as coal and crude oil has emitted high concentrations of harmful gases in the atmosphere, notably CO_2 which is the main contributor to the global warming. Due to which many problems faced by today's world such as ozone depletion and global warming (Singh and Ahmed, 2013). Vehicular pollution has also been a major problem. Moreover, known reserves of fossil fuels of oil or coal are limited. Although fossil fuel reserves are estimated to last for another 60 years, a US-based study based on the known and expected reserves, and the current and expected rate of consumption, has calculated that these reserves can only last for another 30 years. Considering the low quality of coal that India has, it makes sound economic sense to explore and exploit other energy resources. Therefore, alternative sources of energy have become quite important and relevant to today's world. These sources, such as the solar and wind, can never be exhausted and therefore are called renewable (Karthikeyan *et al*., 2013). They cause less emissions and are available locally. Their use can, to a large extent, reduce chemical, radioactive, and thermal pollution. They stand out as a viable source of clean and limitless energy. These are also known as non-conventional sources of energy. Most of the renewable sources of energy are fairly non-polluting and considered clean and eco-friendly (Shahzad *et al*., 2013). In recent years, an interest in wind energy has been growing and many researchers have attempted the development of introduce cost-effective, non-polluting, environmental reliable wind energy conversion systems all over the world (Xu and Sankar, 2000; Gareth and Mishra, 2011). A wind turbine converts the kinetic energy of the wind to produce electricity by rotating the blades of turbines. The rotational energy produced by the rotation of blades is used to operate a mechanical device, such as a water pump, or to produce electricity by means of a generator. It is generally accepted that small-scale generation of wind power is desirable in a number of developing countries. Vertical axis wind turbines of the resistance-type have an important role to play in small-scale power development. Surveys of the available published literature on wind power reveal that, among vertical-axis wind turbine of the resistance-type, only a few have been subjected to scientific investigation. The only type that has been investigated with some degree of thoroughness is the Savonius rotor.

1.2 Present Energy Scenario

The worldwide demand for electricity is expected to triple by 2050, when the fossil fuels account for no more than 60% of all energy consumed, compared to 80% of the energy consumed today. The conventional fossil resources such as oil, natural gas, and coal are non-renewable, and they release a huge amount of pollutants into the atmosphere (Amano, 2017; Prabhukhot and Prabhukot, 2017). Wind energy technology plays a significant role in providing an environmentally friendly energy for domestic and industrial applications (Wong *et al*., 2017; Damak *et al*., 2018). Wind provides nearly 4% of global electricity supply and it has recently become the world's fastest-growing source of renewables. Overall, by the end of 2018, there were about 597 GW of wind power spinning around the globe (GWEC, 2017; WWEA, 2019). It is well known that the economy of a country is measured by the power it generates. As per the report published by Central Electricity Authority (CEA) of India, as on December 2018, the installed power generation capacity of India is 349288 MW of which 74081 MW is renewable energy-based power. There is an addition of 5.6 GW of wind energy in year of 2016-2017. It is to be noted that India's projected energy demand by 2022 is estimated to be 175 GW. Wind energy is the fastest-growing energy technology in the world by a factor of almost 200. It currently makes up a small percentage of our total energy picture, however, the rate at which it is growing promises to make it an important part of our energy mix in the future. During the last few decades, a considerable amount of research has been done on extracting the power from wind using wind turbines. Among the various renewable energy sources, about 47% of power is produced from the wind (CEA Report, 2018). Figure 1.1 shows the contribution of power from the renewable energy sources.

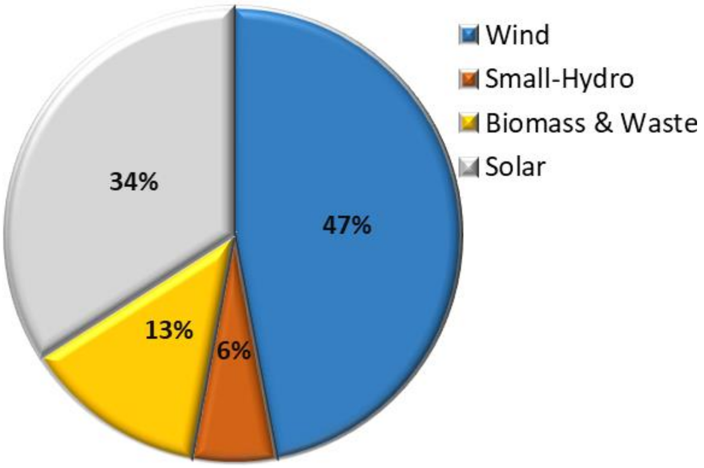

Figure 1.1: Contribution from various renewable energy source

1.3 The Savonius Wind Turbine Rotor

The Savonius rotor is the simplest of all the vertical axis wind turbines. It is named after S. J. Savonius who introduced it in the 1920s (Paraschivoiu, 2002). He reformed the design of Flettener's rotor by dividing a cylinder into half, along with its central axis and relocating the two semi-cylindrical surfaces sideways. This shape is akin to "S" when viewed from the top as shown in Fig.1.2. This type of rotors may be of two, three or higher bladed systems and can be used in single or multi-staged arrangements. The working principle is based on the difference of the drag force between the convex and the concave parts of the rotor blades when they rotate around a vertical shaft (Faizal *et al.*, 2010). These types of turbines are simple to construct, insensitive to wind direction and self-starting (Ogawa *et al.*, 1989). During the complete rotational cycle, various types of flow patterns such as coanda-type (The Coanda effect is the tendency of a fluid jet to stay attached to a convex surface), dragging, overlap, stagnation, and vortex flows are observed around the rotor. Figure 1.2 shows the geometric details of the conventional semicircular bladed Savonius rotor and Fig. 1.3 shows a typical 2-bladed Savonius rotor and drag differential on the rotor.

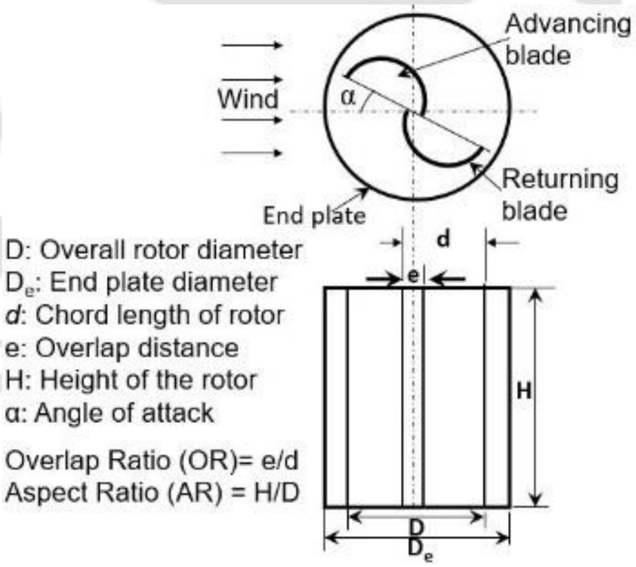

Figure 1.2: Geometric details of conventional Savonius rotor

The efficiency of the *VAWT* is comparatively lesser than *HAWT*. Among the *VAWT*s, Darrieus rotor has the more efficiency than the Savonius rotor. Due to their simple design and low construction cost, Savonius rotors are primarily used for water pumping and to generate wind power on a small scale. Its large starting torque makes it suitable for starting other types of wind turbines that have inferior starting characteristics, such as the Darrieus rotor and Gyro mill (Hayashi *et al*., 2005). Savonius rotors designed with three blades generate favorable torque characteristics. However, it has a poor maximum power coefficient compared to the VAWT with two blades (Ross and Altman, 2011). So, the number of rotor blades has a direct impact on the rotor performance. Akwa *et al*. (2012) affirmed that with the use of end plates on the Savonius rotor there has been an improvement of performance. With the use of twisted blade, the power co-efficient increases considerably (Saha *et al*., 2008).

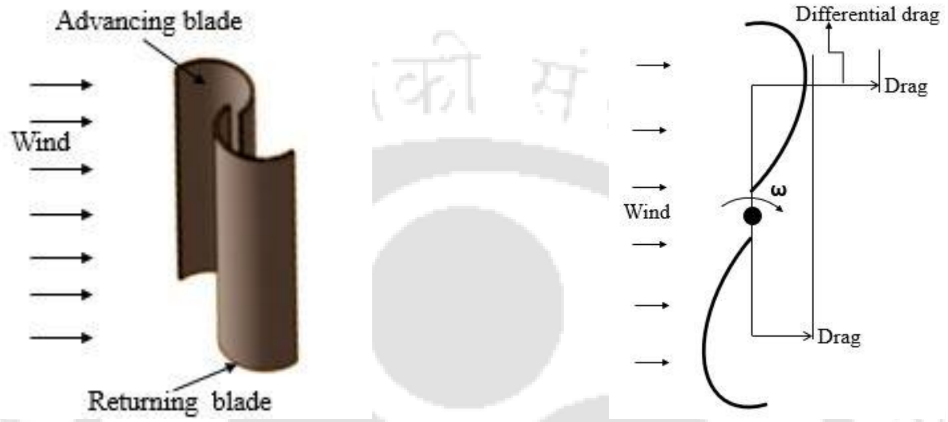

(a) 2-bladed Savonius rotor (b) Differential drag

Figure 1.3: A typical 2-bladed Savonius rotor and differential drag

1.4 Present Objective and Road Map

It is reported in the open literature that numerical simulation with various turbulence models, optimization techniques and soft- computing techniques play a quite crucial role in order to optimize the various parameters of Savonius rotor to find out the best suitable configuration. Even though the experimental investigation has revealed more accurate findings, nevertheless, the computational investigation has given the freedom to carry out a large-scale research with lesser experimental limitations and costs. Till date, various turbulence models such as one equation turbulence model, two-equation, and hybrid *CFD* turbulence models; and soft- computing techniques such as artificial neural network (*ANN*), fuzzy logic and adaptive neuro-fuzzy interface have been used by various researchers for improving the performance of Savonius rotor. It is also found that various numerical and experimental work has been carried out with various blade profiles of the Savonius rotor such as conventional semicircular (Savonius, 1928; Modi *et al*., 1984; Shaughnessy and Probert, 1992; Roy and Saha, 2013; Promdee and Photong, 2016), Bach (Kacprzak *et al*., 2013), Benesh (*Benesh et al*., 1996; Roy, 2014), and twisted (Grinspan *et al*., 2004), elliptical type (Kacprzak *et al*., 2013; Banerjee *et al*., 2014; Alom *et al*., 2016), fish-ridged rotor (Song *et al*., 2013), modified Bach type (Roy, 2014; Roy *et al.*, 2014) and others to enhanced the performance of the rotor. It was found that the elliptical-bladed profile has more potential to harness wind energy efficiently. At the same time, various augmentation techniques have also been used to improve the performance of the Savonius rotor. Notable among them are V-shape wedge deflector, curtains, concentrated and oriented jets, multi-staging, nozzle, venting slot, deflecting plate, guide vane and others (Fujisawa and Gotoh, 1994; Fujisawa *et al.*, 1995; Benesh *et al.*, 1996; Grinspan *et al.*, 2004; D'Alessandro *et al.*, 2010; Emmanuel and Jun, 2011; Irabu and Roy, 2011; Banerjee *et al.*, 2014; El-Askary *et al.*, 2015; Gupta, 2015; Gad-el-Hak, 2016; Ferdoues and Vijayaraghavan, 2016; Frikha *et al.*, 2016; Ducoin *et al.*, 2017). Hence, in the present investigation 2D unsteady simulations are conducted for the newly developed elliptical-bladed Savonius rotor to locate its optimum geometric and aerodynamic parameters and then the vent augmentation technique on the elliptical-bladed rotor has been implemented to reduce the negative torque of the rotor. Thereafter, the 3D unsteady simulations are carried out to predict the flow physics as well as the performance of the rotor. Further, the wind tunnel experiments are conducted to validate the numerical results. Finally, the multi-objective genetic algorithm has been applied to the optimized elliptical profile with the objective to minimize the incoming velocity and to maximize the output torque and lift coefficient. The road map of the present investigation is shown in Fig.1.4.

1.5 Organization of the Thesis

The present report has been organized by concentrating on the improvement in the design and efficiency of Savonius rotor. **Chapter 1** offers the motivation behind the work in the field of wind energy and a brief introduction of the present energy scenario and Savonius rotor. **Chapter 2** introduces the basic concepts of Savonius rotor, various blade profile and augmentation techniques. **Chapter 3** discusses the 2D unsteady investigations of various geometric parameters of the Savonius rotor. **Chapter 4** describes the 2D computational investigations of aerodynamic parameters of the Savonius rotor. **Chapter 5** outlines the 2D unsteady investigation of vent augmentation on elliptical profile. **Chapter 6** elaborates the 3D unsteady investigation of performance parameters, and C_D and C_L of elliptical-bladed rotor. **Chapter 7** highlights the experimental investigation of Savonius rotor. **Chapter 8** outlines the multi-objective genetic algorithm to minimize the incoming velocity and to maximize the torque and lift coefficients of the elliptical and semicircular bladed profile. **Chapter 9** summarizes the conclusions and some future scopes.

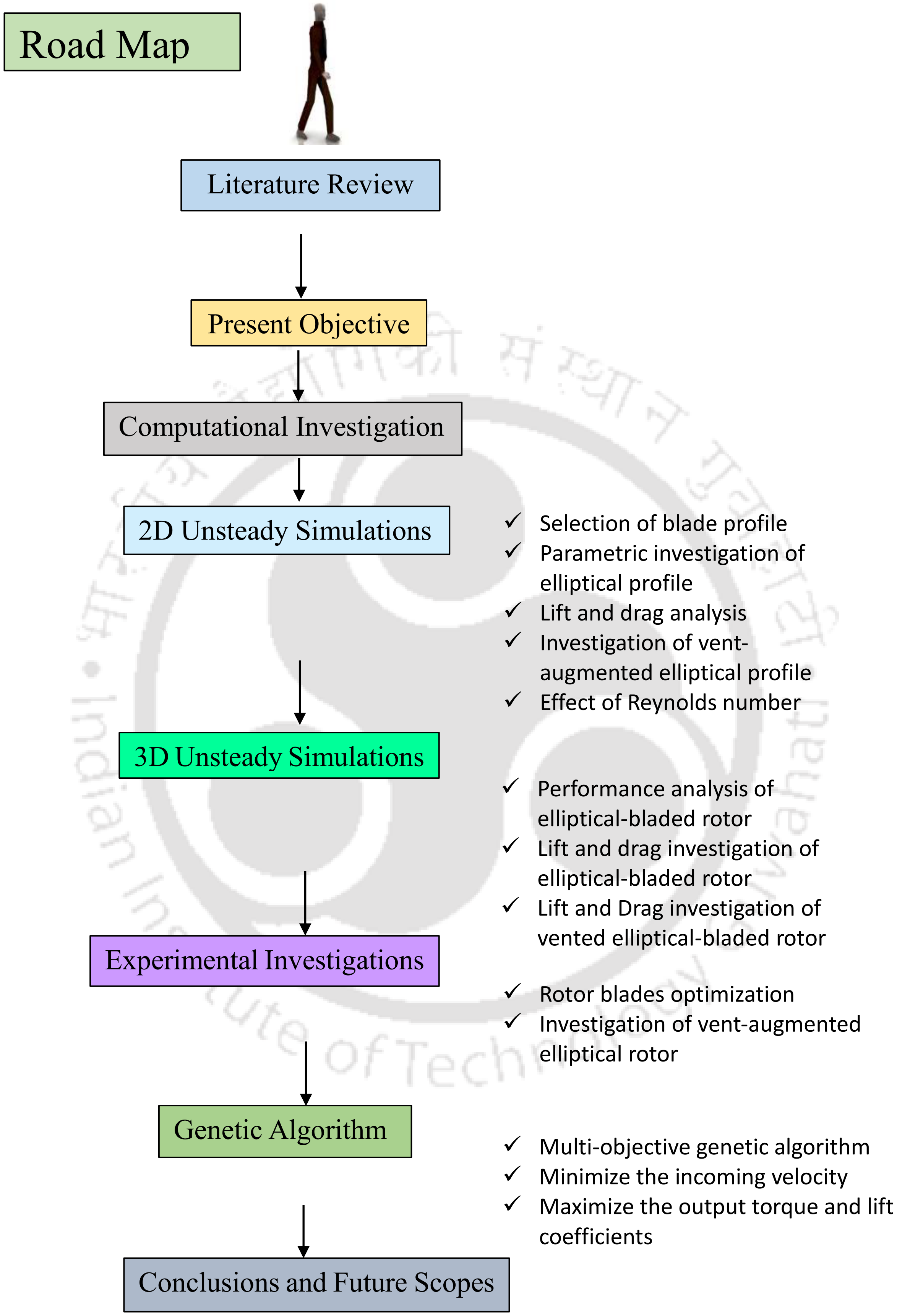

Figure 1.4: Road map of the present investigation

CHAPTER –2

Theory and Literature Review

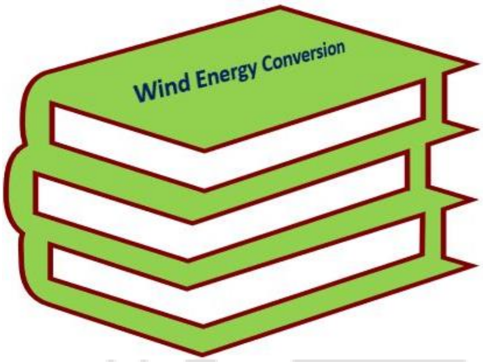

Chapter Outline

Overview

Since 1980s, a host of investigators have conducted numerical and experimental investigations to study and improve the design and performance of Savonius rotors. Nevertheless, most of these studies revolved mainly around the conventional semicircular bladed rotor. A few investigators have carried out numerical and experimental investigation with various geometric and aerodynamic parameters to improve its aerodynamic performance. Although noticeable performance gains were achieved, the designs reported seemed to have been more complex and expensive. Improvement in the performance coefficients and static torque characteristics were also reported with the use of various augmentation techniques. This chapter gives a thorough discussion on various issues reported in open literature.

2.1 Introduction

Though experimental investigation on various parameters have shown some improvements, but still for innovative research, computational studies are desirable for analysis of Savonius rotor. Till now different CFD methods such as finite volume method, finite element method, finite difference method; turbulence models such as one equation turbulence model, two-equation and hybrid CFD turbulence models and soft-computing techniques such as artificial neural network (ANN), fuzzy logic etc. have been carried out by several researchers for improving the performance of Savonius rotor. Combining all, this study will give a clear idea about the different computational methods applied and their effects in order to predict the performance of Savonius rotor as well as the flow physics around the rotor blades. Wind tunnel studies, as well as field tests, have been carried out by a host of investigators to assess the performance characteristics on several Savonius rotor configurations. The variables tested are blade tip speed ratio, aspect ratio, blade overlap, and separation gap, number of rotor blades, effect of shaft, Reynolds number, Blockage ratio, lift and drag and others. The details of the various geometric and aerodynamic parameters and optimization techniques are discussed in the consecutive sections and subsections.

2.2 Geometric Parameters

The performance coefficients (C_T and C_P) are mostly influenced by the various geometric parameters such as tip speed ratio (*TSR)*, overlap ratio (*OR*), aspect ratio (*AR*), number of blades, blade profiles, blade twist angle, the effect of end plates. These parameters are discussed subsections 2.1 and 2.5 with reference to the previous findings available in literature.

2.2.1 Tip speed ratio (TSR)

The tip speed ratio (*TSR = u/V*) is an important non-dimensional parameter that effects the rotor C_P. From the start of the study on Savonius rotor, various researchers have been investigated the *TSR* to find its optimum value. In this context, Sheldahl et al. found that the C_P is optimum at *TSR* ranging between 0.7-1.0. This analysis was further assured by numerous investigators (Fujisawa and Gotoh, 1994; Fujisawa *et al*., 1995; Roy and Saha, 2013, 2015; Huda *et al*., 1992; Kamoji *et al.,* 2008, 2009; Nasef *et al*., 2013; Banerjee *et al*., 2014). Fujisawa and Gotoh, (1994) numerically found that the optimum *TSR* is in the range of 0.8-0.9. Nasef *et al*. (2013) carried out unsteady simulations around a semicircular-bladed rotor using *SST k-ω* turbulence model and found that the optimum *TSR* = 0.90. Table 2.1 shows the researches on the effect of *TSR* by numerous investigators. From this table, it is observed that the C_P is optimum at *TSR* ranging between 0.7-1.0.

Table 2.1: Summary of optimum *TSR* as reported in literature

Authors	*Year*	*Optimum TSR*
Sheldahl et al.	1978	0.7-1.0
Sivasegaram and Sivapalan	1983	0.75
Huda et al.	1992	0.68-0.71
Fujisawa and Gotoh	1994	0.8-0.9
Fujisawa et al.	1995	0.9
Saha and Rajkumar	2006	0.65
Kamoji *et al.*	2008	0.64-0.69
Kamoji *et al.*	2009	0.7-0.9
D'Alessandro *et al.*	2010	0.9-1.02
Nasef *et al.*	2013	0.90
Banerjee *et al.*	2014	0.80
Jeon *et al.*	2015	0.67
Alom *et al.*	2016	0.80
Lee *et al.*	2016	0.45
Ricci *et al.*	2016	0.899

2.2.2 Aspect ratio (AR)

The aspect ratio (*AR =H/D*) of the Savonius rotor is an important geometric parameter. In general, the rotor moment and inertia decrease with the increase of *AR,* but the angular acceleration increases. At higher wind speeds, a higher *AR* rotor is desirable, and vice-versa. As observed in Fig. 2.1, the C_{Pmax} is obtained at *AR* = 0.80 for the semicircular bladed rotor (Roy and Saha, 2013). In 1978, Alexander and Holownia conducted wind tunnel tests on various Savonius rotor configurations at wind speeds of 6-9 m/s. The results show that the C_P is low for low *AR* in case of unshielded rotors without end plates (C_{Pmax} = 0.065 for *AR*=1.2). However, at high *AR* (= 4.8) and with optimum blade shielding configuration, the C_{Pmax} is found to be 0.243.

2.2.3 Overlap ratio (OR)

The overlap ratio ($OR = e/d$) plays a crucial role in the enhancement of C_P of rotor. The static torque coefficient (C_{TS}) increases in single-stage rotor due to the increase in overlapping distance. This is due to the fact that as the overlapping distance increases, the wind flow that passes through the gap is increased. When the wind flows through the gap, it will act on the concave side of the returning blades and generate an effective thrust force. It was reported by Jian *et al.* (2012) that the rotor with $OR = 0.167$ has the capacity to generate the maximum C_P for the one-stage rotor (Fig. 2.2).

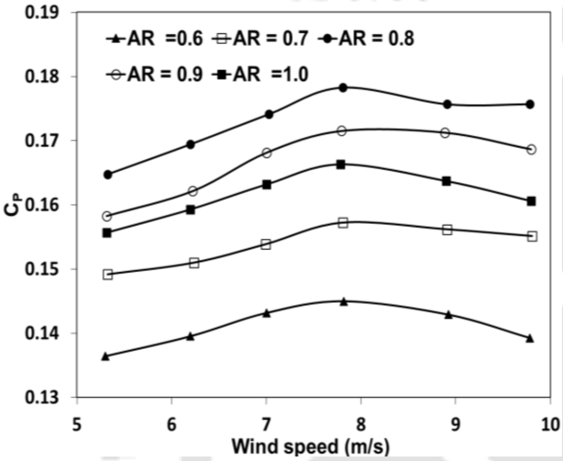

Figure 2.1: C_P vs wind speeds of various *AR* (Roy and Saha, 2013)

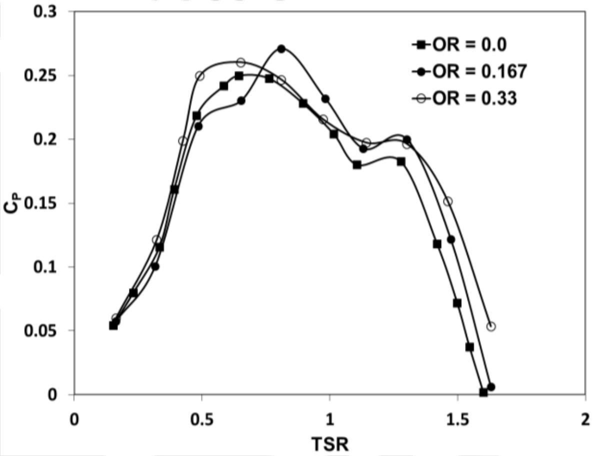

Figure 2.2: C_P vs *TSR* at various *OR* (Jian *et al.* 2012)

Numerous investigations (Ushiyama *et al.*, 1982; Ushiyama and Nagai, 1988; Fujisawa *et al.* 1995; Roy and Saha, 2013) have reported that the 20% overlap on Savonius rotor has important enhancement of C_P over without overlapped systems at velocities 4-8 m/s. Most of the numerical investigations have been carried out using *SST k-ω* turbulence model to find the optimum *OR* (Khan *et al.*, 2013). In most cases, the performance of the rotor is found to be at $OR = 0.15$ (Fujisawa *et al.* 1995; Khan *et al.*, 2013). It is also reported that with the increase of *OR* between 0.1 to 0.5, the C_{TS} increases (Kamoji *et al.*, 2009). For helical bladed rotor, $OR = 0.0$ shows higher C_P than the $OR = 0.1$ and 0.15 (Kamoji *et al.*, 2009).

2.2.4 Number of rotor blades

The C_T and C_P of the Savonius rotor are influenced by the number of rotor blades. The number of blades is usually varied from 2 to 4. As the number of blades is increased to three, the wind which strikes on one blade gets reflected on the succeeding blade, as a result the succeeding blade rotates in negative direction (Saha *et al.*, 2008). Also, vortices are formed behind the returning blades, which reduced the C_P of the rotor. The unsteady simulations are conducted by using multi-physics *FVM* solver ANSYS Fluent with the help of *SST k-ω* turbulence model, found that the 2-bladed Savonius rotor has higher C_P than the 3- and 4-bladed rotor performance. From C_P point of view, the 2-bladed rotor is superior in most of the cases. The maximum C_P for 2-bladed rotor is nearly 1.5 times that of the 3-bladed rotor. Saha et al., 2008 also found that the 2-bladed rotors have higher C_P than the 3-bladed system (Fig. 2.3). For a C_{Pmax}, the *TSR* increases when the numb er of blade is reduced from 3 to 2. However, in 1978, Sheldahl et al. reported a higher static torque in a 3-bladed than the 2-bladed system.

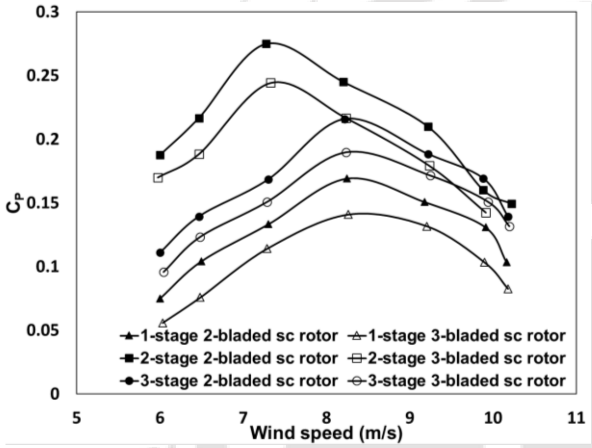

Figure 2.3: Comparison of 2- and 3-bladed Savonius rotors (Saha *et al.*, 2008)

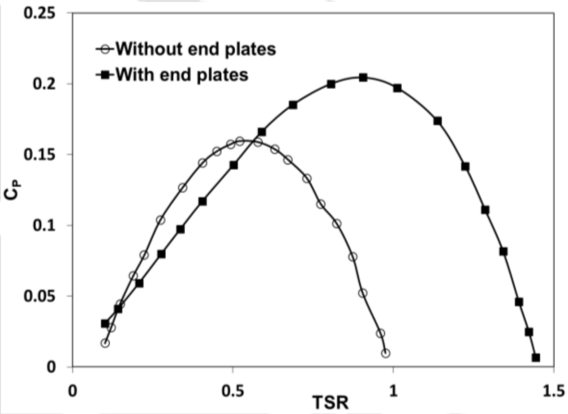

Figure 2.4: Effect of end plates on Savonius rotor performance (Ushiyama and Nagai, 1988)

2.2.5 Effect of end plates

The end plate is an important component attached to either end of a Savonius rotor to enhance the rotor performance. The plates at the rotor ends stop the leakage of air from the concave side of the rotor to the exterior flow, keeping the pressure difference between rotor blades at reasonable levels over the height of the rotor. With the addition of end plates, the rotor also functions more efficiently at higher *TSR*. As shown in Fig. 2.4, the end plates significantly increase the C_P of the rotor. The end plate diameter is generally chosen to be 1.1 times the rotor diameter. It is reported that very high diameters of end plates can dramatically increase the rotor inertia (Alexander and Holownia, 1978; Ushiyama and Nagai,1988) and reduce its performance.

2.2.6 Blockage ratio

The outcome of wall confinements is a significant factor in wind tunnel tests (*WTT*s). Thus, without the blockage ratio (*BR*), the results of *WTTs* suffer from inaccuracy (Jian *et al*., 2012; Jeon *et al*., 2015). Therefore, an appropriate blockage correction method is imperative for all wind tunnel tests, including both closed and open test sections. Ross and Altman, (2011) presented a review paper studying various blockage correction methods such as the wall pressure method, Pope's method, and Maskell's methods for Savonius rotors using their own wind tunnel test results. One of the major parameters affecting the data is the blockage. To have some appreciation of the wall confinement effects, models with an identical geometric shape but with different blockage ratios were tested in boundary layer wind tunnel. According to Sheldahl *et al*. (1978) the finding of *BR* is challenging when a complex shape such as Savonius rotor is tested. Modi *et al*. (1984) investigated extensively the blockage effects in *WTTs*. It was reported that the model with the same size and shape but with a different *BR* showed different results due to the increase in local velocity with blockage. It was found that with the increase in wall confinement from 5% to 20%, the maximum C_P went up to 70% (Fig. 2.5). Plourde *et al*. (2012) reported the influence of *BR* on the actual wind speed to be equivalent to the ratio of the frontal area of the rotor to the cross-sectional area of the wind tunnel. In their experimentation, a *BR* of 0.23 was considered for better power output. Kamoji *et al*. (2008; 2009) performed experiments by considering *BR*s from 20–35% and found that the C_{TS} was enhanced from 0.29 to 0.37 when the *BR* increased from 20% to 35% at Reynolds number = 1.2 x 10^5. Roy and Saha, (2014) developed blockage correlation for an open type test section of their wind tunnel under dynamic loading. The experiments were conducted by considering *BR* = 21.16%, 16% and 12.25%. The blockage effects were found quite much significant and increased with the increase of *BR* and *TSR*. Further, the blockage effects were found negligible at lower *BR* and at lower *TSR*. Ross and Altman, (2011) investigated the wind tunnel blockage effects in a close type test section, and reported its effects to be insignificant for the models within 2% and 3.5% of *BR*. However, the *BR* at 8% and 10% caused some changes in experimental results due to large pressure drops and increase in freestream velocity. The summary of various geometric parameters is shown in the Tables 2.2 and 2.3.

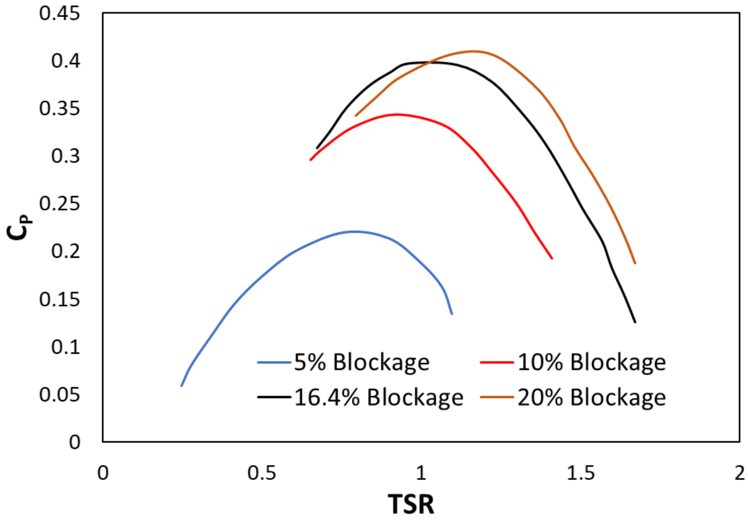

Figure 2.5: Effect of *BR* on the power output of the Savonius rotor (Modi *et al*., 1984)

Table 2.2: Summary of influencing parameters based on experimental investigations

Influencing parameters	*Range*	*Researcher(s)*	*Year*	*No. of blades*	*Optimum performance value*	*C_{Pmax}*
Tip speed ratio	0.4-0.9	Alexander and Holownia	1978	2	0.52	0.147
		Modi and Fernando	1989	2	0.79	0.32
		Fujisawa and Gotoh	1994	2	0.8-0.9	0.17
		Rajkumar and Saha	2006	2	0.65	0.14
		Kamoji *et al.*	2009	2	0.9	0.175
		Damak *et al.*	2013	2	0.4-0.45	0.25
		Jeon *et al.*	2015	2	0.67	0.132
		Lee *et al.*	2016	2	0.45	0.13
Aspect ratio	0.7-1.83	Alexander and Holownia	1978	2	1.2	0.147
		Modi *et al.*	1983	2	0.91	0.16
		Modi and Fernando	1989	2	0.77	0.32
		Grinspan *et al.*	2004	2	1.83	0.1159
		Saha *et al.*	2008	2, 3	1.58	0.19
		Kamoji *et al.*	2009	2	0.88	0.175
		Damak *et al.*	2013	2	1.57	0.25
Overlap ratio	0.0-0.3	Alexander and Holownia	1978	2	0.20	0.147
		Mojola	1985	2	0.25	0.267
		Modi and Fernando	1989	2	0.0	0.32
		Fujisawa and Gotoh	1994	2	0.15	0.17
		Jian *et al.*	2012	2	0.167	0.25
		Damak *et al.*	2013	2	0.242	0.25
Rotor angle	30°-50°	Fujisawa and Gotoh	1994	2	30°-50°	0.17
Reynolds number		Hayashi *et al.*	2005	2	280000	0.16
		Kamoji *et al.*	2009	2	202000	0.2
		Damak *et al.*	2018	2	121000	0.096

Table 2.3: Summary of influencing parameters based on numerical investigations

Influencing parameter	*Researcher(s)*	*Year*	*CFD methodology*	*No. of blades*	*Optimum performance value*
Tip speed ratio	Modi and Fernando	1989	2D discrete vortex formulation	2	1.2
	Zhao *et al.*	2009	FVM with 3D standard *k-ϵ* model	2 3	0.81 0.55
	Dobrev and Massouh	2011	*FVM* with 3D *DES/k-ω SST* model 2D *k-ω SST* model 3D *k-ω SST* model	2	0.8
	Enamuel and Jun	2011	*RNG k-ε*	6	0-0.60
	Kianifar *et al.*	2011	*FVM* with 2D standard *k-ϵ* model	2	0.80 to 1.2
	Mahamed *et al.*	2011	*FVM* with 2D realizable *k-ϵ* model	2/3	0.70/0.80
	Banerjee *et al.*	2014	2D *k-ω SST* model	2	0.80
	Ferrari *et al.*	2017	2D *k-ω SST* model	2	0.80
Aspect ratio	Zhao *et al.*	2009	*FVM* with 3D standard *k-ϵ* model	2	0.60
	Dobrev and Massouh	2011	*FVM* with 3D *DES/k-ω SST* model	2	0.91
	Ferrari *et al.*	2017	3D *k-ω SST* model	2	1.1
Overlap ratio	Fujisawa	1992	FVM and fractional time step	2	0.15
	Menet and Bourabaa	2004	*FVM* 2D two-equation model	2	0.242
	Kianifar *et al.*	2011	*FVM* with 2D standard *k-ϵ* model	2	0.20
	Yakhot *et al.*	1992	*FEM* 3D model	2	0.21
	Enamuel and Jun	2011	*RNG k-ε* model	6	0.16
	Morteza *et al.*	2012	*2D* Reynolds Stress Method	2	0.25
Rotor angle	Altan and Atilgan	2008	*FVM* with 2D Standard *k-ϵ* model	2	45°
	Shaheen *et al.*	2015	2D *k-ω SST* model	2	60°
Reynolds number	Akwa *et al.*	2012	FVM method	2	867000

2. 3 Aerodynamic Parameters

The aerodynamic parameters such as Reynolds number (*Re*), lift and drag forces (D_f and D_L) of Savonius rotor have a strong influence on the Savonius rotor performance. In the light of the reported investigations, they are discussed in the following subsections 3.1 and 3.2.

2.3.1 Reynolds number

The Reynolds number (*Re*) is a significant dimensionless parameter for defining the flow behavior of fluid flow conditions. Generally, with the increase of *Re*, the aerodynamic performance (C_P) increases (Huda *et al*., 1992). As reported, in the range of *TSR* = 0.68 to 0.71, the maximum C_P increases from 15.2% at *Re* =0.8×105 to 17.5% at *Re* =1.5×105 (Huda *et al*., 1992). Further, Kamoji *et al.* (2009) demonstrated an increase of C_P with the increase of *Re* from 0.57×10^5 to 2.019×10^5. This is due to the fact that for the given rotor diameter, with the increase in *Re*, the flow separation is delayed around the rotor blades at high speeds (Fig. 2.6). Sheldahl *et al.* (1978) also reported an increase of C_{Pmax} with the increase in *Re* from 57,700 to 202,000; and at *Re* = 202,000, the maximum C_P (=0.2) occurred at *TSR* = 0.71. Hayashi *et al.* (2005) reported an increase of C_{Pmax} with the increase of *Re* for 1-, 2- and 3-stage Savonius rotors. All these studies and facts were for semicircular-bladed rotors only.

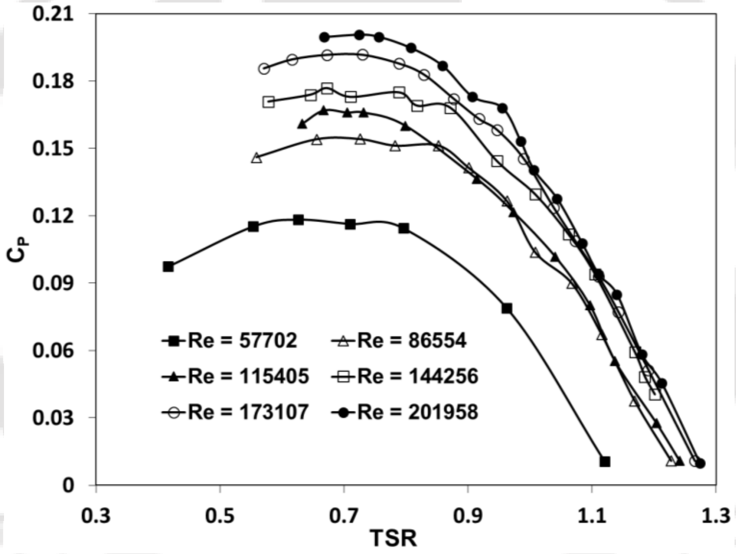

Figure 2.6: C_P vs *TSR* at several *Re* (Kamoji *et al*., 2009)

2.3.2 Drag and lift

Based on aerodynamic forces, the *VAWT*s are categorized into the lift- and drag-based devices. The drag-based rotors are Savonius and Sistan rotors; whereas, the lift-based rotors are H- and Darrieus rotors. Although the drag-based rotors have better self-starting proficiencies than the lift-based *VAWT*s, they have lesser performances. Savonius rotor mainly operates with the application of drag force (D_f), but it also experiences a lesser amount of lift force (D_L). The drag force (D_f) and lift force (L_f) is a function of the relative wind speed at the surface of rotor blades (the difference among the wind speed, *V,* and the speed of the rotor surface, $u = \omega r$) (Manwell *et al*., 2009). The mechanism of drag force generation is shown in Figure 2.7. The drag and lift coefficients can be expressed as follows (Manwell *et al.*, 2009; Roy and Saha, 2013).

$$C_D = \frac{D_f}{\frac{1}{2}\rho A(V-u)^2} \qquad (2.1)$$

$$C_L = \frac{L_f}{\frac{1}{2}\rho A(V-u)^2} \qquad (2.2)$$

The study on drag and lift characteristics of Savonius rotors have been quite few and are limited to semicircular-bladed rotor only. In 1989, Chauvin and Benghrib first addressed the effect of drag and lift coefficients (C_D and C_L) on the semicircular-bladed Savonius rotor from the pressure difference at the upper and the lower surfaces of the rotor. For a semicircular-bladed rotor, Irabu and Roy, (2011) found experimentally the C_{Dmax} to be 1.56 when angle of attack, α = 90° and 270° at *OR* of 0.0. It was also noticed that with the increase of *OR,* the C_D got reduced. The maximum and minimum C_L is found to be around 0.6 and 0.2 at an *OR* of 0.0 and 1.0, respectively. Jaohindy *et al*. (2013) numerically investigated the effect of C_D and C_L in a semicircular-bladed rotor, where C_{Dmax} is found to be around 2.2 in the range of α = 60°-70° and at *TSR* = 0.6. At the same *TSR,* the C_{Lmax} was around 1.72 at α = 30° and 210°. Recently, Roy and Ducoin, (2016) performed 2D unsteady simulation to estimate the C_D and C_L for a newer blade profile. This profile (known as Roy profile) reported a C_{Dmax} of 2.24 at α = 80°. At *TSR* = 0.60, the C_{Lavg} and C_{Lmax} for the Roy profile were found to be 1.19 and 2.07.

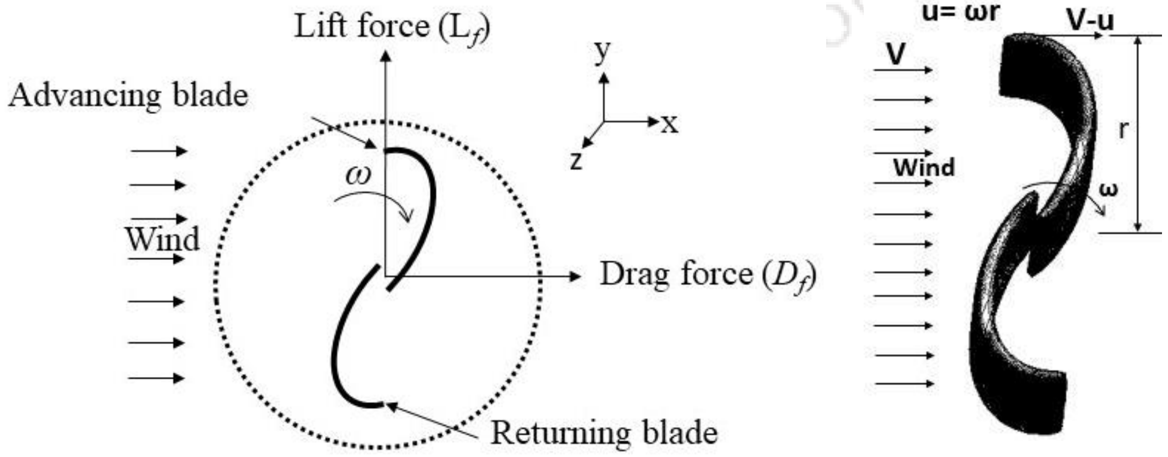

Figure 2.7: Illustration of lift force, drag force and relative wind speed

2.4 Evolution of Blade Profiles and Shapes

Since its inception, several blade profiles have been evolved to enhance the performance of the Savonius rotor. Some of the notable rotor blades investigated by several researchers are conventional semicircular (Newman, 1974; Cheng *et al*., 2018), Bach, (Bach, 1931), Benesh, (1988, 1989, 1992), twisted (Grinspan *et al*., 2004), modified Bach (Roy and Saha, 2015), fish-ridge rotor (Song *et al*., 2013), Roy (Roy, 2014; Roy and Saha, 2015), elliptical (Kacprzak *et al*., 2013; Banerjee *et al*., 2014; Alom *et al*., 2016) and others. All these blade profiles are demonstrated in Fig. 2.8. An elementary study with an elliptical profile has shown its energy harvesting potential, and hence, a higher performance as compared to other profiles. In another numerical study, it is found that the elliptical profile has 10.7% more performance than the conventional semicircular profile (Banerjee *et al*., 2014). Therefore, the elliptical-bladed rotor can be a strong contender in the forthcoming designs of Savonius rotor.

2.4.1 During 1929 -1991

Semicircular rotor

In 1925, S. J. Savonius first developed the conventional rotor consisting of 2 semicircular buckets or blades (Fig. 2.8a). This design was stimulated by the Flettner ship and built over the cutting of the Flettner cylinder in half and touching sideways. Savonius found the C_{Pmax} to be 0.31. However, the wind tunnel investigation conducted by Simonds and Bodek, (1964) in the Brace Research Institute found that the C_{Pmax} is 0.14 at *TSR* = 0.7. Newman, (1976) also explored the Savonius rotor at several *OR*s. It was found that the C_{Pmax} ranges from 0.17 to 0.30 for the conventional *SB* (semicircular-bladed) rotor.

Bach type rotor

After six years of Savonius rotor development with SB, G. Bach (Bach, 1931) conceived a new rotor-blade design in 1931. This rotor, known as Bach rotor, consisted of a straight line and an arc (Fig. 2.8c). Experiments conducted in McGill University wind tunnel demonstrated the C_P for Bach rotor to be higher than the *SB* rotor at lower and higher *TSR*. However, the *SB* rotor had a higher C_P than the Bach rotor at an intermediate *TSR*. In 1986, Ushiyama *et al*. found the C_{Pmax} for Bach rotor to be higher by 9% than the *SB* rotor in the range of *OR* = 0 to 0.3. Modi and Fernando, (1989) conducted the *WTT*s to optimize the geometric parameters of Bach rotor. Table 2.4 shows the summary of various investigations conducted on Bach type rotors.

(a) Semicircular (1929) (b) Semicircular (1930) (c) Bach (1931)

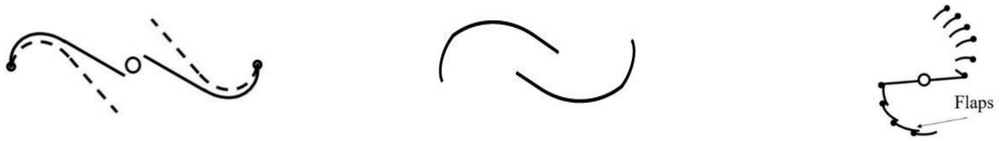

(d) Swinging (1985) (e) Benesh (1988) (f) Slatted (1991)

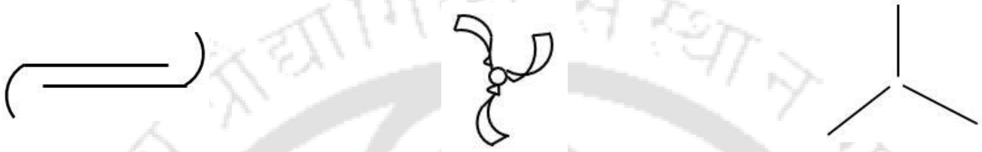

(g) Benesh (1996) (h) Twisted (2004) (i) Sistan (2009)

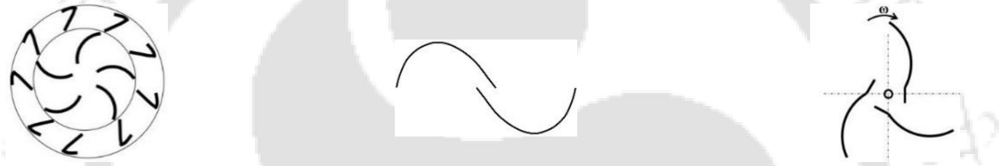

(j) Zephyr rotor (2010) (k) Elliptical (2013) (l) Fish-ridged (2013)

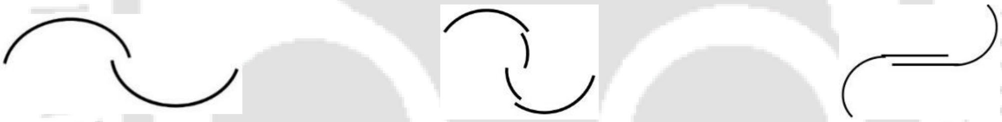

(m) Semi-elliptic 2013 (n) Slotted (2013) (o) Modified Bach (2014)

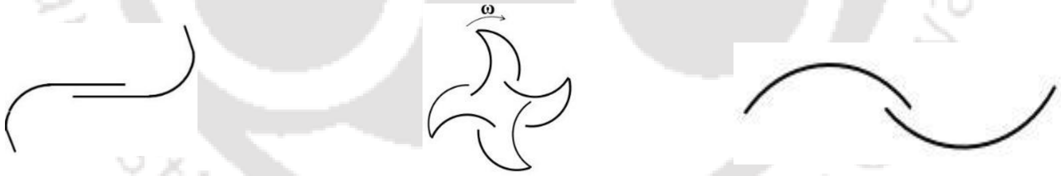

(p) Roy profile (2014) (q) Bronzinus (2014) (r) Incurved (2014)

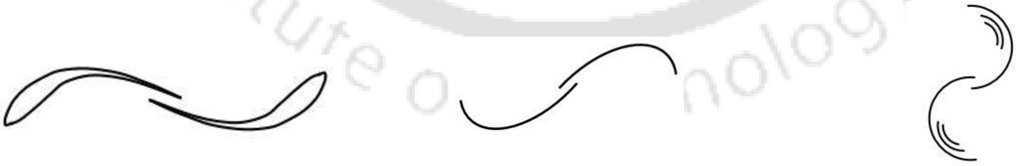

(s) Airfoil shape (2015) (t) New Elliptical (2016) (u) Multiple quarter semicircular (2016)

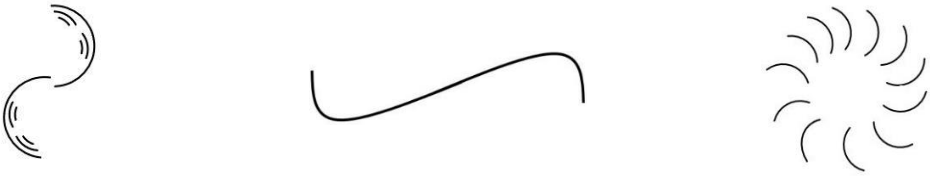

(v) Multiple miniature semicircular (2017) (w) Spline (2017) (x) Banki (2017)

Figure 2.8: Evolution of Savonius rotor profiles

Table 2.4: Reported data of Bach type rotors

Investigators	*Years*	*OR*	*TSR*	C_{Pmax}
Fernando and Modi	1989	0.0	0.79	0.36
Kamoji *et al.*	2009	0.0	0.69	0.21
Zhou and Rempfer	2013	0.0	0.75	0.263
Kacprzak *et al.*	2013	0.0	0.80	0.215
Roy and Saha	2015	0.20	0.72-0.80	0.30

Swinging rotor

Aldoss, (1984) and, Aldoss and Najjar, (1985) developed a novel Savonius rotor profile named as swinging bladed rotor (Fig. 2.8d). With the intention of improving the C_P of the rotor, experiments have been performed to reduce the drag on the upwind blade and to increase the drag on the downwind blade. This is conducted in such a way that the rotor blades swing back when they are on the upwind stroke. The optimum swing angles for the upwind and downwind blades are found to be 50° and 13.5°, respectively. At the optimum blade swing angle, the maximum C_P of the rotor is increased to 23.5% in comparison to the optimum blade swing alone.

Benesh rotor

In 1988, A. H. Benesh, (1988, 1989, 1992) patented a Savonius rotor profile comprising of a straight line and two arcs (Fig. 2.8e). This Benesh profile has not received much attention in terms of research. However, more than two decades later, Roy and Saha, 2015 conducted wind tunnel experiments to investigate the Benesh, modified Bach, semicircular and semi-elliptical profiles. The test results demonstrated the C_{Pmax} to be 0.29 and 0.23 for Benesh and semicircular rotors, respectively. However, the C_{Pmax} of the Benesh profile is found to be lesser than modified Bach nevertheless higher than the other rotors. It was also reported that for the Benesh rotor, the starting capability got improved and the negative C_{TS} got reduced than the semicircular and semi-elliptical rotors. Rahai and Hefazi, (2005) carried out *WTTs* on semicircular and Benesh rotors without and with spanwise slots when the *OR*s are 0.0 and 0.48. It was reported that the C_{Pmax} for Benesh and semicircular rotors are 0.31 and 0.27, respectively in the range of *TSR* = 0.8–1.2.

Slatted-bladed rotor

Instead of using the continuous rotor blade, Reupke and Probert, (1991) established the multiple flaps rotor (Fig. 2.8f). To enhance the wind harvesting capacity, the flaps were hinged in place of the curve part of the rotor. Due to this, the negative drag force of the rotor got reduced because of the wind pressure on the advancing blade, when the rotor advanced towards the wind. The investigation was carried out using sixteen-hinged and thirty-two-hinged flaps in a 2-bladed rotor system. This flaps system enhanced the static torque in comparison to conventional *SB* rotor; however, its C_P was found to be lesser. The C_P for the flapped rotor and semicircular rotor was found to be 5% and 18%, respectively (Fig. 2.9). The modified system, thus, was found improper for harvesting wind power. Tabassum and Probert, 1987 reported an improvement of static torque by 35% for a Bach type rotor with four-hinged flaps over the original rotor of the same geometry and at the same wind speed of 6.67 m/s.

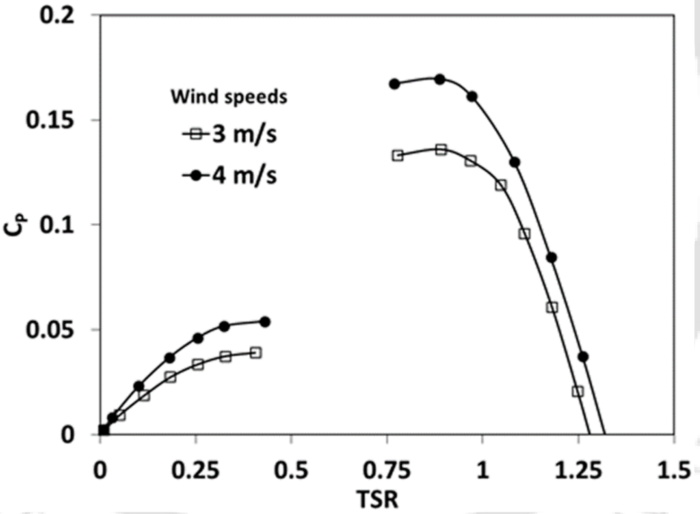

Figure 2.9: C_P vs *TSR* of flaps rotor system at various wind speed (Reupke and Probert, 1991)

2.4.2 During 1996 -2010

Twisted-bladed rotor

The twisted blade (Fig. 2.8h) has shown the advantage of decreasing the negative torque and augmenting the self-starting capability of a Savonius rotor (Grinspan *et al*., 2004; Saha *et al*., 2008; Kamoji *et al*., 2009; Damak *et al*., 2013; Lee *et al*., 2016). In 2004, Grinspan et al. performed *WTT*s for twisted bladed rotor at the twist angle of 10.28° with various gap width (s) from s = 14 to 67 mm (Fig. 2.10). Later, Saha *et al*. (2008) performed *WTT*s for twisted-bladed rotor (twist angle is 12.5°) and reported C_P = 0.19 for the twisted bladed rotor as compared to C_P=0.18 for the *SB* rotor. Kamoji *et al*. (2009) conducted *WTT*s for twisted-bladed rotor (twist angle of 90°) by changing the *OR* = 0.0 to 0.16 and the *AR* = 0.88 to 1.2. At *Re* = 1.5 x10^5, the test results demonstrated C_{Pmax} =0.179 for the twisted rotor (*AR* = 0.88; *OR* = 0.0). In general, the *WTT* demonstrated a higher C_P and an improved self-starting capability of the twisted bladed rotor as compared to the *SB* rotor. It was reported that the rotor with a twist angle of 180^0 had part of downwind surface revealing to the wind at any rotational angle because of 180^0 (Zhao *et al*., 2009; Damak, *et al*., 2013). Also, the helical rotor of twist angle of 180^0 looked like a construction built by two half heights of 90^0 rotors. The C_{Pmax} was found to be around 0.18 at the twist angle of 180^0 (Zhao *et al*., 2009) (Fig. 2.11). The summary of twisted bladed rotor is shown in Table 2.5.

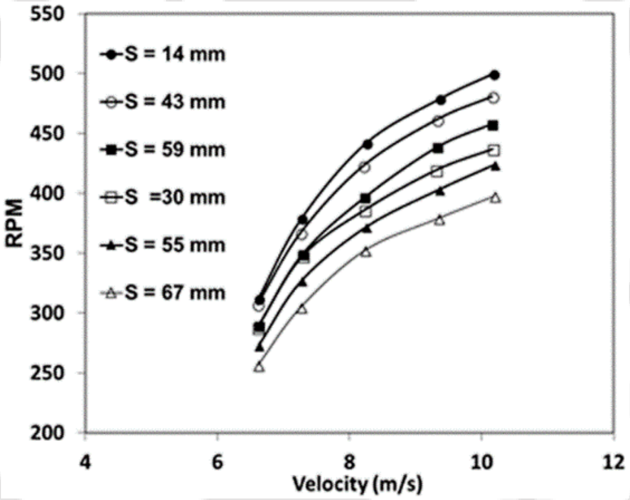

Figure 2.10: *RPM* vs velocity of twisted bladed rotor with various gap width (Grinspan *et al*., 2004)

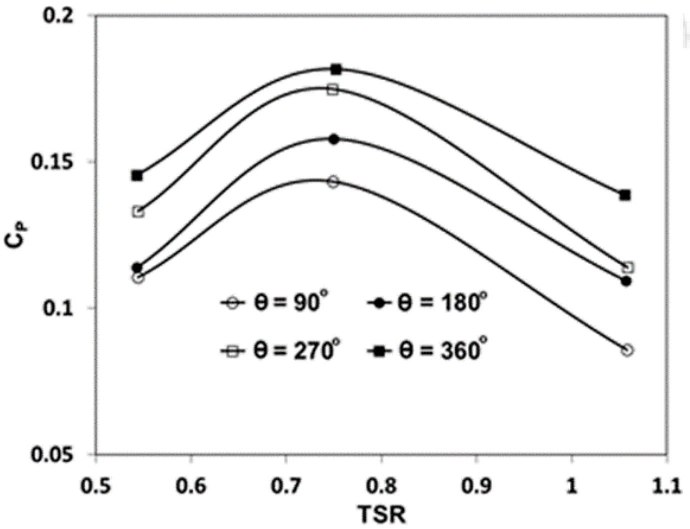

Figure 2. 11: The effect of helical angle on C_P (Zhao *et al*., 2009)

Table 2.5: Reported data of twisted bladed rotors

Investigators	*Year*	*Twist angle (degree)*	*TSR*	*OR*	*AR*	C_{Pmax}
Grinspan *et al.*	2004	10.28	--	0.0	1.83	0.12
Rajkumar and Saha	2006	15	0.65	--	1.83	0.14
Saha *et al.*	2008	12.5	--	--	1.58	0.19
Kamoji *et al.*	2009	90	0.9	0.0	0.88	0.175
Zhao *et al.*	2009	180	0.8	0.3	2.0	0.18
Damak *et al.*	2013	180	0.4-0.45	0.242	1.57	0.25
Jeon *et al.*	2015	180	0.67	--	2.0	0.132
Lee *et al.*	2016	45	0.45	0.167	1.33	0.13
Ricci *et al.*	2016	105	0.899	8.2%	2.6	0.251

Sistan rotor

As mentioned in the introduction section, the original straight-bladed *VAWTs* developed in the Sistan province of Iran were drag-based (Fig. 2.8i). These Sistan rotors capture the wind energy with their individual rotor blades that move slower than the wind (Muller *at al.*, 2009: Chong *et al.*, 2013; Gupta, 2015). It was probably for the first time in 2009, Muller *et al*. tried to explore the performance of a Sistan rotor experimentally. The C_{Pmax} for the Sistan rotor was found to be 0.42. In 2013, Chong et al. used power-augmentation-guide-vane (PAGV) around a Sistan rotor to enhance the rotor performance by amplifying the incoming wind speed. Both the experimental and numerical investigations demonstrated the PAGV to be proficient in enhancing the rotational speed, torque and power output of the Sistan rotor. The PAGV had increased the rotational speed of the rotor by 1.75 times, whereas the rotor torque and power output were amplified by 2.88 and 5.8 times, respectively.

Zephyr rotor

Pope *et al.* (2010) investigated a novel *VAWT* known as Zephyr (Fig. 2.8j) to estimate its operating performance and power output. They conducted 2D and 3D unsteady simulations using k-ε and time average *S-A* turbulence models to calculate the power output. The results obtained from the numerical investigations were compared with their experimental data. The mean velocity was used to perform numerical simulations. From their investigations, the C_P of the rotor was found to be 0.12 at a wind speed of 14 m/s.

2.4.3 During 2013 -2017

Fish-ridge rotor

It was not long ago, Song *et al*. (2013) developed the fish-ridge rotor (Fig. 2.8l) in the pursuit of increasing the C_P of a Savonius rotor. This was done by changing the geometric profiles and number of blades. The rotor blade looked like a fish ridge and comprised of 2-arc-shaped vanes. Although the lengths of the vanes were dissimilar, their radii were equal. The rotor consisted of 3-blades and they were organized regularly around the central axis. The C_{Pmax} for the fish-ridge rotor was found to be 0.231 when the radius of curvature of blade was set at 192.5 mm (Fig.2. 12). The $C_{Pmax,}$ at the optimum geometric parameters such as radius of curvature, arc angle, chord length, was found to be 0.24.

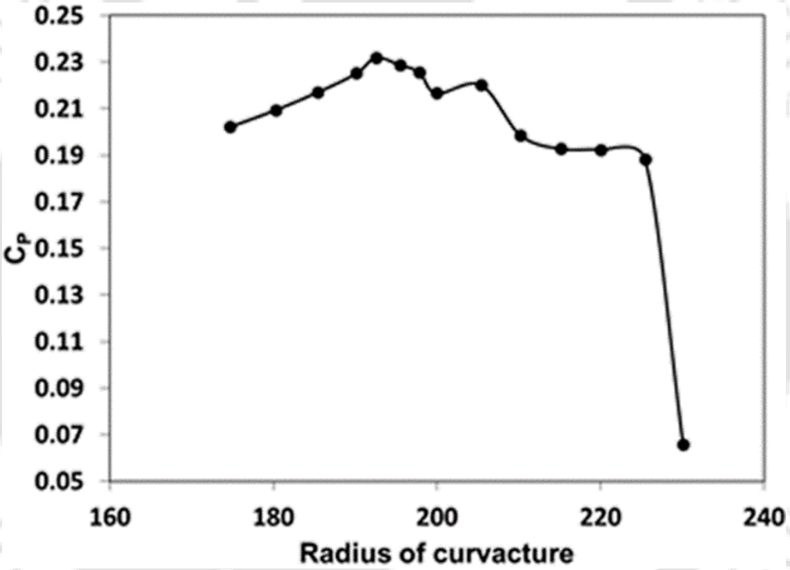

Figure 2.12: Optimization of radius of curvature (Song *et al.,* 2013)

Semi-elliptic bladed rotor

In 2013, Sahim *et al.* used the semi-elliptic rotor (Fig. 2.8m) to enhance the static torque capacity of a combined Darrieus-Savonius rotor. The polyvinyl chloride (*PVC*) material was used to manufacture the semi-elliptic segment with the semi-major axis 66 mm and semi-minor axis 53 mm, so as to make rotor *AR*=0.8. The test results indicated the influence of the distance of Savonius rotor blades from the shaft center on C_P of the combined rotor. It was reported that with the inclusion of the Savonius rotor, the self-starting capability of the Darrieus rotor was augmented at low wind speed. However, the *WTT* conducted by Roy and Saha, (2015) found the C_{Pmax} for the semi-elliptical-bladed rotor to be 0.26 at *TSR* = 0.70-0.75.

Elliptical-bladed rotor

Around the same time when semi-elliptic rotor came into limelight, Kacprzak *et al*. (2013) established the elliptical-bladed rotor (Fig. 2.8k) to improve the wind energy capturing capability. Soon after, Banerjee et al., 2014 established a dissimilar category of elliptical-profile by cutting an ellipse at an angle of θ =50° and found an improvement of C_P by 10.70% in comparison to the conventional semicircular profile. Inspired by the work of Kacprzak *et al.* (2013), Banerjee *et al*. (2014) and Alom *et al*. (2016) optimized the elliptical-bladed rotor numerically by varying θ and reported a gain in C_P by 18.18% over the semicircular-profile at θ = 47.5° (Fig. 2.13). Thus, the elliptical-profile seems to be a strong competitor in the future designs of Savonius rotor.

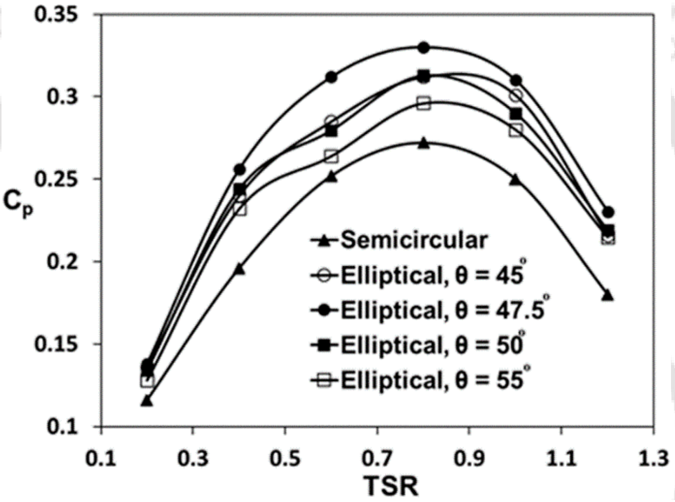

Figure 2. 13: *Cp* vs *TSR* at various sectional cut angle of ellipse (Alom *et al*., 2016)

Slotted-bladed rotor

Alaimo *et al.* (2013) proposed a novel blade profile, named as the slotted bladed rotor (Fig. 2.8n). In their investigation, the static and dynamic simulations were conducted for the rotor by varying the slot position using the commercial code COMSOL. The numerical simulation showed an improvement of the static torque with the location of the slot near the blade root. However, at the dynamic condition, the optimized slotted blade had shown improved performance at low angular velocity than the conventional Savonius rotor.

Incurved-bladed rotor

In 2014, Driss *et al.* proposed an incurved blade for the Savonius rotor (Fig. 2.8r). This comprised of two half incurved blades characterized by the height (*H*) =300 mm, chord length (*d*) = 100 mm and the blade arc angle = 120°. The blades were connected in a common axis with a shaft diameter equal to 10 mm. The Solid works flow simulation were conducted using the standard *k-ε* turbulence model to investigate the flow physics around the rotor. The unsteady results had shown an improved flow field around the incurved rotor than the semicircular-rotor.

Bronzinus rotor

Gerardo and Molfino, (2014) recommended a novel blade profile known as Bronzinus (Fig.2.8q). This design, developed in 2014, by comparison and optimization of conventional Savonius rotors. The Bronzinus single wind turbine blade comprised of 4-blades, and thus, the whole rotor was made up of 8-blades with dimension *H*=710 mm; *D* = 300 mm. The numerical study was carried out using *CFD* tool for five rotor models. To assess their flow physics, a total of 25 simulations were carried out for each of the five turbines by varying the wind speed from 1 to 25 m/s. The simulated result showed a higher C_P (= 0.25) of the Bronzinus than the conventional Savonius rotor (Fig. 2.14).

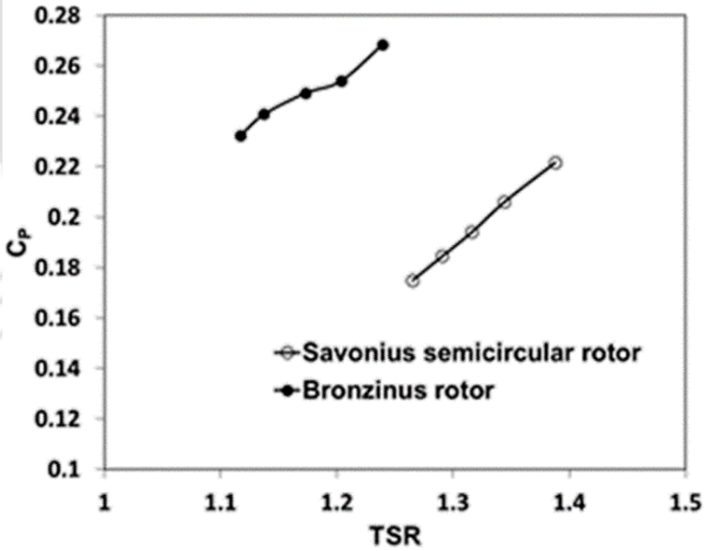

Figure 2.14: C_P vs *TSR* of Bronzinus rotor (Gerardo and Molfino, 2014)

Modified Bach rotor

Roy and Saha, (2013), and Roy *et al*. (2014) have developed a new blade profile from the basic Bach profile, and they named this as the modified Bach profile (Fig. 2.8o). To achieve this profile, unsteady simulation is performed on the basic Bach type profile by changing the overlap distance from 0 to 0.5*d* (*d* =blade chord length) and blade arc angle from 90° to 165°. The simulated results show an enhanced design of the Bach type rotor at an overlap distance of 0.4d and a blade arc angle of 135°. The modified Bach type profile has shown an improvement of C_P and C_T than the conventional semicircular profile at optimum TSR = 0.72-0.80 (Roy and Saha, 2015). The C_{Pmax} is found to be 0.30 at the TSR range of 0.72-0.80.

Roy rotor

After a series of numerical and experimental studies with Bach and Benesh rotors, the research group at IIT Guwahati (Roy and Saha, 2015; Roy, 2014) has come up with a novel blade profile, termed as the Roy profile. The profile (Fig. 2.8p) comprised of numerous individual arcs, where all the dimensions are specified in terms of the blade chord length (*d*). This profile is created by changing the geometric arcs, overlap distances, and magnitudes of blade profiles. Due to alternation of blade arc, the Roy profile could increase the static C_T and reduce the negative torque of the rotor. The C_{TS} of novel blade profile is found higher by 31.6%, 22.0%, 11.1% and 4.2% than the semicircular, semi-elliptical, Benesh and modified Bach type, respectively; whereas the C_{Pmax} of the profile is found to be 0.31 at the range of TSR = 0.75-0.82 (Fig. 2.15).

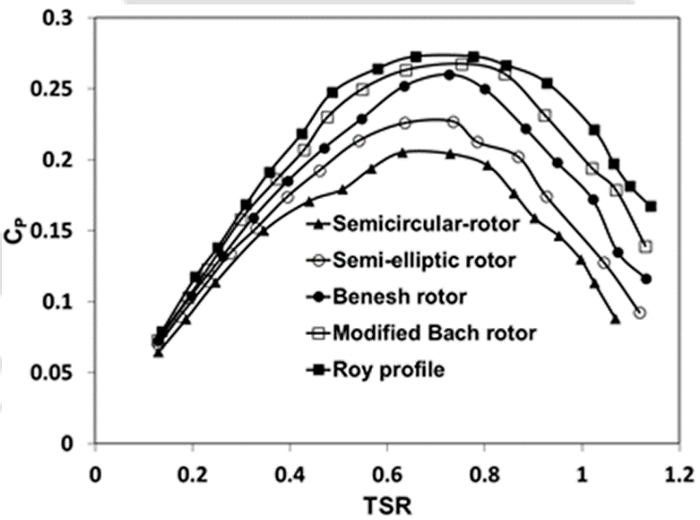

Figure 2.15: Variation of C_P with TSR of several rotor profile (Roy and Saha, 2015)

Airfoil shaped rotor

In the year 2015, Turtuferi *et al.* redesigned the Goettingen 462 airfoil by increasing the camber by 30% above the chord length where attention was mainly focused on the suction side curvature and to the leading-edge radius. The novel airfoil section (Fig. 2.8s) was categorized by a 33% camber and placed at 45% of the chord line, and hence it was designated as SR3345 airfoil. The camber was moved towards the tip of the rotor to increase the torque contribution in certain angular positions, of low-pressure zones of the airfoil suction side. The second airfoil section was designated as SR5050 airfoil since it had 50% camber and placed at 50% of the chord line and was obtained by comprising the thickness distribution of the NACA 0012 airfoil over a mean camber line of suitable shape (Fig. 2.16). The C_{Pmax} was found to be around 0.22 for the SR3345 and around 0.25 for the SR5050 (Fig. 2.17).

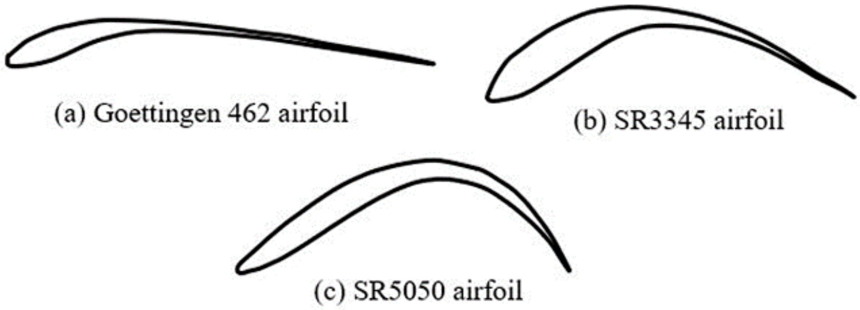

Figure 2.16: Various airfoil shapes of Savonius rotor (Turtuferi *et al.*, 2015)

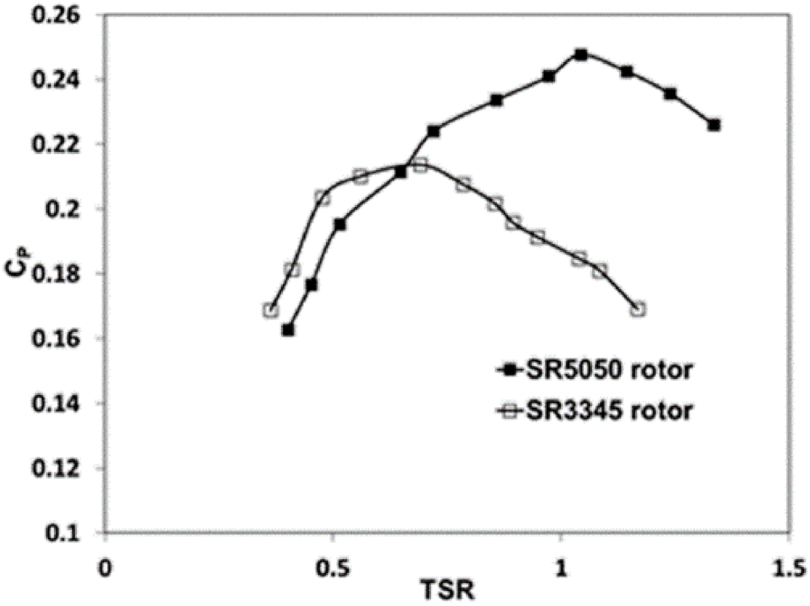

Figure 2.17: C_P vs TSR of Savonius rotor using two SR profiles (Turtuferi *et al.*, 2015)

Multiple quarter semicircular-bladed rotor

Sharma and Sharma, 2016 proposed a new profile for its use in Savonius rotors. As seen in Fig. 2.8u, this profile was developed by the inclusion of two extra quarter circular profile inside the *SB* rotor. Unsteady simulations, using *SST k-ω* model, were conducted with this profile whereby the C_{Pmax} was found to be 0.23. In this study, an improvement of C_P by 8.89% was obtained in comparison to the semicircular profile when they were tested at a wind of wind speed of 8.23 m/s (Fig. 2.18).

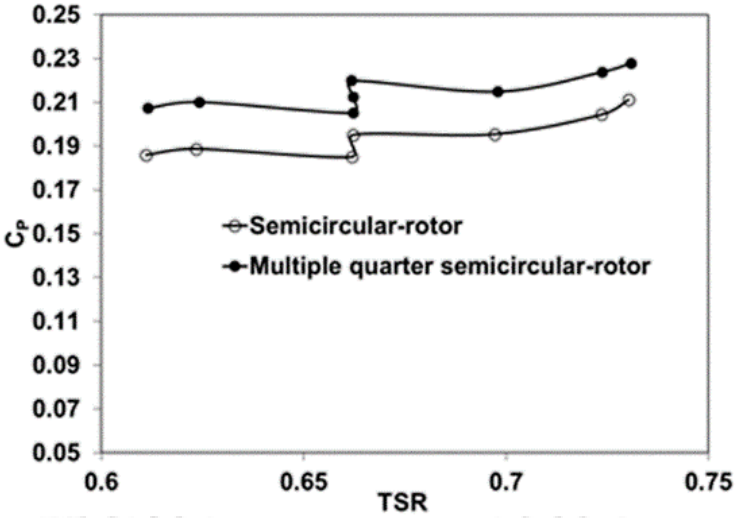

Figure 2.18: Variation of C_P with *TSR* of multiple quarter rotor (Sharma and Sharma, 2016)

Multiple miniature semicircular-bladed rotor

A year later, Sharma and Sharma, (2017) proposed one more design of Savonius rotor profile that consisted of two concentric layers with the actual rotor profile (Fig. 2.8v). The layers comprised of two co-radial small blades separated circumferentially by a small distance. The unsteady simulation was conducted with this profile using *k-e* and *SST k-ω* turbulence models reported a C_{Pmax} of 0.226 at the same wind speed of 8.23 m/s. There was a performance enhancement of 8.92% than the semicircular-profile (Fig. 2.19).

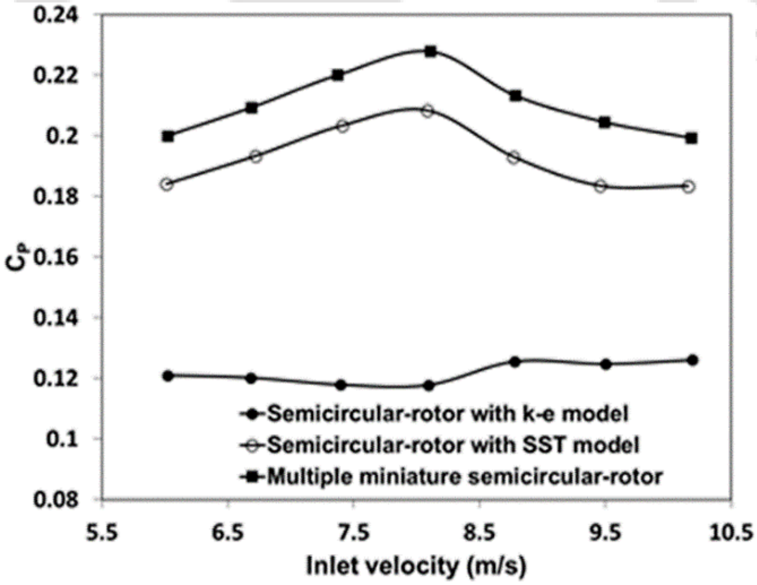

Figure 2.19: Variation of C_P with inlet velocity of multiple miniature rotor (Sharma and Sharma, 2017)

Spline-curved rotor

Very recently in 2017, Mari *et al*. proposed a novel Savonius rotor profile, named as spline-curved rotor (Fig. 2.8w). Unsteady simulations are conducted for spline 20, spline 30, and spline 40 by varying the angle defining spline curve blade geometry. The Spallart-Allmaras *(S-A)* turbulence model is used to carry out the simulations. The numerical results show the C_{Pmax} to be 0.25 for spline 40 (Fig. 2.20).

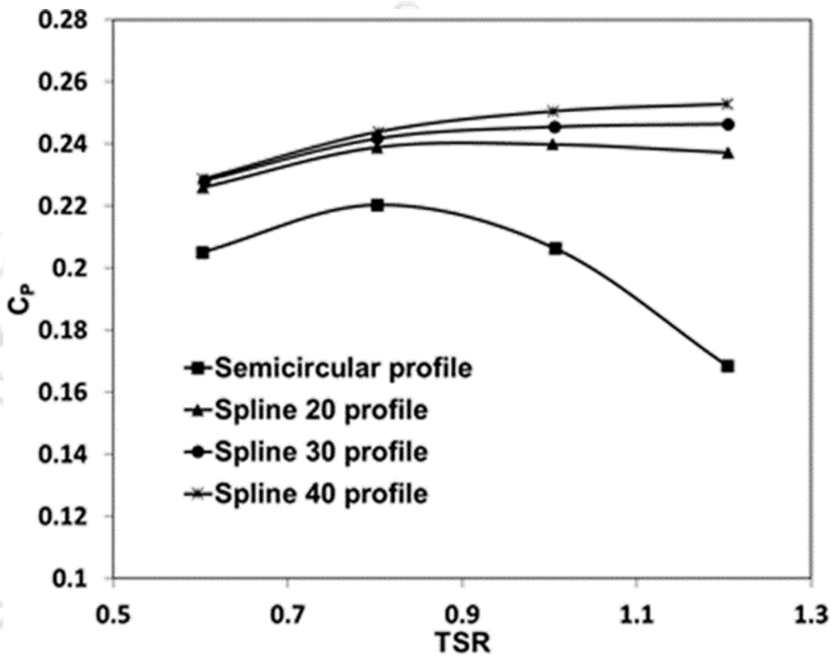

Figure 2.20: C_P vs *TSR* of various spline curves
(Mari *et al*., 2017)

Banki rotor

Tian *et al*. (2017) for the first time used the Banki rotor as a *VAWT* (Fig. 2.8x). In their investigation, a total of 20 blades was chosen in the rotor to harvest the energy from the wake produced by the vehicles in the highways. Unsteady numerical simulations were performed using commercial ANSYS Fluent to estimate the power generation. From the unsteady simulation, it has been found that the *VAWT* of Banki type could produce an average power of 139.60 W.

The key findings with the use of various blade profiles and shapes of vertical-axis Savonius rotors are summarized in Table 2.6.

Table 2.6: Summary of investigated rotor profiles

Blade profile	*Year*	*Investigator(s)*	*Figure*	*Methodology*	*TSR*	*OR*	*AR*	C_{Pmax}
Semicircular	1978	Alexander and Holownia	Fig. 2.8a	Experimental	0.52	0.20	1.2	0.147
Semicircular	1984	Owaga	Fig. 2.8b	DVM	0.0	--	1.0	0.17
Twisted	2004	Grinspan *et al.*	Fig. 2.8h	Experimental	--	0.0	1.83	0.1159
Bach	2013	Kacprzak *et al.*	Fig. 2.8c	CFD (2D)	0.80	0.0	--	0.178
Fish-ridged	2013	Song *et al.*	Fig. 2.8l	CFD (2D)	0.5	--	--	0.23
Elliptical	2013	Kacprzak *et al.*	Fig. 2.8k	CFD (2D)	0.80	0.15	--	0.172
Semi-elliptical	2013	Sahim *et al.*	Fig. 2.8m	Experimental	0.80	--	0.8	0.08
Modified Bach	2014	Roy *et al.*	Fig. 2.8o	Experimental	0.72-0.80	0.4d	1.0	0.30
Roy (New)	2014	Roy	Fig. 2.8p	Experimental	0.75-0.82	0.68d	1.0	0.31
Bronzinus	2014	Gerardo and Molfino	Fig. 2.8q	CFD (2D)	--	0.20, 0.30	--	0.25
Airfoil shape	2015	Tartuferi *et al.*	Fig. 2.8s	CFD (2D)	0.65	--	--	0.22
New elliptical	2016	Alom *et al.*	Fig. 2.8t	CFD (2D)	0.80	0.20	--	0.33
Multiple quarter semicircular	2016	Sharma and Sharma	Fig. 2.8u	CFD (2D)	--	--	--	0.2266
Multiple miniature semicircular	2017	Sharma and Sharma	Fig. 2.8v	CFD (2D)	--	--	--	0.226
Spline-curved	2017	Mari *et al.*	Fig. 2.8w	CFD (2D)	1.0	0.0	1.0	0.2477
Banki rotor	2017	Tian *et al.*	Fig. 2.8x	CFD (3D)	0.0625	--	1.5	0.0004

2.4.4 Principal observations on blade profiles/shapes

(a) With respect to *AR*, at higher wind speed, higher *AR* models are found suitable; whereas at low wind speed, the lower *AR* models are found more suitable. The optimum *AR* (for C_{Pmax}) of the semicircular and twisted bladed rotors is found to be 0.80 and 1.5-2.6, respectively. Further, the optimum *TSR* for semicircular, Bach, twisted and elliptical profiles are 0.7-1.0, 0.72-0.80, 0.899 and 0.80 respectively at the C_{Pmax}.

(b) The static torque of the rotor is improved by the existence of the overlap distance. This is mainly caused by the augmented pressure on the concave side of the returning blade, and due to the flow through the overlap. The optimum *OR* lies in the range of 0.15-0.25 depending upon the working conditions.

(c) In general, with the increase in *Re*, the C_P is found to improve, however, the optimum *Re* is found to be in the range of $1.2 \times 10^5 – 2.02 \times 10^5$. Although the drag is the main driving force, the Savonius rotor is not a pure drag-driven device, and there is a little lift force that contributes to the rotor C_P.

(d) Amongst the turbulence models used for numerical simulation, it was mostly the *SST k-ω* model that gave better prediction capabilities than the other turbulence models.

(e) The twisted bladed profile has improved the C_P of the rotor marginally by reducing the rotor negative torque. The C_{Pmax} for a twisted bladed rotor is found to be 0.251 at the twist angle of 105°.

(f) The airfoil shape might improve or reduce the rotor C_P and therefore it requires in-depth analysis computationally and experimentally.

(g) The Roy profile might be potential contender for small-scale stand-alone applications in both rural and urban areas. There seems to be an improvement of starting torque by 31.6% than the conventional semicircular profile.

(h) The newly developed elliptical-bladed rotor shows an approximate C_P of 0.33. This profile shows an improvement of 18.18% in comparison to the semicircular profile.

(i) The spline profile may enhance the C_P of the rotor; however, a thorough investigation is necessary with its various profile configuration.

(j) The blade profiles of Savonius rotor can be optimized by using evolutionary algorithms such as *ANFIS* and *GA* to improve the C_P.

(k) The new elliptical and Roy profiles are recommending their use in the Savonius rotor to enhance their C_P. However, thorough and systematic studies need to be done to arrive at their optimum geometric and aerodynamic parameters. Having arrived at a suitable design configuration, both geometrically and aerodynamically, suitable augmentation techniques can also be implemented for enhancing their performance further.

2.5 Augmentation Techniques

The Betz limit shows the maximum performance of a wind turbine to be 59.3%, however, this limit can be exceeded by an augmentation system. An augmenter concentrates the wind flow and increases the mass flow through its area. Since the power generated by a wind turbine is proportional to the cube of the incoming wind speed, a slight increase in the incoming wind speed can significantly improve the turbine performance. The wind pressure exerted to the concave part of the returning blade of a Savonius rotor produces a high negative torque and this drops its total power. By means of an augmenter, the negative drag of the rotor is decreased by avoiding the air from striking the returning blade of the rotor. The starting capability of the Savonius rotor is improved with the aid of these techniques. Hitherto, several augmentation techniques such as V-shaped deflector, nozzle, multi-staging, twisted blades, valve, curtain plates, windshields, obstacle shield, venting slot, flat plate shield, concentrator, flaps and guide vanes and others (Fig. 2.21) have been used to improve the C_P.

It was sometime around 1978 that Alexander and Holownia used a combination of flat and a circular shields (Fig. 2.21) and reported a maximum C_P of 0.243. Morcos *et al.* (1981) also used a wind shields in front of the rotor and reported a maximum C_P of 0.34 (Fig. 2.21b). *Ogawa et al.* (1986) and Huda *et al.* (1982) also used the deflector plate (Fig. 2.21c) and reported a maximum C_P of 0.212 and 0.21, respectively. When multiple flaps are used instead of using continuous rotor blade, the negative drag of the rotor is reduced (Reupke and Probert, 1991) (Fig. 2.21d). The use of V-shaped wedge deflector (Fig. 2.21e) at the upstream of the rotor harnessed about 19.7% more power than a standard rotor without a deflector. Shikha et al., 2003 used a convergent nozzle (Fig. 2.21f) at the front of advancing blade of a six-bladed Savonius rotor to enhance the power extraction at low wind speeds. The use of two-stage rotor (Fig. 2.21g) developed an improved torque and power coefficients in comparison to a single-stage rotor (Menet, 2004).

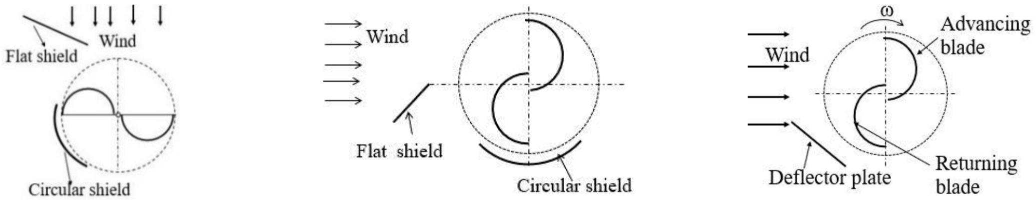

(a) Wind shields
(Alexander and Holownia,1978)

(b) Wind shields
(Morcos *et al.*, 1981)

(c) Deflector plate
(Ogawa and Yoshida, 1986)

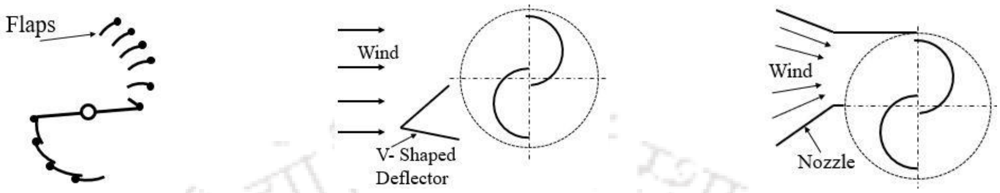

(d) Slatted blade
(Reupke and Probert, 1991)

(e) V-shaped deflector
(Shaughnessy and Probert, 1992)

(f) Nozzle
(Shikha *et al.*, 2003)

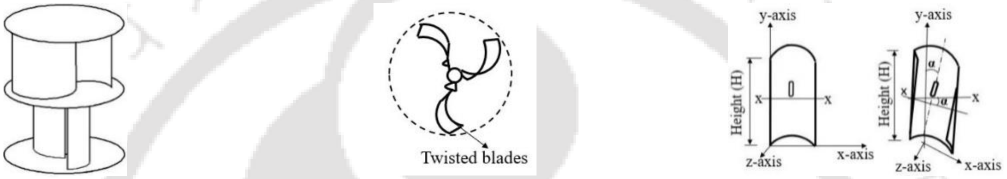

(g) Multi-staging
(Menet, 2004)

(h) Twisted blades
(Grinspan *et al.*, 2004)

(i) Valve
(Rajkumar, and Saha, 2006)

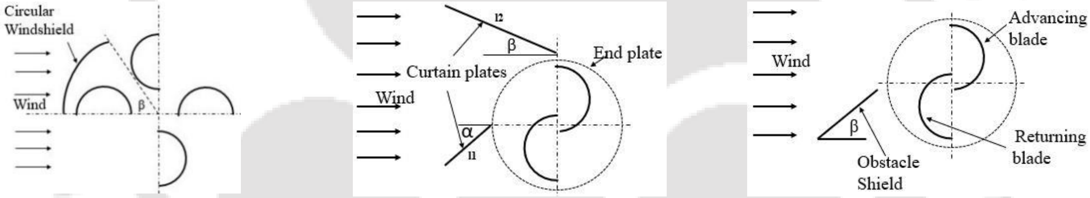

(j) Circular windshield
(Hu *et al.*, 2009)

(k) Curtain plates
(Altan and Atilgan, 2010)

(l) Obstacle shield
(Mohamed *et al.*, 2010)

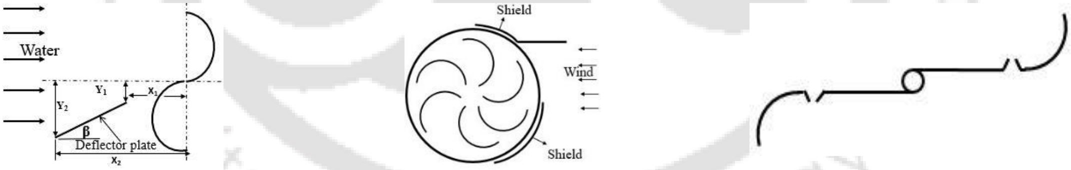

(m) Deflector plate
[Golecha *et al.*, 2010]

(n) Shield
[Emmanuel and Jun, 2011]

(o) Venting slots
[Abraham *et al.*, 2012]

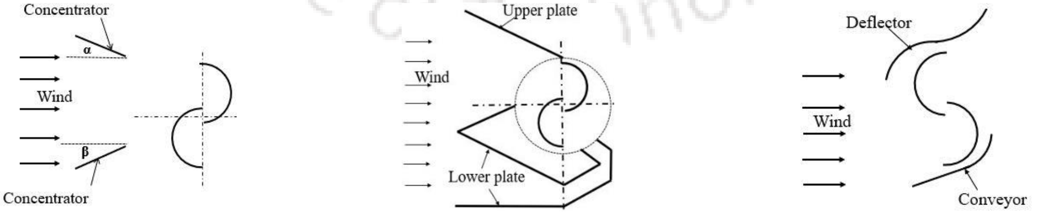

(p) Concentrators
(Roy *et al.*, 2014)

(q) Guide vane
(El-Askary, 2015)

(r) Conveyor-deflector curtain
(Tartuferi *et al.*, 2015)

Figure 2.21: Various types of augmentation techniques

Twisted bladed (Fig. 2.21h) rotor has proved to have a better self-starting capacity than the semicircular bladed rotor (Grinspan *et al.*, 2004). Again, the use of valves (Fig. 2.21i) in semicircular blades reduces the negative torque on the rotor (Rajkumar and Saha, 2006). Circular windshield (Fig. 2.21j) has been also employed to reduce the wind pressure that exerts on the returning (or driven) blade of the rotor (Golecha *et al*., 2011). The use of curtain plate at the rotor front allows a maximum amount of wind to impinge on the advancing blade thereby reducing the negative torque (Altan and Atilgan, 2010). It is reported that the use of obstacle shield (Fig. 2.21l) at the front of returning blade improves the rotor performance up to 30% (Mohamed *et al*., 2010). Golecha *et al*. (2011) used a deflector plate (Fig. 2.21m) in front of the advancing blade and reported a 50% increase in performance than the semicircular bladed rotor. It was also reported that with the use of shield (Fig. 2.21n) in a six-bladed Savonius rotor, the C_P could reach upto 0.50 (Emmanuel and Jun, 2011). Abraham et al., 2012 studied the effect of venting (Fig. 2.21o) on a Savonius rotor both experimentally and numerically to reduce drag on the returning blade. Roy *et al.* (2014) employed concentrators (Fig. 2.21p) in the rotor front and reported a maximum C_P of 0.32. Guide vane (Fig. 2.21q) also improves the performance of the rotor (El-Askary *et al*., 2015). The conveyor-deflector curtain (Fig. 2.21r) in a conventional Savonius rotor improved the C_P up to 0.30 (Tartuferi *et al*., 2015). The summary of various augmentation techniques employed till date with their corresponding C_{pmax} is shown in Table 2.7 in a chronological manner. These techniques are discussed briefly in the following section.

2.5.1 Wind shields and deflector plates

The obstacle shield located ahead of the returning blade may be of flat or circular type or both to decrease the active pressure on it. Alexander and Holownia, (1978) performed experiments in a low-speed wind tunnel and found a performance improvement 74% with a shielded Savonius rotor of high *AR* (Fig. 2.21b). Morcos *et. al*. (1981) also used similar type of shields to cover the returning blade of the rotor and reported a maximum C_P of 0.34 (Fig. 2.22). Hu *et al.* (2009) carried out a numerical simulation using *RNG k-ε* turbulence model around a conventional Savonius rotor with a circular shield. The simulation was carried out for different inclination angle β = -90°, -45°, 0°, 15°, 30°, 45° and 60° to optimize β (Fig. 2.21j) and found an improvement of 107% at β = 30°. Similarly, Mohamed *et al.* (2010 and 2011) used the obstacle shield (Fig. 2.21l) in front of the returning blade to reduce the negative torque of the rotor. It was reported that optimally placed obstacle shield improves the C_P by 27.3% for the 2-bladed system at *TSR*= 0.7 (Fig. 2.22).

Table 2.7: Various augmentation techniques and observation

Investigators	***Year***	***Augmenter used***	***Observation***
Alexander and Holownia	1978	Wind shields	C_{Pmax} = 0.243
Morcos *et al.*	1981	Wind shields	C_{Pmax} = 0.34
Ogawa *et al.*	1984	Deflector plate	C_{Pmax} = 0.175
Reupke and Probert	1991	Slatted blade	C_{Pmax} = 0.18
Shaughnessy and Probert	1992	V-shaped deflector	19.7% increase of C_P from the conventional rotor.
Huda *et al.*	1992	Deflector plate	20% increase of C_P from the conventional rotor.
Shikha *et al.*	2003	Nozzle	Increase of wind speed by 2 to 3 times.
Menet	2004	Multi-staging	Improved C_P than the single stage rotor.
Grinspan *et al.*	2004	Twisted blade	C_{Pmax} = 0.1159
Rajkumar and Saha	2006	Valve	Reduces negative torque.
Irabu and Roy	2007	Guide box tunnel	Increase in C_P by 1.5 times for 3-bladed and 1.23 times for 2-bladed rotors.
Hu *et al.*	2009	Circular shield	Reduces wind pressure on the returning blade.
Altan and Atilgan	2010	Curtain design	C_{Pmax} = 0.38
Mohamed *et al.*	2011	Obstacle shielding	C_{Pmax} = 0.258
Golecha *et al.*	2011	Deflector plate	50% increase of C_P from the conventional rotor.
Emmanuel and Jun	2011	Shield	C_{Pmax} = 0.50
Abraham *et al.*	2012	Venting slots	Reduces negative torque.
Roy *et al.*	2014	Concentrators	C_{Pmax} = 0.33
El-Askary *et al.*	2015	Guide vane	C_{Pmax} = 0.52
Tartuferi *et al.*	2015	Conveyor-deflector curtain	C_{Pmax} = 0.30

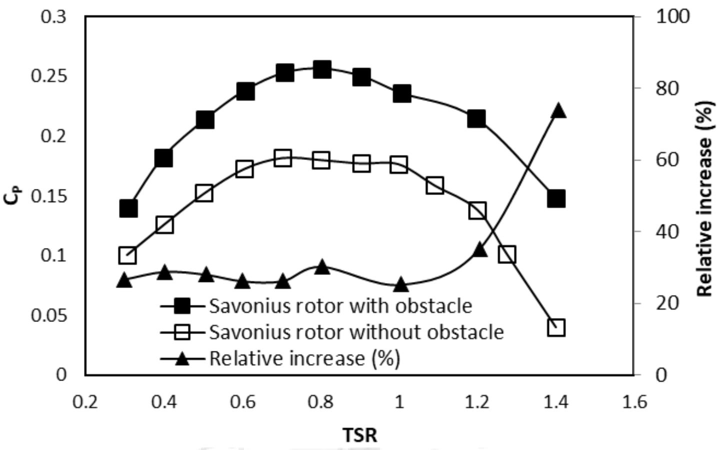

Figure 2.22: C_P vs *TSR* for rotor without and with obstacle (Mohamed *et al.*, 2010)

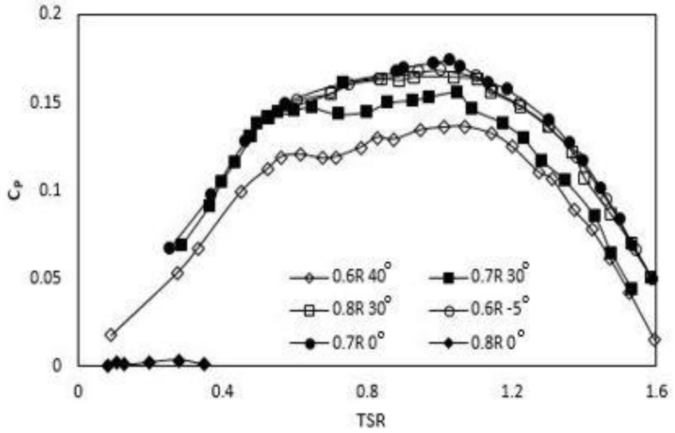

Figure 2.23: C_P vs *TSR* for various deflector azimuthal angle (Ogawa *et al.*, 1989)

Usually, the deflecting plate is placed in front of the returning blade (Fig. 2.21c) to reduce the reverse force acting on it (Ogawa and Yoshida, 1986; Huda *et al.*, 1992; Golecha *et al.*, 2011). In this regard, Ogawa and Yoshida, (1986) and Ogawa *et al.* (1989) carried out several wind tunnel experiments by varying the deflector azimuthal angle in the range 0-75° at δ=0.20. They found the C_P to improve by 27% when the deflector azimuthal angle is 30° (Fig. 2.23). Interestingly, in the recent past, the deflector plates have also been used in water turbine applications where Golecha *et al.* (2011) performed experiments with a modified Savonius rotor in an open water channel at a Reynolds number of 1.32 x 10^5. Eight various location of the plate was used by varying the geometric parameters such as X_1, X_2, Y_1 and Y_2. The deflector plate angle (β) completely depends on the geometrical parameters such as X_1, X_2, Y_1 and Y_2 (Fig. 2.21m). Where, the parameter Y_2 is static at 145 mm. However, the warning parameters for deflector plates are X_1 = 135–230 mm, X_2 = 135–230 mm and for Y_1 = 0–108 mm. The extreme values of X_1 and X_2 are kept static at 230 mm. The least value is selected on the basis that the plate would not block the end plates of the turbine during revolution. It was reported that the deflector plate located at the optimum location improved the C_P up to 50% at *TSR*= 0.82.

2.5.2 V-shaped deflectors, nozzle and multi-staging

In practice, the V- shaped deflector is placed in front of the Savonius rotor (Fig. 2.21e), so that the wind flow resistance is encountered by the returning blade of the rotor. A series of wind tunnel experiments have been carried out by varying the deflector wedge semi-angle between 5-45°. With the optimally inclined deflector, the rotor extracts about 20% more power than the conventional Savonius rotor (Fig. 2.24). Such an important enhancement, achieved by a simple design, recommends that the practice of partly blocked wedges is extremely suitable. When the deflector plate is placed in the optimal location with wedge semi-angle of 37°, the rotor operates over a wider range of *TSR* (Shaughnessy and Probert, 1992).

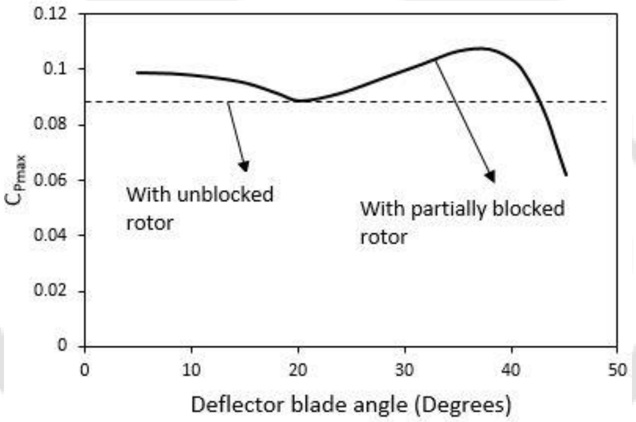

Figure 2.24: Variation of C_P with deflector plate angle (Shaughnessy and Probert, 1992)

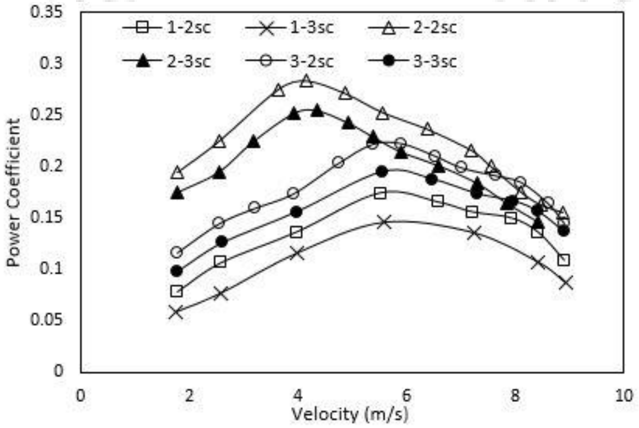

Figure 2.25: Variation of C_P with velocity for various rotor configuration (Saha *et al*., 2008) (1-2sc: 1-single stange, 2-two bladed semicircular)

The application of nozzle is to magnify the wind velocity before it encounters with the Savonius rotor (Shikha *et al*., 2003). When a convergent nozzle (Fig. 2.22f) is employed, the negative torque of the rotor is reduced, and the effective wind speed is augmented. Wind tunnel experiments with five nozzle models are conducted for 2-, 4- and 6-bladed conventional Savonius rotor having overlap ratios of 1/3 and 1/6. The wind velocity at the nozzle inlet is varied from V_1 = 0.6 to 0.9 m/s to amplify the outlet velocity to V_2 = 3 to 3.5 m/s when the length of the nozzle is 55 cm. When the nozzle length is increased to 80 cm, the inlet velocities are varied from V_1 = 0.6 to 0.8 m/s to obtain outlet velocities from V_2 = 2 to 2.9 m/s. The 6-bladed Savonius rotor is found to enhance the power extraction at low wind speed under the application of convergent nozzle at the rotor front.

The conventional Savonius rotor mainly has two disadvantages on torque characteristics. Firstly, it has a large fluctuation of torque at some initial rotation of the turbine, and secondly, it has some angular positions where the torque becomes negative or even quite small thereby reducing the rotor performance. As a result, the starting torque of a conventional Savonius rotor would be so low that the rotor cannot start on its own. Hence, to improve its static torque characteristics, staging of rotor (Fig. 2.21g) has been done (Menet, 2004; Hayashi *et al*., 2005; Huda *et al*., 1992; Frikha *et al*., 2016). As the staging of rotor is increased from 1 to 2, the C_P becomes higher; but when the number of staging is increased from 2 to 3, the C_P reduces due to the increased inertia of the rotor. Wind tunnel experiments demonstrates the optimal number of staging of the rotor to be 2 (Saha *et al*., 2008]. The C_P for 2- and 3-stages conventional rotor is found to be 0.29 and 0.23, respectively (Saha *et al*., 2008). This is accomplished by setting the phase lift at an angle 90° to each other for the 2-stage, and at 120° for the 3-stage rotor, as shown in (Fig. 2.25). These arrangements increase the starting capability of the rotor. Hayashi *et al.* (2005) noticed that a lower peak C_P of a 3-stage rotor in comparison to its corresponding single-stage rotor. Staging results in the reduction of *AR* of the individual stages of a 3-stage rotor as compared to that of a single-stage design. The 3-stage rotors are better at low wind speeds as they have the uniform coefficient of static torque. Experimentally it has been reported that the multi-staging has shown a reduction of power and dynamic torque for the same rotor. Thus, the multi-staging of rotors seems to provide a better starting ability at low speeds with some reduction in performance (Kamoji *et al*., 2009).

2.5.3 Guide box, Curtain plates and Shields

About a decade ago, Irabu and Roy, (2007) used the guide box tunnel augmentation technique to improve the output power and to prevent the rotor from strong wind disaster. The guide box tunnel is a passage in which the test rotor is involved. In order to adjust the input power, the area ratio between the inlet and outlet is varied from 0.3 to 0.7 Irabu and Roy, (2007). Various experiments were conducted at Reynolds number of 6.05 x10^4 and 9.08 x 10^4 to obtain the adequate configuration that would provide the maximum C_P. It was found that the maximum C_P with guide box of the area ratio 0.43 was increased by 1.5 times in 3-bladed system, and 1.23 times in the 2-bladed system. Further, with the use of guide box tunnel there was no negative torque in the complete rotation of the rotor when the guide box entrance opening angle was in between 60° to 90°.

Altan and Atilgan, (2008, 2010) used a novel arrangement of curtains at the rotor front with the intention of improving its performance by preventing the negative torque that opposing the rotor rotation. Experiments with three different curtains, oriented at varying inclinations (Fig. 2.21k) were carried out in a low-speed wind tunnel with δ=0.15 and the gap distance of 2.6 cm. The highest rotor power has been found from curtain 1 at around 8 W when α = 45° and β = 15°. There was 16% improvement of performance in case of curtain 1 as compared to curtain less rotor (Fig. 2.26).

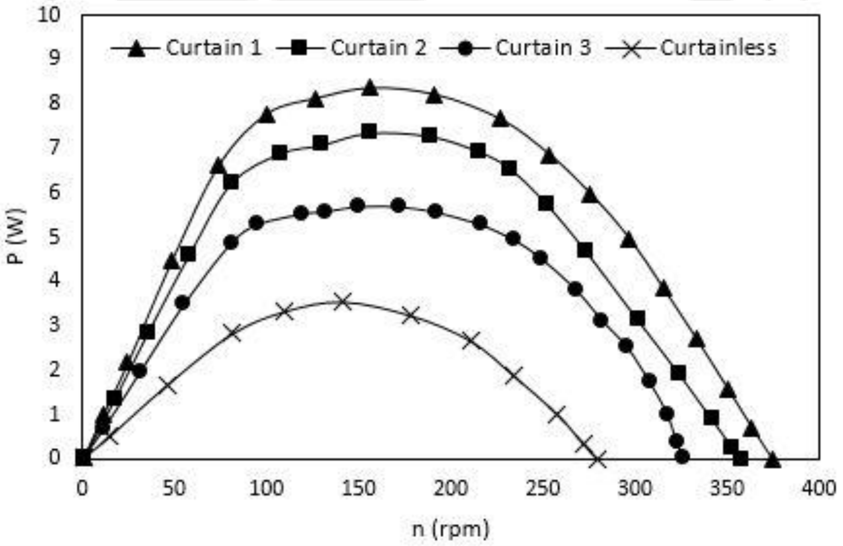

Figure 2.26: Power vs *RPM* for various curtain designs (Altan and Atilgan, 2010)

Sometime during 2011, Emmanuel and Jun used a different type of shield arrangement (Fig. 2.21n) in a six-bladed Savonius rotors. This arrangement is slightly different from the types used by Alexander and Holownia, (1978), Morcos *et al*. (1981) and Hue *et al.* (2009). The goal of the investigators (Emmanuel and Jun, 2011) was to suppress the pressure exerted on the convex part of the rotor. In this connection, various configurations of the six-bladed rotor have been examined using 2D unsteady simulation with *RNG k-ε* turbulence model. In the study, the six-bladed rotor without shield is found to have lower efficiency but still higher than a conventional two-bladed Savonius rotor. The six-bladed rotor with shields and with stator has indicated maximum C_P of around 0.4 and 0.5, respectively, however this occurs at dissimilar *TSR*s (Fig. 2.27).

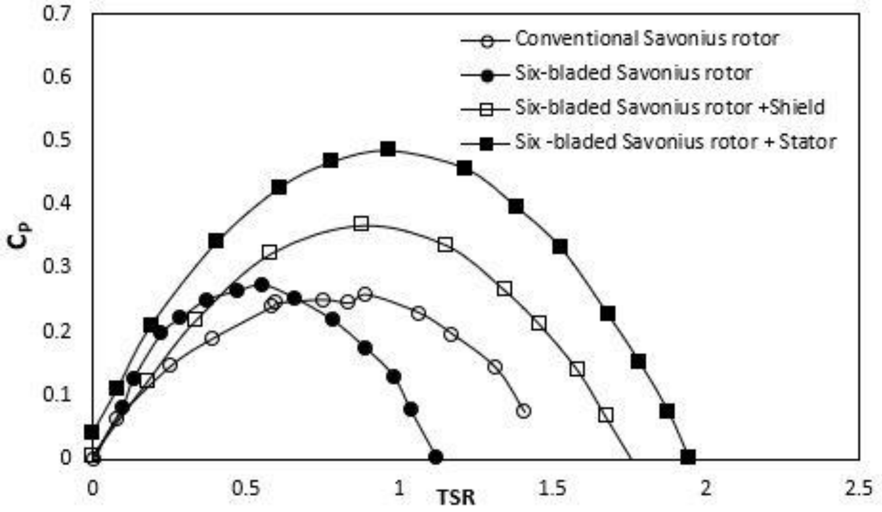

Figure 2.27: Variation of C_P with *TSR* for various rotor configurations (Emmanuel and Jun, 2011)

2.5.4 Venting slots, concentrators and guide vane

Abraham *et al.* (2012) and Plourde *et al.* (2012) have used venting slots which is found more effective and simpler in design than the valves used by the past investigators (Plourde *et al*., 2012). The rotors have been tested without and with venting slots to minimize the thrust loading on the returning blade. Wind tunnel experimentations are carried out to determine the power vs. load parameterized with various wind speeds. At each wind speed, the generator is connected to a resistive load that could be effortlessly varied. The load resistances have been varied from 20 Ω to approximately 1000 Ω to determine the resulting power curve (Fig. 2.28). They have observed a quite weak dependence on electrical load for the unvented and uncapped case, however, the performance is found strongly linked to the electrical system for the capped and vented case. This suggests that the electrical system should be designed appropriately while linking to the rotor.

Roy *et al*. (2014) have studied and investigated the performance and starting characteristics of Savonius rotor employing concentrators, a technique similar to those of nozzle (Fig. 2.21f) and curtain plates (Fig. 2.21k). This augmenter is used so that the major portion of the wind is incident on the concave side of the rotor. The experiments are conducted in a low speed wind tunnel at the wind velocity of 6.2 m/s, where loads are applied progressively with respected to the corresponding rotational speeds. With the augmenters placed α = 40°, and β =10°, the rotor obtains a peak C_P of 0.32, a value competitive to that of a lift-type turbine. This shows an overall performance improvement of 47.5% as compared to a semicircular-bladed Savonius rotor without concentrators (Fig. 2.29).

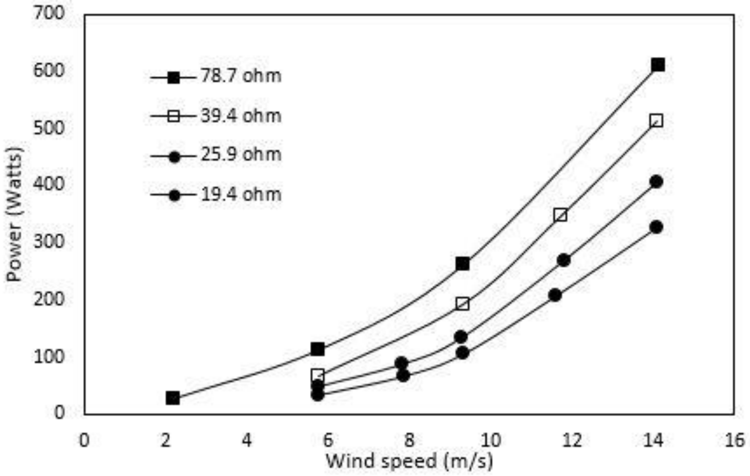

Figure 2.28: Variation of power vs wind speeds for a vented- and -capped rotor (Abraham *et al*., 2012)

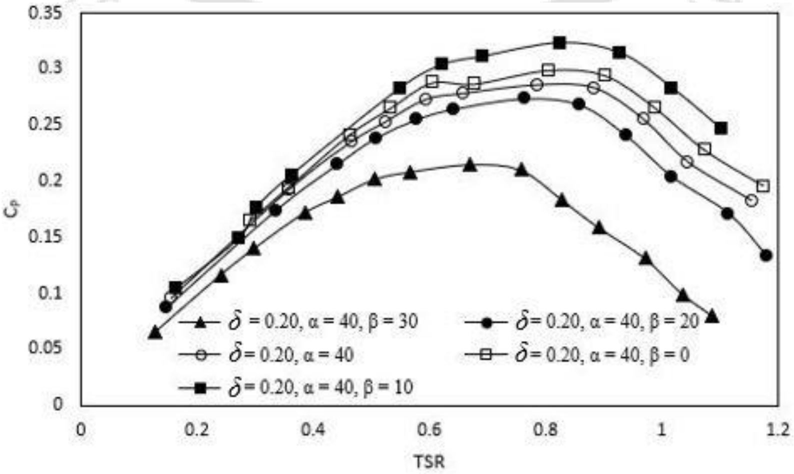

Figure 2.29: C_P vs *TSR* at various orientations of the concentrators (Roy *et al*., 2014)

The main idea of using guide vane in Savonius rotor is to improve the wind harvesting capacity of incoming air at the cost of structural complexity. Three designs, as illustrated in Fig. 2.30, have been investigated by El-Askary *et al*. (2015). The purpose is to minimize the negative torque and increase the exerted positive torque by guiding the incoming air effectively and smoothly. In this context, the Design-III is found to give an adequate developing length and reduced entrance effect. Numerical analysis using *FVM* solver ANSYS Fluent with *SST k-ω* turbulence model is carried out with for each of the design. As seen from Fig. 2.31, the Design-III shows the peak C_P of 0.50. Though the novel designs produced robust vortex shedding and large eddies behind and around the new design that needs more special treatments from the point of noise generation.

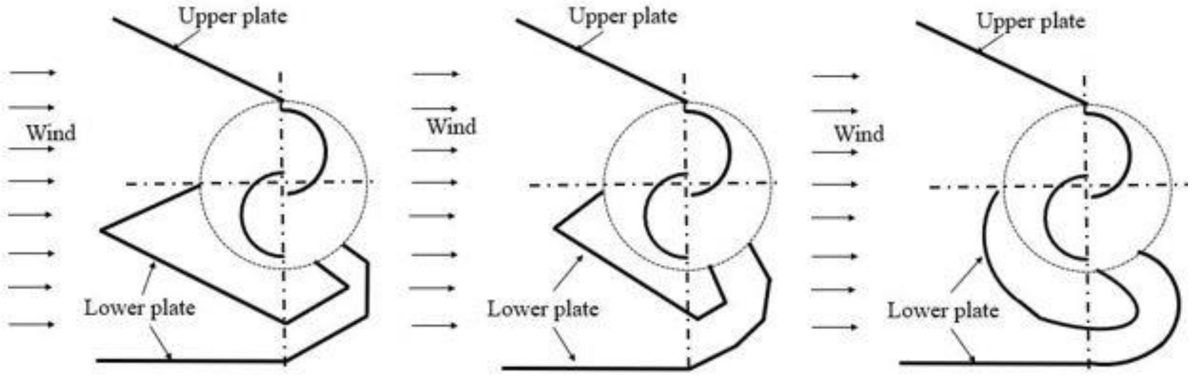

(a) Design-I (b) Design-II (c) Design-III

Figure 2.30: Different guide vane designs
(El-Askary *et al*., 2015)

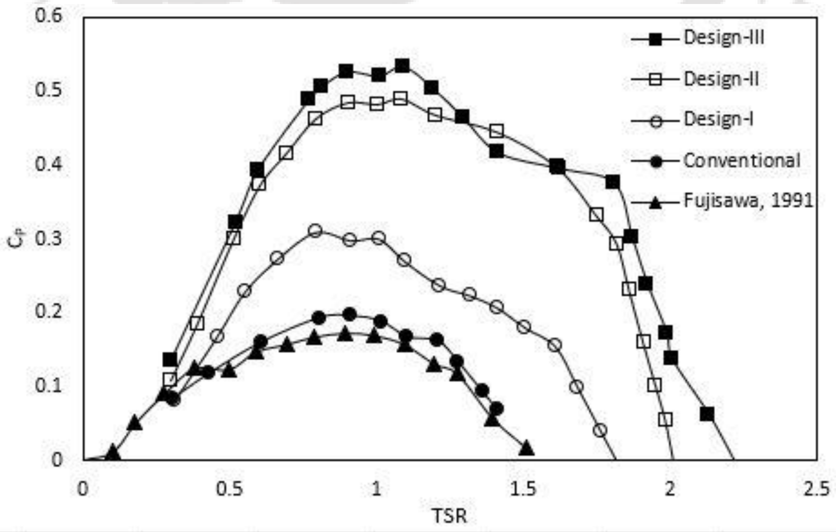

Figure 2.31: C_P vs *TSR* for various guide vane positions
(El-Askary *et al*., 2015)

2.5.5 Principal observations on augmentation techniques

(a) The augmentation techniques (with additional cost and complexity to the rotor system) enhance the self-starting capability, amplify the wind speed, improve the visual impact, prevent blade cracking, and stop bird assaults. Other advantages include mounting of additional features to the system such as rainwater harvester and solar panel.

(b) The augmenters such as V-shaped wedge deflector, curtain, obstacle shield, shields reduce the exerted wind pressure on the returning blade of rotor and hence raise the net positive torque. With the use of deflector plate at the rotor front, the C_P can be enhanced up to 20-50% than a rotor without the deflector. On the other hand, the use of shield in a six-bladed Savonius rotor can improve the C_P up to 0.50. These augmenters do not offer much structural complexity to the rotor system.

(c) With the employment of guide box tunnel and convergent nozzle, the C_P of a semicircular-bladed rotor may increase up to 1.5 and 3 times. The convergent nozzle cuts down the negative torque and increases the wind harvesting capacity of the turbine rotor. The guide box increases the rotor system complexity resulting a lesser C_P, however, the nozzle makes the rotor lesser complex with a gain in C_P. An optimally designed guide vane can bring a maximum C_P of 0.52, however, there is a chance of strong vortex shedding and high wake is generated around and behind the rotor leading to high noise generation.

(d) The use of hinged flaps in a Bach type Savonius rotor can increase the static torque by 35% relative to the one without flaps. However, the hinged flaps increase the structural design complexity of the rotor system.

(e) The venting-slots, if properly designed and oriented, can raise the C_P by 7.5% over the conventional rotor without slots. The performance is found to be maximum when the venting slot is oriented at 30° above and below the central axis of the rotor blade. The venting slots are easier to be incorporated in rotor blades.

(f) The foregoing analysis suggests the use of deflector plate(s), valves and especially the venting slots in an elliptical-bladed rotor to improve the C_P without bringing much complexity to the turbine system. The location of augmenters in the elliptical-bladed rotor blades can be optimized with the help of numerical methods followed by wind tunnel experiments.

2.6 Optimization Methods and Algorithms

Optimization is a technique for finding and recognizing the best contender from a group of alternatives without having to openly enumerate and assess all possible alternatives (Mohamed, 2011; Zhou *et al*., 2018; Ramadan *et al*., 2018; Chan *et al*., 2018). In this context, Mohamed *et al*. (2011) used an evolutionary algorithm (*EA*) using *OPAL* (Optimization of algorithms) by coupling with ANSYS Fluent to optimize the Savonius rotor blade profiles. In their investigation, five points have been chosen in the profile, where the two end points of the profile are fixed and other three points are variable with a certain range. The variable three points have been optimized by *EA* with an aim to maximize the C_P. This optimal blade profile could improve the C_P by 38.9% at *TSR* = 0.7. Sargolzaei and Kianifar, (2010) used *ANFIS* (Adaptive neuro–fuzzy inference system), *FIS* (Fuzzy inference system), and *RBF* (Radial basis function) optimization techniques in Savonius rotor and perform an extensive comparison test. From the optimization study, the *ANFIS* showed more accurate results in comparison to other two techniques. Ferdoues *et al*. (2017) used a multi-objective genetic algorithm (*GA*) using OpenFOAM *CFD* software to optimize the geometric parameters of an external-axis wind turbine. From the analysis, a total of 10 number of blades is found optimum at *TSR* =0.32.

Very recently, Chan *et al*. (2018) applied *GA* to optimize the Savonius rotor blade profiles to improve the C_P. In their analysis, a total of five points were chosen in a natural cubic spline curve where three points were considered variables keeping the two ends points fixed. The variable three points were optimized using *EA* based *GA* with the objective is to maximize the C_P. The flow chart for a typical *GA* process is shown in Fig.2.32. From their study, the optimized blade profile had shown an improvement of C_P by 33% as compared to the conventional semicircular profile. Roy et al. 2018 used the differential evolutionary (*DE*) based inverse optimization technique to optimize the geometric parameters of the Savonius rotor. This *DE* based inverse technique reduced the overall dimension of the Savonius rotor by 9.8%

with respect to their experimental data. Neto *et al.* (2018) performed multi-objective optimization using metaheuristics for the rotor blade geometry to maximize the rotor C_P and to minimize the blade mass. With the intention of improving the C_P, Mohammadi *et al.* (2018) used Artificial Neural Network (*ANN*) and *GA* to optimize the geometric parameters of Savonius rotor. The *ANN* was used to analyze a logical interaction among dependent and independent variables and defined a cost function based on the same empirical data. This function was then optimized by *GA* and the best amount for each parameter was identified. The maximum C_P was found to be 0.222 with the optimized geometric parameters (OR = 0.159, AR = 0.89, $Re = 1.2 \times 10^5$).

Multi-objective genetic algorithm (MOGA) can be applied in 2D elliptical profile with the objective to minimize the incoming velocity and to maximize the output torque and lift coefficients (C_T and C_L). The MOGA can be performed using ANSYS direct optimization technique. The maximum number of iterations, the maximum pareto percentage, mutation and crossover probability may be considered appropriately for the elliptical profile.

2.7 Concluding Remarks

From the above review, it appears that using the appropriate computational methodology, computational research is a promising concept for optimizing the power output as well as starting ability of the Savonius rotor. It is found that the finite volume method with *SST k-ω* turbulence model has shown to be the most effective *CFD* method. Till date, the influencing parameters of Savonius rotor are optimized to some extent with the help of computational and experimental investigation for the conventional semicircular-bladed Savonius rotor. While the elliptical-bladed Savonius rotor has improved geometric and aerodynamic performances than the semicircular-bladed rotor but its influencing parameters are not optimized either numerically or experimentally. Thus, further research is required for the elliptical-bladed Savonius rotor to optimize its various influencing parameters. In this context, initially, 2D unsteady simulations have been conducted to find its optimum geometric parameters such as blade profiles, overlap ratio, effect of number of blades and shaft. Thereafter, the augmentation technique has been implemented to the elliptical-bladed rotor to find its aerodynamic drag and lift coefficients (C_D and C_L), and performance coefficients (C_T and C_P). The genetic algorithm optimization technique has further been employed on the elliptical-bladed profile to improve its performance.

CHAPTER –3

2D Unsteady Simulations for Optimizing the Geometric Parameters

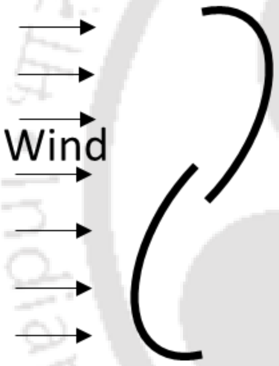

Chapter Outline

Overview

In this chapter, 2D unsteady simulations have been carried out on the semicircular, Benesh, Modified Bach and elliptical-bladed profiles to arrive at the selection of the most suitable one. Amongst these, the elliptical profile has shown the maximum power coefficient (C_P). Thereafter, various geometric parameters of elliptical profile have been studied and optimized. In each case, the torque and power coefficients (C_T, C_P) are calculated at the rotating conditions. The effect of blade overlap ratio (OR) on the elliptical profile is analyzed in the range of OR = 0.00–0.30. A better C_P is identified at OR = 0.15. Further, a series of unsteady simulations are carried out on 2-, 3-, and 4-bladed elliptical profiles to analyze the effect number of blades on the rotor performance. The effect of shaft and Reynolds number on the rotor performance has also been investigated numerically.

3.1 Introduction

2D unsteady simulations have been carried out using multi-physics FVM solver ANSYS Fluent with the help of *SST k-ω* turbulence model to optimize the geometric and the aerodynamic parameters of elliptical-bladed Savonius rotor in the following sections and subsections.

3.2 Geometric Details

The elliptical profile under consideration has been reported earlier (Alom *et al*., 2016). This profile is developed by considering the ratio of semi-minor and semi-major axes of the ellipse to be *OM*/*OP* = 2/3 (Fig. 3.1). The overall diameter of the rotor (*D*) and height (*H*) is taken as 210 mm and 230 mm (Roy and Ducoin, 2016), whereas the blade thickness is taken as 0.63 mm. The point *A* is at 54% of *PO* starting from *O* to get the required blade chord length (*d*). The chord length of the blade is *BB'*. The *D* of the semicircular profile is kept similar to that of the elliptical profile. For both profiles, the *OR* is fixed at 15% of *d* (Alom *et al.,* 2016). The sectional cut angle ($\theta = 47.5^{o}$) of the elliptical profile has been optimized from numerical simulation and this has been reported earlier (Alom *et al*., 2016). In the investigations, two earlier blade profiles such as a conventional semicircular type, and a Benesh type (Benesh, 1988, 1989) are used in the Savonius rotor Furthermore, a profile developed from the basic Bach type rotor, named as modified Bach profile (Roy and Saha, 2015), is also selected for the study. The overall diameter (D=210 mm) is kept constant for all the tested profiles (Fig. 3.2).

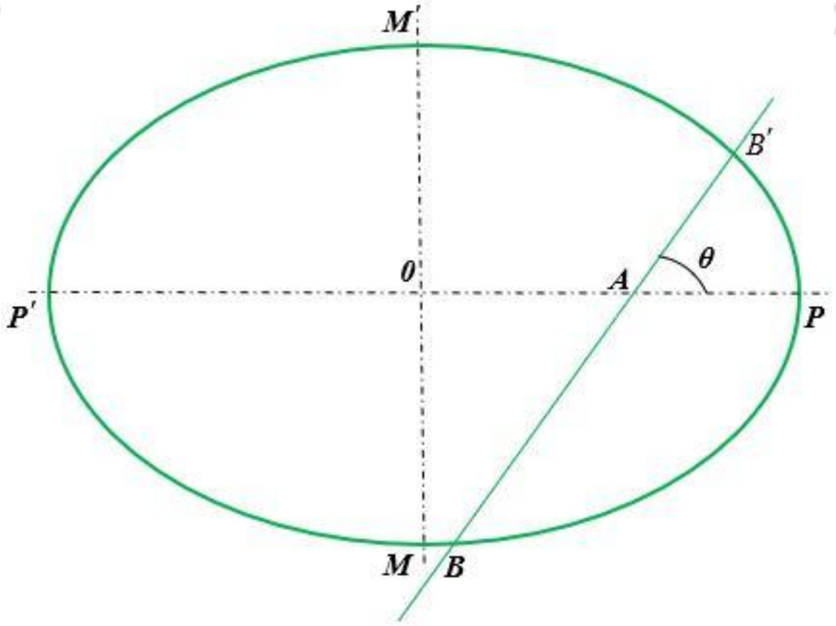

Figure 3.1: Sectional cut angle of the ellipse

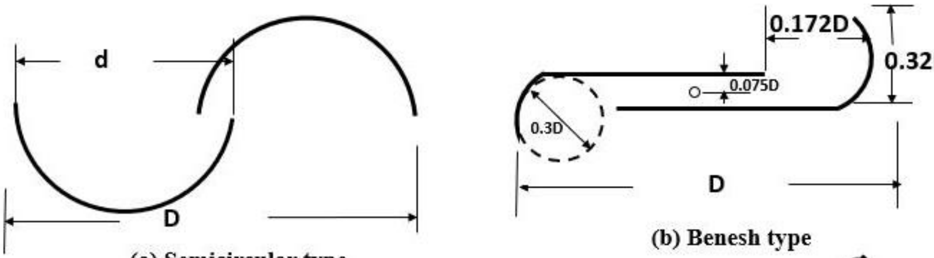

(a) Semicircular type

(b) Benesh type

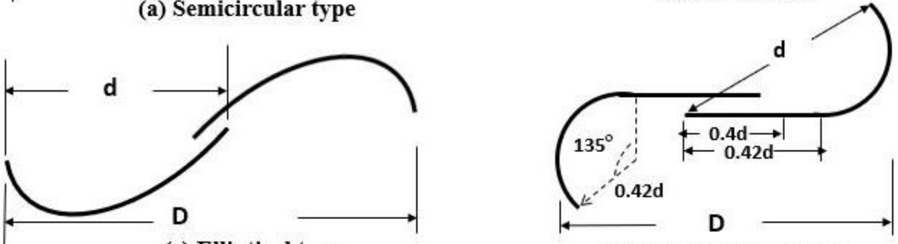

(c) Elliptical type

(d) Modified Bach type

Figure 3.2: Dimension of various blade profiles

3.3 Validation of 2D Elliptical Profile

The 2D results of the non-vented elliptical profiles with varying sectional cut angle (θ) have been validated with the available data of the non-vented elliptical-bladed profile of Banerjee *et al.* (2014) with the sectional cut angle (θ) = 50^0. The numerical investigation predicts that the peak C_P for elliptical-bladed profile is 0.31 at *TSR* = 0.8 and OR = 0.20 (Banerjee *et al.*, 2014). The present numerical analysis found that the peak C_P for elliptical-bladed profile is 0.312 at TSR = 0.8 and OR = 0.20 and the nature of the C_P vs TSR curve shows a similar behavior with Banerjee *et al.* 2014 (Fig. 3.3). Thus, there is an error of 0.6% in the present investigation than the available results (Banerjee *et al.*, 2014). The results are also presented for θ = 47.5^0 and found higher C_P than that of the θ = 50^0.

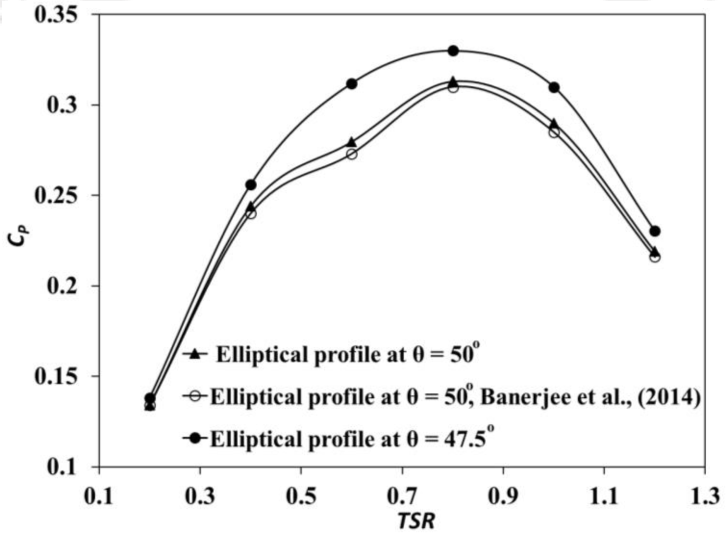

Figure 3.3: C_P vs *TSR* plot of the elliptical-bladed rotor
(Banerjee *et al.* 2014)

3.4 Computational Methodology

The meshing, boundary conditions, selection of turbulence model, and solver set up are discussed in this section.

3.4.1 Meshing

The computational domain and meshing of 2D and 3D domains can be seen in Fig. 3.4. The computational domain is discretized using ANSYS Fluent meshing (ANSYS Inc, 2009; Banerjee *et al*., 2014; Alom *et al*., 2016). The discretization is done by unstructured triangular grids for the 2D domain, whereas unstructured tetrahedron grids have been chosen for the 3D domain. This is because unstructured mesh methods logically offer the possibility of incorporating adaptivity. Also, it offers flexibility in generating a mesh flow domain for a complex flow problem (Alakashi *et al*., 2014). The domain consists of two sections, viz., the outer rectangular stator and the inner circular rotor. The two sections are separated by a sliding interface. Edge sizing and body sizing operation are performed to generate the mesh. The dimensions of the domain are taken as $14D \times 6D$ and $14D \times 6D \times 2D$ for 2D and 3D, respectively (Roy and Ducoin, 2016). It is to be noted that for 3D, the height of the domain is kept twice the height of rotor blades such that the flow can pass over and under the rotor blades (Abraham *et al*., 2012). For greater accuracy at the boundary region of the blades, inflation is provided with a first layer thickness from the wall is $9.5\times10^{-5}D$, a growth rate of 1.2. The first layer thickness from the blade is calculated (White, 2011; Sharma and Sharma, 2016) using the following equations:

$$y^{+} = \frac{\rho u_t y}{\mu} \tag{3.1}$$

where, u_t = friction velocity, $y+$ = non-dimensional parameter, y = distance of first node from wall, ρ = density of fluid, μ= viscosity of fluid.

The frictional velocity can be calculated as

$$u_t = \left(\frac{\tau_\omega}{\rho}\right)^{(0.5)} \tag{3.2}$$

where τ_ω denotes the wall shear stress, which can be calculated using Eqs.3.3 and 3.4.

$$\tau_{\omega} = \frac{1}{2} C_f \rho V^2 \tag{3.3}$$

The value of local coefficient of friction C_f is estimated by the empirical formula as:

$$C_f = [2\log(\mathrm{Re}) - 0.65]^{-2.3} \tag{3.4}$$

The maximum number of inflation layer is 10 with the growth rate of 1.2 (Fig. 3.4). In the numerical model, the dimensionless wall distance y+ value is less than one in the viscous sub-layer region. This value of y+ is found to be adequate as reported by Roy and Ducoin, (2016).

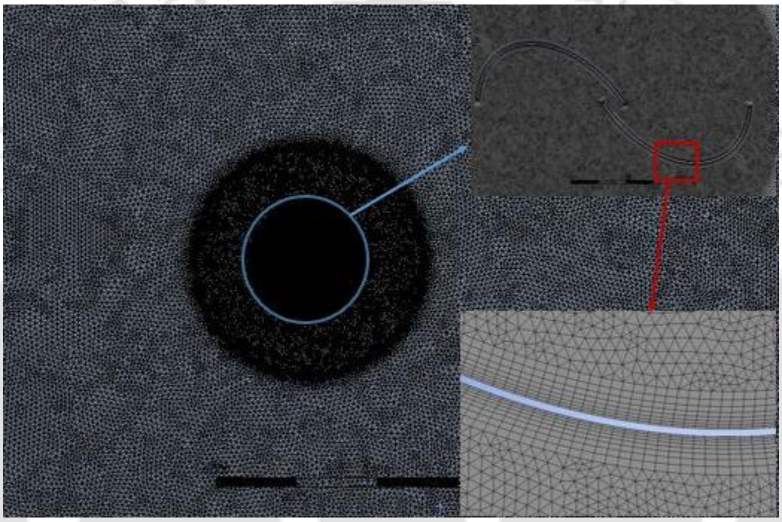

(a) 2D mesh

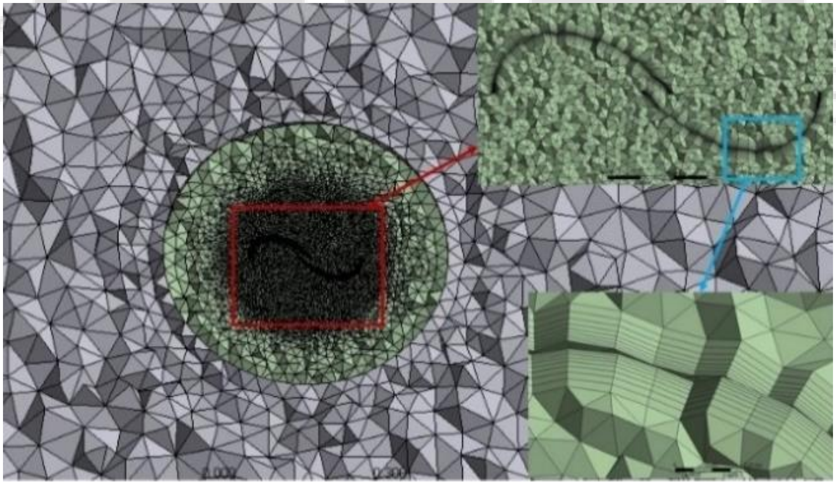

(b) 3D mesh

Figure 3.4: Mesh generation around the rotor

3.4.2 Grid and time step independence study

The grid independence and *time step independence* tests have been carried out for 2D and 3D unsteady simulations. The numbers of grids are varied from 70860 to 304330 for 2D, and from 422145 to 893452 for 3D. There is no change in torque coefficient (C_T) for 169900 and 229992, hence, the grid with 169900 elements is chosen for 2D simulations and 893452 for 3D simulations in all the computational domains (Fig. 3.5). From Fig. 3.6 and Table 3.1, it has been observed that for the higher degree/step (2°/step and 3°/step) the average C_T is found to be lesser. This is because the flow physics near the rotor blades are not captured properly. As the time step size at 0.5°/step and 1°/step are found to have properly captured the flow physics around the rotor, 1°/step is chosen to reduce the computational time.

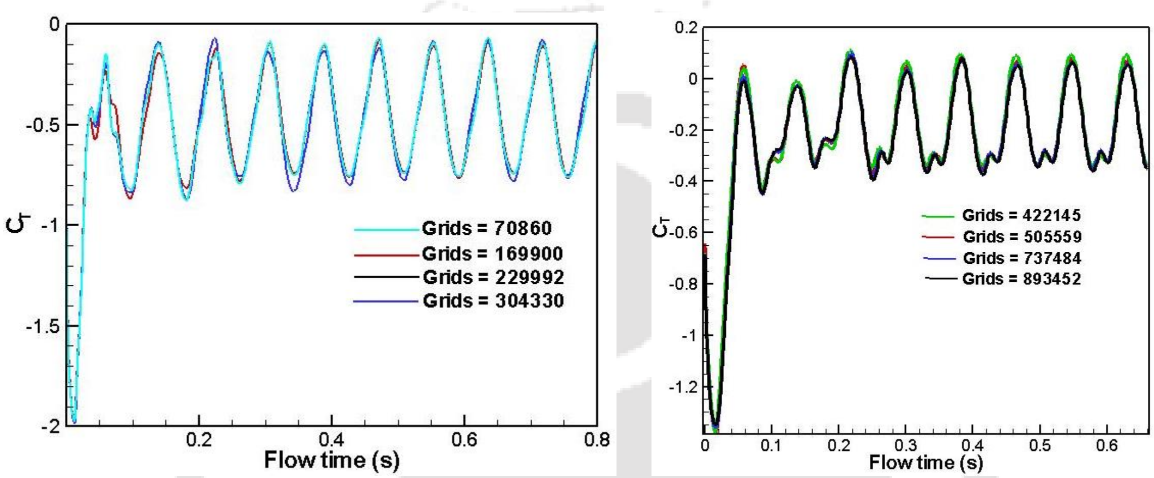

(a) 2D grids (b) 3D grids

Figure 3.5: Grid independence test

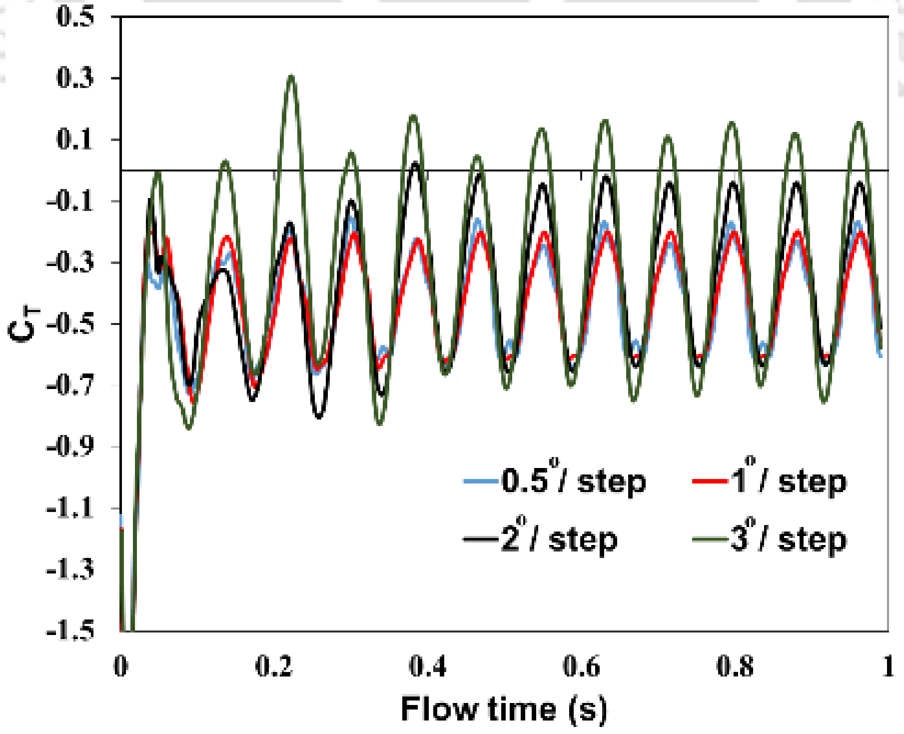

Figure 3.6: Time step independence test

Table 3.1: Average C_T at various degree of rotation

Degree of rotation	Average C_T
0.5°	0.39
1°	0.41
2°	0.31
3°	0.27

3.4.3 Details of the boundary conditions and governing equations

After the meshing, boundary conditions are assigned to the computational domains. The inlet is given a velocity boundary condition with V = 6.2 m/s as this velocity is chosen for the wind tunnel experiments. The outlet is assigned to a pressure outlet with atmospheric pressure. Turbulence intensity level of 1% is assigned to both inlet and outlet boundaries (Roy and Ducoin, 2016). The rotor blades are given no-slip boundary condition. They are treated as moving walls with a certain rotational speed. The top, bottom and side walls are assigned symmetry boundary condition to ensure that the velocity transverse to the flow is zero. The inner circular section is the rotating zone with rotational speed set with respect to *TSR*. Figure 3.7 shows the details of boundary conditions.

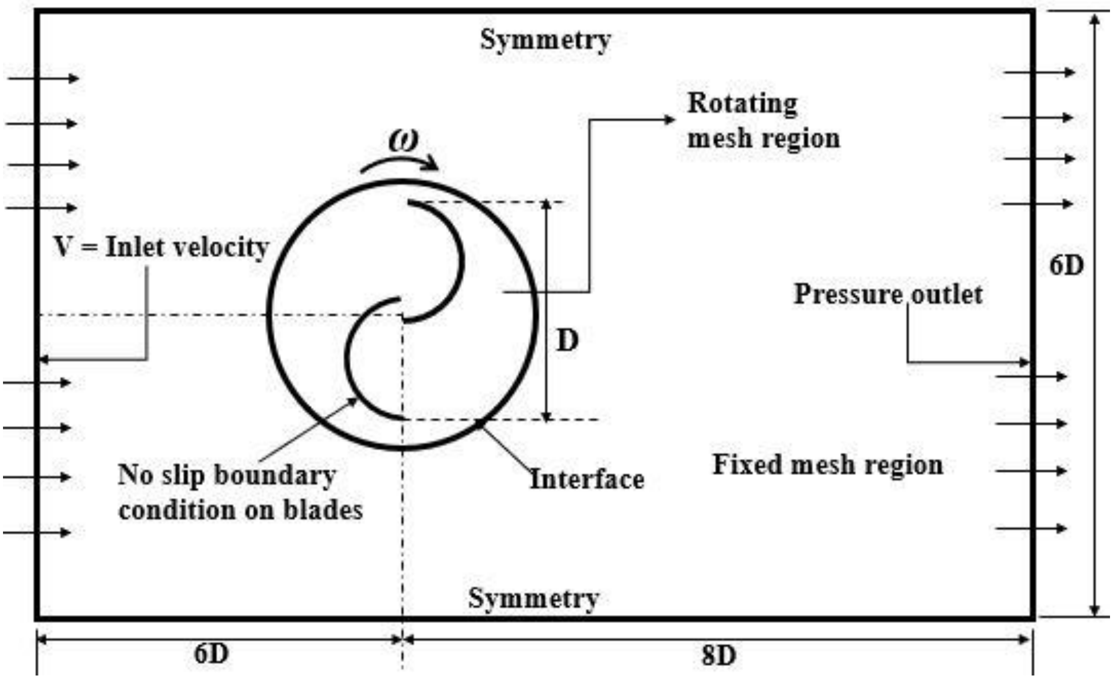

Fig. 3.7. Boundary conditions and computational domain

The initial conditions provide the starting values for all the dependent variables that describe the instantaneous condition of an individual particle and include the following:

Gauge pressure = 0 Pa, *X*-velocity (*u*) = 6.2 m/s, *Y*-velocity = 0 m/s, *Z*-velocity = 0 m/s, turbulent kinetic energy (*k*)= 0.005766 m^2/s^2 and specific dissipation rate (ω)= 0.8437 1/s.

The ANSYS Fluent solves the unsteady RANS equations along with the equations of SST *k-ω* turbulence model and mass conservation (Song *et al*., 2015). The mass conservation and RANS equations can be expressed by eqns. (3.5) and (3.6). The details of these equations are discussed in Appendix.

$$\frac{\partial \bar{u}_j}{\partial x_j} = 0 \tag{3.5}$$

$$\frac{\partial \bar{u}_i}{\partial t} + \bar{u}_j \frac{\partial \bar{u}_i}{\partial x_j} = -\frac{1}{\rho}\frac{\partial \bar{p}}{\partial x_i} + \frac{\partial}{\partial x_j}\left(\nu \frac{\partial \bar{u}_i}{\partial x_j}\right) + \frac{1}{\rho}\frac{\partial\left(-\rho \overline{u_i' u_j'}\right)}{\partial x_j} + \bar{f}_i \tag{3.6}$$

where, t is the time, ρ is the density of fluid, u is the velocity, x_i and x_j are the Cartesian coordinate components, i and j can take values of 1, 2, and 3 in order to take three dimensions into account, p is the pressure, ν is the kinematic viscosity, and f_i is the body force per unit volume. However, the body force (f_i) in the present investigation is neglected.

The $-\rho \overline{u_i' u_j'}$ is generally known as Reynolds stress. The details of the SST *k-ω* turbulence model are as follows:

$$\frac{\partial}{\partial t}(\rho k) + \frac{\partial}{\partial x_i}(\rho k u_i) = \frac{\partial}{\partial x_j}\left(\Gamma_k \frac{\partial k}{\partial x_j}\right) + \tilde{G}_k - Y_k \tag{3.7}$$

$$\frac{\partial}{\partial t}(\rho \omega) + \frac{\partial}{\partial x_i}(\rho \omega u_i) = \frac{\partial}{\partial x_j}\left(\Gamma_\omega \frac{\partial \omega}{\partial x_j}\right) + G_\omega - Y_\omega + D_\omega \tag{3.8}$$

where, D_ω represents the cross-diffusion term. G_k is the generation of turbulence kinetic energy due to mean velocity gradients. G_ω is the generation of ω. Y_k and Y_ω are the dissipation of k and ω due to turbulence. However, the turbulent viscosity, μ_t, the turbulent Prandtl numbers, σ_k and σ_ω are computed as given in Appendix.

3.4.4 Selection of turbulence model and ANSYS Fluent solver set up

The flow around the Savonius rotor is turbulent in nature. Past studies conducted by several investigators reveal that the *SST k-ω* model has better prediction capabilities (Modi *et al*., 1990; Menter, 1994; Howell *et al*., 2010; Plourde, 2012; Song *et al*., 2015). Hence, this model, commonly used to obtain mean properties in the turbulent flow near the wall region, is applied in the present study. This model comprises the features of *k-ϵ* turbulence model to obtain values away from the wall region (Song *et al*., 2015).

In the present analysis, all the simulations are performed using sliding mesh method (rotating frame of reference) in which meshes are rotated without changing its shape and size. Hence, the time step size is calculated based on 1°/step rotation of the rotor at *TSR*=0.6. The time step size is taken as 0.0004582 sec with the number of time steps being 2160 and 1440 for 2D and 3D simulations, respectively. The simulations are carried out for 6 and 4 complete rotation of the rotor for 2D and 3D simulations, respectively. However, the dynamic steady state is achieved after the first rotation. The maximum iterations per time step are taken as 20. The convergence criteria for stopping the solution is chosen to be 10^{-5}. The conservative terms are discretized by using second-order upwind scheme and the temporal terms are discretized with the help of second order implicit method. A *SIMPLE* (Semi-Implicit Method for Pressure Linked Equations) scheme is chosen for pressure-velocity coupling for better stability of solutions.

3.4.5 Calculations of performance coefficients

As reported, the power coefficient (C_P) of a wind turbine is defined as the ratio of the maximum power attained from the wind ($P_{turbine}$) to the total power accessible from the wind ($P_{available}$) (Fujisawa, 1992; Emmanuel and Jun, 2011; Treuren, 2015; Ohya *et al.*, 2017) and can be expressed by

$$C_P = \frac{P_{turbine}}{P_{available}} = \frac{T_{turbine} \times \omega_s}{\frac{1}{2}\rho A V^3} = \frac{T_{turbine}}{\frac{1}{2}\rho A V^2 R}\frac{R\omega_s}{V} = C_T \times TSR \tag{3.9}$$

The torque coefficient (C_T) is defined as the ratio of the actual torque generated by the rotor (T_{rotor}) to the theoretical torque accessible in the wind ($T_{available}$) (Manwell *et al.*, 2009; Emmanuel and Jun, 2011) and can be expressed by

$$C_T = \frac{T_{turbine}}{T_{avaialble}} = \frac{T_{turbine}}{\frac{1}{2}\rho A V^2 R} = \frac{F \times r_p}{\frac{1}{2}\rho A V^2 R} \tag{3.10}$$

3.5 Selection of Rotor Blade Profile

Initially, 2D unsteady simulations are carried out for various Savonius rotor profiles without the presence of central shaft. The torque coefficient (C_T) and power coefficient (C_P) are calculated and discussed with respect to *TSR*. The numerical variations of C_T and C_P are shown in Fig. 3.6. It is important to study the optimum *TSR* to obtain the maximum power output of the rotor. In the present analysis, it is observed that the rotational speed of the rotor reduces with the application of load and thus, the variation of C_T decreases with the increase of *TSR*. From the numerical analysis, the peak C_P of 0.34 is obtained for the elliptical profile at *TSR* = 0.80; whereas at the same *TSR*, the peak C_P is found to be 0.27, 0.29 and 0.30 for the semicircular, Benesh and modified Bach profiles, respectively (Fig. 3.8). Thus, there is an improvement of C_P in the elliptical profile than the semicircular, Benesh and modified Bach profiles by 26%, 17% and 13%, respectively.

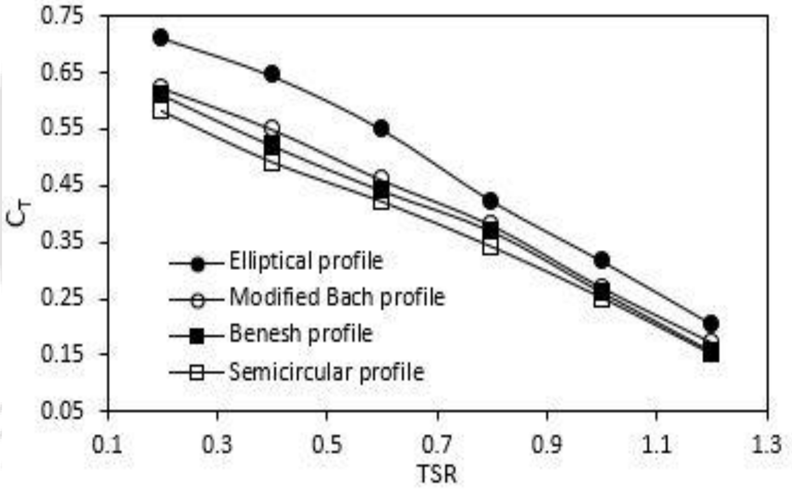

(a) C_T vs TSR

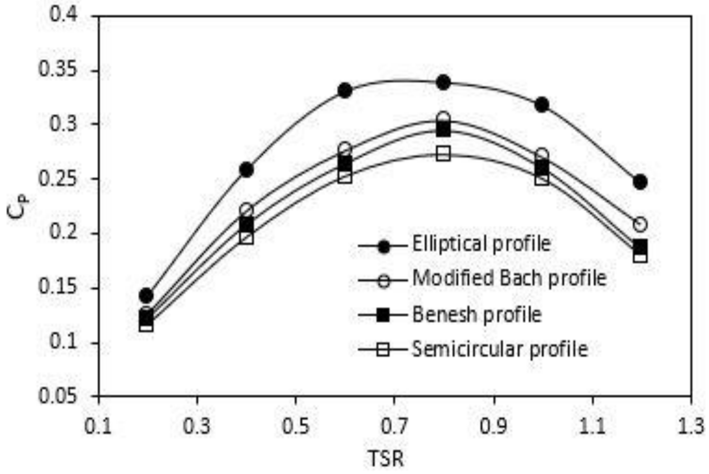

(b) C_p vs TSR

Fig. 3.8: Performance coefficients obtained from 2D numerical simulation

3.5.1 Velocity contours

The velocity contours of the several rotor profiles are shown in Fig 3.9. The velocity around the surface of the elliptical-bladed profile observed to be in the range of 5-6 m/s, while the velocity for the other profiles lies in the range of 4-5 m/s. The formation of wake on the concave side of returning profile of semicircular, Benesh and modified Bach profiles is found to be larger than the elliptical profile. Also, there is a smaller velocity region on the convex side of returning elliptical profile, indicating its lesser negative drag over the other profiles. This reflects a higher C_P of the elliptical profile. The region of maximum velocity at the rotor tip is lesser in the elliptical profile than the others (Fig. 3.9d), and as a result, the flow separation is delayed in the elliptical profile. Further, the improved overlapping flow is observed in elliptical profile over the other rotor blade profiles. Hence, the C_D, C_T and C_P are higher in elliptical profile than the other profiles.

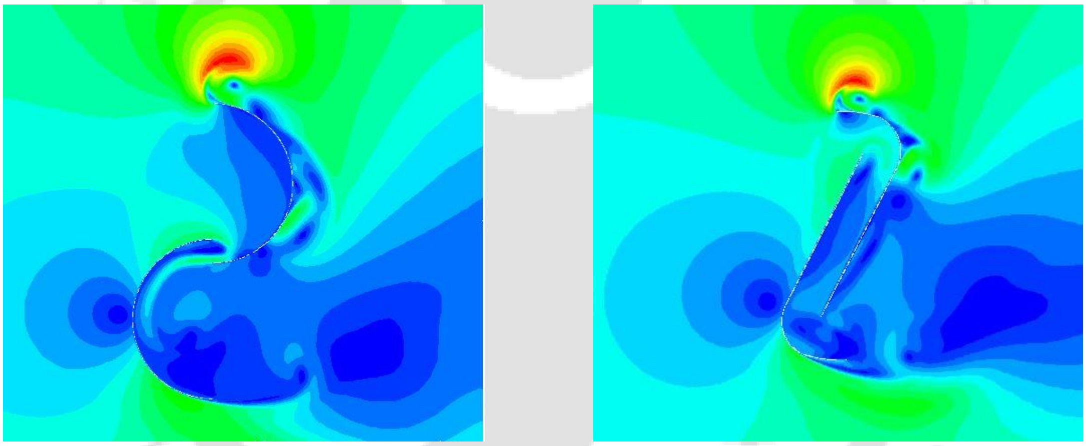

(a) Semicircular (b) Benesh

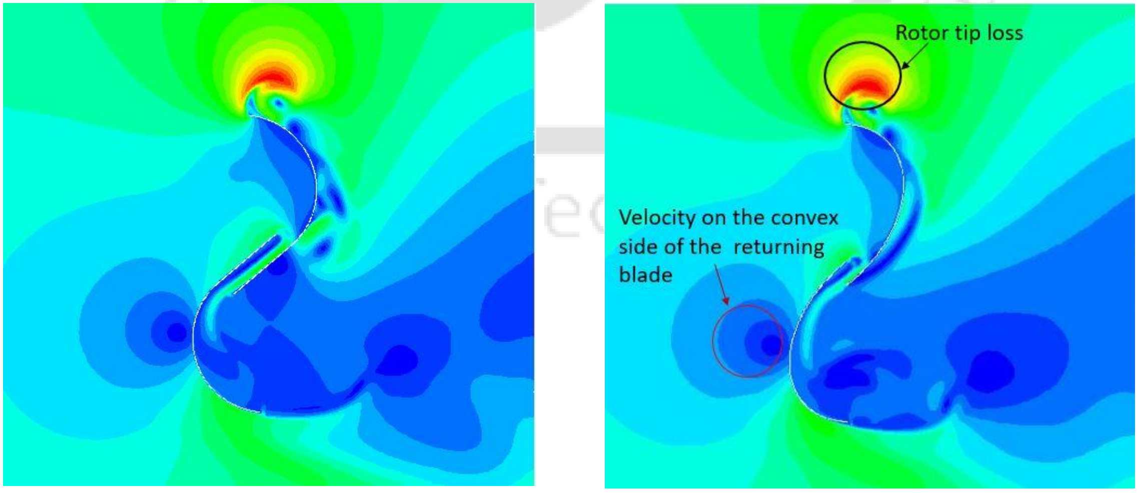

(c) Modified Bach (d) Elliptical

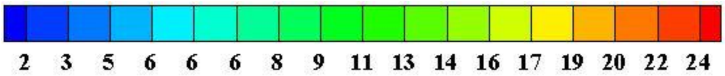

Fig. 3.9: Velocity magnitude (m/s) of various rotor profiles at TSR = 0.80

3.5.2 Total pressure contours

The total pressure contours of several rotor profiles are shown in Fig 3.10. It is clearly observed that the total pressure in the advancing elliptical profile is in the range of 40-70 N/m^2, however, this is found to be lesser in other profiles. The low-pressure region, forming the recirculation behind the advancing profile, is found to be higher in the semicircular, Benesh and modified Bach profiles over the elliptical profile. Also, the region of higher pressure on the convex side of the returning elliptical profile is lesser over the others, and as a result, the resulting torque is higher in the elliptical profile.

(a) Semicircular (b) Benesh

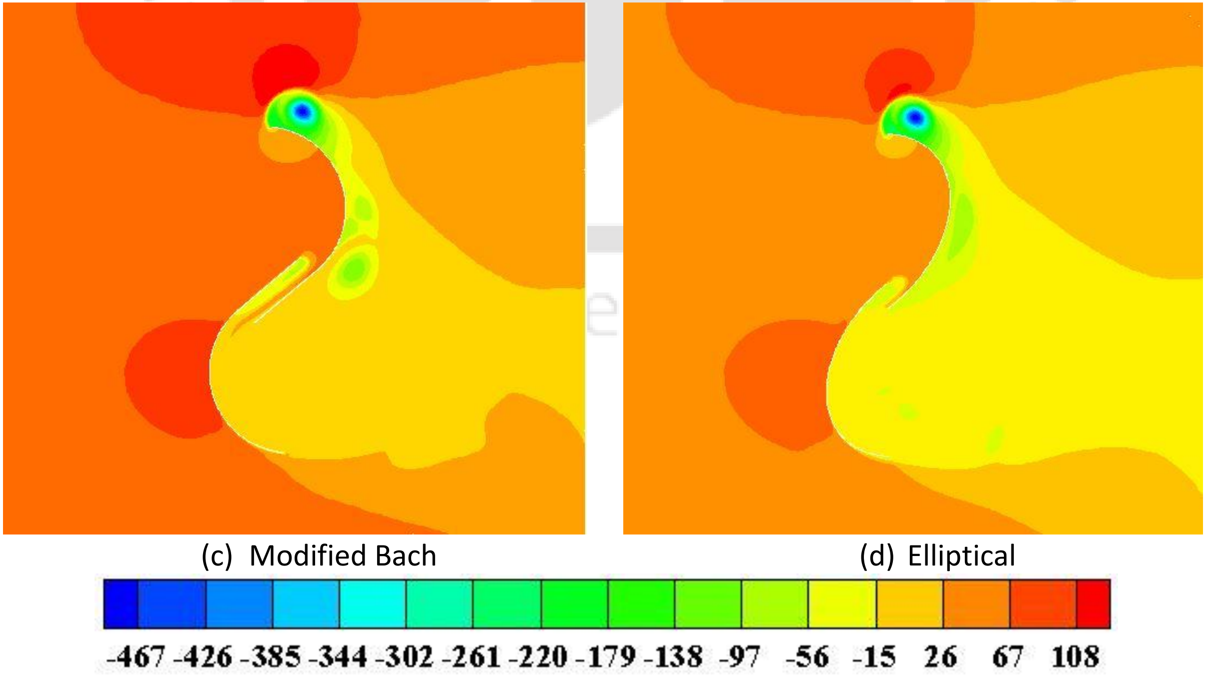

(c) Modified Bach (d) Elliptical

Figure 3.10: Total pressure (N/m^2) contours of various rotor profiles at TSR = 0.80

It is obvious from the contours that there is high fluctuation in total pressures leading the high turbulence behind the rotor blades of semicircular, Benesh and modified Bach profiles over the elliptical profile showing a performance improvement of the latter. It is believed that due to higher blade curvature in semicircular-profile, the flow separation occurs earlier over other profiles with lesser blade curvature (Fig. 3.11). The adverse pressure gradient is much higher at the tip of semicircular, Benesh and modified Bach profiles than the elliptical profile (Fig. 3.11). As a result, the flow separation takes place earlier in all the profiles except the elliptical one showing its higher C_D and hence higher C_T and C_P.

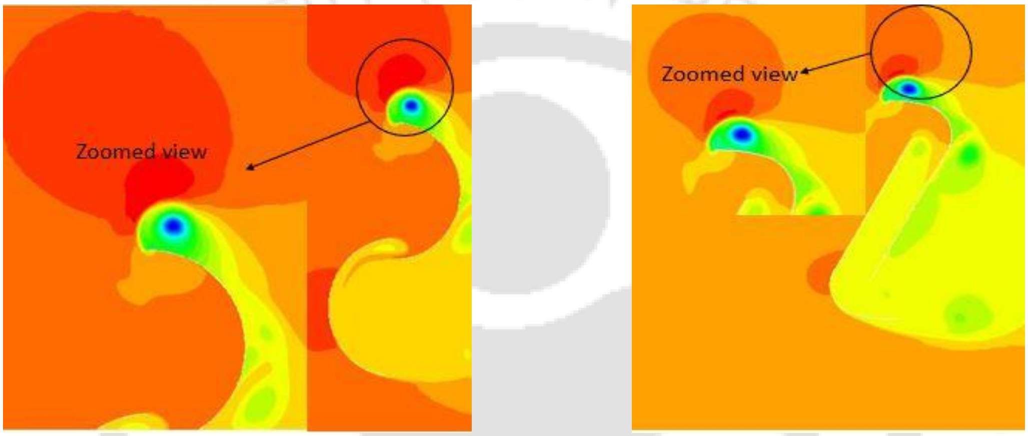

(a) Semicircular (b) Benesh

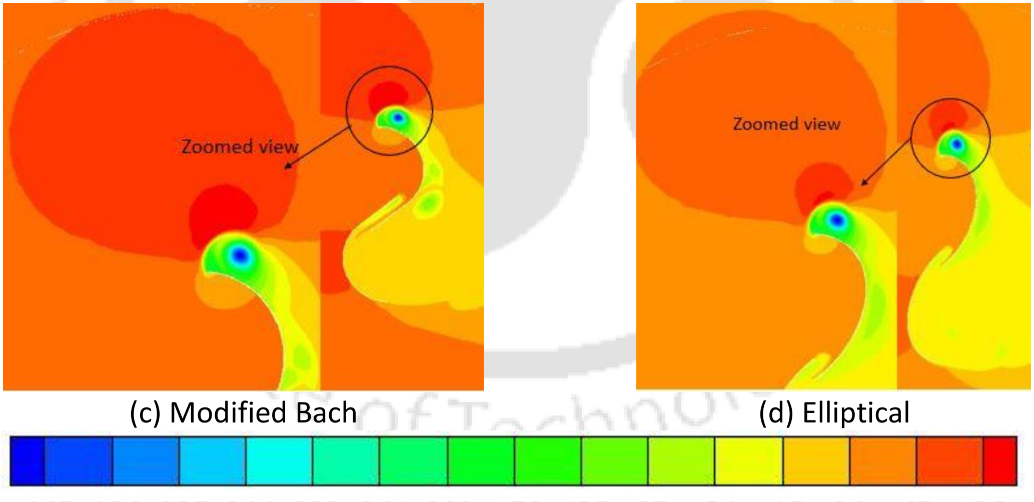

(c) Modified Bach (d) Elliptical

Figure 3.11: Zoomed view of total pressure (N/m^2) contours at the rotor tip

3.5.3 Turbulence intensity contours

Figure 3.12 shows the turbulence intensity contours of tested rotor profiles. Turbulence intensity is the ratio of the root-mean-square of the velocity of fluctuations to the mean flow velocity. It is the property of turbulent flow by which the degree of flow disturbance is measured. It is evident that the turbulence intensity near the elliptical-profile is lesser and is in the range of 0.06 to 0.11%. However, the turbulence intensity for semicircular and Benesh profiles are observed to be in the range of 0.08 - 0.18%; whereas for the modified Bach profile, the range of turbulence intensity is found be 0.08 - 0.16%. Thus, the magnitude of turbulence intensity is found much lesser in case of the elliptical profile which reduces the formation of vortices at the downstream of the rotor. Also, there is a smooth flow field behind the returning elliptical profile than other profiles. Thus, a higher C_P of the elliptical profile is observed.

(a) Semicircular (b) Benesh

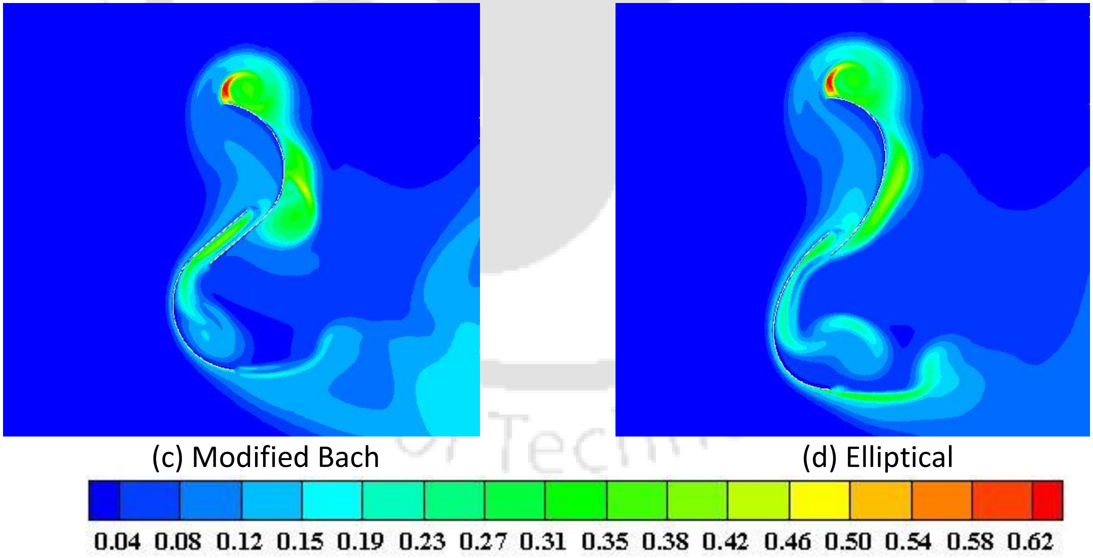

(c) Modified Bach (d) Elliptical

Figure 3.12: Turbulence intensity (%) contours of various rotor profiles at *TSR* = 0.80

3.6 Optimization of Overlap Ratio

A series of 2D unsteady simulations are conducted with an aerodynamically optimized elliptical profile without shaft. As stated earlier, the optimized profile has a sectional cut angle (θ) of 47.5^0. The *OR* of this profile is varied in the range of 0.0 to 0.30 to arrive at the optimum value. The torque coefficient (C_T) and power coefficient (C_P) are calculated and analyzed with respect to *TSR*. Figures 3.13 and 3.14 demonstrate the variations of C_T and C_P with *TSR* at various *OR*s. It is observed that with the application of load, the rotational speed on the rotor reduces, and thus the trend of C_T decreases with an increase of *TSR*. Nevertheless, the performance is found to be optimum at *TSR* = 0.8. At this *TSR*, the peak C_P of 0.34 is obtained for the elliptical profile at *OR* = 0.15; whereas at the same *TSR*, the elliptical profile shows a peak C_P of 0.33 at *OR* =0.20. The simulation thus exhibits a performance improvement of 3% at *OR* = 0.15.

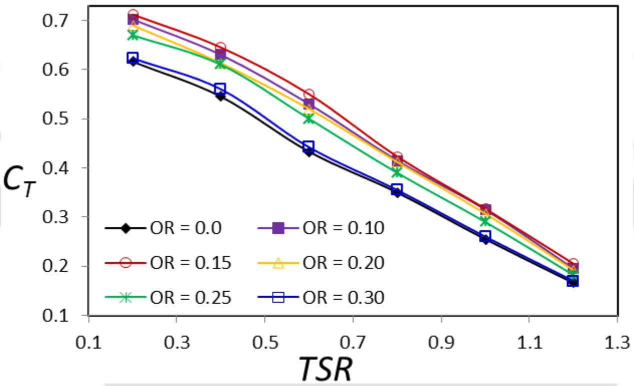

Figure 3.13: Variation of C_T with *TSR*

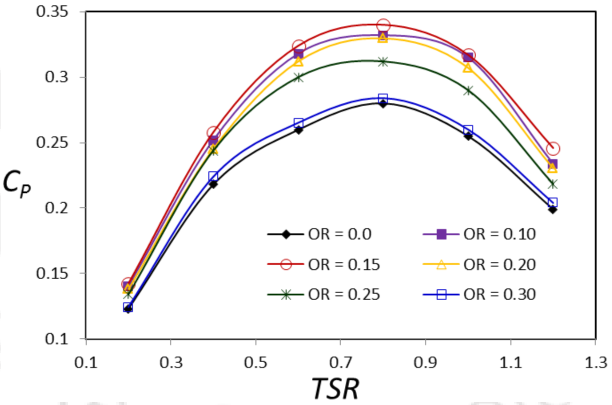

Figure 3.14: Variation of C_p with *TSR*

3.6.1 Analysis of velocity contours

Figure 3.15 shows the velocity contours of the elliptical-bladed profiles at various *OR* ranging from 0.0 to 0.30. At *OR* = 0.15, the velocity magnitude is within the range of 4-6 m/s near the advancing blade, whereas in other cases, the velocity magnitude found to be lesser. At *OR* = 0.15, the velocity gets accelerated near the tip of blades and there is a reasonably elevated velocity magnitude near the surface of the elliptical profiles as over the contours with other *OR*s. At the same *OR* (= 0.15), it is also seen that the velocity on the convex side of the returning blade is reasonably lesser over the velocities of other profiles. The boundary layer separation usually takes place due to excessive momentum loss near the profile curvature, and this momentum loss at the tip of the rotor profile is lesser. This indicates a lesser chances of flow separation over other *ORs*. Due to this, there is a reduction of negative torque of the profile resulting an enhancement in aerodynamic drag of the rotor and hence the higher C_T and C_P.

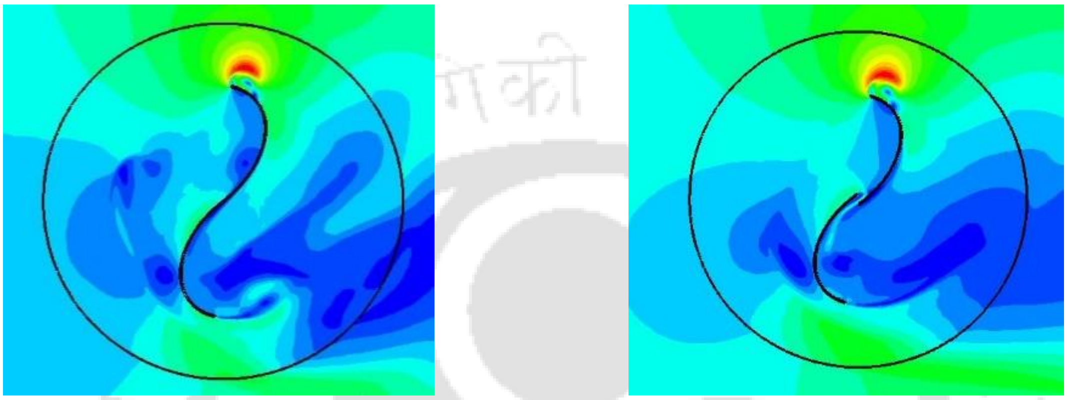

(a) *OR* = 0.0 *(b)* *OR* = 0.10

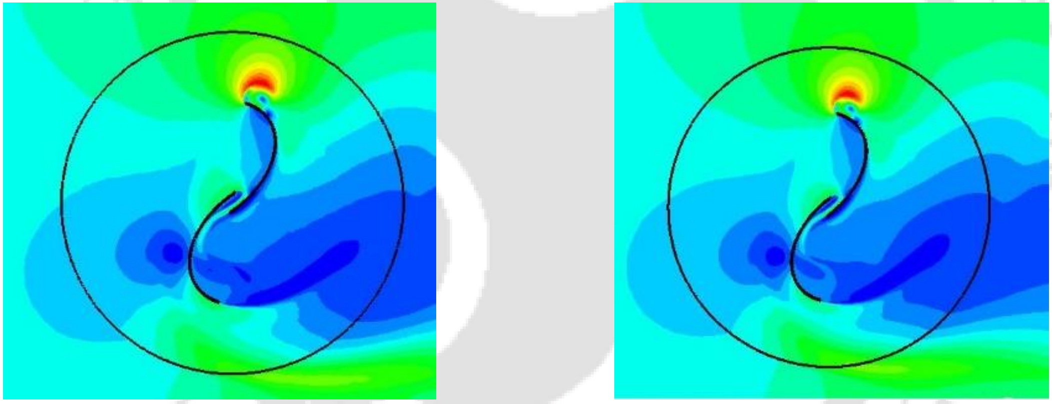

(c) *OR* = 0.15 *(d)* *OR* = 0.20

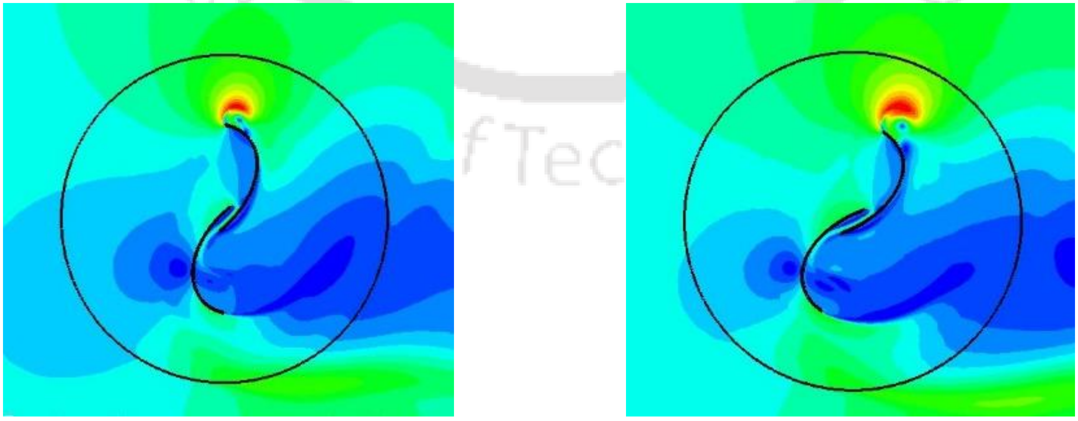

(e) *OR* = 0.25 *(f)* *OR* = 0.30

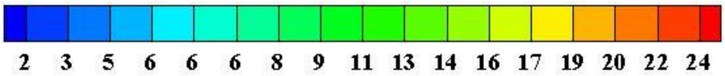

Figure 3.15: Velocity contours (m/s) of the elliptical profile at various ORs with TSR = 0.8

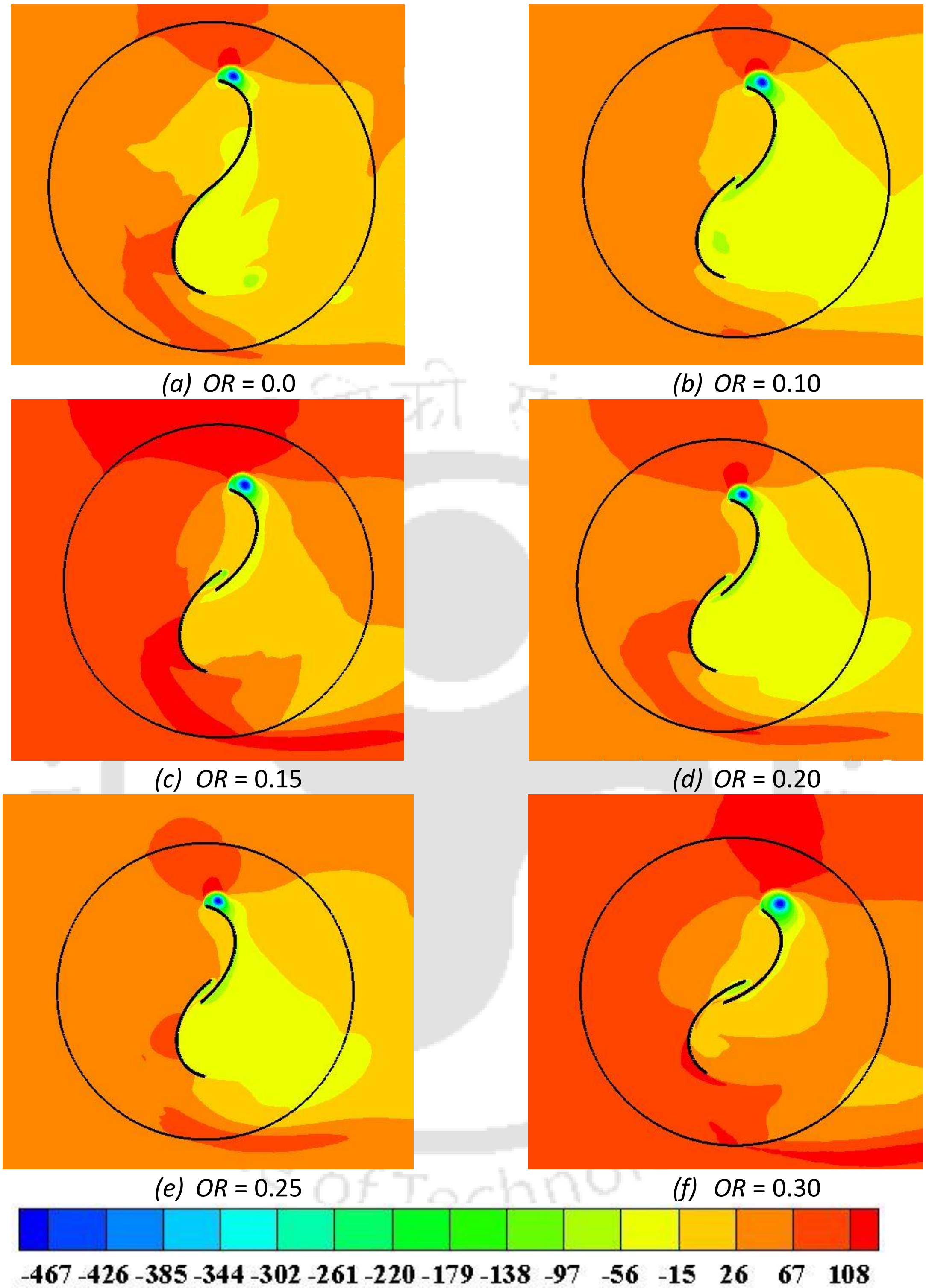
(a) *OR* = 0.0 (b) *OR* = 0.10

(c) *OR* = 0.15 (d) *OR* = 0.20

(e) *OR* = 0.25 (f) *OR* = 0.30

Figure 3.16: Total pressure (N/m^2) contours of elliptical profile at various OR with TSR = 0.8

3.6.2 Analysis of total pressure contours

Figure 3.16 depicts the total pressure contours obtained for the elliptical profile at the tested range of *ORs*. A reasonably higher total pressure is experienced by the advancing blade of the elliptical profile at *OR* = 0.15 in contrast to the data obtained with other *ORs*. As a result, the boundary layer separation seems to be prevented or delayed causing an improved pressure recovery. This may be the reason for obtaining a performance enhancement at *OR* = 0.15. Furthermore, the *OR* that determines the free space at the center plays a vital role as it minimizes the effect of pressure on the convex part and permits the wind flowing to the other side, thereby impinging on the other concave part of the rotor profile. It is observed that the total pressure on the concave part of the returning blade is higher than the other profiles. The effect of overlapping flow is more prominent in case of *OR* = 0.15 to that of other *OR*s.

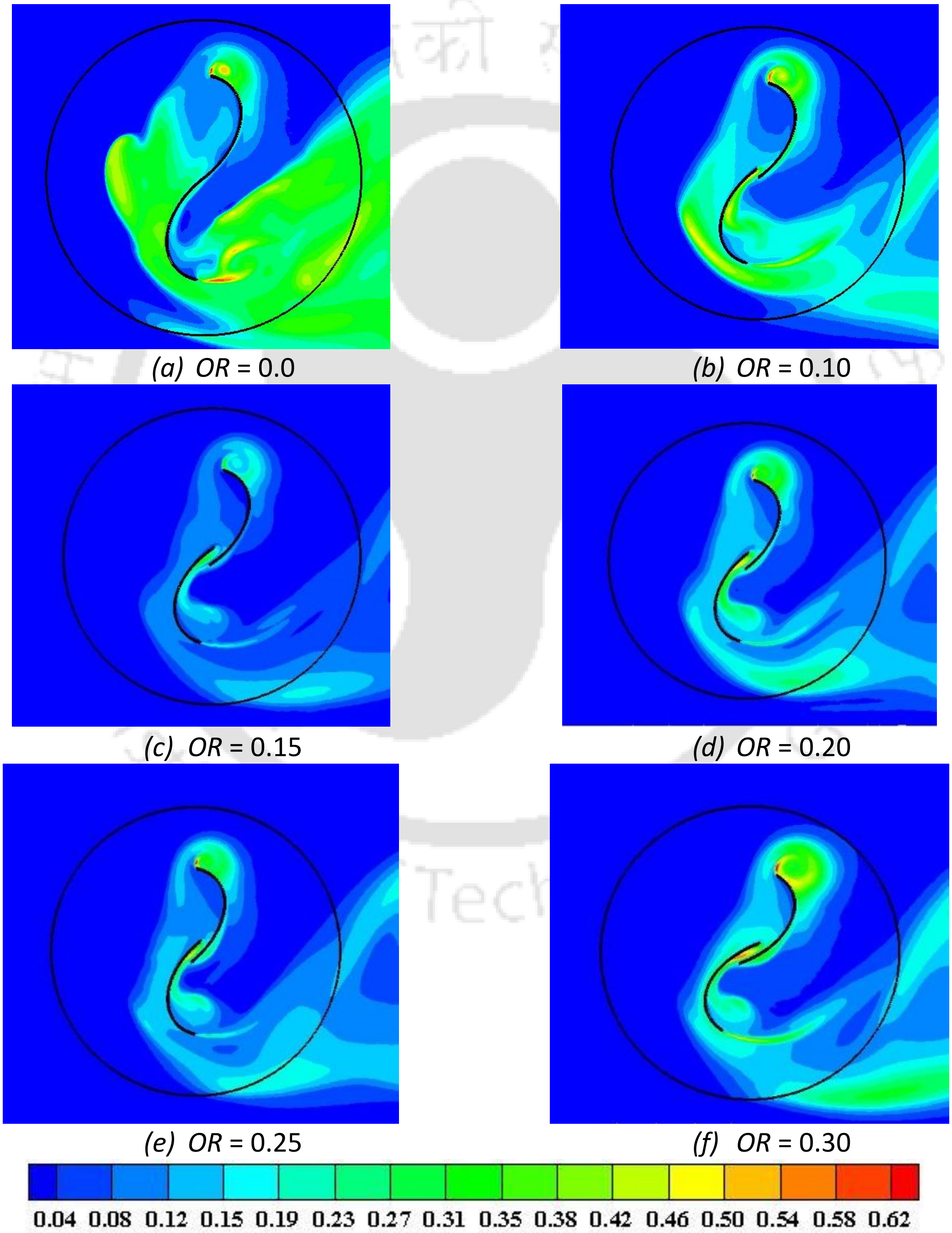
(a) *OR* = 0.0

(b) *OR* = 0.10

(c) *OR* = 0.15

(d) *OR* = 0.20

(e) *OR* = 0.25

(f) *OR* = 0.30

Figure 3.17: Turbulence intensity (%) contours of elliptical profile at various OR with TSR = 0.8

3.6.3 Analysis of turbulent intensity contours

Figure 3.17 shows the turbulence intensity contours of the elliptical profile at various *ORs*. It is clearly observed that the magnitude of turbulence intensity in case of *OR* = 0.15 is within the range of 0.15 to 0.19%, however, in all other test cases, the magnitude of turbulence intensity is within the range of 0.23 to 0.35%. Thus, the magnitude of turbulence intensity for *OR* = 0.15 is lesser over the magnitudes with other *ORs*. This cuts down the formation of vortices at the downstream of the rotor thereby increasing its performance.

3.7 Effect of Number of Blades

The 2D unsteady simulations are also carried out to study the effect of number rotor blades without the presence of shaft. The simulation is carried out for 2-, 3- and 4-bladed elliptical profiles to optimize the number of rotor blades. The numerical simulation is also carried out to investigate the influence of rotor shaft with the optimized number of blade profiles. In general, for all the cases, with the application of load, the rotational speed of the rotor reduces, and thus, the trend of C_T decreases with the increase of *TSR* (Fig. 3.18). As seen in Fig. 3.19, the 2-bladed elliptical profile shows higher power coefficients over the tested range of *TSR*s over the 3- and 4-bladed systems. The 2-bladed profile shows a peak C_P of 0.34, whereas for the 3- and 4-bladed profiles, the peak C_P is found to be 0.29 and 0.24, respectively. The power coefficients in 3- and 4-bladed systems are believed to be reduced due to the formation of vortices at the downstream of the returning blades. In the 2-bladed system, the rotor without shaft shows higher values of torque coefficients over the tested range of *TSR*s (Fig. 3.20). With the presence of shaft, the power coefficients of the 2-bladed system are reduced because of the reduction in overlapping flow. The peak C_P is found to be 0.31 for the 2-bladed elliptical profile in the presence of the central shaft (Fig. 3.21).

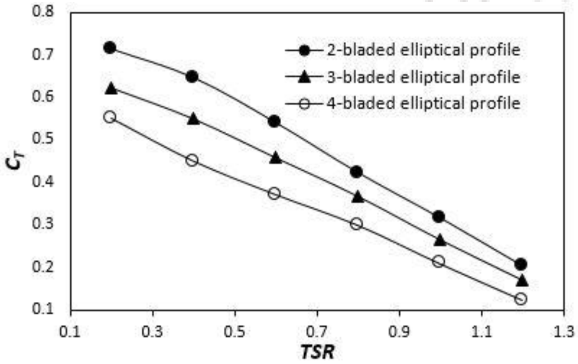

Figure 3.18: C_T vs *TSR* for 2-, 3- and 4-bladed elliptical profiles

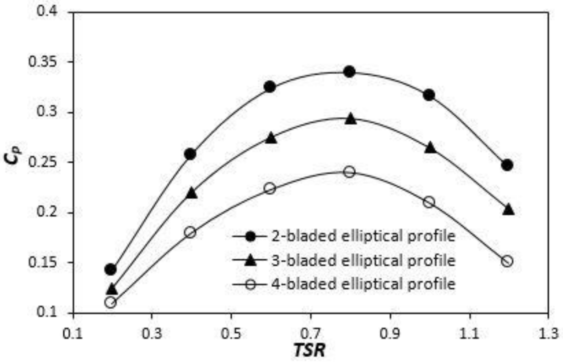

Figure 3.19: C_P vs *TSR* for 2-, 3- and 4-bladed elliptical profiles

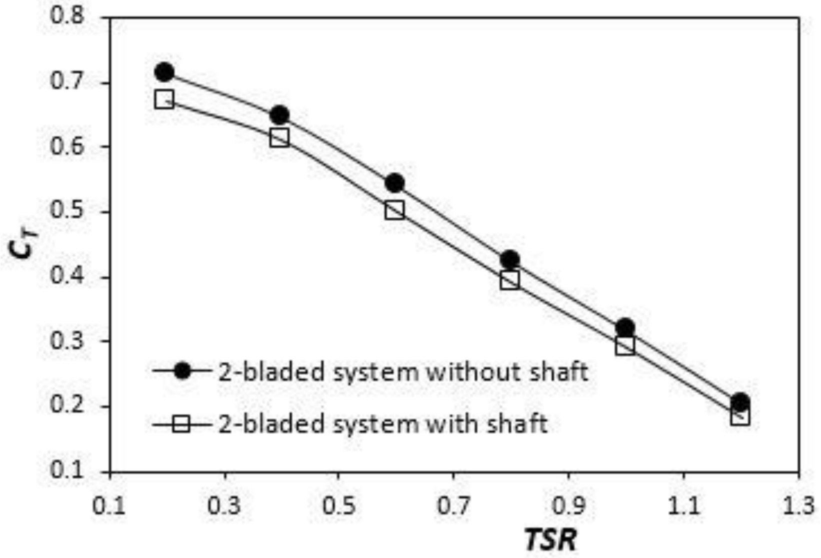

Figure 3.20: C_T vs *TSR* for the elliptical-bladed profiles without and with shaft

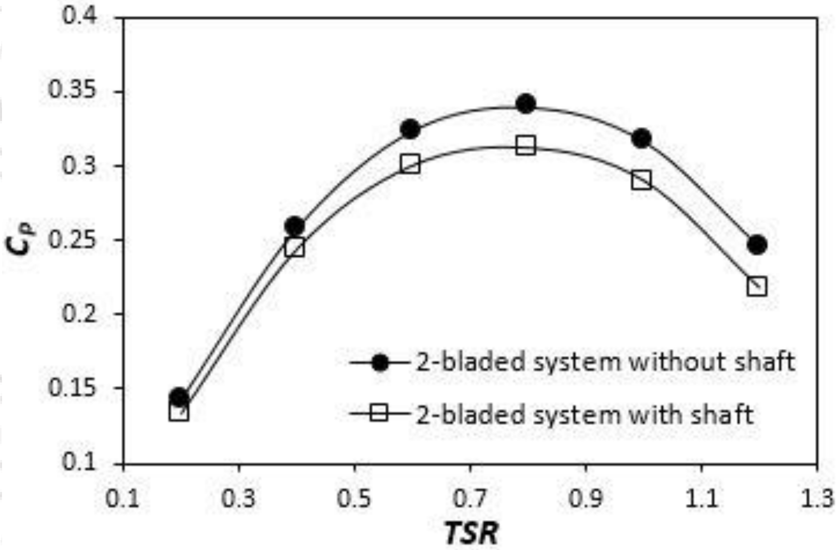

Figure 3.21: C_P vs *TSR* for the elliptical-bladed profiles without and with shaft

3.7.1 Analysis of velocity contours

Figure 3.22 shows the velocity contours of the elliptical profile for the 2-, 3- and 4- bladed systems. The magnitude of velocity near the surface of 2-bladed profile is approximately in the range of 5-6 m/s, whereas in 3- and 4-bladed systems, the velocity magnitude lies in the range of 4-5 m/s. It is also observed that at the tip of the advancing blade of 2-bladed system, the magnitude of velocity lies in the range of 10-15 m/s, whereas for the other two cases, the velocity magnitude lies in the range of 12-18 m/s. This clearly implies that the tip losses are pronounced in the 3- and 4-bladed systems over the 2-bladed system. Thus, there is a lesser chances of flow separation in the 2-bladed system and this obviously brings an improvement in its performance coefficients.

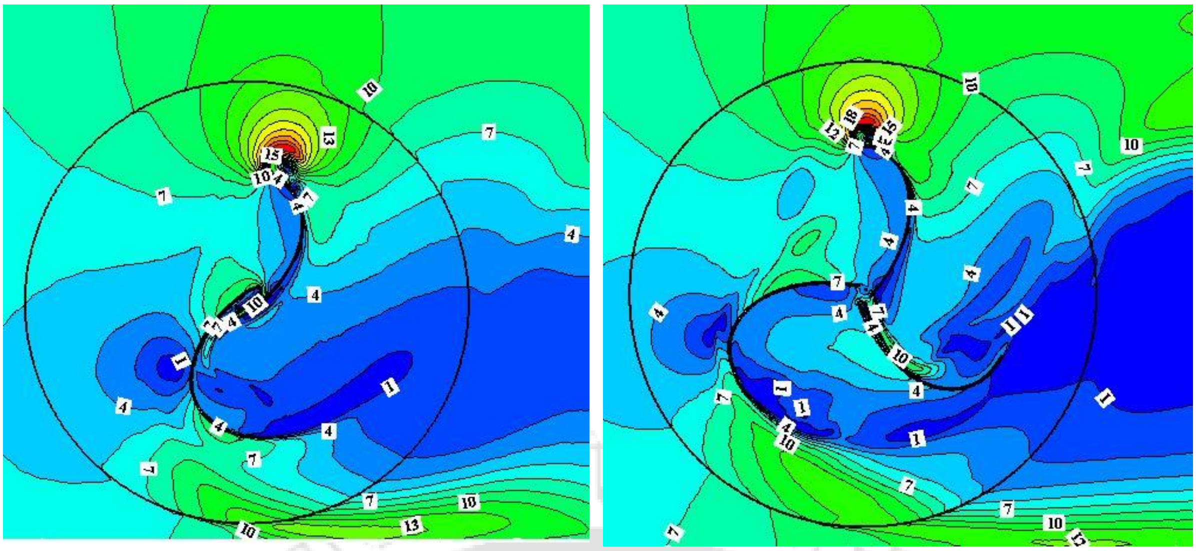

(a) 2-bladed system (b) 3-bladed system

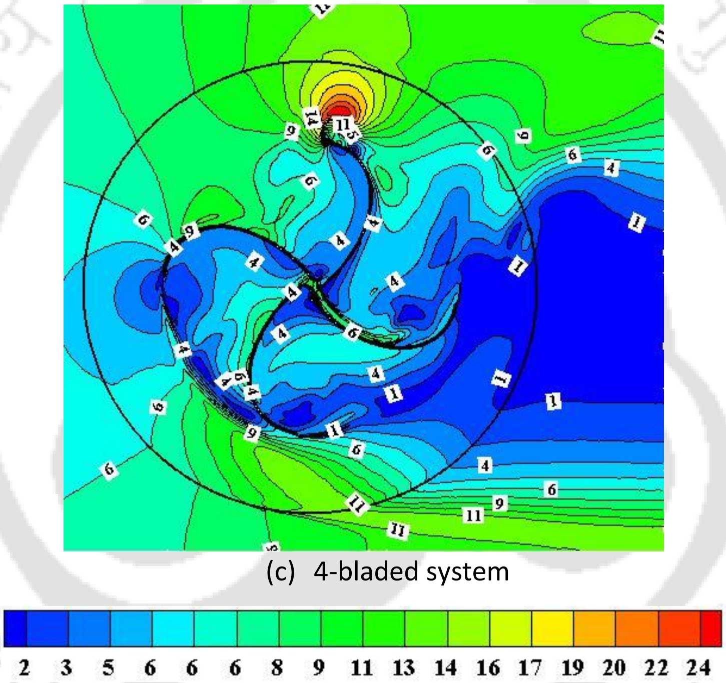

(c) 4-bladed system

Figure 3.22: Velocity magnitute (m/s) contours of the elliptical profiles at *TSR* = 0.8

3.7.2 Analysis of total pressure contours

Figure 3.23 shows the total pressure contours of 2-, 3- and 4-bladed elliptical profiles. The recovery of pressure behind the rotor blades in 3- and 4-bladed systems is not taking place due to the wake formation. The total pressure behind the returning blade of the 3-bladed system shows a magnitude of -12 N/m^2 whereas the 4-bladed system shows a magnitude of -22 N/m^2 behind the returning blades. But in the advancing blades, a positive total pressure is observed. The total pressure behind the returning blades of 3- and 4-bladed systems become lesser and hence an adverse pressure gradient exists behind the rotor blades. As a result, the flow separation is more in 3- and 4-bladed rotor systems. Therefore, it is evident from the plots that there is high fluctuation in total pressures leading the high turbulence behind the rotor blades.

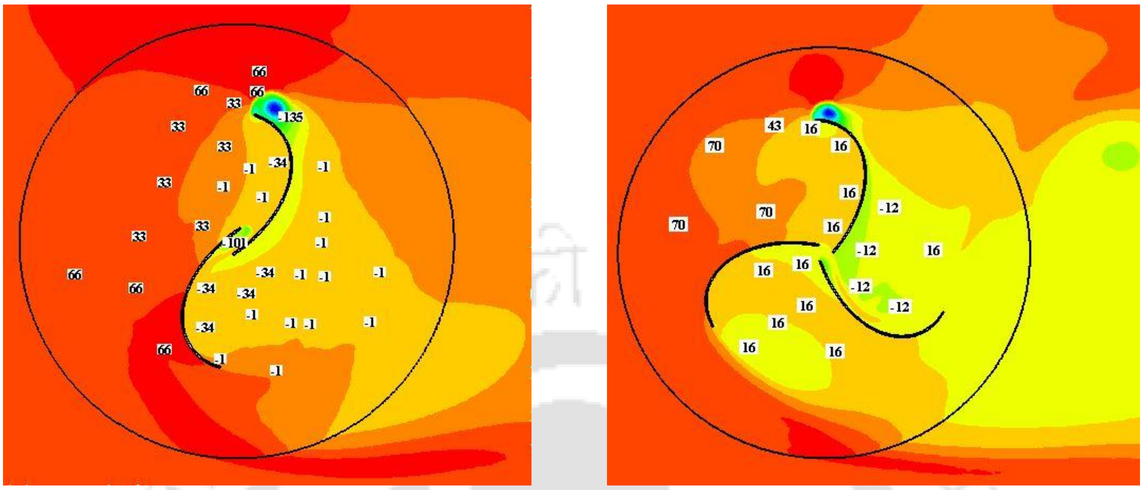

(a) 2-bladed system (b) 3-bladed system

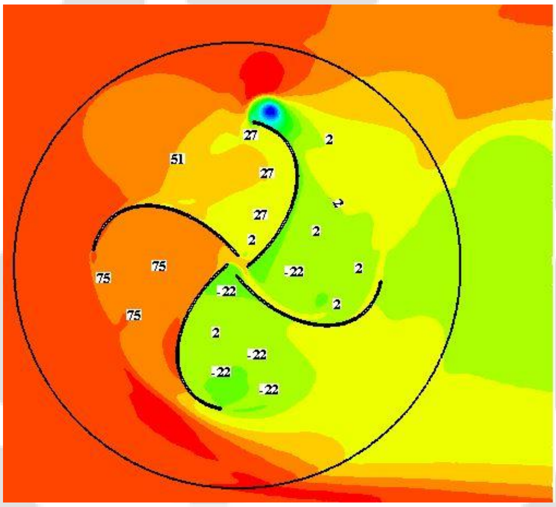

(c) 4-bladed system

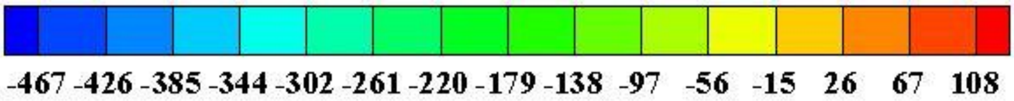

Figure 3.23: Total pressure (N/m^2) contours of the elliptical profiles at *TSR* = 0.8

3.7.3 Turbulence intensity contours

Figure 3.24 show the turbulence intensity contours. It is seen that at the tip of the advancing blade, the flow is separated leading to the formation of wake behind the returning blades. The formation of wake is larger in 3- and 4-bladed systems than the 2-bladed system reducing the performances in 3- and 4-bladed systems. It is also observed that the magnitude of turbulence intensity in case of 2-bladed system is lesser and is within the range of 0.09 to 0.11%, however, for the 3-bladed system, the turbulence intensity is in the range of 0.15 to 0.22%, and for the

4-bladed system, in the range of 0.17 to 0.28%. Hence, the magnitude of turbulence intensity in the 2-bladed system is much lesser, which diminishes the formation of vortices at the downstream of the rotor blades and hence improves the power coefficients.

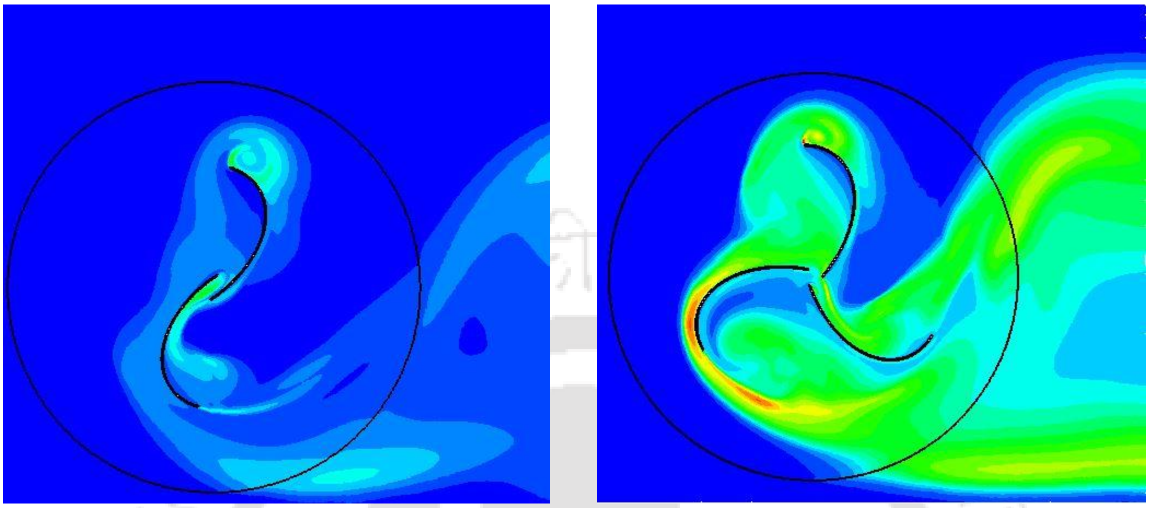

(a) 2-bladed system (b) 3-bladed system

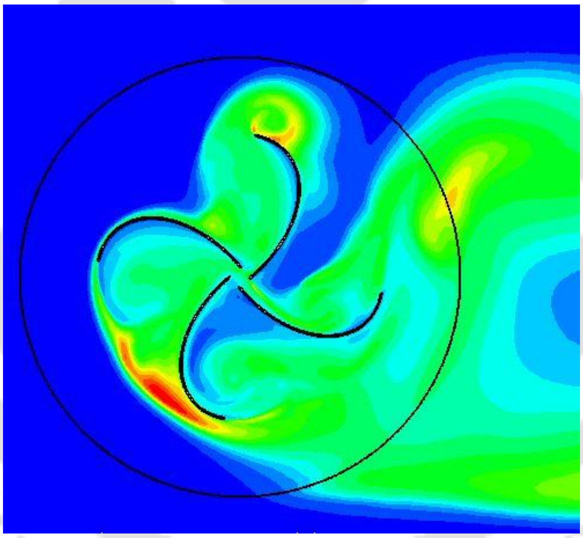

(c) 4-bladed system

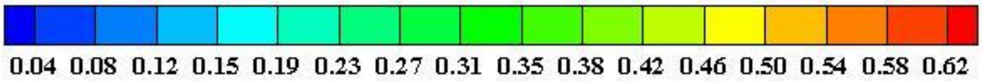

Figure 3.24: Turbulence intensity contours of the elliptical profiles at *TSR* = 0.8

3.7.4 Analysis of streamline patterns

Figure 3.25 shows the streamline patterns of 2-, 3- and 4-bladed systems. There is a formation of recirculation in the returning blade of 3- and 4- bladed systems but in case of 2-bladed system no such recirculation is observed. Hence, the fluid is rotating about an axis which gives rise to the formation of vortices at the downstream of 3- and 4-bladed systems. But in case of

2-bladed system, there is no formation of vortices at the downstream of the rotor, and as a result the performance coefficients is found to be more in the 2-bladed system.

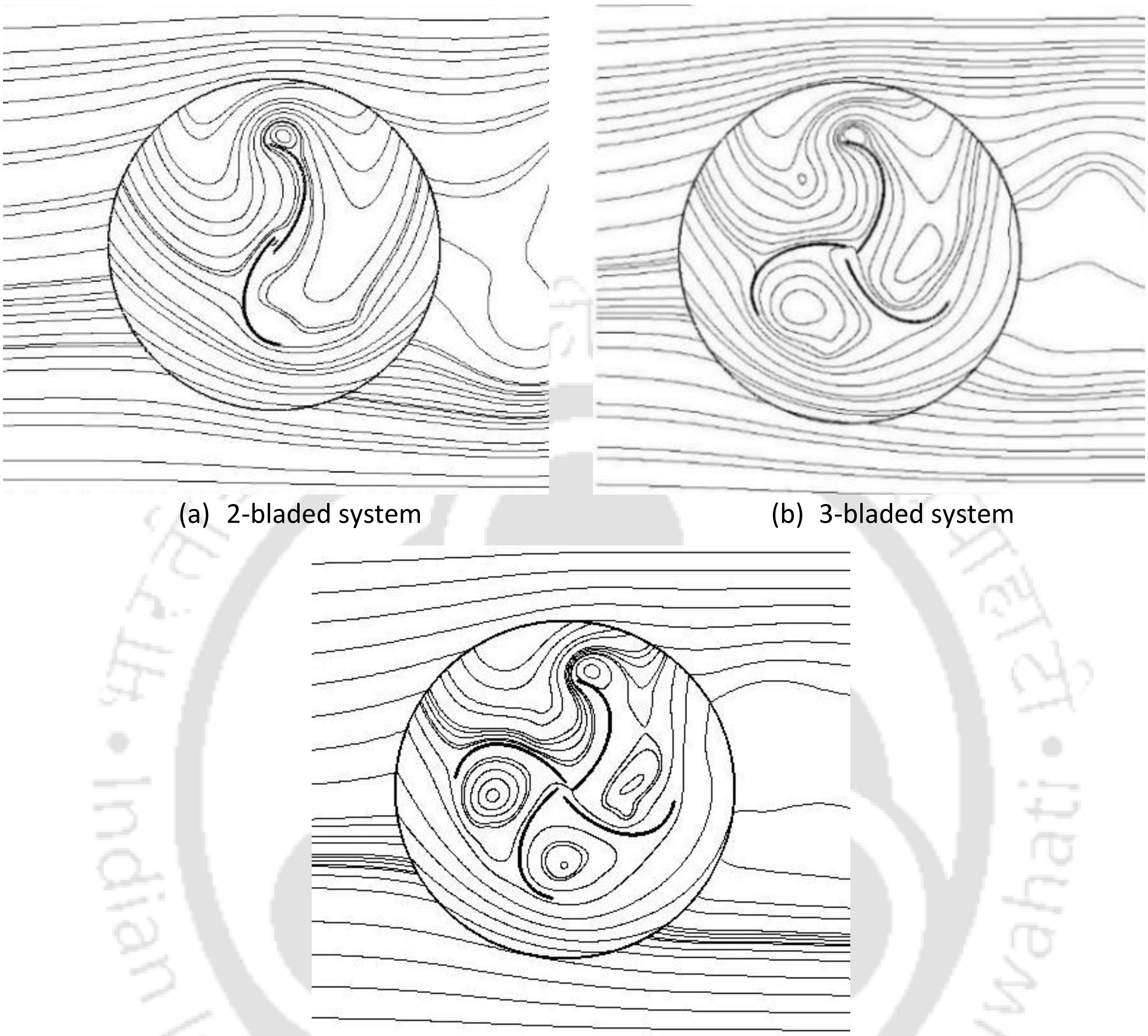

(a) 2-bladed system (b) 3-bladed system

(c) 4-bladed system

Figure 3.25: Streamline patterns of 2-, 3- and 4-bladed elliptical profiles at *TSR* = 0.8

3.8 Effect of Shaft

3.8.1 Analysis of velocity contour

Figure 3.26 shows the velocity contours of the elliptical-bladed profile without and with the presence of shaft on the rotor. The magnitude of velocity is found to be comparatively higher in the elliptical profile without the shaft. Furthermore, the overlap ratio that determines the free space at the center plays a vital role as it minimizes the effect of pressure on the convex part and permits the air flowing to the other side, thereby impinging on the other concave part of the rotor profile. The overlapping flow is more prominent in the 2-bladed profile without the shaft at the center. Due to the presence of shaft at the center of the rotor, the vortices are formed near the surface of the concave side of returning blade, and this is the main reason for the deterioration of rotor performance.

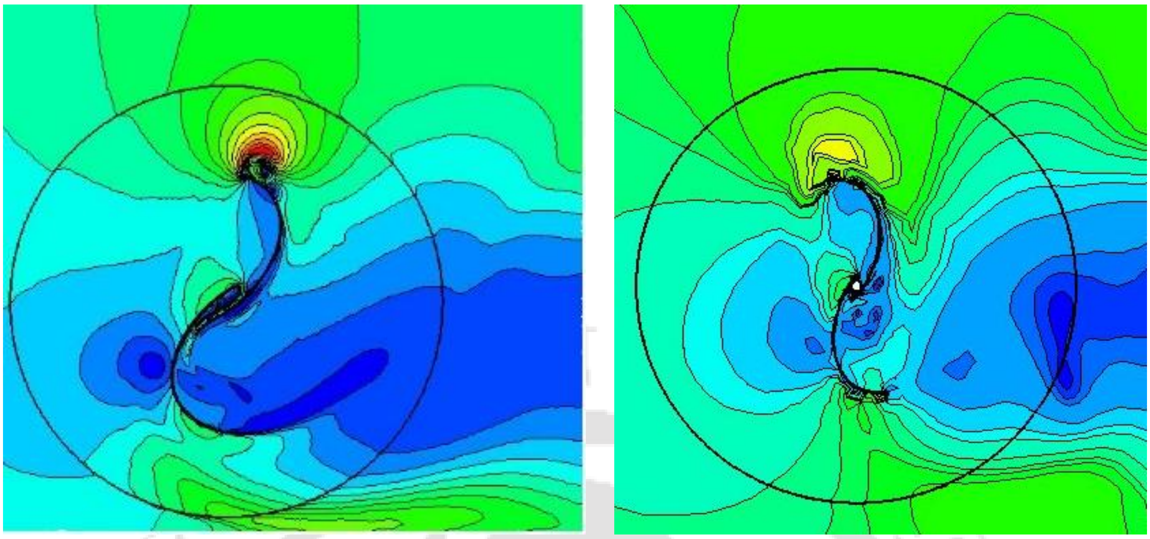

(a) Rotor without shaft (b) Rotor with shaft

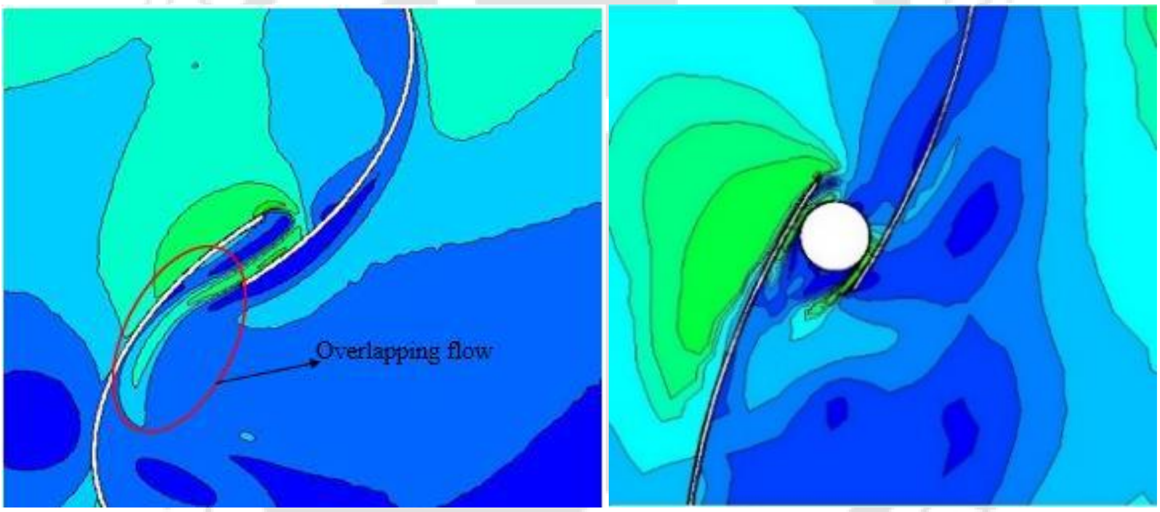

(c) Zoomed view of rotor without shaft (d) Zoomed view of rotor with shaft

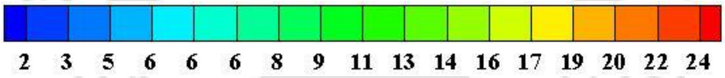

Figure 3.26: Velocity magnitute (m/s) contours of elliptical profiles with and without shaft at *TSR* = 0.80

3.8.2 Analysis of streamline patterns

The streamline patterns of the 2-bladed elliptical profile without and with the rotor shaft is depicted in Fig. 3.27. It is evident that in the presence of shaft, the overlapping flow is reduced, and the small flow recirculation occurs in the concave side of the returning blade profile. Thus, there is a lesser amount of air impinging on the concave side of the returning blade of the rotor thereby deteriorating the performance of the rotor with the shaft.

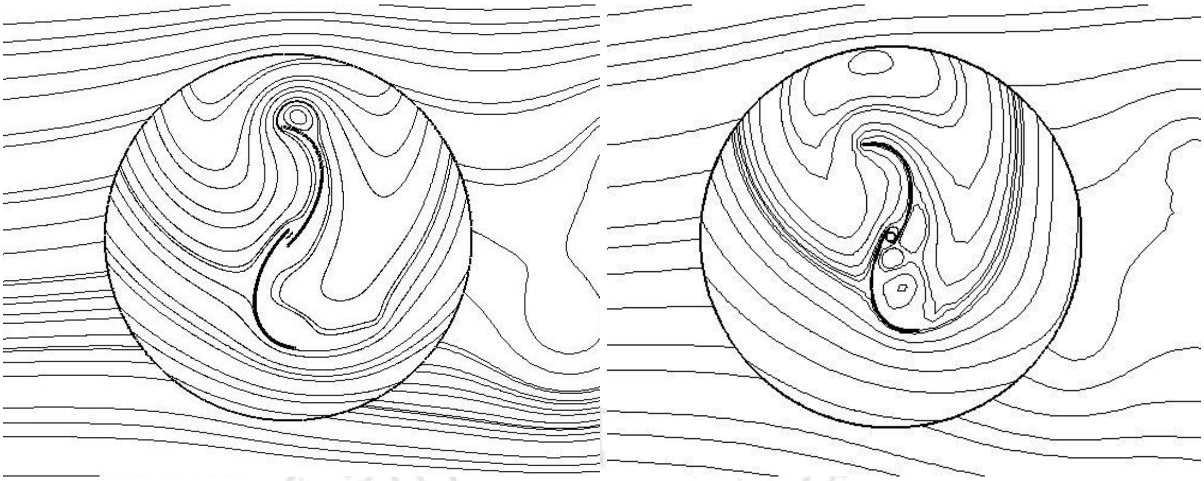

(a) Rotor without shaft (b) Rotor with shaft

Figure 3.27: Streamline patterns of elliptical profiles without and with shaft at *TSR* = 0.80

3.9 Effect of Reynolds Number

In the present investigation, the rotor profiles have been tested numerically at various Reynolds number, *Re* =0.72 x10^5, 0.89 x 10^5 and 1.01 x 10^5 corresponding to the wind speeds of 5 m/s, 6.2 m/s and 7 m/s. Usually, the C_P of the rotor is increased with the increased in *Re* (Kamoji et al., 2009; D'Alessandro et al., 2010). The results obtained from the unsteady simulation are shown in Table 3.2, and it is observed that with the increase of *Re*, the C_P of the rotor profile in each case also increase. In the tested Reynolds number, the elliptical profile demonstrates the maximum C_P over the other profiles. The increased C_P is because for a given rotor diameter the flow separation around the rotor profiles are delayed at higher wind speeds and this happens slightly in the lower side of the returning profile. As a result, there is pressure recovery with the contribution of lift force, thereby enhancing the C_T and C_P of the rotor profiles.

Table 3.2: Power coefficient (C_P) at various Reynolds number

Profiles	*Re* = 0.72 x 10^5		*Re* = 0.89 x 10^5		*Re* = 1.01 x 10^5	
	C_{Pmax}	*TSR*	C_{Pmax}	*TSR*	C_{Pmax}	*TSR*
Elliptical profile	0.29	0.80	0.34	0.80	0.35	0.90
Semicircular profile	0.25	0.80	0.27	0.80	0.29	0.80
Modified Bach profile	0.28	0.80	0.30	0.80	0.32	0.90
Benesh profile	0.23	0.80	0.29	0.80	0.30	0.80

3.10 Concluding Remarks

A series of 2D unsteady simulations are carried out with Benesh, modified Bach and elliptical profiles using *SST k-ω* turbulence models. From the simulated results, the elliptical-profile shows a peak C_P of 0.34 at *TSR* = 0.8; whereas the semicircular, Benesh and modified Bach profiles show a peak C_P of 0.27, 0.29 and 0.30, respectively at the same *TSR*. Also, the number rotor blades and the effect of shaft have been investigated. Amongst the 2-, 3- and 4-bladed elliptical profiles, 2-bladed elliptical profile shows the maximum C_P without the central shaft. The unsteady simulations show a peak C_P of 0.34 for the 2-bladed system at the optimum *OR* = 0.15. With the presence of shaft, the 2-bladed system shows a peak C_P of 0.31 at *TSR* = 0.8. Thus, there is a performance improvement by 10% in the 2- bladed elliptical profile without shaft in comparison to the rotor with shaft. Further, the effect of Reynolds numbers (Re) have investigated and it is found that with the increase in *Re,* the C_P is also increased in the newly developed elliptical profile.

CHAPTER –4

Drag and Lift (2D) Analysis

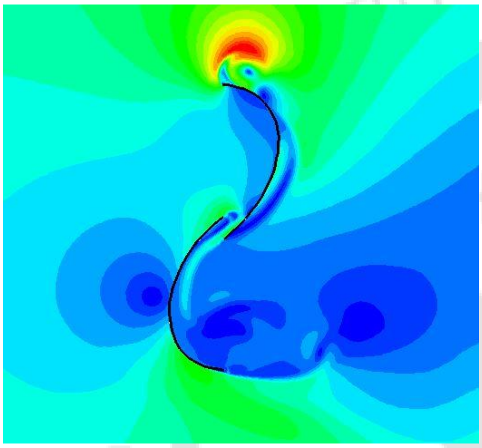

Chapter Outline

Overview

The Savonius rotor is mainly a drag-based wind turbine, however, the lift force also contributes to its performance. For a better aerodynamic design of the Savonius rotor, drag and lift characteristics have to be investigated extensively. In the present chapter, drag and lift of the various rotor profiles such as elliptical, modified Bach, Benesh and semicircular have been investigated. The average drag and lift coefficient (C_D and C_L) for the elliptical, modified Bach, Benesh and semicircular profiles are found to be 1.43, 1.41, 1.25 and 1.35, and 0.95, 0.95, 1.32 and 0.96, respectively at TSR = 0.6. This shows an improvement of average C_D by 6% in elliptical profile over the semicircular profile.

4.1 Introduction

The Savonius rotor is a drag driven machine, however a minor amount of lift force is also influencing the performance of the rotor. Hence, in this chapter 2D unsteady simulations have been conducted to investigate the various Savonius rotor profiles to estimate its drag and lift coefficients (C_D and C_L).

4.2 Validation of the Results

The present 2D and 3D unsteady simulations are carried out in ANSYS Fluent using SST *k-ω* turbulence model at *Re* = 0.892x10^5 based on the rotor diameter (*D*). However, the 2D unsteady results are validated with the 2D unsteady results (*Re*= 1.23x10^5) of Roy and Ducoin, (2016) at *Re*= 1.23x10^5. The present 2D investigation of C_D and C_L (Figs. 4.1 and 4.2) illustrates minor variations to that of the reported data (Roy and Ducoin, 2016). In the present study, the average values of C_D and C_L are found to be 1.38 and 1.0, respectively as opposed to 1.35 and 0.85 obtained by Roy and Ducoin, 2016. Thus, there is an error of 2.2% and 17.6% in the average C_D and C_L values in the present investigation over the reported data (Roy and Ducoin, 2016). Furthermore, the present 3D unsteady results are validated with the 3D unsteady results of Jaohindy *et al*. (2013) at *Re* = 1.31x10^5 (Fig. 4.3). All the simulations have been carried out at a *TSR* of 0.6. As seen in Fig. 4.3, the behavior of C_D in all the cases are found to be similar.

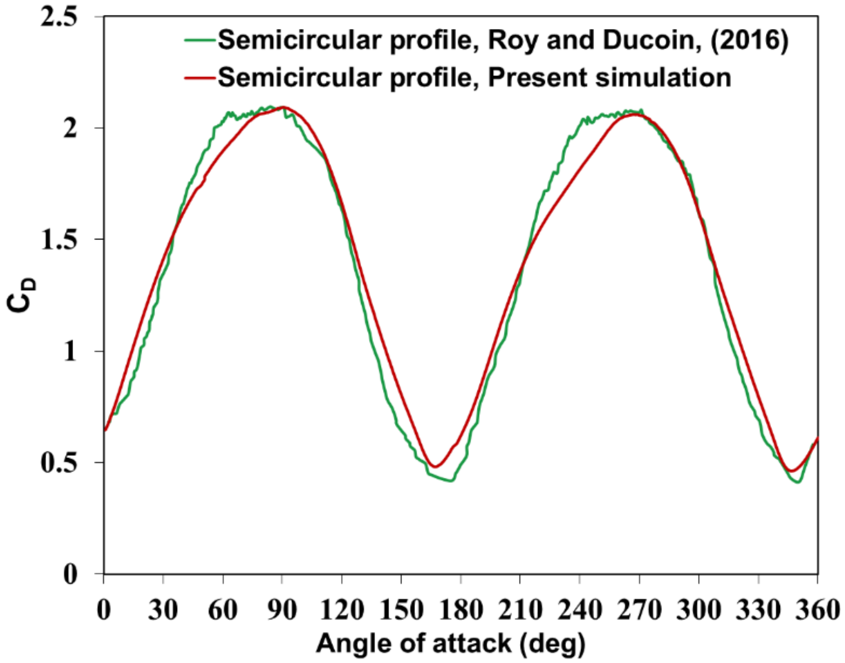

Figure 4.1: Validation of present 2D C_D with the available results

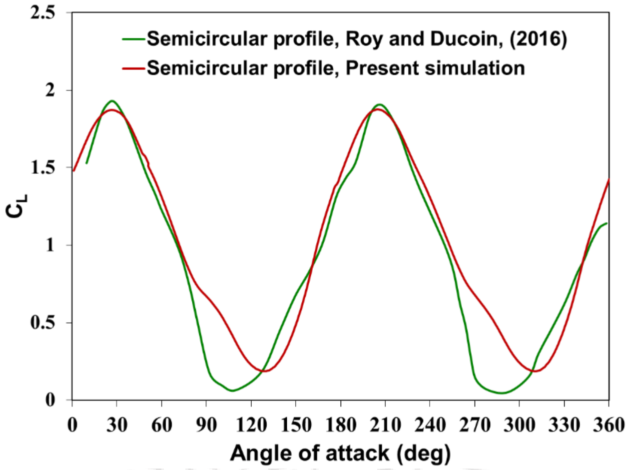

Figure 4.2: Validation of present 2D C_L with the available results

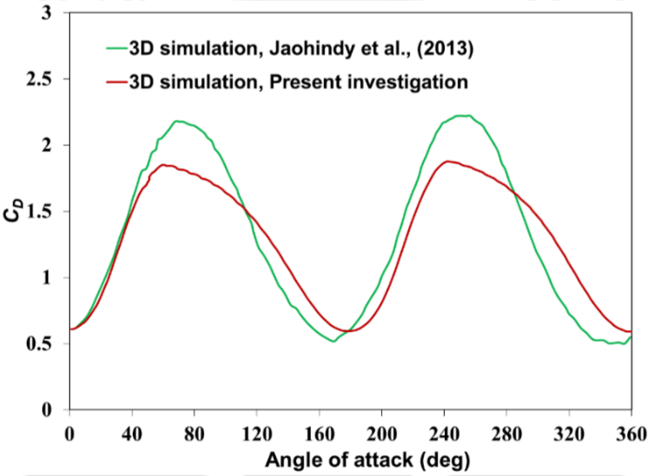

Figure 4.3: Validation of present 3D results with the available results

4.3 Drag and Lift of Elliptical Profile

In this section, results of the 2D unsteady simulation of the elliptical profile are discussed along with the results of semicircular profiles. The comparison of C_T for the elliptical and semicircular profile is shown in Fig. 4.4 where the C_T of the former is found to be higher than the later. This causes the C_P of the elliptical-profile to be higher. Figure 4.5 show the polar variation of C_D and C_L for the tested elliptical and the semicircular profiles. For the elliptical profile, the C_D polar diagram shows improved results in the range of α =30° to 120° and again in the range of α = 210° and 300°. For this profile, the C_{Dmax} is found to be 2.43 both at α = 84° and 266°; whereas the same is observed to be 2.07 at α = 91° and 270°for the semicircular profile. Thus, there is an increase of C_{Dmax} by 17.4% in the elliptical profile over the semicircular profile.

As the elliptical profile has a nearly straight trailing edge (*TE*) and a leading edge (*LE*) with higher curvature than the semicircular profile, they mainly cause a difference in pressure drag. The magnitude of pressure drag on the advancing blade of elliptical-profile is higher than the semicircular-profile at the first quarter of the rotational cycle ($\alpha < 40°$). Furthermore, the straight *TE* of the blades also acts positively and accelerates the moment of the rotor. Also, the wind incident on the advancing blade is more focused towards the *LE* in the range α = 110°-140° because of higher curvature of elliptical-profile. Hence, the average C_D for a complete rotation of elliptical and semicircular profile is found to be 1.43 and 1.35, respectively. Hence, there is higher average C_D by 6% in the elliptical profile than the semicircular profile.

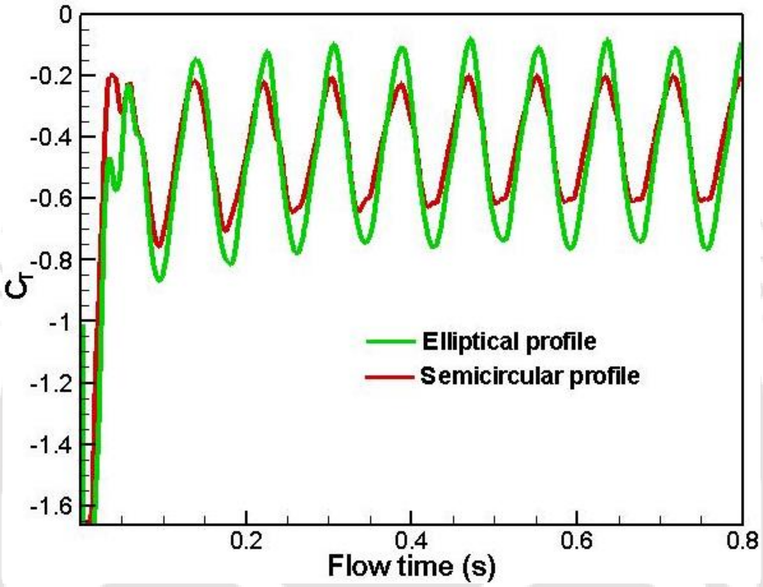

Figure 4.4: Comparison of C_T for 2D elliptical and semicircular profiles at TSR = 0.6

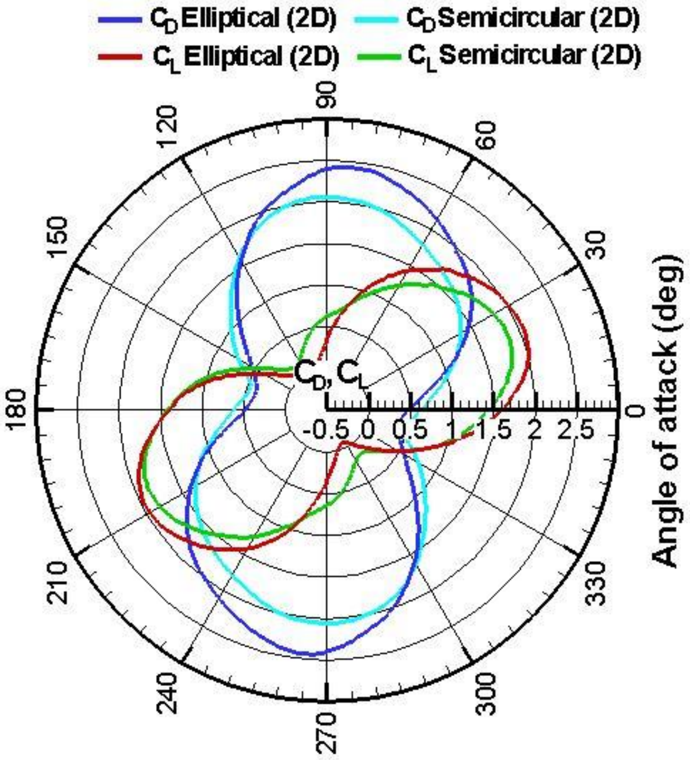

Figure 4.5: Variation of C_D and C_L for the elliptical and semicircular profiles at *TSR* = 0.6

The polar representation shows an improved C_L for the elliptical profile roughly between 0° and 80°. This improved pattern is again repeated between 200° and 250°. The average C_L for the elliptical and semicircular profile is found to be 0.95 and 0.96, respectively. Between 90° and 160°, the elliptical profile has an inferior C_L as compared to the semicircular profile. Due to symmetry, the pattern repeats after every half rotation. There is no apparent change in the location of C_{Lmax}. It is observed that the C_{Lmax} is 2.05 and 1.96 at $\alpha = 23°$ and 210°, respectively for the elliptical profile; whereas the C_{Lmax} is 1.85 and 1.84 in semicircular profile at $\alpha = 23°$ and 203°. Hence, there is 10.8% and 6.5% higher C_{Lmax} in the elliptical profile than the semicircular profile. However, the average C_L is 1% lesser in elliptical profile over the semicircular profile.

The geometry of the elliptical profile proves advantageous to have higher C_L over the semicircular profile. The pressure gradient on the suction side is improved because of the higher curvature of the elliptical profile. An increase in lift is achieved due to the vertically oriented normal pressure. Thus, for the elliptical profile, lift is generated by the suction side of advancing blade. From Figure 4.6, it is seen that with the application of load, the C_T decreases. However, the C_{Pmax} is found to be 0.34 and 0.27 for elliptical and semicircular profile at $TSR = 0.8$.

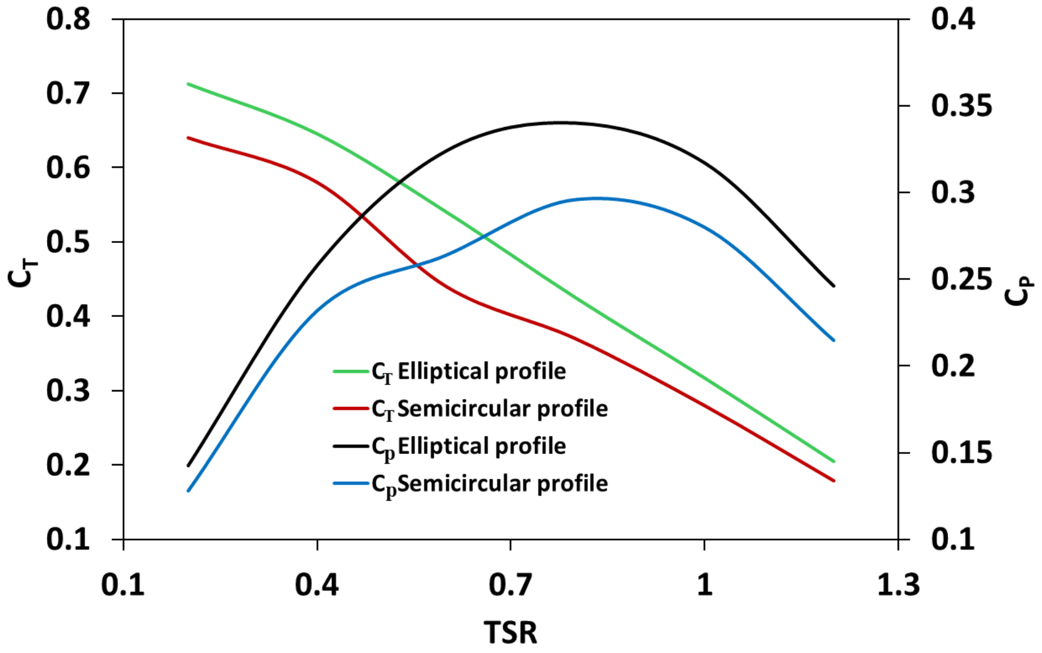

Figure 4.6: 2D unsteady variation of C_T and C_P with *TSR* of the tested rotors

4.3.1 A*nalysis of velocity contours*

Figure 4.7 shows the velocity magnitude contours of the elliptical and the semicircular profiles. In the present work, the velocity contours at *TSR* = 0.6 are shown for α = 90°and 150°. The tip losses occur at the blade tip of the advancing profile of the elliptical-profile is lesser than the semicircular-profile. On the concave side of advancing profile, air gets accelerated because of the free stream flow acceleration near the tip of returning profile. Also, the maximum velocity is observed near the surface of the advancing elliptical profile because of higher C_D. Since the Savonius rotor is a drag-driven machine, hence a higher C_D would result in a higher C_P.

The transverse flow from the concave side of advancing profile goes to the concave side of returning profile via the overlap region and this reduces the negative drag. Also, the flow traverse from the advancing to returning profile is more prominent in case of the elliptical profile at α = 90° (Fig. 4.7a). Also, at α = 90°, the magnitude of velocity near the blade surface is around 4-6 m/s for the elliptical-profile, while for the semicircular profile is 3-5 m/s. It is also clearly observed from Figure 4.7 that the magnitude of recirculation is higher behind the returning semicircular profile than the returning elliptical profile. This leads to an overall reduction in negative drag resulting in an increased C_D for α = 90° (Fig. 4.5). From Fig. 4.7, it is also observed that the flow traverse is prominent between the profiles. Hence, C_D for the elliptical profile in the range of α = 30-120° and 210-300° is found superior to that of the semicircular profile.

4. 3.2 *Analysis of total pressure contours*

Figure 4.8 shows the total pressure contours of the elliptical and the semicircular profiles. The contours at *TSR* = 0.6 are taken at α = 90° and 150°. A higher total pressure near the advancing blade of the elliptical profile is observed and it lies in the range of 0-40 N/m^2 at α =90°; however, for the semicircular profile, the range of total pressure is -10 to 20 N/m^2 at the same α. The low-pressure zone is also observed at the convex side of the advancing profile that helps in creating the pressure difference leading to the rotation of rotor. It is observed that such pressure difference is higher in the elliptical profile than the semicircular profile. This results a higher C_D in the elliptical profile, and consequently, a higher C_P. The region of higher pressure is also larger in case of the elliptical profile. As a result, delayed or no boundary layer separation takes place leading to an improved pressure recovery. It is also observed that on the concave part of returning profile, the total pressure is higher for the elliptical profile. This makes the elliptical profile to perform better than the semicircular profile.

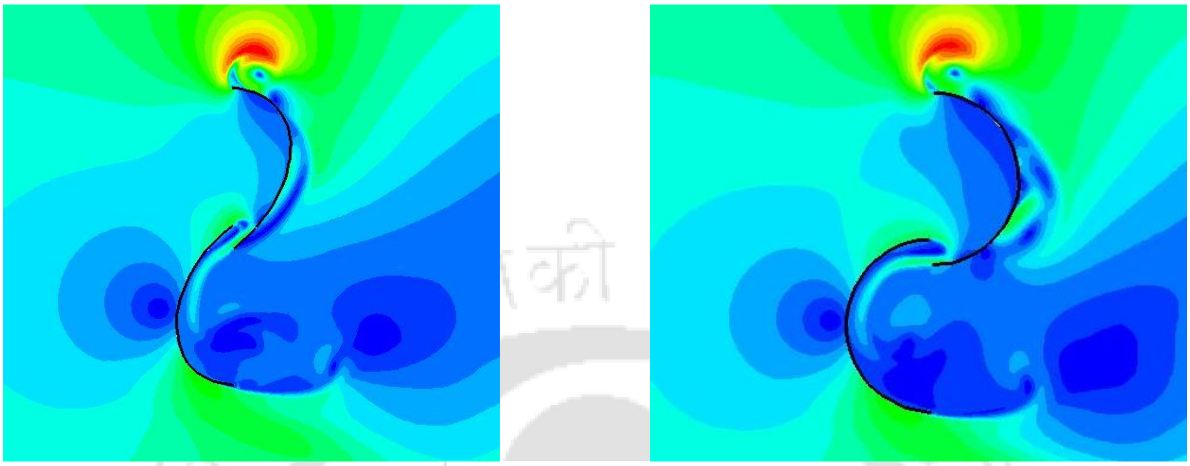

(a): Angle of attack 90°

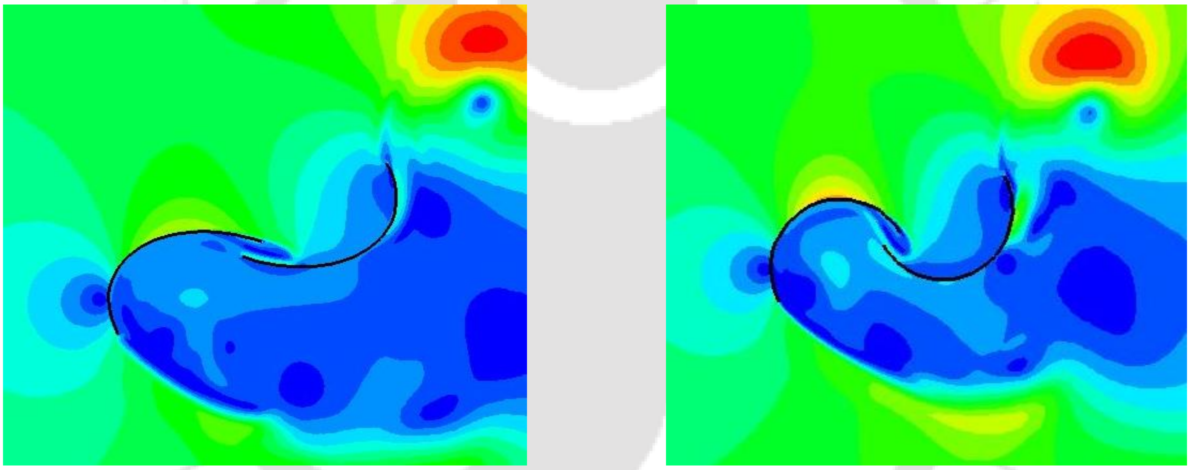

(b): Angle of attack 150°

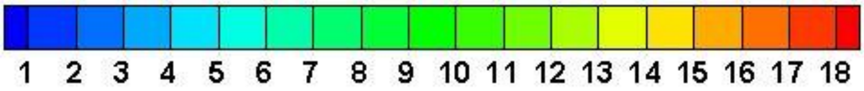

Figure 4.7: Velocity magnitude (m/s) contours of elliptical and semicircular profiles at *TSR* = 0.6

4.3.3 Analysis of turbulent intensity contours

Figure 4.9 show the turbulence intensity contours of the elliptical- and semicircular profiles at $\alpha = 90^\circ$. As in the earlier case, the contours are plotted for $TSR = 0.6$. At $\alpha = 90^\circ$, the magnitude of turbulence intensity around the elliptical profile is in the range of 0.04 – 0.08; whereas for the semicircular profile, the range is 0.05 – 0.1 at the same α. Hence, the turbulence intensity in the elliptical profile is much lower, which diminishes the formation of vortices downstream of the rotor, thereby improving its C_D and C_L as well as C_P.

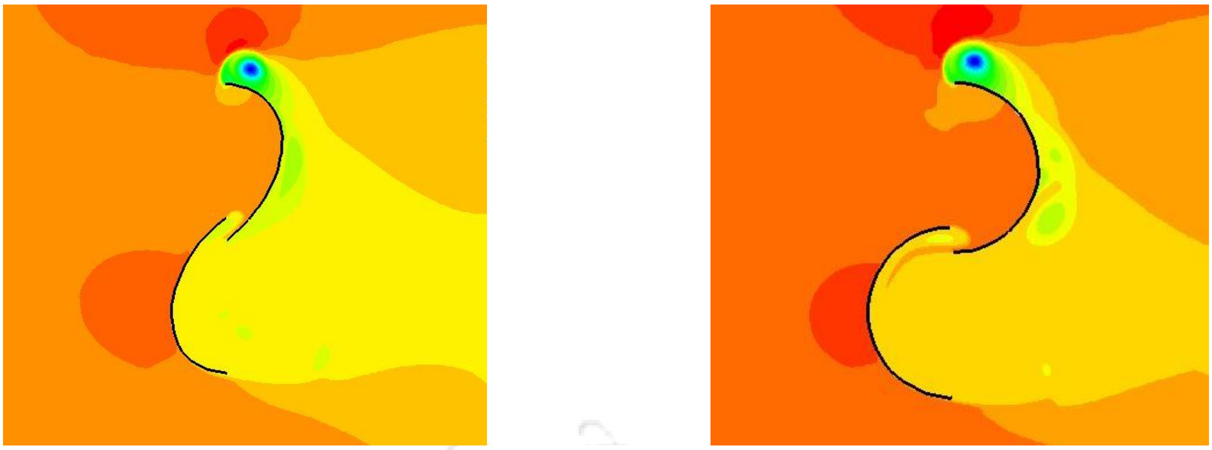

(a): Angle of attack 90°

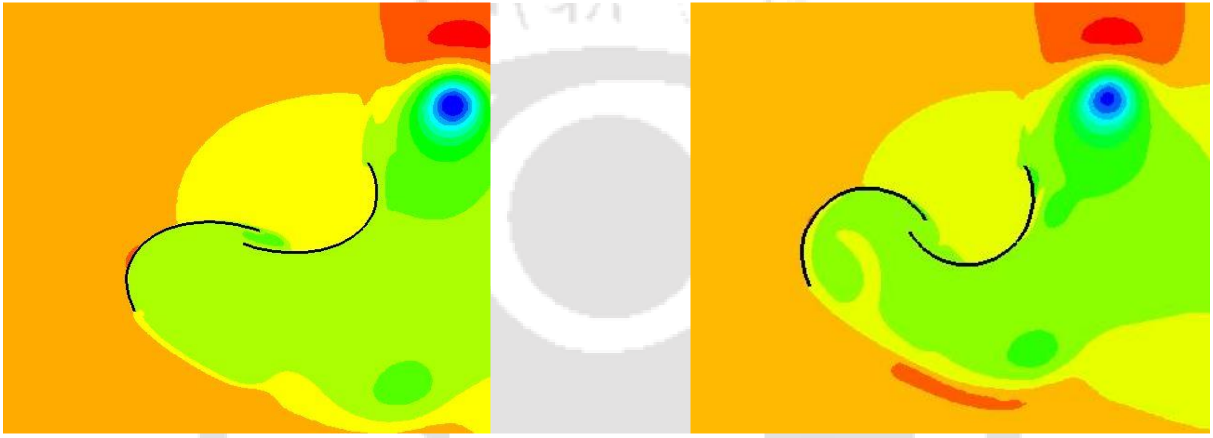

(b): Angle of attack 150°

Figure 4.8: Total pressure (N/m^2) contours of elliptical and semicircular profiles at *TSR* = 0.6

Angle of attack 90°

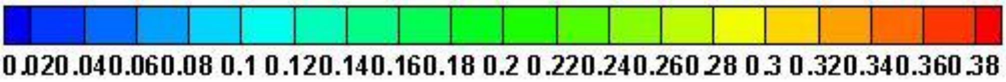

Figure 4.9: Turbulence intensity (%) contours of elliptical and semicircular profiles at *TSR* = 0.6

4.4 Drag and Lift of Other Profiles

In the present study, 2D unsteady simulations are performed of modified Bach and Benesh profile to analyze the influence of C_D and C_L on the rotor performance. The simulations are also conducted for a semicircular profile to compare the results. Figures 4.10 and 4.11 show the polar variation of C_D and C_L respectively, for modified Bach and Benesh profile. The modified Bach profile exhibits better C_D compared to the other two profiles, closely followed by semicircular profile (Fig. 4.10). The C_{Davg} for modified Bach and Benesh profile is found to be 1.41 and 1.25, respectively. But, the C_{Davg} for the conventional semicircular profile is found to be 1.35. Hence, there is 4.5% enhancement in C_{Davg} for modified Bach profile and 8.0% reduction in C_{Davg} for Benesh profile than the conventional semicircular profile. The C_{Dmax} for the modified Bach profile is found to be 2.31 at $\alpha = 96^{\circ}$ and 276°. Also, the C_{Dmax} for Benesh profile is found to be 1.98 and 2.01 at $\alpha = 75^{\circ}$ and 256°. The C_{Lavg} for modified Bach, Benesh and semicircular profiles are found to be 0.95, 1.32 and 0.96, respectively. The C_{Lmax} for modified Bach is found to be 1.97 at $\alpha = 30^{\circ}$ and 210°, whereas for Benesh profile it is found to be 2.25 and 2.21 at $\alpha = 15^{\circ}$ and 196°. Hence, the lower C_L value is going to affect the performance by a very small margin, in modified Bach profile.

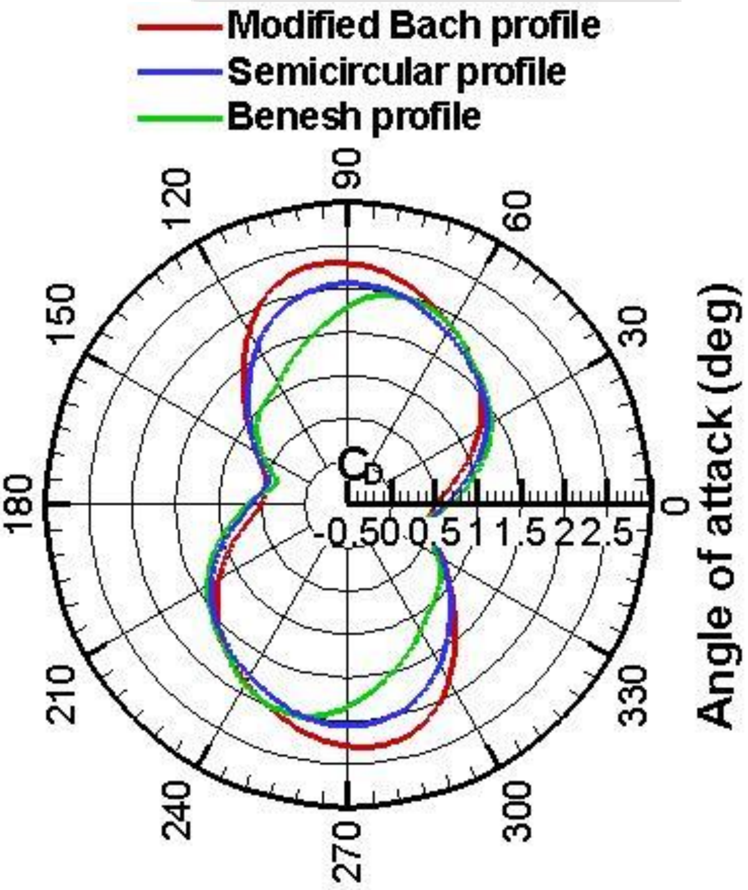

Figure 4. 10: C_D of various profiles at $TSR = 0.6$

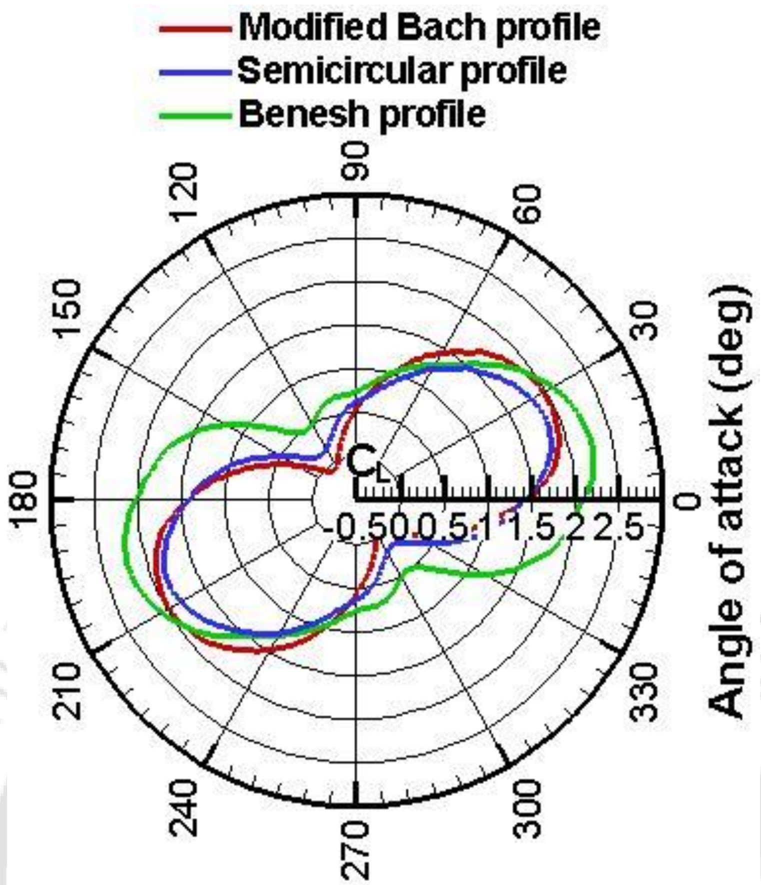

Figure 4. 11: C_L of various profiles at *TSR* = 0.6

Figure 4.12 shows the velocity contours of modified Bach, Benesh and semicircular profiles at *TSR* = 0.6. Although, the contours are taken at various *α* but only *α* =30° and 90° contours are reported in the paper. The velocity magnitude near the surface of the advancing blade is nearly 4-5 m/s for modified Bach, 6-7 m/s for Benesh profile and 3-4 m/s for semicircular profile. The formation of vortices behind the returning profile for Benesh and semicircular profile is more than the modified Bach profile. The overlap region helps the flow to cross over from the concave side of advancing blade to the concave side of returning blade. This flow traverse is most prominent in case of modified Bach profile. This leads to an overall reduction in negative drag resulting in increased C_D for the modified Bach profile.

Figure 4.13 shows the total pressure contours for the modified Bach, Benesh and semicircular profiles at *TSR* = 0.6. The maximum total pressure near the surface of the advancing profile is observed to be around 10–50 N/m^2 for modified Bach, -10–30 N/m^2 for Benesh and 0–40 N/m^2 for semicircular profile at *α* = 90°. Also, the flow separation is delayed for modified Bach more than the other profiles. This results in improved pressure recovery at the blade boundary. As a result, the C_D is found to be more in modified Bach profile than the other profiles. Hence, the performance of the modified Bach profile is found better than the Benesh and semicircular profile.

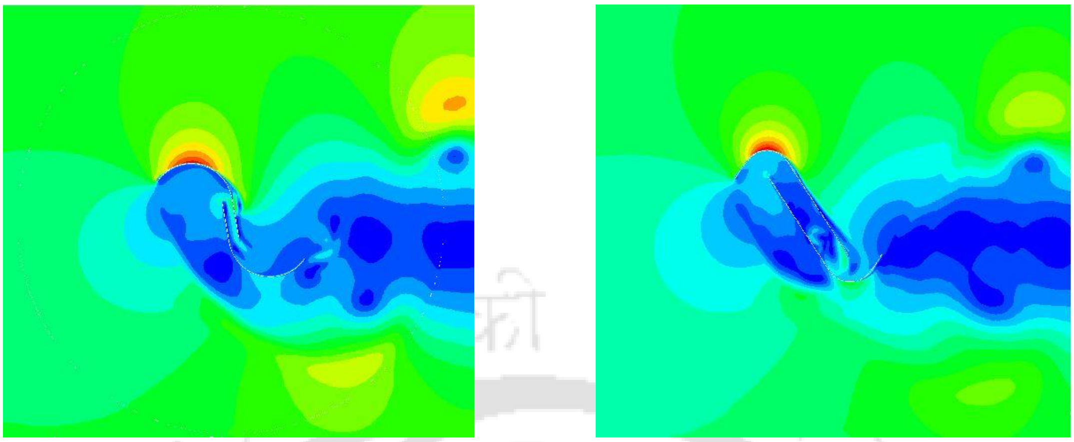

(a) Modified Bach α = 30° (b) Benesh α = 30°

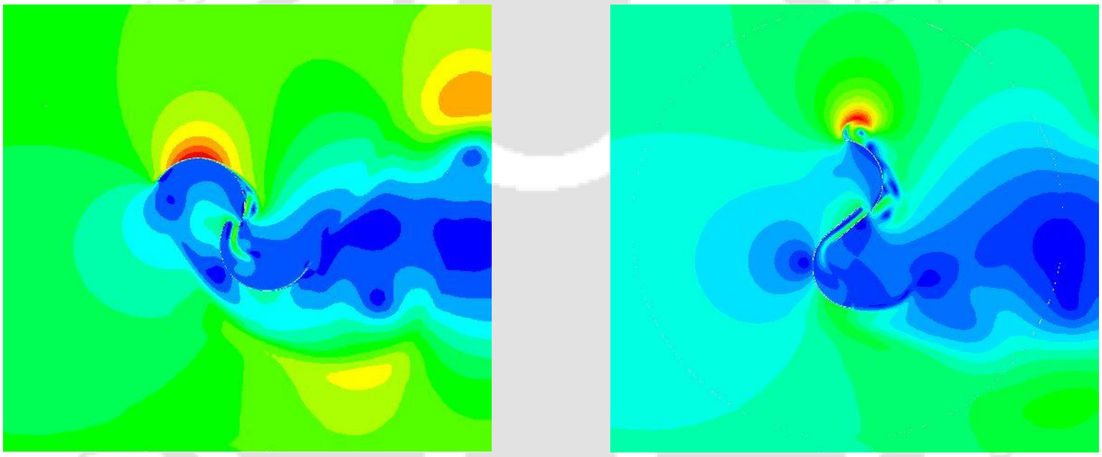

(c) Semicircular α = 30° (d) Modified Bach α = 90°

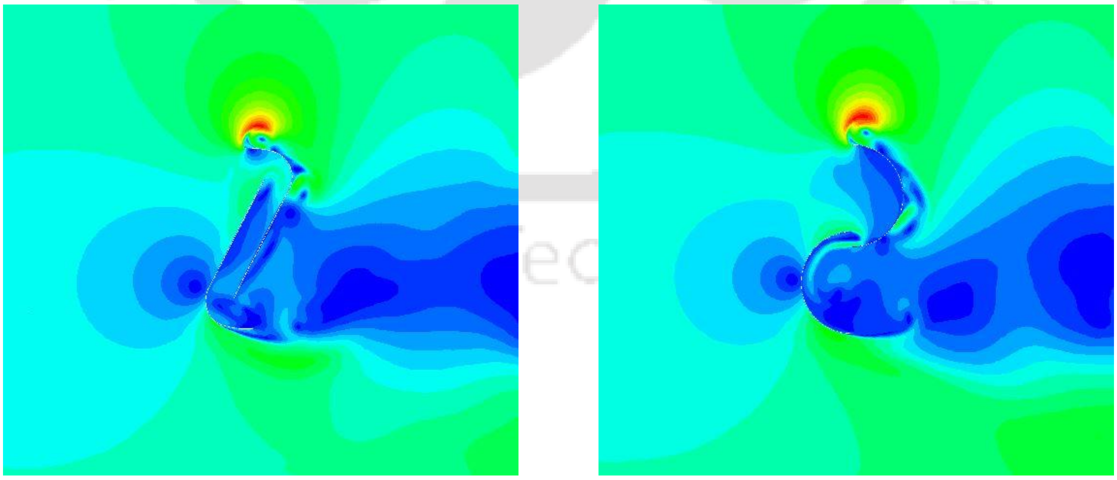

(e) Benesh α = 90° (f) Semicircular α = 90°

Figure 4.12: Velocity magnitude (m/s) contours of various profiles at *TSR* = 0.6

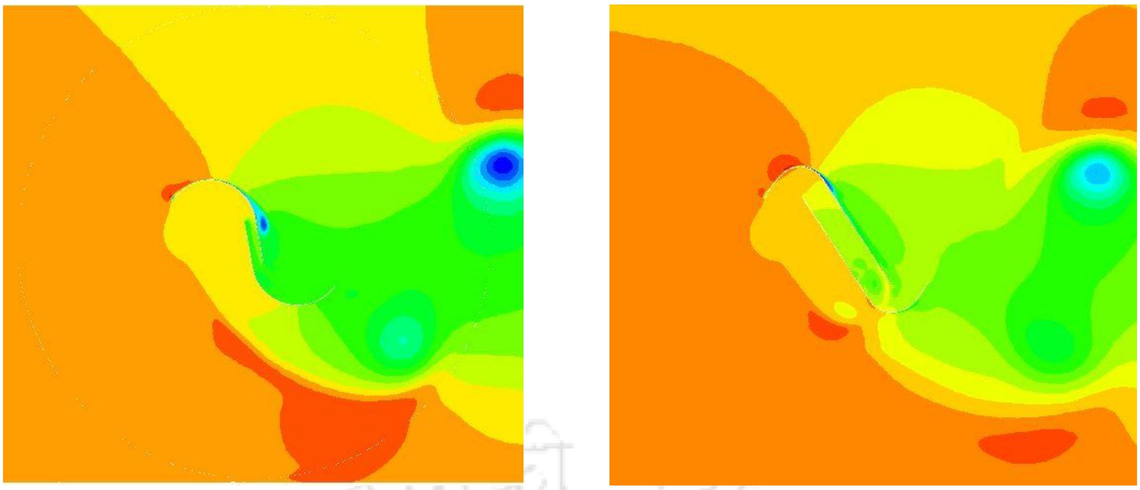

(a) Modified Bach α = 30° (b) Benesh α = 30°

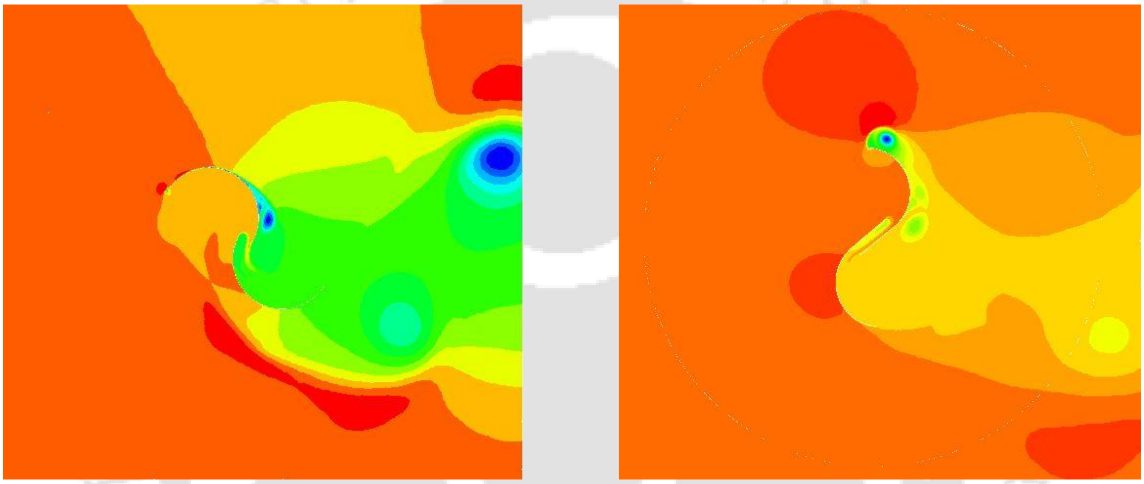

(c) Semicircular α = 30° (d) Modified Bach α = 90°

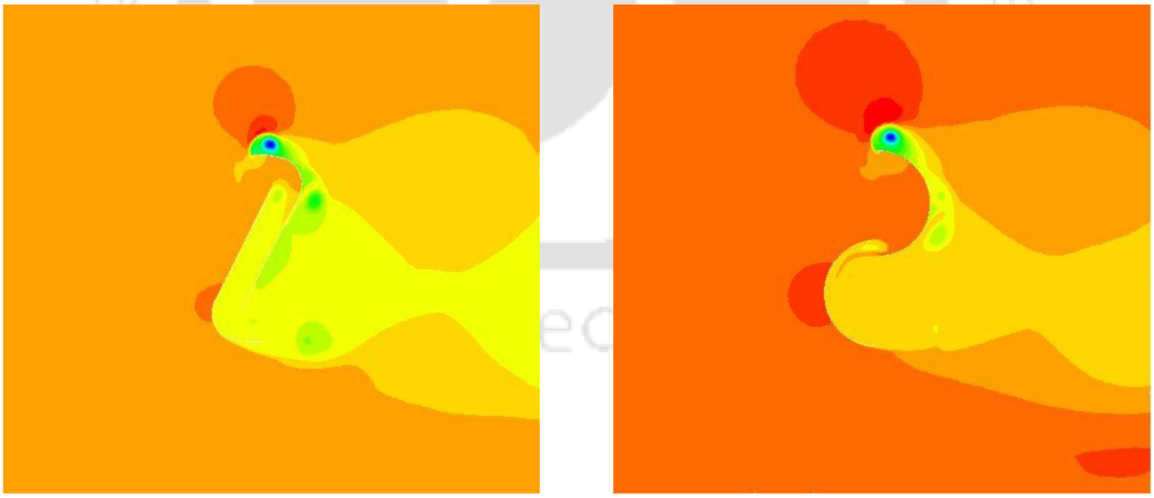

(e) Benesh α = 90° (f) Semicircular α = 90°

Figure 4.13: Total pressure (N/m^2) contours of various profiles at *TSR* = 0.6

Figure 4.14 shows the turbulence intensity contour of various Savonius rotor profiles. The contours are generated at α = 90°. It is observed from the Figs that the range of turbulence intensity is about 0.04-0.1% for modified Bach, 0.06-0.14% for Benesh and 0.1-0.2% for semicircular profile. More is the turbulence intensity lesser would be the performance of the profile. Also, the formation of eddies behind the Benesh and semicircular profiles is more than the modified Bach profile. This makes the modified Bach to perform better than the Benesh and semicircular profiles

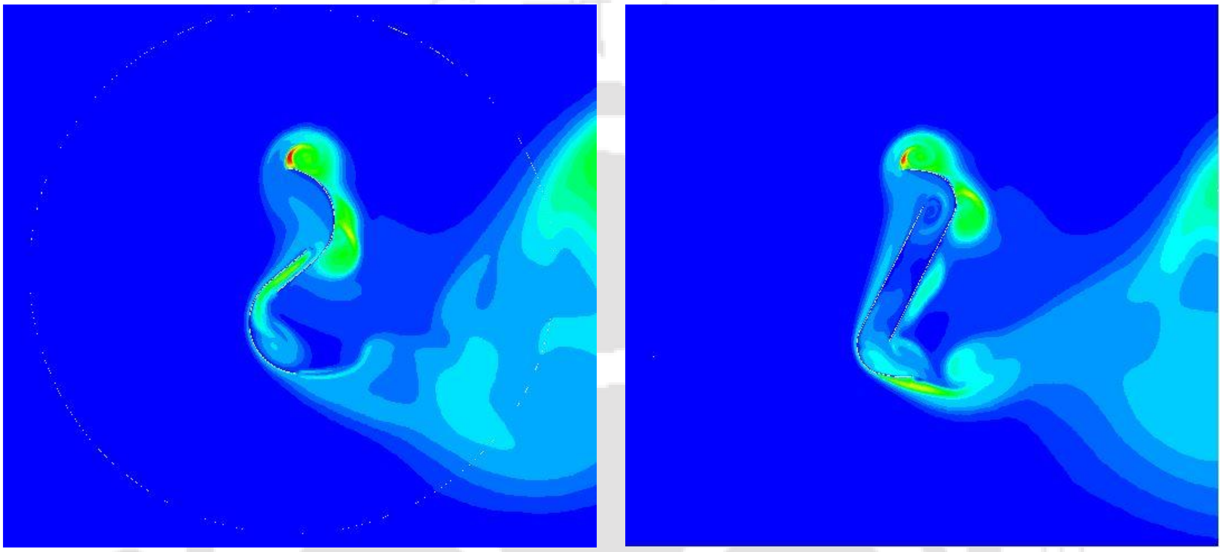

(a) Modified Bach α = 90° (b) Benesh α = 90°

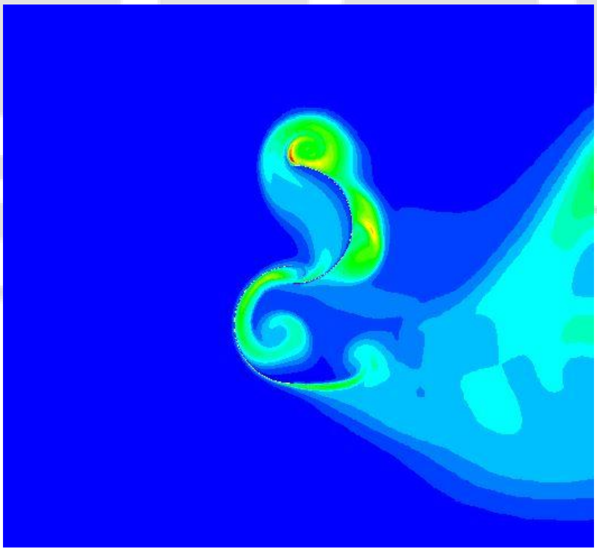

(c) Semicircular α = 90°

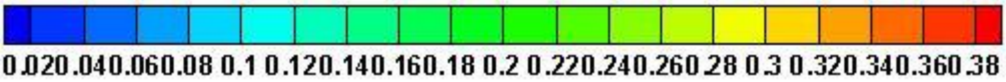

Figure 4.14: Turbulence intensity (%) contours of various profiles at *TSR* = 0.6

4.5 Concluding Remarks

With an objective of increasing efficiency of Savonius rotor, several studies have been conducted to study its C_P and C_T. In the present study, an attempt has been made to investigate the drag and lift characteristics of an elliptical-bladed Savonius rotor. 2D unsteady simulations are carried out using *SST k-ω* turbulence model around the elliptical, modified Bach, Benesh and semicircular profiles. From the 2D unsteady simulations, the C_{Dmax} for elliptical-profile is found to be 2.43 at α = 84° and 266° respectively; however, for the semicircular profile, C_{Dmax} is found to be 2.07 corresponding α =91° and 270°. Hence, there is an improvement in C_{Dmax} of 17.4% in elliptical profile over the semicircular profile. For the elliptical profile, the C_{Lmax} is predicted to be 2.05 and 1.96 at α = 23° and 210°, respectively; while for the semicircular profile, the C_{Lmax} is 1.85 and 1.84 at α = 23° and 203°. Hence, there is 10.8% and 6.5% higher C_{Lmax} in the elliptical profile than in the semicircular profile. Thereafter, the average C_D for a complete rotation of elliptical and semicircular profile is found to be 1.43 and 1.35, respectively. Thus, there is higher average C_D by 6% in the elliptical profile than the semicircular profile. Further, the C_L and C_D are also estimated for the modified Bach and Benesh profile to have a comparison in a common platform. The average C_D of modified Bach and Benesh are found to be 1.41, 1.25, respectively. Hence, in modified Bach profile, there is an improvement of C_D by 4.5% over the semicircular profiles. However, in case of C_L, the modified Bach profile has shown inferior values as compared to the others. The C_{Lavg} are found to be 0.95 and 1.32 for the modified Bach and Benesh, respectively. Hence, the elliptical profile seems to be a contender for small-scale power generation in rural as well as in urban areas.

CHAPTER –5

Vent Augmentation Technique

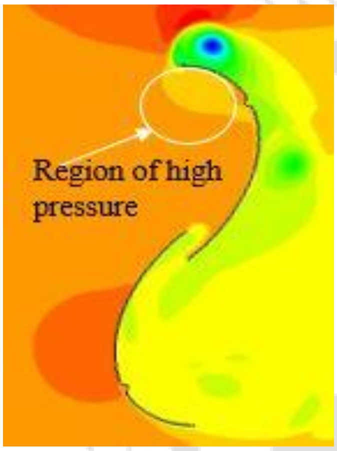

Chapter Outline

Overview

The augmentation techniques generally improve the performance of the Savonius rotor; they make the rotors more complex. Among the reported techniques, the simple vent-augmenters give marginal performance improvement. In this chapter, the performance of the vent-augmented (vented) elliptical profile has been estimated. Further, the C_D *and* C_L *of the vented elliptical profiles have been calculated. Results have also been generated for the semicircular profile with vents. From the 2D unsteady results, it has been observed that the vented semicircular profile shows a considerable improvement in* C_D *and* C_L*. The* C_D *and* C_L *for the vented elliptical profile is found to be 1.45 and 0.98, respectively. Whereas for the vented semicircular profiles, the* C_D *and* C_L *are predicted to be 1.39 and 1.04, respectively. However, for the non-vented elliptical profile the* C_D *and* C_L *are found to be 1.43 and 0.95; while for the semicircular profiles, it is 1.35 and 0.96, respectively.*

5.1 Introduction

Various augmentation techniques have been used to improve the performance of the Savonius rotor. However, these techniques make the system more complex. The vent-augmentation technique reduces the complexity of the rotor, hence this technique has been used with the semicircular and elliptical profiles to investigate its influence on the rotor profiles. Initially, the position of the venting slots on the rotor profiles have been optimized in a basic semcircular profile and then the optimized location has been chosen for the elliptical profile to estimate its C_D, C_L, C_T, and C_P.

5.2 Optimizing the Location of Vents

The details of vent gap are calculated as per the past study by Abraham *et al*. (2012). In the present study, three location of vents have been chosen to find its optimum position. One pair of vents lies on the blade central axis (Fig. 5.1a); whereas the other two pairs are oriented at of 30^o on either side of the central axis (Figs 5.1b and 5.1c). The dimension of the vent gap is taken as 0.04D m.

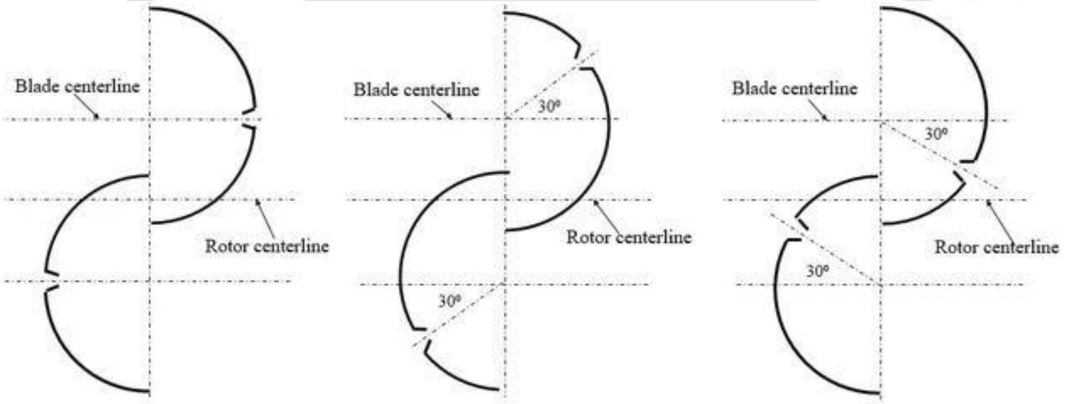

(a) Design-I (b) Design-II (c) Design-III

Figure 5.1: Vents at three different positions on the semicircular-bladed profiles

The vent has a diverging section on the concave side of the blade. This is done to facilitate the smooth flow of air while the blade is returning and reduce loss of wind energy by preventing the escape of air through the vent in case of advancing blade. To optimize the position of vent, three cases have been considered. As stated earlier, one pair of vents lies on its central axis; whereas the other two pairs are oriented at angle of 30^o on either side of the central axis. Figures 5.2 and 5.3 show the variation of C_T and C_P over the range of *TSR* = 0.2 to 1.2. Design-II has an improved C_P than the other two designs. From the unsteady results, the C_{pmax} = 0.29 for Design-II as opposed to C_{pmax} = 0.27 for the conventional semicircular profile. Thus Design-II shows an enhancement in power co-efficient by 7.4% over the conventional semicircular profile. It has been observed that velocity on the convex side of returning blade of Design-II is comparatively lesser than Design-I and Design-III.

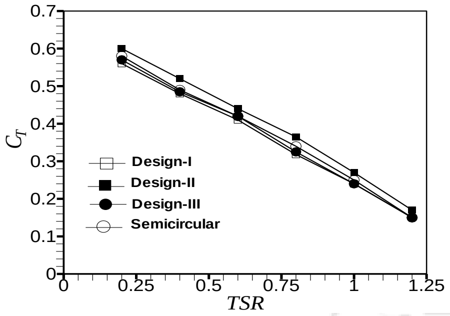

Figure 5.2: Variation of C_T with *TSR*

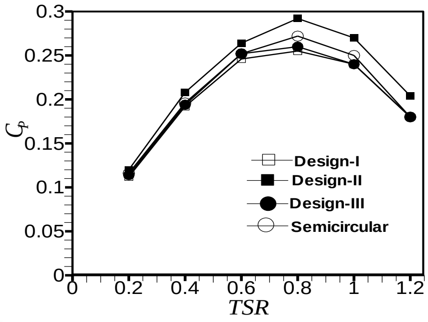

Figure 5.3: Variation of C_p with *TSR*

5.2.1 Analysis of velocity contours

Figure 5.4 shows the velocity contours of the semicircular-bladed profile without and with vent. As compared to other designs, the near the tip of the blades velocity gets accelerated and there is a comparatively higher velocity near the surface of Design-II. It is also seen that the velocity on the convex side of the returning blade of Design-II is comparatively lesser than for the other designs. Usually, the boundary layer separation takes place due to excessive momentum loss near the profile curvature, and in Design-II, this momentum loss at the tip of the rotor profile is lesser. Because of this, there is a reduction of negative torque in Design-II causing an improvement in performance.

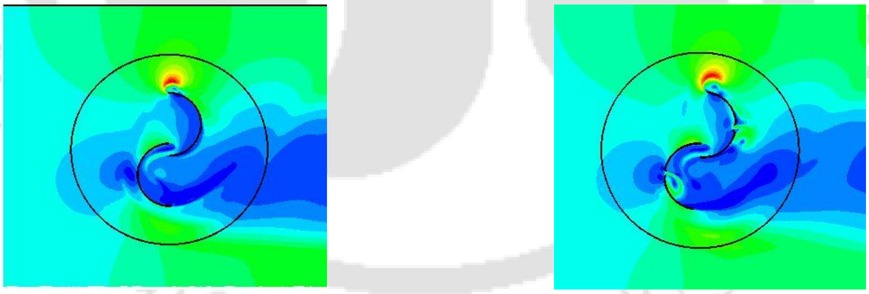

(a) Semicircular (b) Design-I

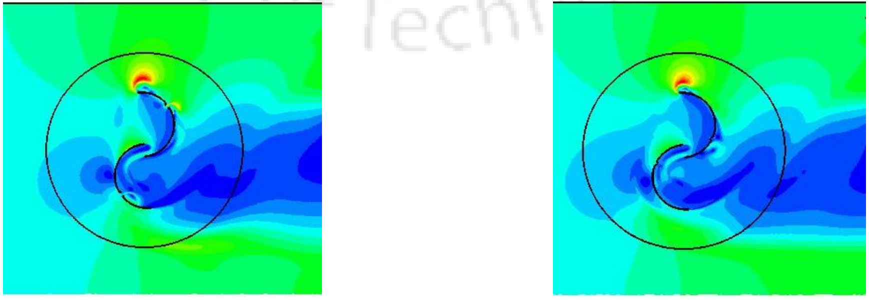

(c) Design-II (d) Design-III

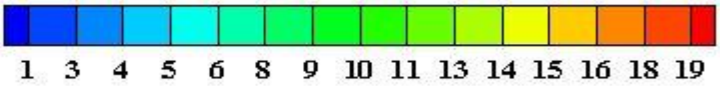

Figure 5.4: Velocity contour of the semicircular-bladed profile with vents

5.2.2 *Analysis of total pressure contours*

The pressure contours of the semicircular-bladed profile without and with vent are shown in Figures 5.5. All the pressure contours represent the total pressure at an optimum *TSR* = 0.8. A comparatively higher total pressure is observed on the advancing blade and lesser pressure on the returning blade in Design-II (Fig. 5.5b) in comparison to semicircular (Fig. 5.5a), Design-I (Fig. 5.5c) and Design-III (Fig. 5.5d). As evidenced, Design-II is capable of preventing or delaying the flow separation. As a result, negative torque is cut down and the resultant torque is increased thereby improving the performance.

(a) Semicircular (b) Design-I

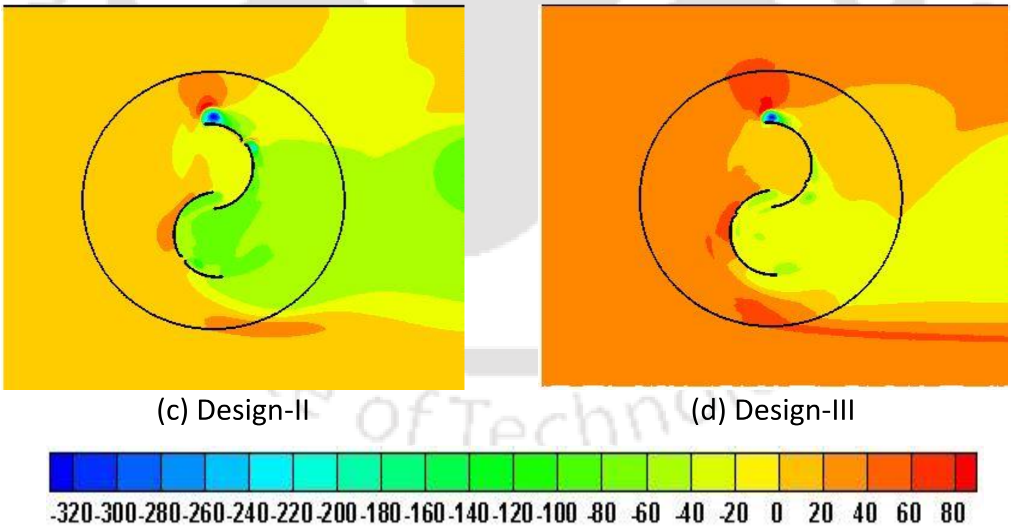

(c) Design-II (d) Design-III

Figure 5.5: Total pressure contour of the semicircular-bladed profile with vents

5.2.3 *Analysis of turbulent intensity contours*

Figures 5.6 shows the turbulence intensity contours of the semicircular-bladed profile without and with vent. The magnitude of turbulence intensity in case of Design-II is found to be lesser as compared to other tested profiles. Because of this, there is a reduction in the magnitude of vortices at the downstream of the blade profile. Design-II, thus, shows an improved performance.

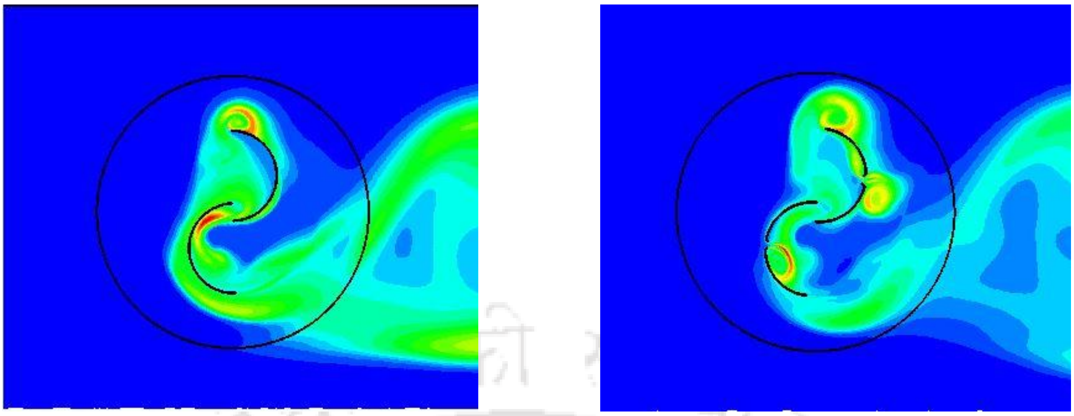

(a) Semicircular (b) Design-I

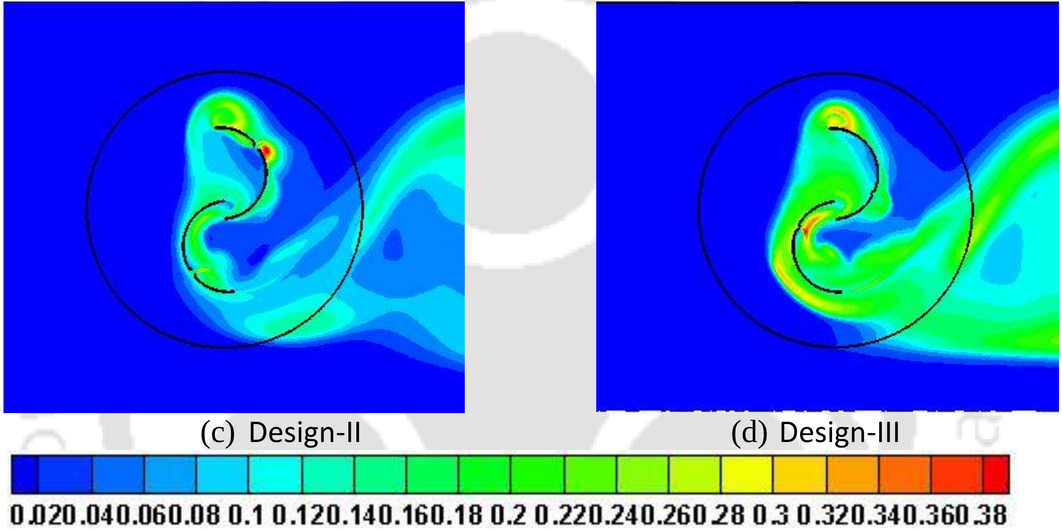

(c) Design-II (d) Design-III

Figure 5.6: Turbulence intensity contour of the semicircular-bladed profile with vents

5.3 Vent-augmenters on Elliptical Profile

2D unsteady simulations are conducted on the elliptical profile by implementing vent-augmentation technique at the optimum location (such as Design-II in Fig. 5.1). The torque coefficient (C_T) and power coefficient (C_P) are calculated and discussed with respect to *TSR*. Further, the total pressure, velocity magnitude and turbulence intensity contours generated are analyzed. Figures 5.7 and 5.8 demonstrate the variations of C_T and C_P for the vented and non-vented elliptical profiles. It has been observed that with the application of load, the rotational speed on the rotor reduces, and hence the trend of C_T decreases with the increase of *TSR*. However, the performance is found to be optimum at *TSR* = 0.8. At this *TSR*, the peak C_P of 0.35 is obtained for the vented elliptical profile. Whereas, the non-vented elliptical profile shows a peak C_P = 0.34 at *OR* = 0.15. On the other hand, for the semicircular profile, the simulation results show a peak C_P of 0.27 at *TSR* = 0.8. Hence, the non-vented elliptical profile demonstrates an improvement of C_P by 26% while the vented profile demonstrates an improvement of 30% over the semicircular profile.

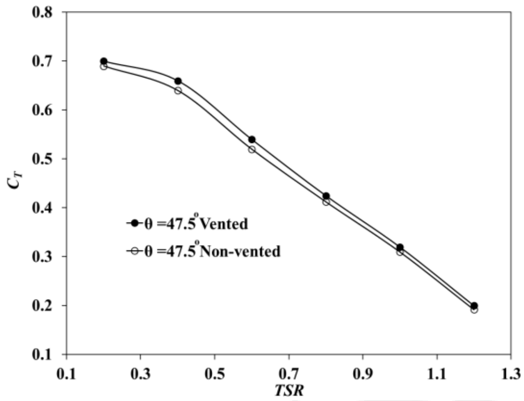

Figure 5.7: Variation of C_T with *TSR* for the vented elliptical profile

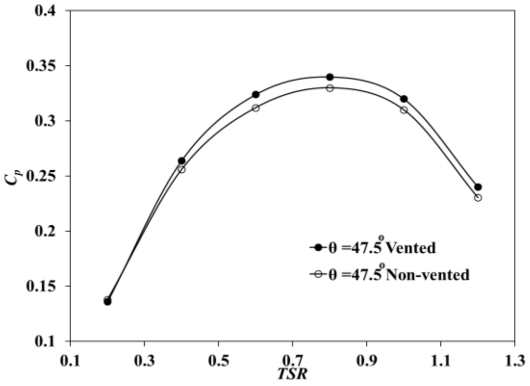

Figure 5.8: Variation of C_P with *TSR* for the vented elliptical profile

As observed in Figure 5.9, the total pressure on the convex side of the returning blade is reduced in the vent-augmented elliptical profile. A comparatively higher total pressure is detected near the advancing vented profile, thereby improving its performance. From Figure 5.10 the high-velocity zone is noticed near the surface of the advancing profile of vented elliptical-profile in comparison to the non-vented elliptical profile. For the vented-elliptical profile, the convex side of returning blade shows a velocity magnitude of around 1.26 m/s; whereas for the non-vented elliptical profile, it is around 1.43 m/s. This demonstrates a reduction of the negative drag in the vented-elliptical profile (Figure 5.10). Furthermore, the overlapping flow is more pronounced in the vented-elliptical profile. Thus, overall, the negative torque of the blade profile gets reduced by the venting slots as reported earlier.

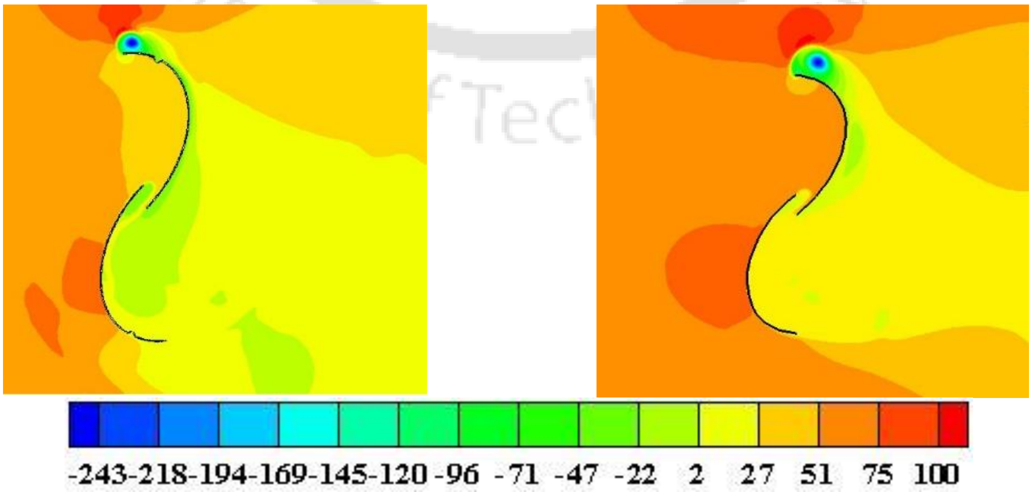

Figure 5.9: Total pressure (N/m^2) contours of the vented and non-vented elliptical profiles at *TSR* = 0.80

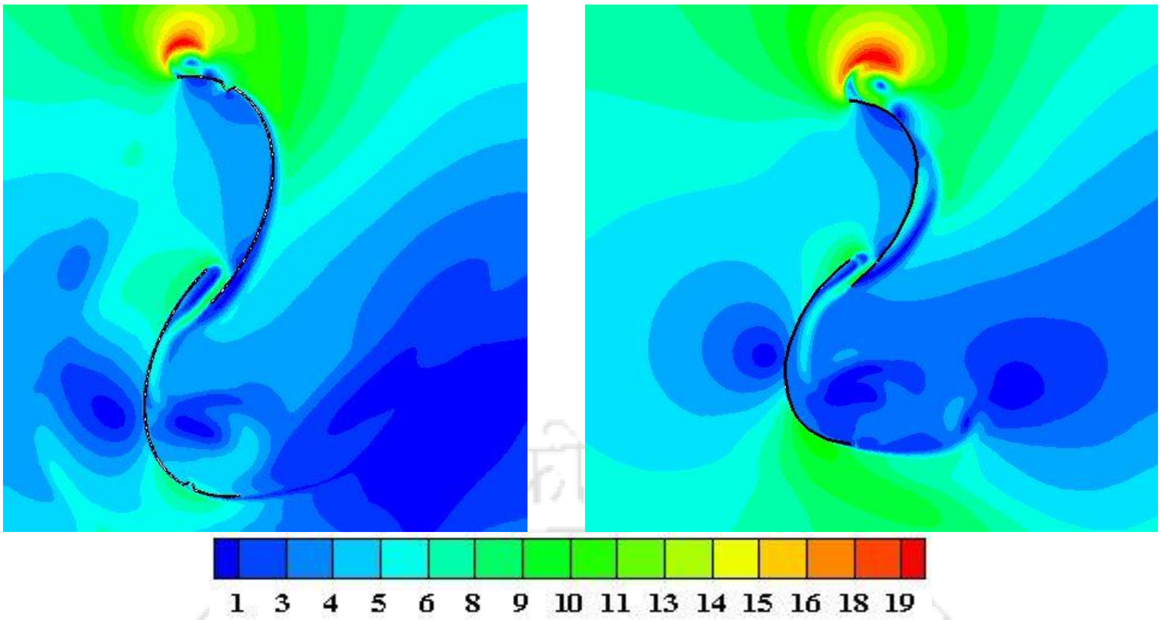

Figure 5.10: Contours of velocity magnitude (m/s) of the vented and non-vented elliptical profiles at *TSR* = 0.80

5.4 Drag and Lift of Vented Elliptical Profile

The polar variation of C_D and C_L for vented and non-vented elliptical and semicircular profiles are shown in Figs 5.11 and 5.12. The average C_D for vented and non-vented -elliptical profiles are found to be 1.45 and 1.43. Thus, there is an increase in average C_D by 1.4% and 7.4% in the vented elliptical profile than the non-vented elliptical and semicircular profiles, respectively. However, the average $\mathrm{C_D}$ for vented and non-vented semicircular profiles are found to be 1.39 and 1.35. Thus, there is an increase in average C_D by 3.0% in the vented semicircular profile than the non-vented semicircular profile. The polar diagram of C_D shows enhanced results in the range of $\alpha = 30°$ to 85° and again in the range of $\alpha = 210°$ and 250° for the vented elliptical profile than the non-vented elliptical profile. The C_{Dmax} is found to be 2.42 and 2.43 for the vented and non-vented elliptical profiles at $\alpha = 84°$; whereas the same is observed to be 2.15 and 2.07 at $\alpha = 80°$ and 91° for the vented and non-vented semicircular profiles, respectively. Also, the average C_L for vented and non-vented elliptical profiles are found to be 0.98 and 0.95. Hence, there is an increase of average $\mathrm{C_L}$ by 3.2% in the vented elliptical profile than the non-vented elliptical profile. Nevertheless, the average C_L for vented and non-vented semicircular profiles are found to be 1.04 and 0.96. The C_{Lmax} for the vented and non-vented elliptical profiles are found to be 2.08 and 2.05 at $\alpha = 23°$. Hence, in case of the vented elliptical profile, the C_{Lmax} is improved by 1.5% than the non-vented elliptical profile. Thus, there is an increase of average C_L by 8.3% in the vented semicircular profile than the non-vented semicircular profile. The C_{Lmax} for the vented and non-vented semicircular profiles are found to be 1.90 and 1.85 at α = 23°.

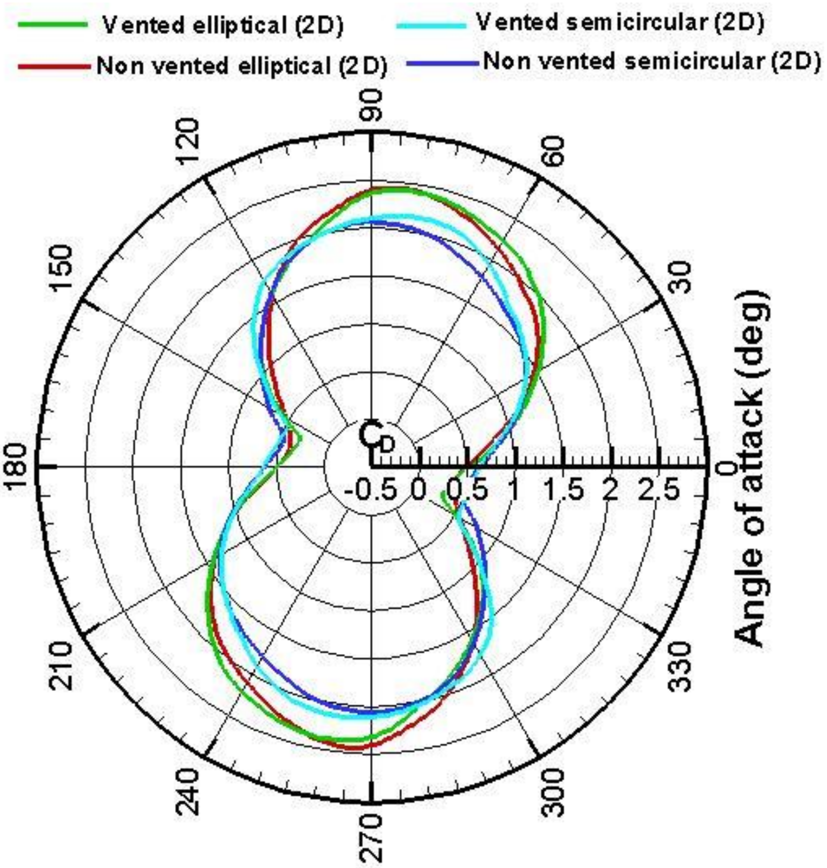

Figure 5.11: Variation of C_D for the tested profiles at *TSR* = 0.6

Figures 5.13a and 5.13b show the velocity contours of vented and non-vented elliptical profiles at α = 90° and 150°. Figure 5.13c shows the velocity contours of vented and non-vented semicircular profiles. Also, at α = 90°, the magnitude of velocity near the blade surface is around 4-6 m/s for the vented and non-elliptical-profiles. However, there is a formation of vortices behind the returning blade of non-vented elliptical profiles. Such vortices are almost negligible in case of the vented elliptical profile, which reduced its negative torque. Also, the magnitude of velocity in convex side of the returning blade is lower in vented elliptical profile than the non-vented elliptical profile. The overlapping is also found to be more prominent is vented elliptical profile than the non-vented elliptical profile. The vortices formed in non-vented semicircular profile is larger than vented semicircular profile, while for the vented and non-vented semicircular profiles the magnitude of velocity near the surface of the advancing profile is found to be around 3-5 m/s. It is also observed that the tip losses are more prominent in the non-vented elliptical and non-vented semicircular profile than the vented profiles. Thus, the C_D is found to be more in vented elliptical and vented semicircular profiles than their corresponding the non-vented profiles.

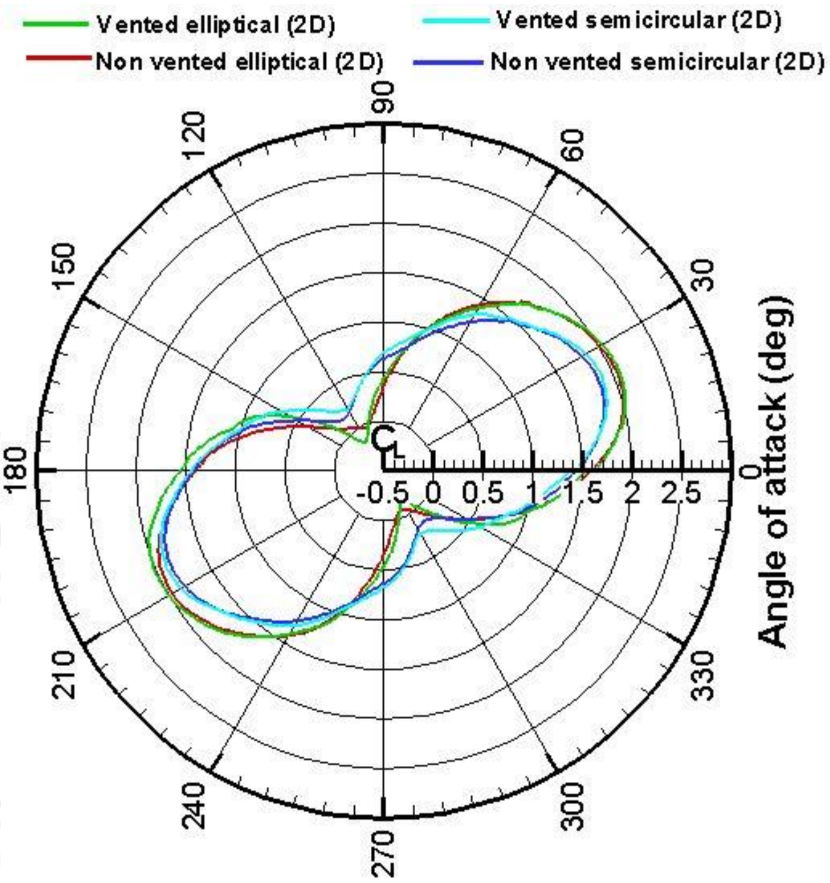

Figure 5.12: Variation of CL for the tested profiles at TSR = 0.6

Figure 5.14 shows the total pressure contours of the vented and non-vented elliptical and semicircular profiles, respectively. The magnitude of total pressure near the concave surface of the advancing profile is found to be around 0-40 N/m^2 for both vented and non-vented elliptical profiles at α = 90°; nevertheless, for the semicircular profile, the range of total pressure is -10 to 20 N/m^2 at the same α. The magnitude of higher total pressure zone is observed to be more in the concave side of the advancing profile of vented elliptical profile than the non-vented elliptical profile. Also, the magnitude of the low-pressure region in convex part of the returning profile is higher in vented elliptical and semicircular profiles than the non-vented elliptical and semicircular profiles, respectively. As a result, delayed or no boundary layer separation takes place leading to an improved pressure recovery, leading to a reduction of the negative torque of the rotor and hence improvement of overall C_D of the rotor.

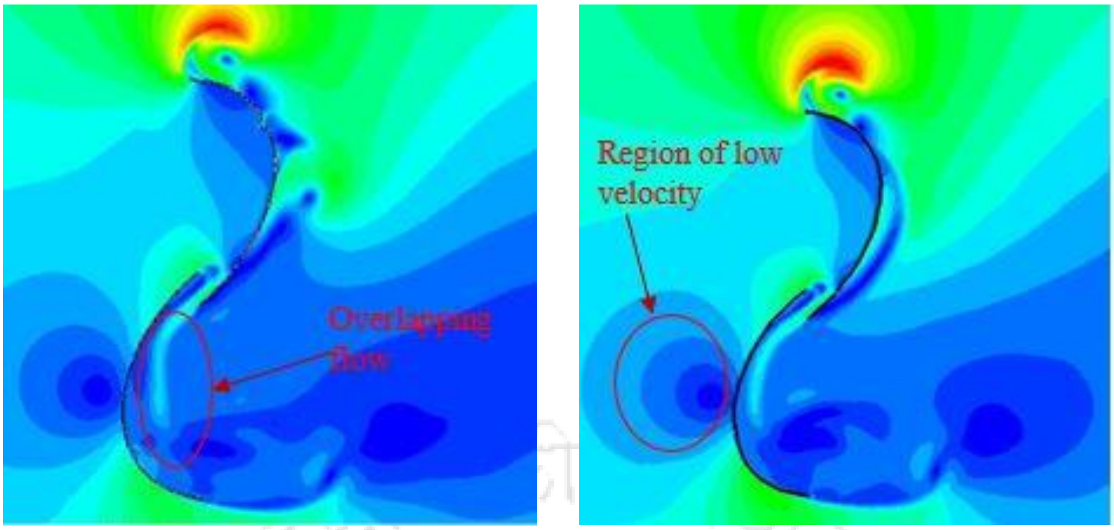

(a): Elliptical α = 90°

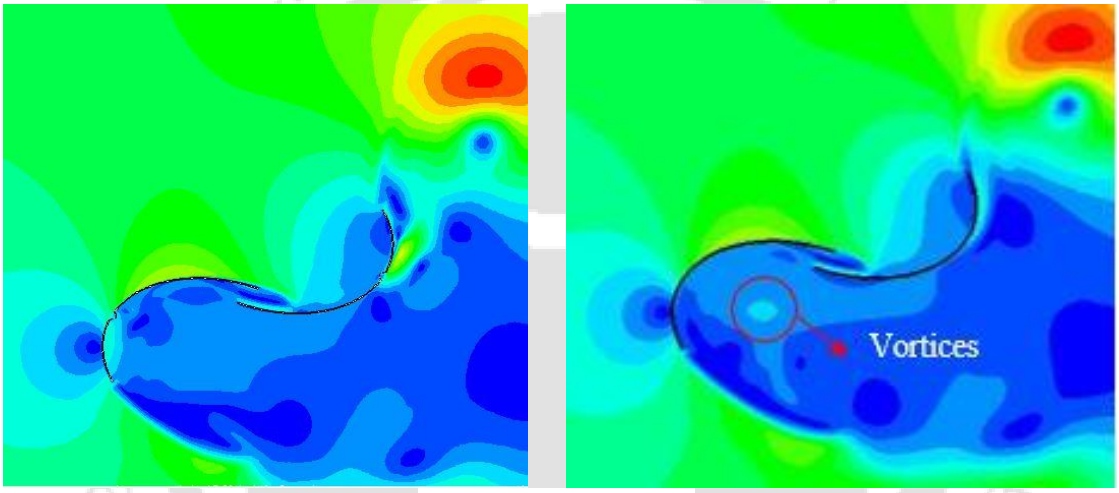

(b): Elliptical α = 150°

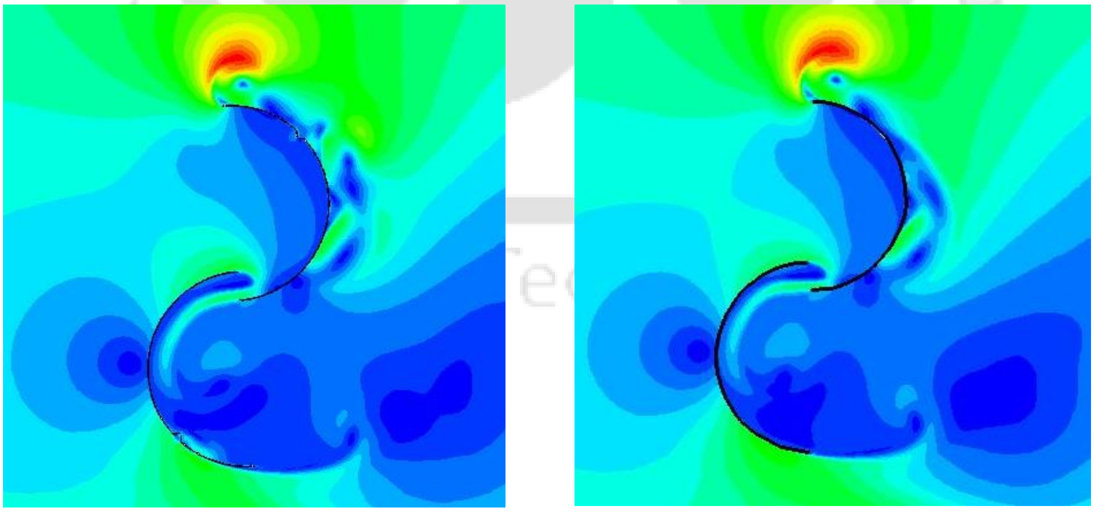

(c) Semicircular α = 90°

Figure 5.13: Velocity magnitude (m/s) contours of elliptical and semicircular profiles at *TSR* = 0.6

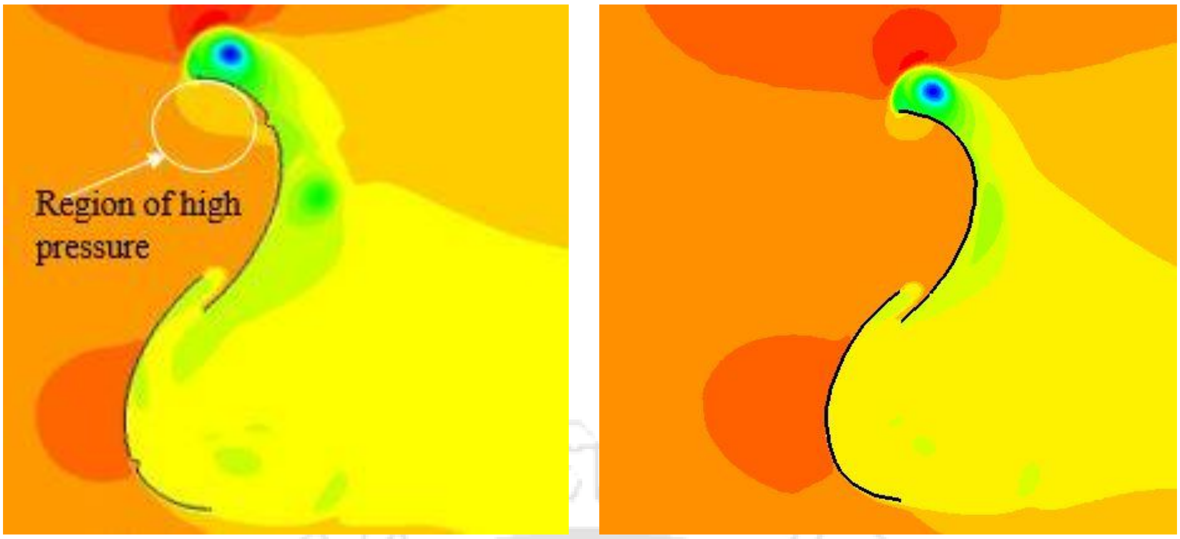

(a): Elliptical profile at α = 90°

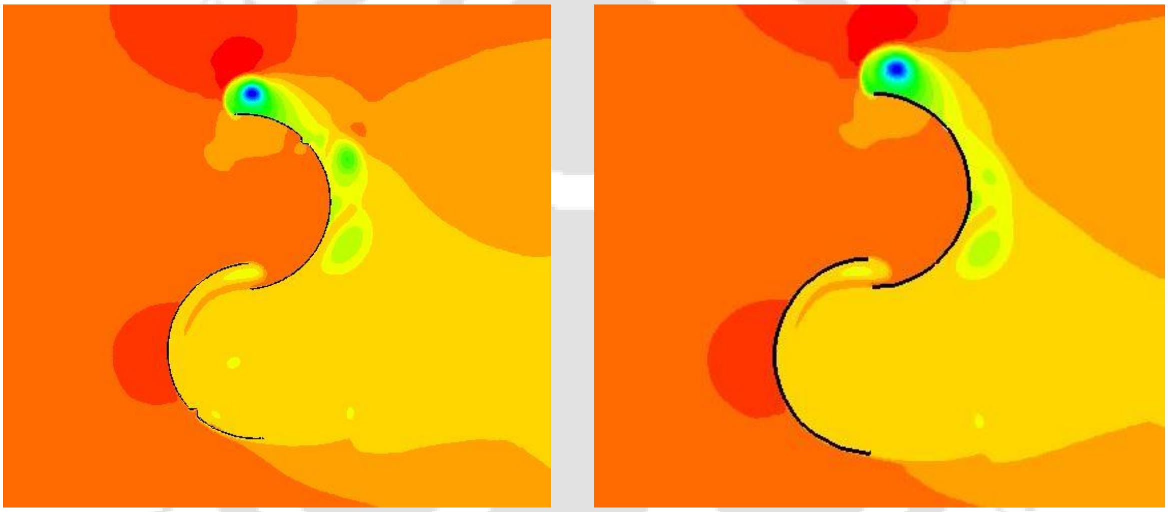

(b): Semicircular profile at α = 90°

Figure 5.14: Total pressure (N/m^2) contours of elliptical and semicircular profiles at *TSR* = 0.6

Figure 5.15 shows the turbulence intensity contours of the vented and non-vented elliptical profiles at α = 90° and at *TSR* = 0.6. The magnitude of turbulence intensity around the vented and non-vented elliptical profiles is around 0.04% – 0.06% and 0.04% – 0.08%, respectively. Also, the region of low turbulence intensity in the concave side of the advancing vented elliptical profile is larger than the non-vented elliptical profile. Hence, the turbulence intensity in the vented elliptical profile is much lower, which diminishes the formation of vortices downstream of the rotor.

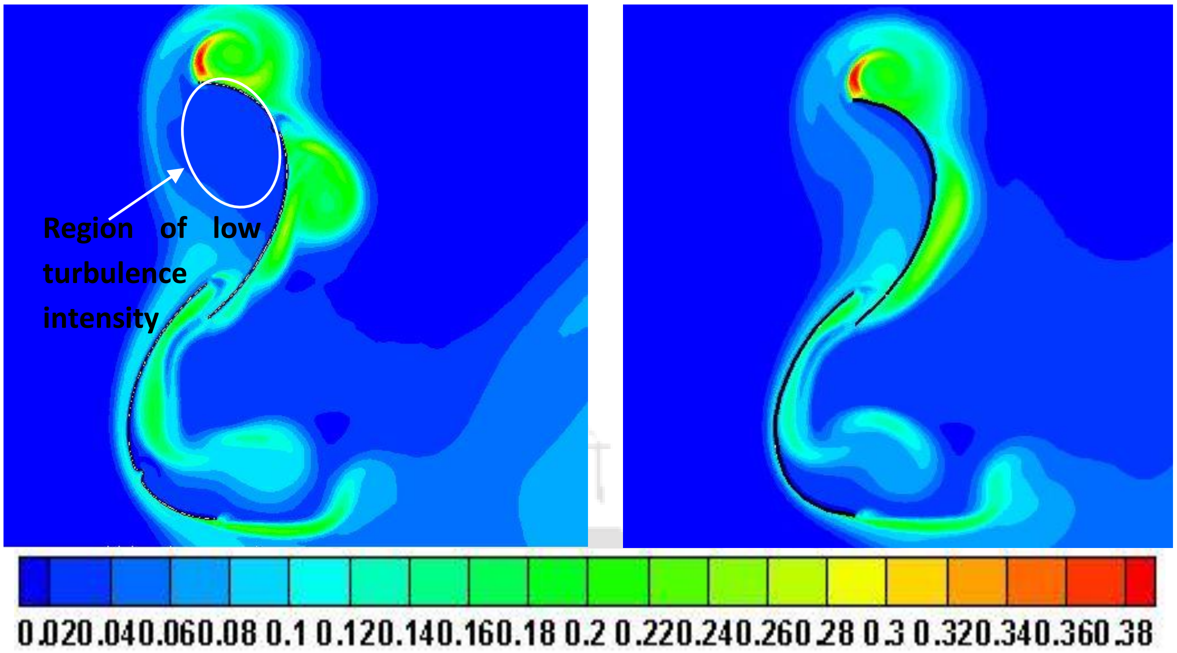

(a) Vented elliptical profile (b) Non-vented elliptical profile

Figure 5.15: Turbulence intensity (%) contours of vented and non-vented elliptical profiles (α = 90°; *TSR* = 0.6)

5.5 Concluding Remarks

The numerical simulation demonstrates an increase in C_P of the Savonius rotor when the vents lie 30^0 above and below the centre axis of the blade (Design-II). From the numerical simulation, Design-II shows a C_{pmax} = 0.29 as opposed to C_{pmax} = 0.27 for the conventional semicircular profile. Design-II thus shows an improvement in C_p by 7.4% over the conventional semicircular profile. Hence, the rotor with the vents as depicted in Design-II has shown improved C_p as compared to the other two cases. The vented elliptical profile with the optimum position (Design-II) with $\theta = 47.5^0$ shows a C_{Pmax} of 0.35, whereas the non-vented elliptical and semicircular profiles indicate the highest C_{Pmax} of 0.34 and 0.27, respectively. The C_D and C_L for the vented elliptical and semicircular profiles have also been conducted numerically. The average C_D for the elliptical and semicircular profiles with vents are found to be 1.45 and 1.39; whereas the average C_D for the elliptical and semicircular profiles without vents is found to be 1.43 and 1.35, respectively. Thus, there are an enhancement of C_D by 1.4% and 3.0% in the vented elliptical and semicircular profiles than the non-vented elliptical and semicircular profiles, respectively. The average C_L for the vented elliptical and semicircular profiles are found to be 0.98 and 1.04; whereas the same for the non-vented elliptical and semicircular profiles are found to 0.95 and 0.96, respectively.

CHAPTER –6

3D Unsteady Simulations

Chapter Outline

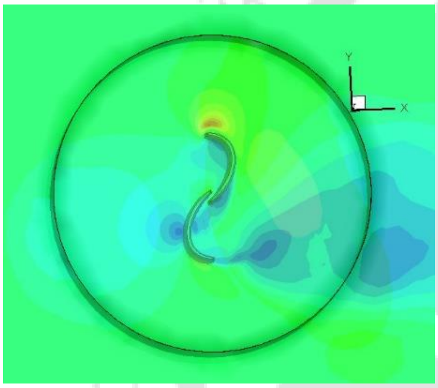

Overview

A series of 3D unsteady simulations have been conducted for the vented and non-vented-elliptical and semicircular bladed rotors to calculate their performance coefficients. The flow physics around the rotors is also analyzed. Furthermore, the C_D and C_L *of the vented and non-vented elliptical and semicircular bladed rotors have also been calculated and compared with those of the 2D* C_D and C_L. *From the 3D unsteady simulations, the average* C_D and C_L *for the vented elliptical-bladed rotors are found to be 1.32 and 0.51, respectively. Whereas, the same for the non-vented elliptical-bladed rotor are predicted to be 1.31 and 0.48, respectively. However, the average* C_D and C_L *for the vented semicircular bladed rotor are found to be 1.28 and 0.53, respectively; while the same for the non-vented semicircular bladed rotors are found to be 1.26 and 0.55, respectively.*

6.1 Introduction

The 3D unsteady simulations are conducted on the elliptical-bladed rotor using FVM based CFD software ANSYS Fluent with the help of SST k-ω turbulence model to predict the flow behavior accurately. The simulations are also carried out for the semicircular bladed at the identical conditions to have a direct comparison. The 3D simulations are also conducted for the vented and non-vented elliptical-bladed rotor to estimate its performance coefficents (C_T and C_P) and aerodynamic coefficients (C_D and C_L).

6.2 Analysis of Performance Coefficients

A series of 3D unsteady simulations are performed with the vented elliptical-bladed rotor, and results are compared with the non-vented elliptical-bladed rotor at V = 6.2 m/s. As is done earlier, the continuity, Reynolds Averaged Navier-Stokes equations (RANS) and two equation eddy viscosity model *SST k-ω* are numerically solved by the commercial *FVM* based solver ANSYS Fluent. The time-dependent torque coefficients are obtained by averaging over different time intervals. The rotor performances are analyzed in respect of averaged torque and power coefficients. It is observed that after the initial period, it follows almost a cyclic path, and hence, the torque coefficient (C_T) is averaged to give a more accurate value. The maximum C_T of the vented elliptical-bladed rotor is found to be $C_T = 0.17$, thus giving a peak C_P of 0.14 at *TSR* = 0.8 and *AR* = 0.7, while the non-vented rotor shows a peak C_P of 0.13 at the same *TSR* and *AR*. Figures 6.1 and 6.2 show the variation of C_T and C_P for the vented and the non-vented elliptical-bladed rotor where a marginal performance improvement of 7.7% is observed for the vented elliptical-bladed rotor than the non-vented rotor (Figure 6.2).

To study the flow characteristics, all the contour plots are generated at the optimum *TSR* (= 0.8) fixing the *AR* at 0.7. The velocity and pressure contours of 3D elliptical-bladed rotors are shown in Figures 6.3 and 6.4. For the vented elliptical rotor, the maximum velocity is found to be 12.0 m/s, while the non-vented elliptical rotor shows a maximum velocity of 11 m/s. It is observed that there is an improved overlapping flow around the vented elliptical blades and a high-velocity zone near the blade surface. This reduces the chances of flow separation thereby yielding better results for the vented rotor. The total pressure near the advancing blade of the vented-elliptical-bladed rotor is around 30-40 N/m^2; whereas it is around 10-30 N/m^2 in the case of non-vented elliptical-bladed rotor. Hence, a higher total pressure is observed in vented-elliptical-bladed rotor than the non-vented rotor. Thus, there is an improvement in the flow characteristics resulting a higher value of C_P. The intensity of total pressure on the concave side of the advancing blade of the vented rotor is higher than the non-vented rotor. The total pressure on the returning blade of the vented-rotor is observed to be lesser than the non-vented rotor. Hence, the negative torque on the vented rotor gets reduced thereby improving the rotor performance.

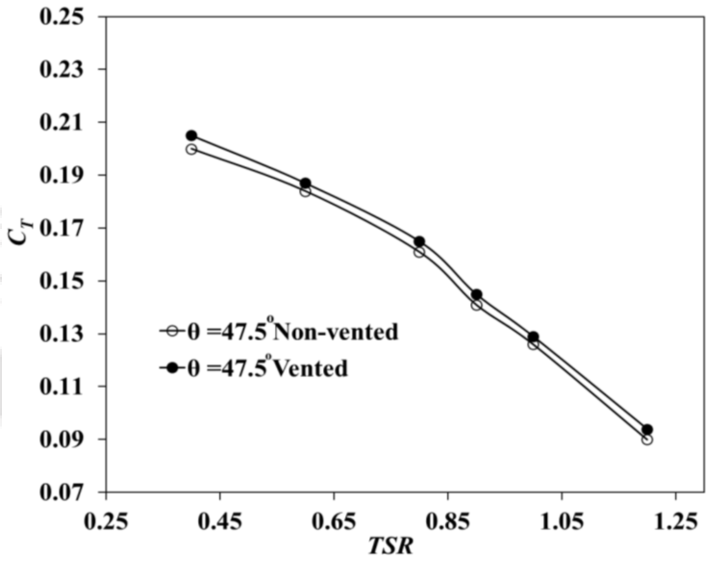

Figure 6.1: Variation of C_T with *TSR* of the vented and non-vented elliptical-bladed rotor

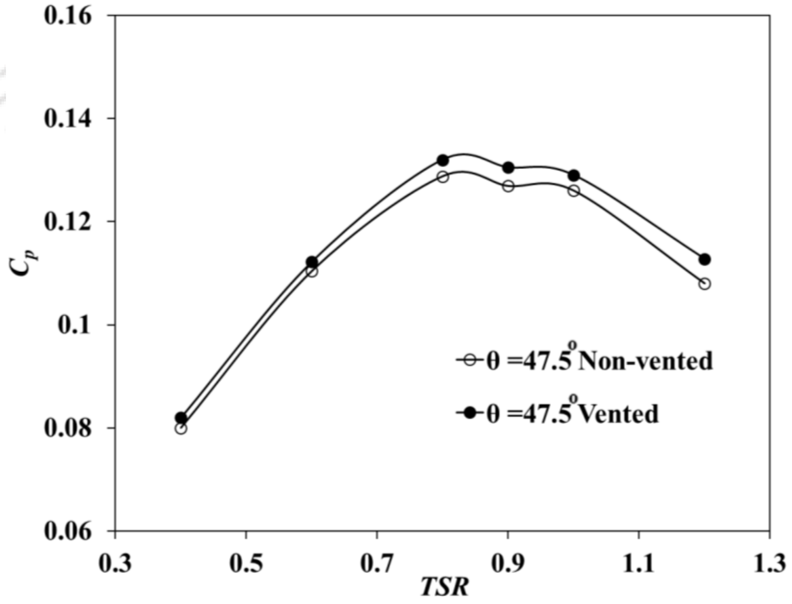

Figure 6.2: Variation of Cp with TSR of the vented and non-vented elliptical-bladed rotor

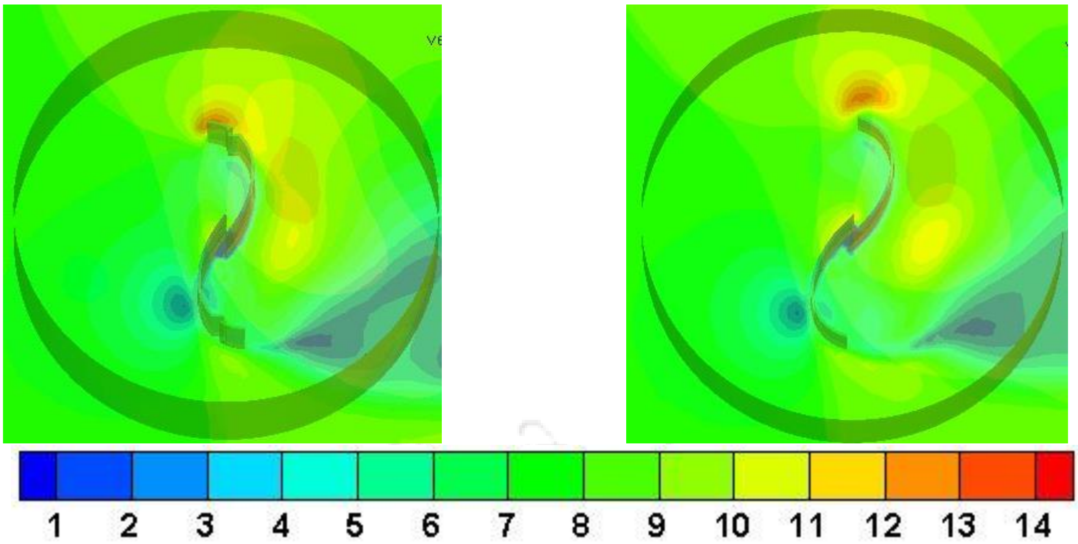

Figure 6.3: Velocity contours (m/s) of the vented and non-vented elliptical-bladed rotor at *AR* = 0.7 and *TSR* = 0.8

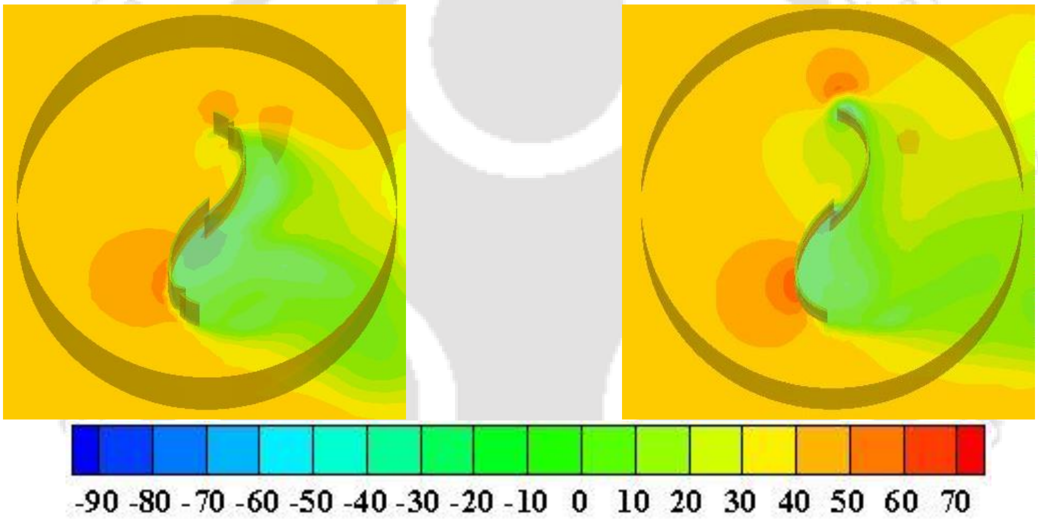

Figure 6.4: Total pressure (N/m^2) contours of vented and non-vented elliptical-bladed rotor at *AR* = 0.7 and *TSR* = 0.8

6.3 Drag and Lift Analysis of Non-vented Elliptical-bladed Rotor

From the 3D unsteady simulation, the C_D and C_L are estimated for elliptical and semicircular bladed rotors at *TSR* = 0.6 and *AR* = 1.09. The average C_D for the elliptical-bladed rotor is 1.31 and for the semicircular bladed rotor is 1.26. Thus, there is an improvement in average C_D by 4% in elliptical-bladed rotor than the semicircular bladed rotor. The maximum C_D is found to be 2.18 and 2.19 at α =70° and 249°, respectively for the elliptical-bladed rotor, while, for the semicircular-bladed rotor, the maximum C_D is found to be 1.83 and 1.85 at α = 64° and 244° (Fig. 6.5). The average C_L for the elliptical-bladed rotor is 0.48 and for the semicircular-bladed rotor is 0.55. The maximum C_L for the elliptical-bladed rotor is found to be 1.46 and 1.43 at α = 32° and 211° respectively, and whereas for the semicircular bladed rotor is 1.27 and 1.24 at the same α (Fig. 6.5). The comparison of present 2D and 3D unsteady results semicircular and elliptical-bladed rotor are shown in Figs. 6.6 and 6.7, where the nature of C_D and C_L are similar. From Figs it is evident that the 2D unsteady results are over predicted since the effect of third dimension is neglected where the 3D tip vortices can induce a complex 3D vortex flow. The C_D in 2D simulations are over predicted by 9.4% and 6% in elliptical and semicircular profiles, respectively than the 3D unsteady simulations of elliptical and semicircular-bladed rotors.

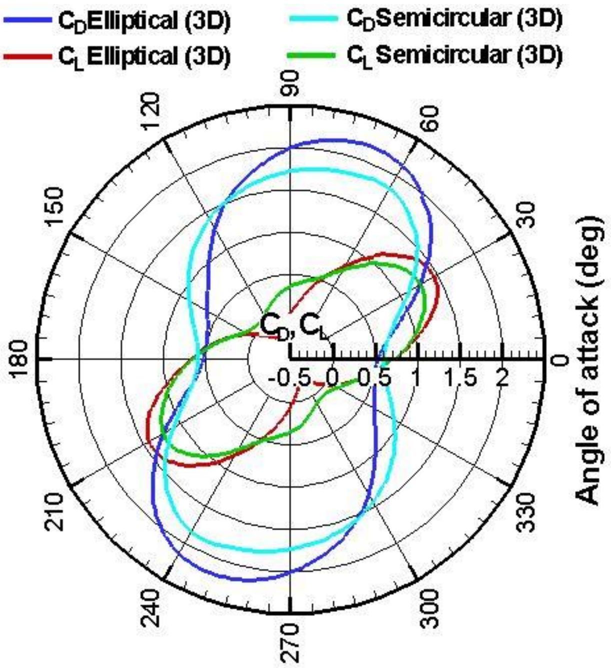

Figure 6.5: Variation of the C_D and C_L for the elliptical and semicircular-bladed rotors at TSR = 0.6

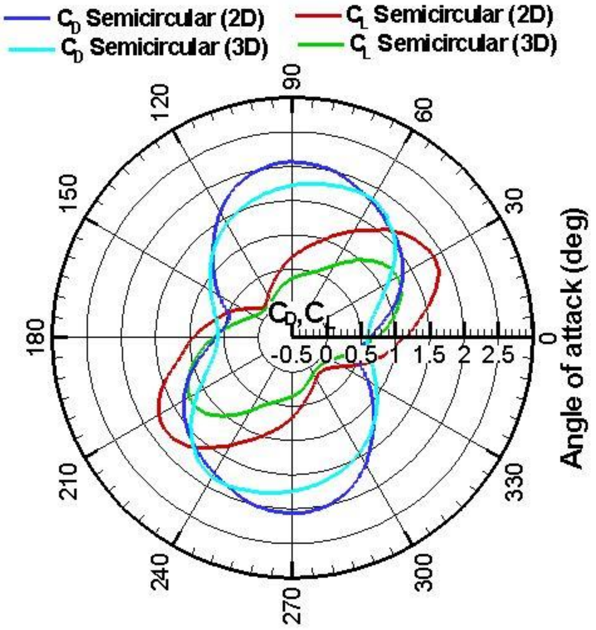

Figure 6.6: Comparison of the C_D and C_L of semicircular profile (2D) and semicircular bladed rotor (3D) at TSR = 0.6

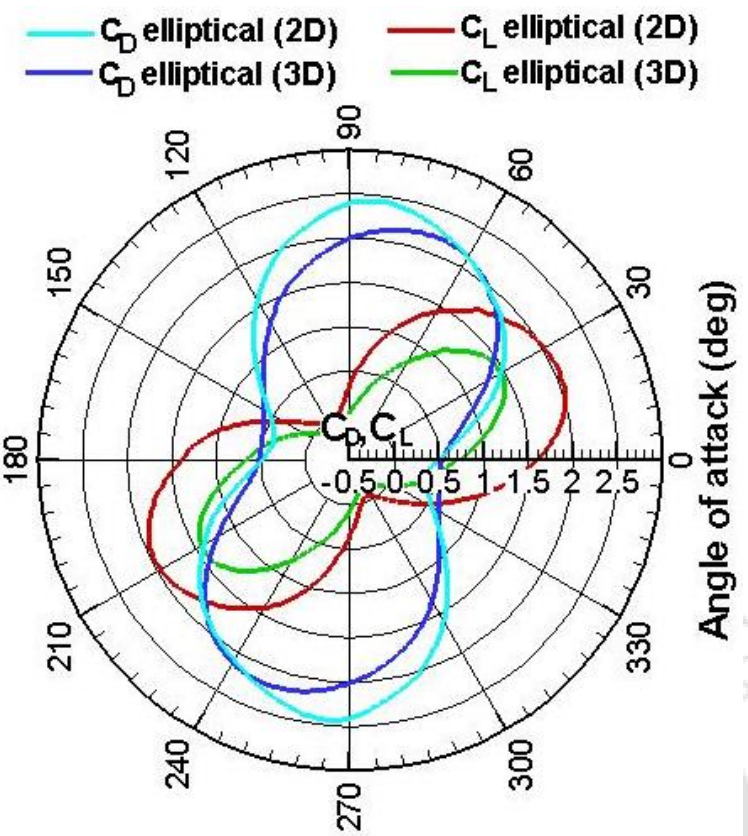

Figure 6.7: Comparison of the C_D and C_L of elliptical profile (2D) and elliptical-bladed rotor (3D) at TSR = 0.6

To study the flow characteristics, the velocity, total pressure, and turbulence intensity contours are generated for 3D elliptical- and semicircular-bladed rotors (Figures 6.8 through 6.10). For 3D unsteady results, at α = 90°, the maximum velocity near the surface of the advancing blade is found to be in the range of 4-5 m/s and 3-4 m/s for the elliptical- and semicircular-bladed rotors, respectively. Whereas for 2D unsteady results, the velocity is found to be 4-6 m/s and 3-5 m/s for the elliptical- and semicircular profiles. In case of 2D, a quite small vortices are observed behind the returning elliptical profile, however in case of 3D, the vortices are almost negligible. But the magnitude of vortices is larger in the semicircular profile (2D) than the vortices formed in the semicircular-bladed rotor (3D). Again, at α = 150°, the maximum velocity is found to be 6-7 m/s and 3-4 m/s for the elliptical- and semicircular-bladed rotors, respectively. It is also clear from Fig. 6.8 that the vortices formed behind the returning semicircular-bladed rotor reduces its average C_D and as a result the C_T and C_P are found lesser as compared to the elliptical-bladed rotor. It is further observed from Fig. 6.8b that the tip losses are lesser in elliptical-bladed rotor than the semicircular-bladed rotor. This make the elliptical-bladed rotor to have higher C_D than the semicircular-bladed rotor.

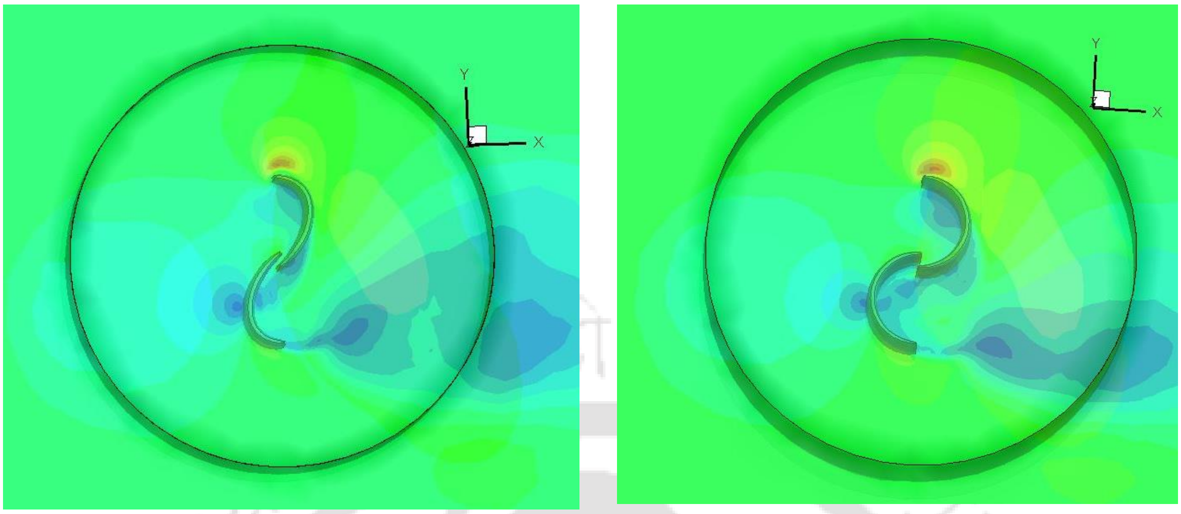

(a) Angle of attack = 90°

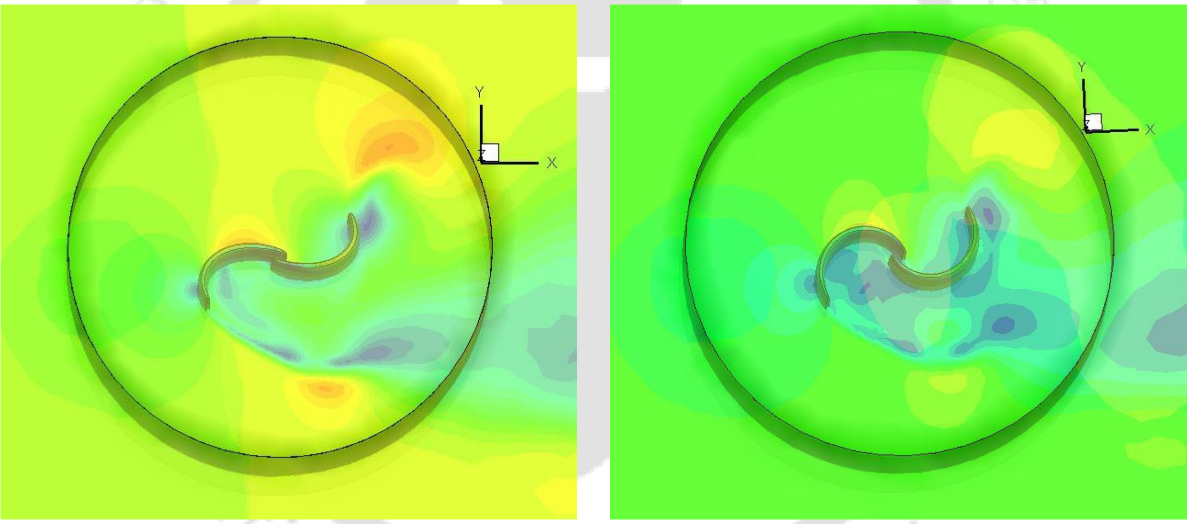

(b) Angle of attack = 150°

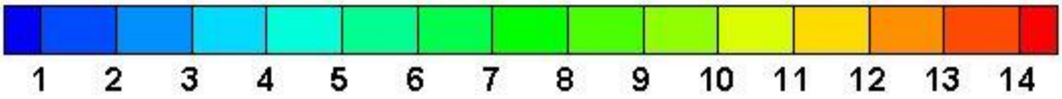

Figure 6.8: Velocity magnitude (m/s) contours of elliptical and semicircular bladed rotors at TSR = 0.6

The total pressure near the surface of the elliptical-bladed rotor is more than the semicircular-bladed rotor (Fig. 6.9). The total pressure near the surface of the elliptical-bladed rotor is around 0-20 N/m^2, whereas for the semicircular-bladed rotor is 0-10 N/m^2 (Fig. 6.9a). Therefore, the boundary layer separation is delayed which reduced the pressure drag on the returning bucket. This is due to increased pressure recovery that occurs in the elliptical-bladed rotor, also with the increasing of the lift force for some angular positions such as α = 15°-60° and 190°-240°, increasing the moment of the rotor. It is observed that there is an enhanced overlapping flow around the elliptical-bladed rotor. Hence, a higher total pressure is observed in elliptical-bladed rotor than the semicircular-bladed rotor. Thus, there is an improvement in the flow characteristics resulting in a higher performance value. Also, the turbulence intensity in the elliptical-bladed rotor is lesser than the semicircular-bladed rotor. Table 6.1 shows the summary of all the Savonius rotor blades.

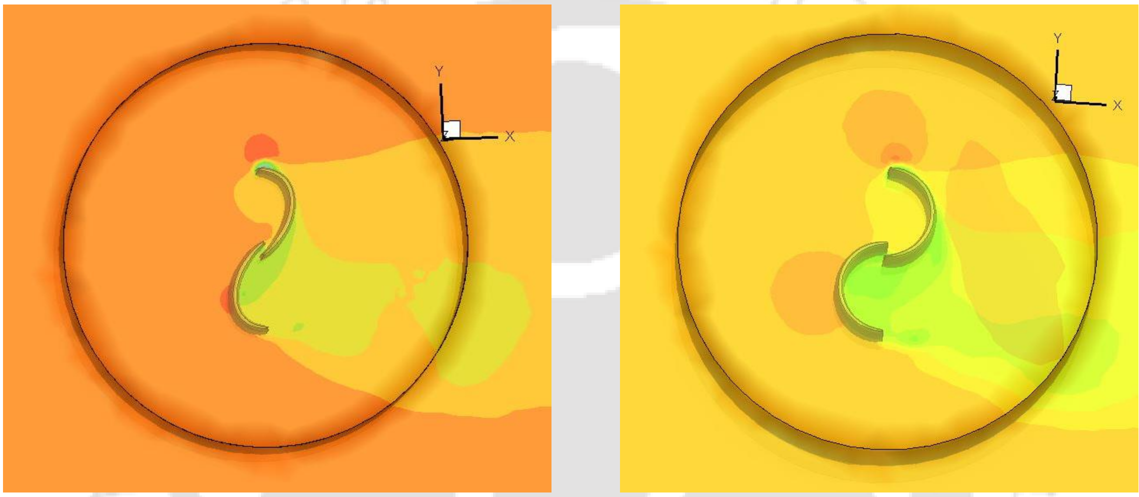

(a) Angle of attack = 90°

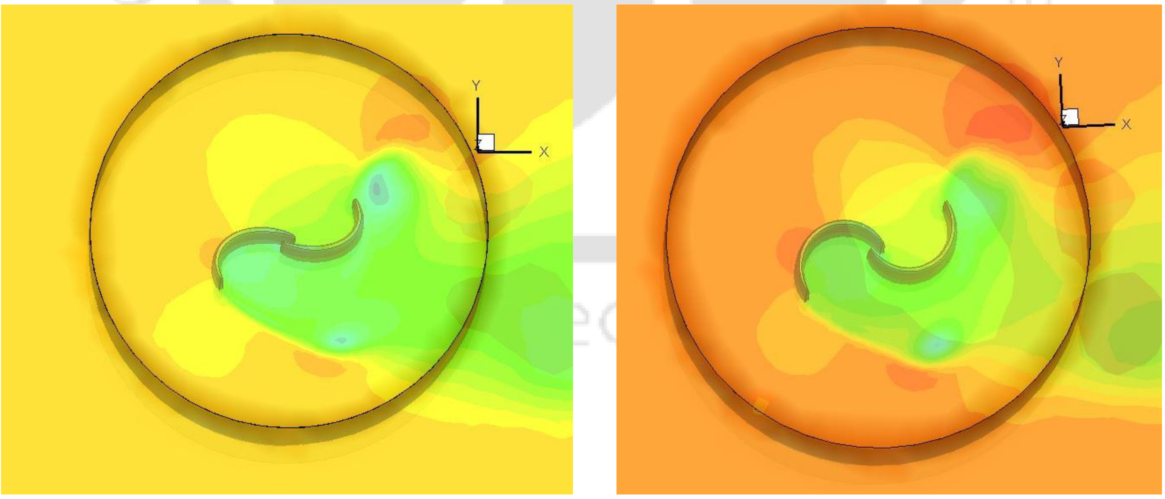

(b) Angle of attack = 150°

Figure 6.9: Total pressure (N/m^2) contours of elliptical and semicircular bladed rotors at TSR = 0.6

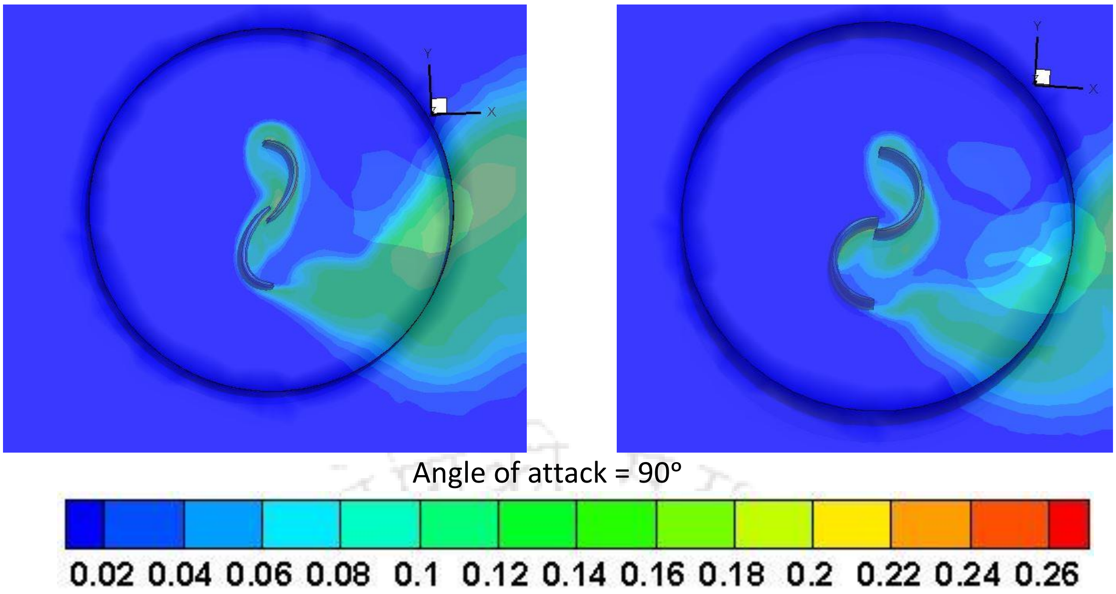

Figure 6.10: Turbulence intensity (%) contours of elliptical and semicircular bladed rotors at TSR = 0.6

6.4 **Drag and Lift of Vented Elliptical-bladed Rotor**

The 3D unsteady simulations are performed for vented and non-vented elliptical and semicircular bladed rotors using same turbulence model as that of 2D. The polar diagrams of C_D and C_L for the vented elliptical and semicircular bladed rotors is shown in Figs 6.11 and 6.12. Both the C_D and C_L is drawn at *TSR* = 0.6. From the diagrams, it is estimated that the average C_D for the vented and non-vented elliptical-bladed rotors is found to be 1.32 and 1.31. Thus, there is an increase of average C_D by 0.8% in the elliptical-bladed rotor with vent-augmenters than the same rotor without vent-augmenters. The average C_D for the vented and non-vented semicircular bladed rotors is found to be 1.28 and 1.26. Hence, there is an increase in average C_D by 1.6% in semicircular bladed rotor with vent than the same rotor without vent. The average C_L for the vented and non-vented elliptical-bladed rotors is found to be 0.51 and 0.48. Thus, there is an increase of average C_L by 6.3% in elliptical-bladed rotor with vents than the same rotor without vents. The average C_L for the vented and non-vented semicircular-bladed rotors is found to be 0.53 and 0.55, respectively.

The comparisons of C_D and C_L (2D and 3D) are shown in Figs 6.13 and 6.14. It is observed that the 3D unsteady results are under predicted since the third dimension (height of the rotor) of the rotor is assuming to be infinite in 2D unsteady simulations hence the effect of height is neglected in 2D simulations. Also, in 3D unsteady simulations, 3D tip vortices can induce a complex 3D vortex flow which reduces the overall C_D and C_L than the 2D results.

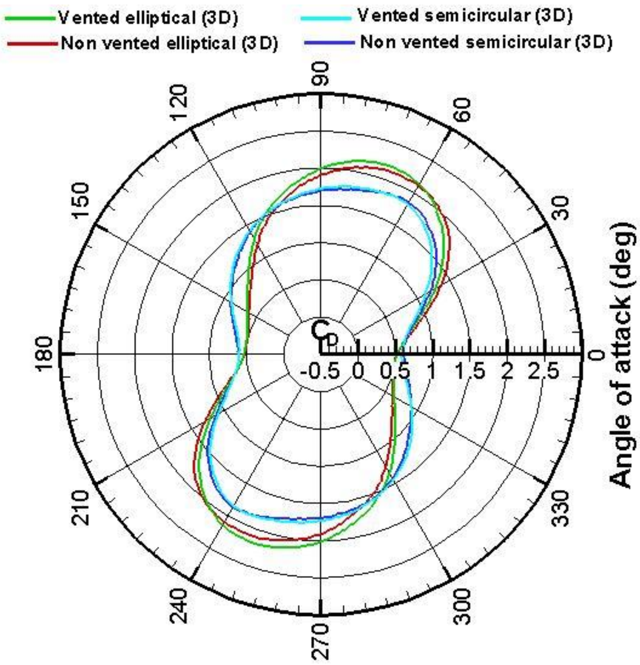

Figure 6.11: Variation of the C_D for the elliptical and semicircular-bladed rotors at *TSR* = 0.6

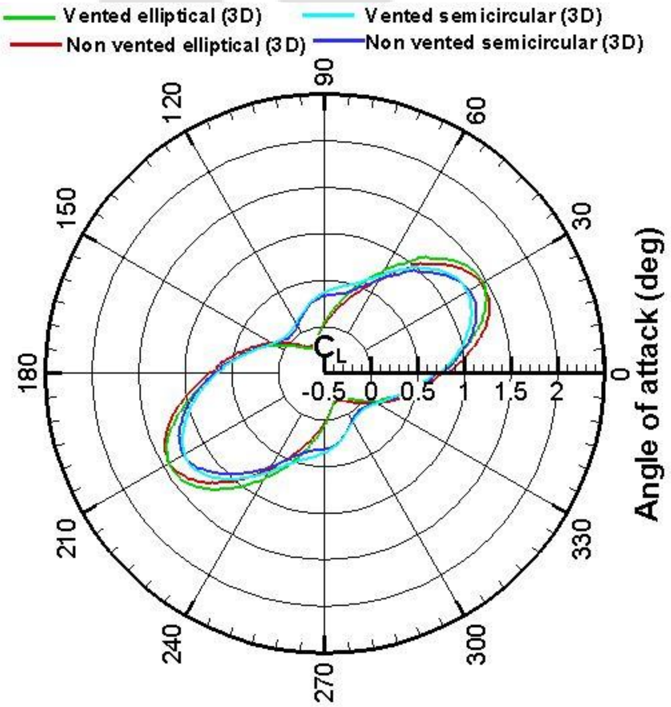

Figure 6.12: Variation of the C_L for the elliptical and semicircular-bladed rotors at *TSR* = 0.6

To investigate the flow physics, the velocity, total pressure, and turbulence intensity contours are generated for 3D vented and non-vented elliptical- and semicircular-bladed rotors (Figures 6.15 through 6.17). For 3D unsteady results, at α = 90°, the maximum velocity near the surface of the advancing blade for vented and non-vented elliptical-bladed rotors is found to be around 4-5 m/s. However, due to having the venting slot on the rotor blades, the region of higher velocity zone is more in elliptical-bladed rotor with vents than the rotor without vents. Also, the region of low velocity zone in convex side of the returning of elliptical-bladed rotor with vent is higher than the rotor without vents, which reduces the negative drag of the rotor. As a result, the overall C_D is more in vented elliptical-bladed rotor.

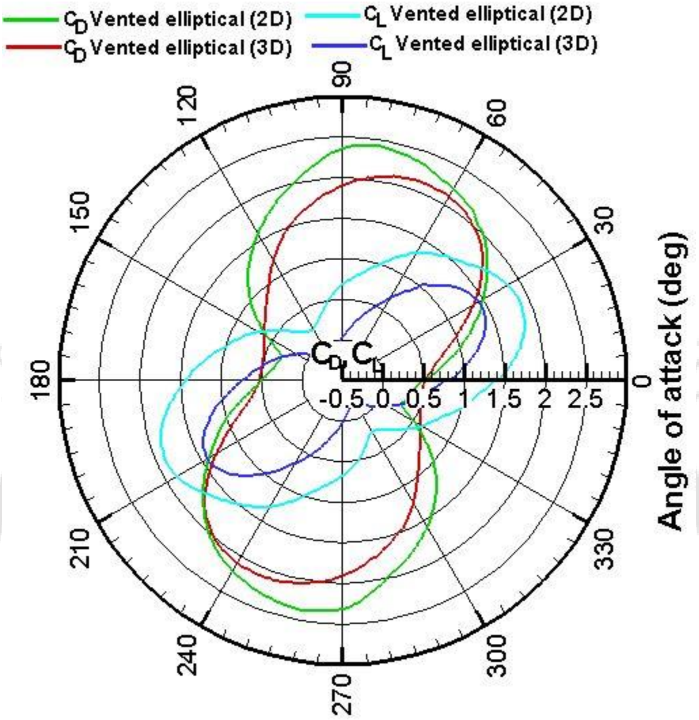

Figure 6.13: Comparison of the C_D and C_L of the vented elliptical profile/blade at TSR = 0.6

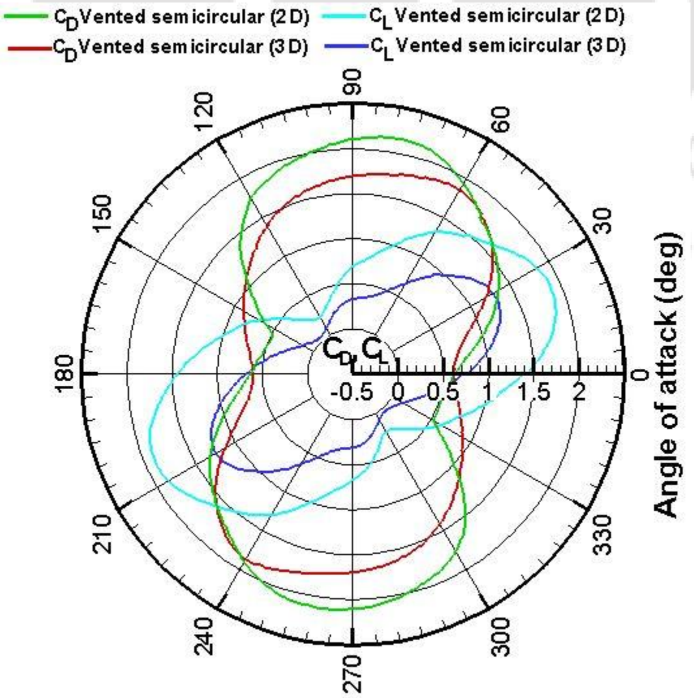

Figure 6.14: Comparison of the C_D and C_L of the vented semicircular profile/blade at TSR = 0.6

The overlapping flow which strikes the concave side of the returning blade is found more in elliptical-bladed rotor with vent than the rotor without vent. All these reduces the negative drag of the rotor, as a result, the overall C_D is enhanced for the vented elliptical-bladed rotor.

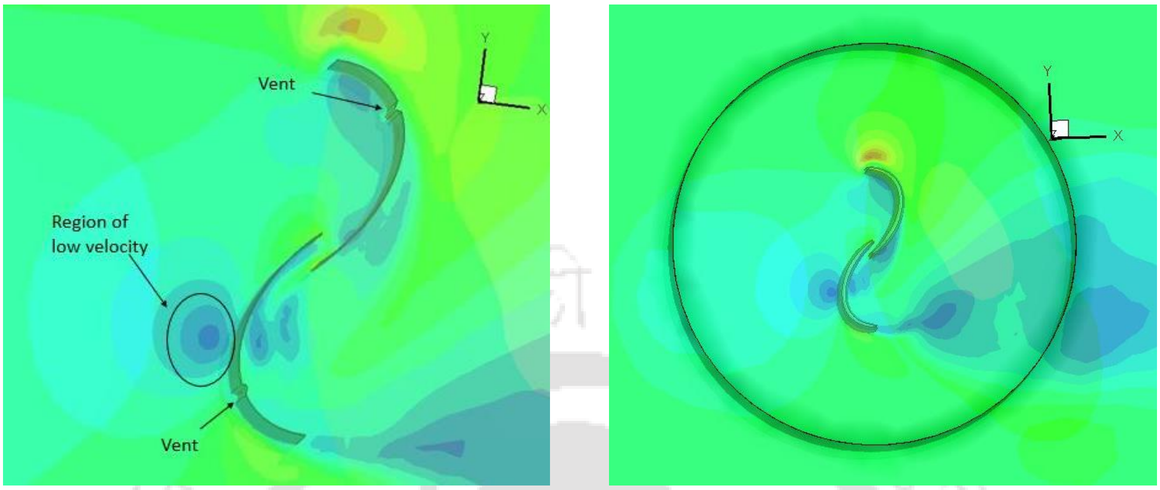

(a) Elliptical α = 90°

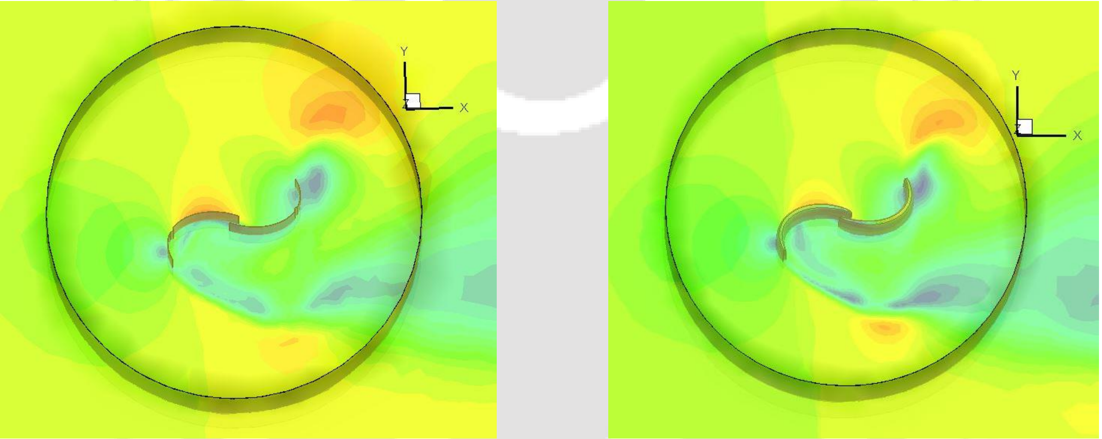

(b) Elliptical α = 150°

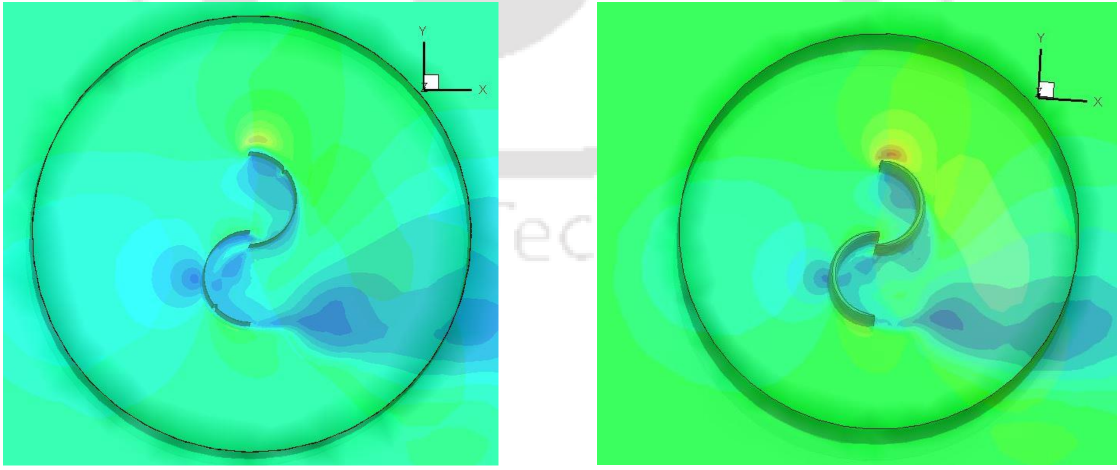

(c) Semicircular α = 90°

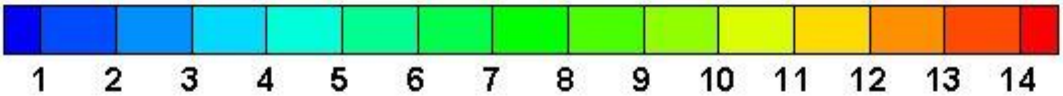

Figure 6.15: Velocity magnitude (m/s) contours of elliptical and semicircular bladed rotors at *TSR* = 0.6

The total pressure for the elliptical-bladed rotor with and without vents are shown in Fig. 6.16. The total pressure near the surface of the elliptical-bladed rotor with and without vents are found to be around 0-20 N/m^2, however, the region of high-pressure zone is observed to be more in concave side of advancing elliptical-bladed with vent rotor than the rotor without vent. Hence, the boundary layer separation is delayed which reduced the pressure drag on the returning bucket of vented rotor. In case of 2D, the vortices formed behind the returning blade of elliptical-bladed rotors are much larger than the vortices formed behind the returning blades of elliptical-bladed rotor in 3D cases. It is clearly observed from the 2D and 3D velocity contours of elliptical-bladed rotors that the tip vortices are more profound in 2D cases than the 3D cases. However, the 3D vortices induced a complex 3D vortex flow which reduced the overall C_D and C_L than the 2D results. Figure 6.17 shows the turbulence intensity contours of elliptical-bladed rotor with and without vents at α = 90°. The magnitude of turbulence intensity is in the range of 0.04%-0.06% in elliptical-bladed rotor with vents; whereas, it is 0.06%-0.08% in rotor without vents. Hence, the magnitude of turbulence intensity is more in elliptical-bladed rotor without vent than the rotor with vent. As a result, the overall C_D and C_L is more vented rotor than the non-vented rotor.

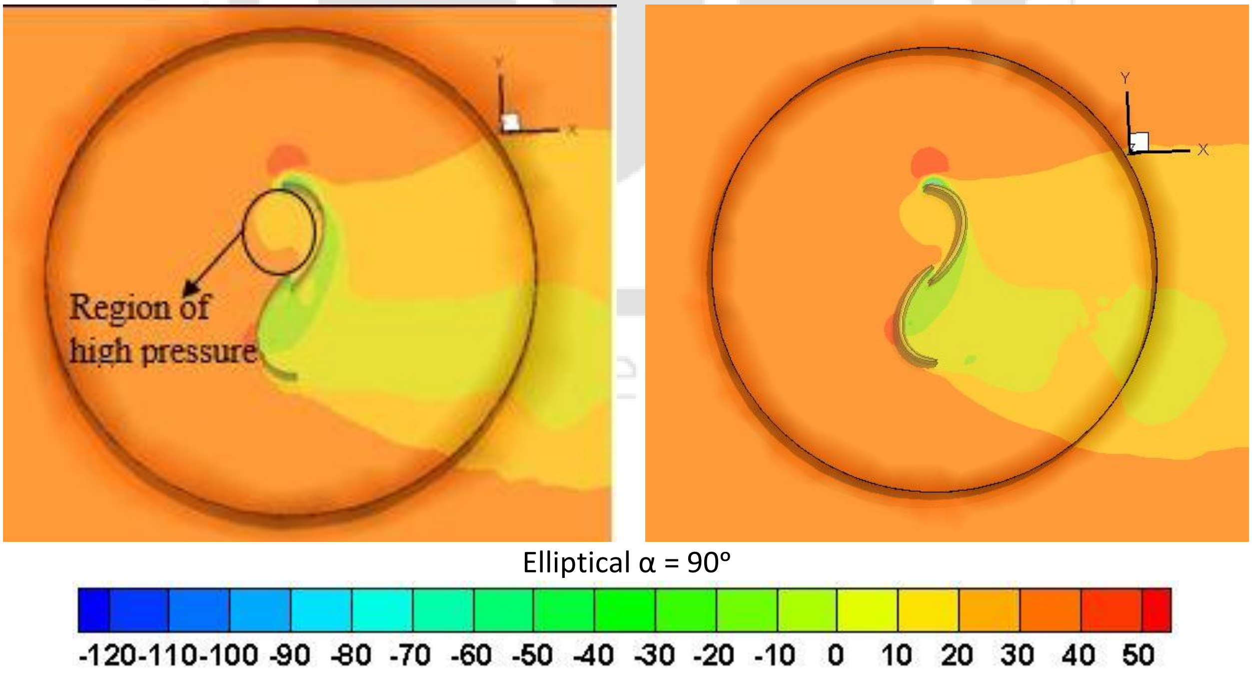

Figure 6.16: Total pressure (N/m^2) contours of vented and non-vented elliptical rotors at TSR = 0.6

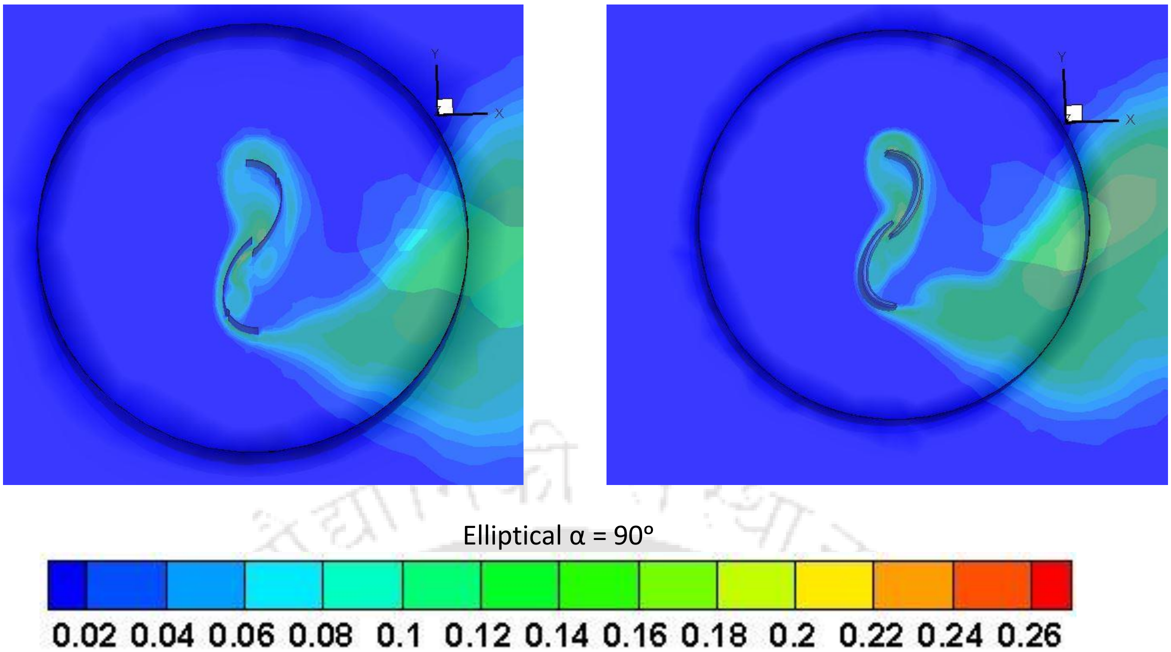

Figure 6.17: Turbulence intensity (%) contours of vented and non-vented elliptical-bladed rotors at TSR = 0.6

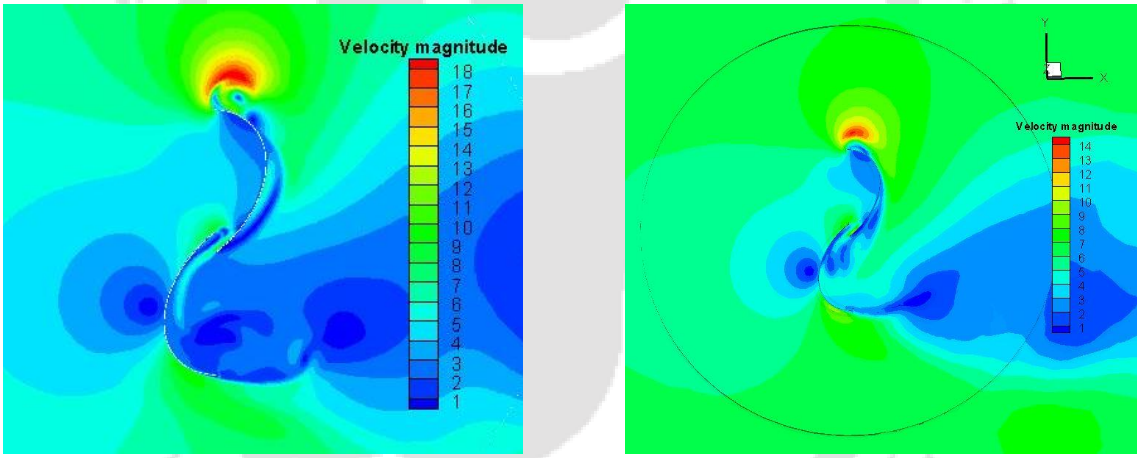

2D simulation 3D simulation

(a) Velocity contours

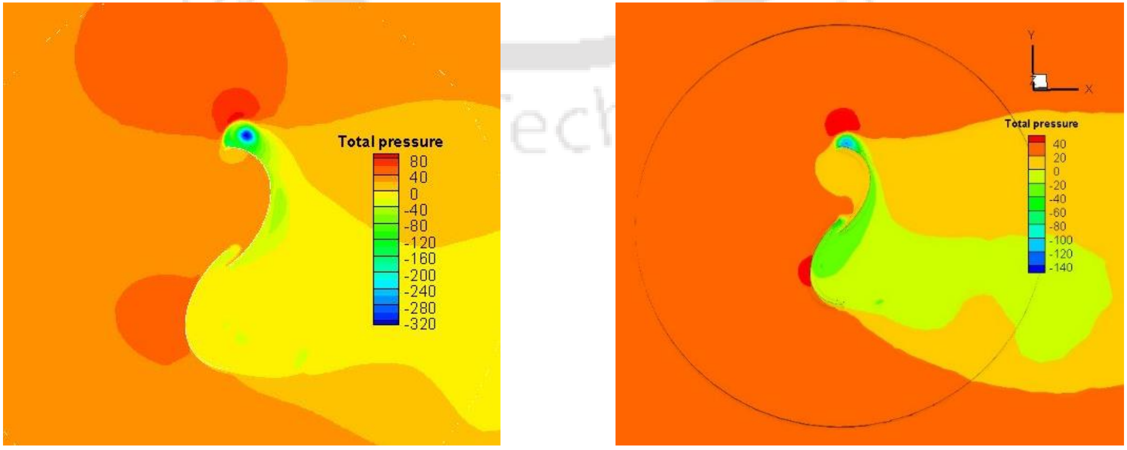

2D simulation 3D simulation

(b) Total pressure contours

Figure 6.18. Velocity and total pressure contours of elliptical profile at TSR = 0.6.

6.5 Comparison of 2D and 3D Simulations

It can be clearly observed from Figure 6.18 that the nature of the flow pattern remains the same in 2D and 3D unsteady simulations. The maximum velocity is observed near the advancing profile/rotor in 2D and 3D simulations (Fig. 6.18). However, there is a lesser magnitude of velocity in case of 3D simulated results (Le *et al.*, 2014). The total pressure contour shows a comparatively higher total pressure in the advancing profile/rotor in both 2D and 3D simulations. Hence, the 3D unsteady results are under predicted since the third dimension (height of the rotor) of the rotor is assumed to be infinite in 2D unsteady simulations. Also, in 3D simulations, tip vortices can induce a complex 3D vortex flow which reduces the overall C_D and C_L over the 2D results.

6.6 Concluding Remarks

The 3D unsteady simulations are carried out at V = 6.2 m/s and at, *ARs* of 0.7 and 1.09. The vented rotor shows a $C_{pmax} = 0.14$ at TSR = 0.8, while the non-vented rotor shows $C_{pmax} = 0.13$ at the same TSR and at AR = 0.7. The 3D unsteady simulations are also carried out to analysis the aerodynamic drag and lift characteristics of elliptical and semicircular-bladed rotor at AR = 1.09. From the simulation, the average C_D is found to be 1.31 and 1.26 for the elliptical and the semicircular-bladed rotor, respectively. The C_{Dmax} is found to be 2.19 at $\alpha = 70°$ and 249°, respectively for the elliptical-bladed rotor, while, for the semicircular-bladed rotor, the C_{Dmax} is found to be 1.83 and 1.85 at $\alpha = 64°$ and 244°. The average C_L is found to be 0.48 and 0.55 for the elliptical and the semicircular bladed rotor, respectively. The C_{Lmax} for the elliptical-bladed rotor is found to be 1.46 and 1.43 at $\alpha = 32°$ and 211° respectively, and for the semicircular-bladed rotor is 1.27 and 1.24 at same α. The C_L and C_D are also calculated for the vented elliptical- and semicircular- bladed rotors. The average C_D for the vented elliptical and semicircular bladed rotors is found to be 1.32 and 1.28, respectively. The average C_L for the vented elliptical and semicircular rotors is found to be 0.51 and 0.53, respectively.

Table 6.1: Summary of numerical and experimental results

Profiles	**Investigators**	**Year**	**2D Numerical** (C_D, C_L)				**3D Numerical/Experimental** (C_D, C_L)				**Experimental** (C_P at AR = 1.09)
			C_{Davg}	C_{Dmax}	C_{Lavg}	C_{Lmax}	C_{Davg}	C_{Dmax}	C_{Lavg}	C_{Lmax}	C_P
Semicircular	Irabu and Roy (Experimental)	2011	--	--	--	--	0.80	1.55	--	1.4	--
Semicircular	Jaohindy *et al.* (Numerical)	2013	--	--	--	--	--	2.2	--	1.72	--
Roy	Roy and Ducoin	2016	1.38	2.24	1.19	2.07	--	--	--	--	--
Modified Bach	Present investigation (Numerical)		1.41	2.31	0.95	1.97	--	--	--	--	--
Benesh			1.25	2.01	1.32	2.25	--	--	--	--	--
Elliptical			1.43	2.43	0.95	2.05	1.31	2.18	0.48	1.46	0.19
Vented elliptical			1.45	--	0.98	--	1.32	--	0.51	--	--
Semicircular			1.35	2.06	0.96	1.85	1.26	1.83	0.55	1.27	0.15
Vented semicircular			1.39	--	1.04	--	1.28	--	0.53	--	--

CHAPTER –7

Experimental Investigation

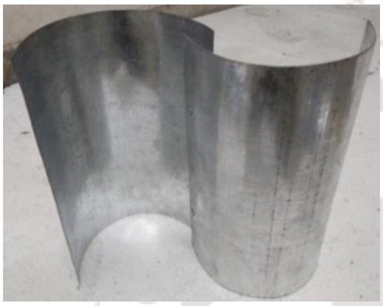

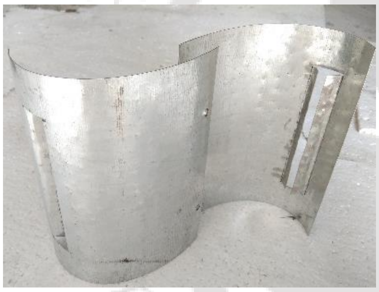

Chapter Outline

Overview

A series of experiments are conducted in a low-speed subsonic wind tunnel to validate the numerical results. The experiments are performed for the elliptical, modified Bach, Benesh and semicircular-bladed rotors to estimate their aerodynamics performance parameters. From the wind tunnel experiments, the maximum C_P for the elliptical, modified Bach, Benesh and semicircular bladed rotor are found to be 0.19, 0.16, 0.16 and 0.15, respectively. Experiments are also conducted for the vented elliptical-bladed rotor to investigate its influence on the rotor aerodynamic performances.

7.1 Introduction

Once the computational work is completed, the experimental work is carried out to verify the results. From the computational work, the optimum number of blades for the best performance is found to be two. The two bladed systems have used to carry out the wind tunnel experiments and their performance is determined based on the C_T and C_P values. Experiments are conducted for elliptical, modified Bach and Benesh profile to choose the better rotor blade. In identical conditions, the performance of the semicircular rotor is also calculated, and both results are compared graphically. Another experiment is carried out to determine the effect of vent-augmentation of on the rotor performance. In this chapter, a brief introduction to the wind tunnel, its components, devices used for the experiments, experimental procedure and results are discussed.

7.2 Wind Tunnel Test Setup

Wind tunnel is an essential tool to study the experimental aerodynamics where several aerodynamic bodies are tested. If the bodies are tested inside the tunnel, it is called a 'closed type test section'. When the bodies are tested at the end of the tunnel, it is referred to as 'open type test section' (Fig. 7.1). This exercise continues to develop and remains to be a bedrock in the progress for a wide range of bodies such as airplane wings, aerospace and road vehicles, wind turbines, sport balls and others.

To carry out wind turbine research, a low speed wind tunnel with an open test section was developed at IIT Guwahati (Grinspan, 2002). Since then, the wind tunnel has been used for carrying out experimental research of Savonius rotor (Grinspan *et al*., 2004; Rajkumar, 2004; Thotla, 2006; Saha and Raj Kumar, 2006; Saha *et al*., 2008; Roy, 2014).

The wind tunnel mainly consists of: (i) a fan section, followed by an inlet section, (ii) diffuser section, (iii) settling chamber that contains the coarse screen, a honeycomb structure and a fine screen to make the wind flow streamlined, (iv) a nozzle section to accelerate the flow, and (v) an open test section which includes the turbine model and the necessary instrumentation. Figure 7.2 shows the various components of the low speed wind tunnel. The rating of the motor connected to the fan is 0.5 HP. The open type test section is placed at the exit of the nozzle of the wind tunnel.

Figure 7.1: The wind tunnel test facility

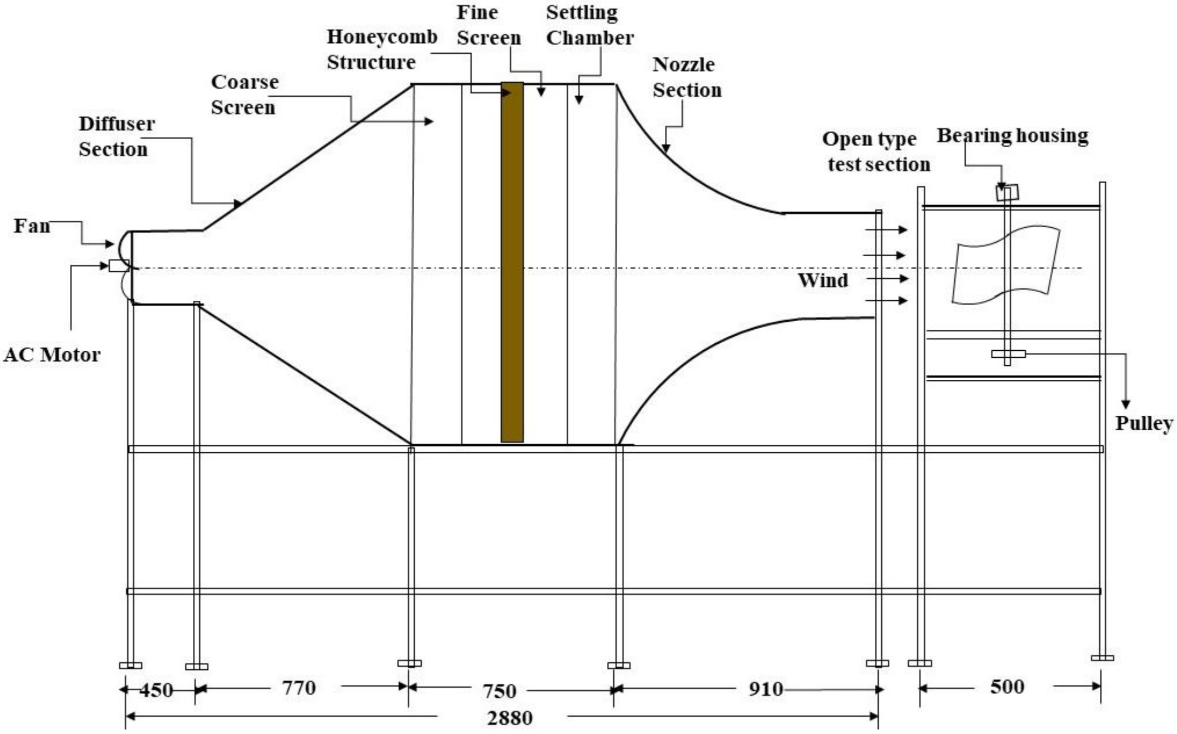

Figure 7.2: Schematic diagram of the wind tunnel

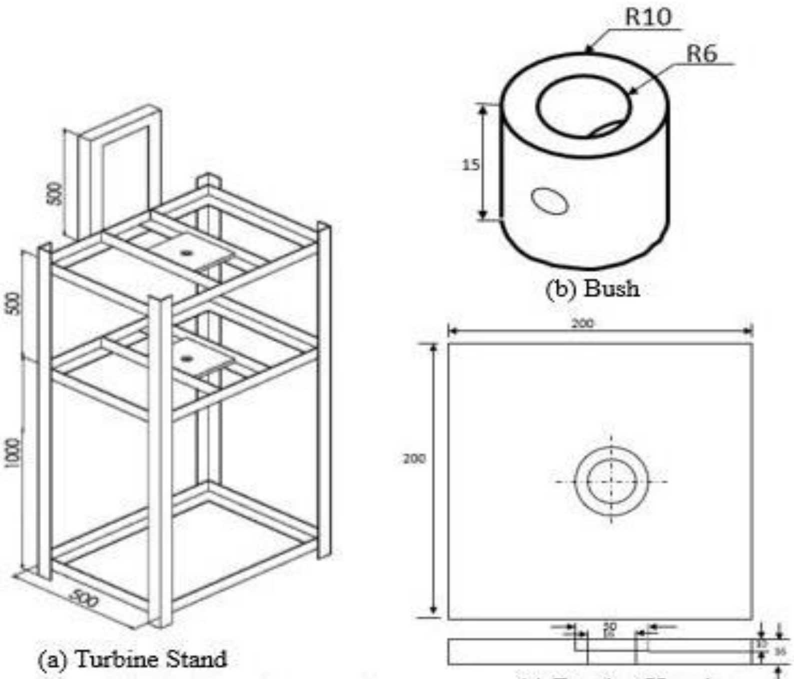

(a) Turbine Stand

(b) Bush

(c) Bearing Housing

All the dimensions are in mm

Figure 7.3: Various components of test facility

The dimensions of the test section measure a height of 500 mm, width of 500 mm, and a length of 700 mm. It means, it provides a frontal area of 500 × 500 mm^2 for an aerodynamic design to be tested. When the rotors are fitted in the test section, they are 250 mm away from the exit of the tunnel. The test section is manufactured using mild steel angles of 50 mm × 50 mm × 4 mm, whereas the tunnel sides are fabricated from galvanized iron sheets of thickness 1.6 mm. The test section consists of two bearing houses at two different heights, to allow the rotation of the wind turbine. An aluminium rod of 12 mm passes through the bearings, having two bushes, made of nylon material. These bushes help the blades and the rod to hold and rotate together. The test section also has a mass balance holder, where two spring mass balances are suspended. The difference between their readings give the values of load applied. Various components for the test facility are shown in Figure 7.3.

7.3 Fabrication of Rotor Blades

The wind turbine blades for this experiment are manufactured using 0.5 mm thick *GI* (Galvanized Iron) sheets with an aspect ratio of 0.7 and 1.09. This material is strong enough to withstand the flow-field of the wind ranging from 0 to more than 10 m/s. The vented elliptical-bladed rotor is manufacture with AR = 0.7. Figure 7.4 shows the different blades used for this experiment.

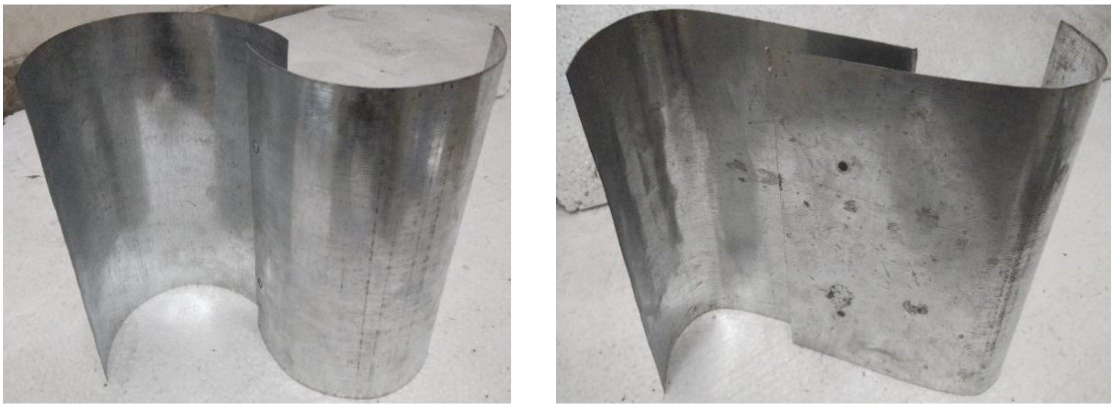

(a) Semicircular bladed rotor (b) Benesh

(c) Elliptical-bladed rotor (d) Modified Bach

(e) Vented elliptical-bladed rotor (f) Zoomed view of vent

Figure 7.4: Tested Savonius rotor blades

7.4 Measurement Procedures

As stated above, wind speed is measured using a digital anemometer having an operating range of 0-20 m/s and an accuracy of ± 2%. To determine the air velocity, anemometer detects change in some physical property of the fluid or the effect of the fluid on a mechanical device inserted into the flow. It senses the moving air with a rotary sensor, which acts very much like a weather vane and can be likened to the blades of a fan. The measurement units for anemometers include: Feet per minute (ft/min), meters per second (m/s), kilometers per hour (km/hr), miles per hour (mph), nautical miles per hour (knots), and Beauforts. Figure 7.5 shows a typical digital anemometer.

Figure 7.5: A digital anemometer

Table 7.1: Wind speed measurements at different input voltages.

Input Voltage to Fan (volts)	Wind Speed (m/s)
160	3.8
170	4.3
180	5.5
190	6.2
200	6.8
210	7.5
220	8.5
230	9.6

The input voltage is varied from 160-230 volts by means of a voltage regulator and corresponding wind speed is measured using a digital anemometer (Table 7.1). It is observed that the wind speed remains almost constants in a rectangular area of around 250 ×250 mm around the center. However, it increases towards the corners due to corner effect of nozzle section. Taking this in mind, averaged value of wind speed is calculated from several positions.

Figure 7.6: Front and side views of torque measurement unit

Torque measurement is done by applying some loads on the rotors. These loads are applied using spring mass balances. A pulley is attached to the shaft of the rotor and a rope is passed around it, which is attached to two mass balances (Figure 7.6). The *RPM* of the shaft is controlled by giving appropriate load through mass balance. When the shaft starts rotating, one of the mass balances works on the tight side, and the other works on the slack side. The difference between their readings is the working load on the shaft (Figure 7.7). A digital tachometer having range 0-50000 RPM with accuracy ± 1.0 % is used to measure the rotational speed of the rotor.

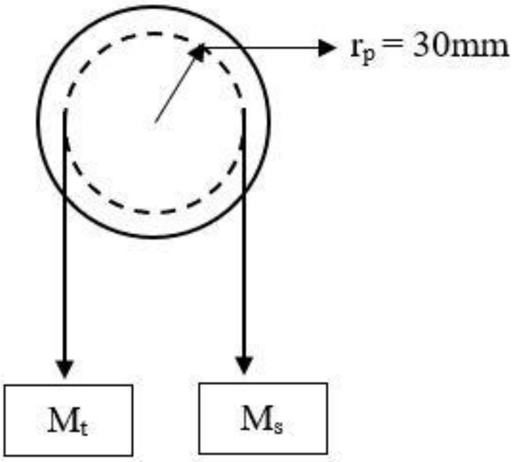

Figure 7.7: Top view of the pulley showing tight and slack side loads

Once the required RPM is achieved by adjusting the load on the shaft, the readings on both mass balances are taken. And the total torque output is calculated as:

$$\text{Torque Output } (T_O) = (M_t - M_s) \times g \times r_p \qquad (7.1)$$

Total torque input to the system can be calculated as,

$$\text{Torque Input } (T_i) = 0.5\rho A V^2 R \qquad (7.2)$$

Where ρ is air density, A is area of the blades (D×H), V is the speed of the wind and R is the radius of blades (D = R/2). Using these two values the coefficient of torque can be calculated as:

$$C_T = \frac{Torque\ Output}{Torque\ Input} = \frac{T_O}{T_i} = \frac{(M_t - M_s)gr_p}{0.5\rho A V^2 R} \qquad (7.3)$$

Once the C_T value calculated, coefficient of power can be calculated as

$$C_P = C_T \times TSR \qquad (7.4)$$

The uncertainties of the experiments are estimated by means of the sequential perturbation technique (Moffat, 1982; Kline, 1985) and it is found to be 4.5%, 4.8% and 2.9% for C_P, C_T, and T calculations, respectively.

7.5 Error Analysis

In the experimental procedure, it is not possible to get exactly the same value every time when the readings are taken. These readings keep changing, however, in a quite small magnitude, as more and more values are taken. The average values are taken as a final result; however, it is equally important to analyse that what the error range is in these results. From this analysis, the accuracy of the experimental result is judged. This analysis is done by calculating the standard deviation given by the expression (Holman, 2004; Roy, 2014):

$$\sigma = \sqrt{\frac{1}{J}\sum_{i=1}^{J}(x_i - m)^2} \times 100\% \qquad (7.5)$$

where, σ is the percentage standard deviation, J is the number of data taken, m is the mean value and x is the measured value. Several data are taken for a fixed mechanical load and shaft speed and error analysis is done for all cases. The error analysis is carried out for elliptical and semicircular bladed rotor at V = 6.2 in all the cases.

From the results of error analysis, it is found that for elliptical-bladed rotor, the percentage deviation is within ± 4.6 %, while for semicircular rotor, it is within ± 3.9 % (Figs 7.8 through 7.11). This analysis indicates that the fluctuations in these experiments are very less, and the accuracy of average data taken is very high. In all the later reported results, the mean values of all the measured data have been used for the analysis of SSWTs.

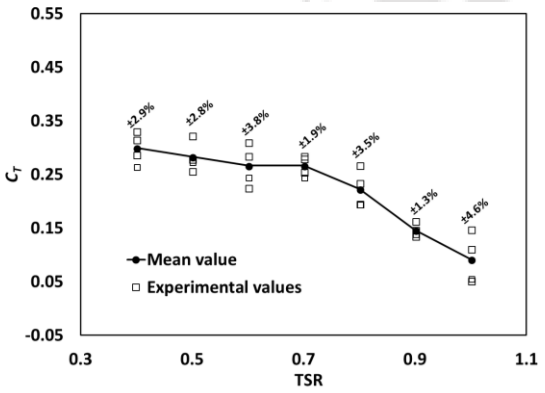

Figure 7.8: Standard deviation of C_T for elliptical-bladed rotor at V = 6.2 m/s

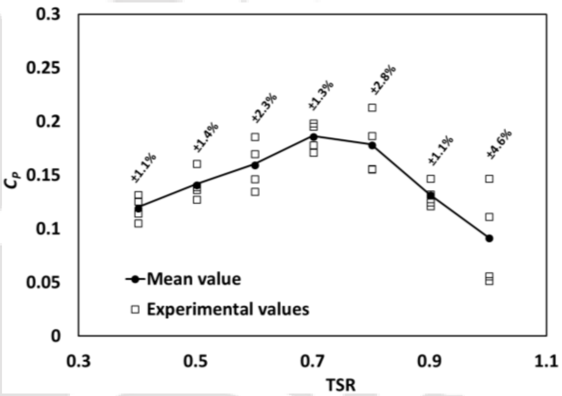

Figure 7.9: Standard deviation of C_P for elliptical-bladed rotor at V = 6.2 m/s

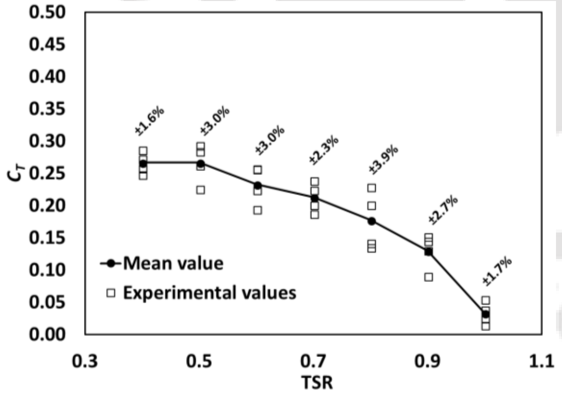

Figure 7.10: Standard deviation of C_T for semicircular bladed rotor at V = 6.2 m/s

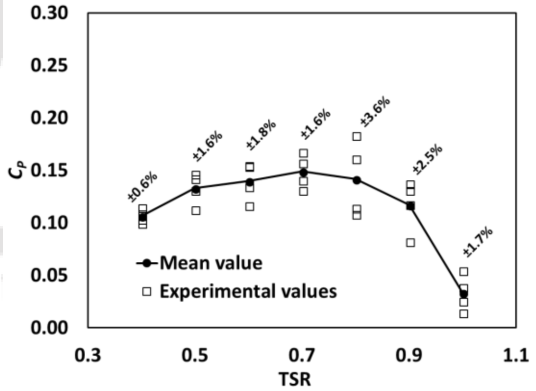

Figure 7.11: Standard deviation of C_P for semicircular bladed rotor at V = 6.2 m/s

7.6 Rotor Blade Optimization

The Savonius rotor, since its inception, has undergone various design modifications in terms of blade geometry and the blade profiles. The conventional semicircular profile of the rotor has been investigated extensively. A host of other blade profiles have been developed in the last few decades, notable among which are Benesh, modified Bach, and elliptical types. The experimental peak C_P values for the elliptical-bladed and semicircular-bladed rotors are found to be 0.19 and 0.15 at *TSR* = 0.7 (Fig. 7.12); whereas the peak C_P for Benesh and modified Bach rotors are found to be 0.16 at *TSR* = 0.6 and 0.8, respectively. Thus, the elliptical-bladed rotor shows an improvement of C_P by 27% as compared to the semicircular-bladed rotor. This improved C_P is due to the fact that the elliptical-bladed rotor has an almost straight trailing edge (*TE*) and a leading edge (*LE*) with higher radius of curvature than the conventional semicircular-bladed rotor. They primarily cause a difference in pressure drag. The magnitude of pressure drag on the advancing blade of elliptical-bladed rotor is higher than the semicircular-bladed rotor. Moreover, the straight *TE* of the returning blade also acts positively and accelerates the moment of the rotor. Also, the straight LE delays the flow separation on the elliptical-bladed rotor leading to an enhanced pressure recovery. As a result, the negative torque of the rotor is reduced thereby enhancing the overall C_D as well as C_T and C_P *of* the rotor.

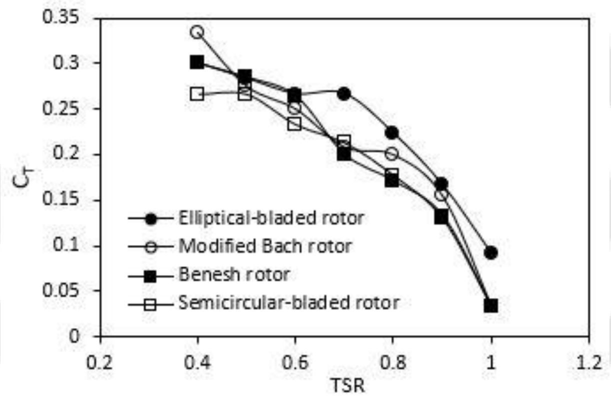

(a) C_T vs *TSR*

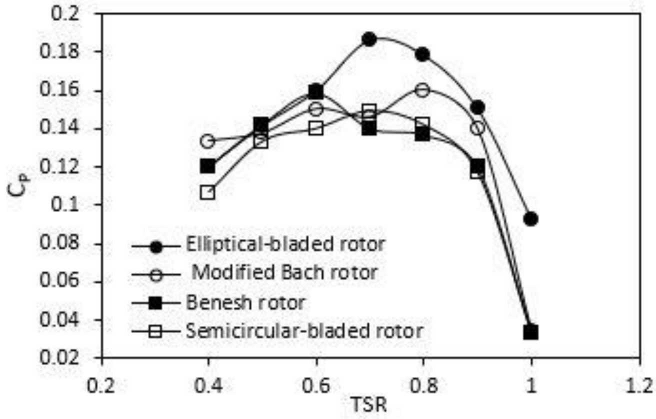

(b) C_p *vs TSR*

Figure 7.12: Performance coefficients obtained from wind tunnel experiments

The 2D unsteady results have been validated with the *WTT*s data (Fig.7.13). Nevertheless, the C_P is found to be higher in 2D unsteady results than the experimental results. This is because in 2D unsteady simulation, the effect of the third dimension is ignored, and several other losses involved in *WTT*s such as frictional losses between bearing and shaft, shaft and pulley, errors in measuring instruments are not considered. However, it can be observed that the 2D unsteady numerical and the experimental results show similar behavior of C_T and C_P (Fig. 7.13).

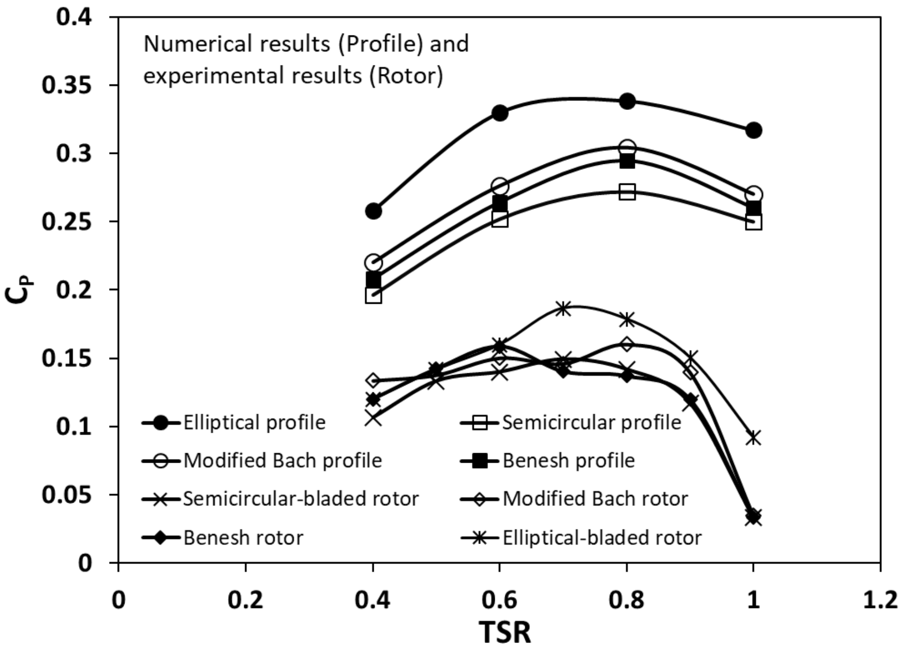

Figure 7.13: Comparison of numerical and experimental results

However, in practice, while presenting the experimental results, the blockage effect must be considered (Abraham *et al*., 2012; Plourde *et al*., 2012). The blockage correction factor (*f*) is mainly dependent on the category of wind tunnel test section and blockage ratio (*BR* = area of turbine model to the area of test section). The investigations related to blockage correction are generally carried out in closed type test sections (Biswas *et al*., 2007; Akwa *et al*., 2012; Roy and Saha, 2016; Chen and Liou, 2011). Though, the relationships used for a closed type test section is not suitable for an open type test section (Roy and Saha, 2015). Hence, Roy and Saha, (2016) have established new relationships for blockage corrections in the wind tunnel experiments of Savonius rotor in an open test section, where the blockage correction factor (*f*) is used to correct the measured parameters such as wind speed (*V*), mechanical load applied to the turbine (*F*), and rotational speed of the turbine (*N*). The obtained relationships are as follows (Roy and Saha, 2015):

$$V^* = V(1 - \frac{1}{5} f) \quad (7.6)$$

$$F^* = F(1 - f) \quad (7.7)$$

$$N^* = N(1 - f) \quad (7.8)$$

where V^*, F^*, and N^* are blockage corrected value.

The blockage correction factor is a function of the *TSR* and blockage ratio (*BR*). From the above relationships, suitable blockage correction factors of $f = 4$–9% are incorporated corresponding to various *TSR*s and *BR* of 21.16% (Roy and Saha, 2015). With the addition of blockage correction, the C_{pmax} for the semicircular, Benesh, modified Bach and elliptical-bladed rotors are found to be 0.146, 0.156, 0.156 and 0.185, respectively (Fig. 7.14).

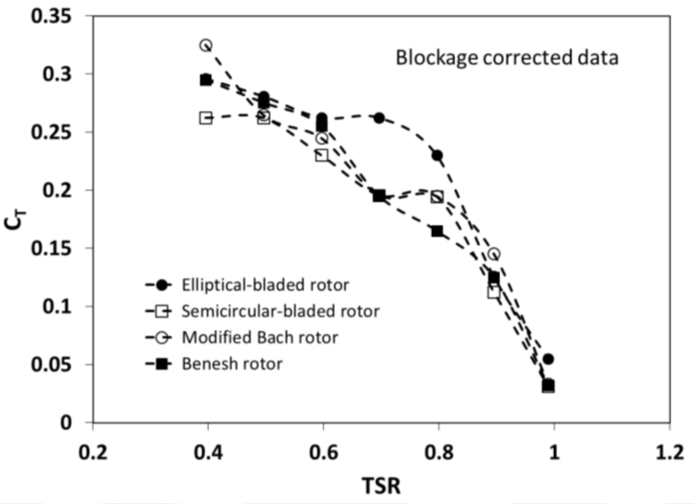

(a)* C_T vs *TSR

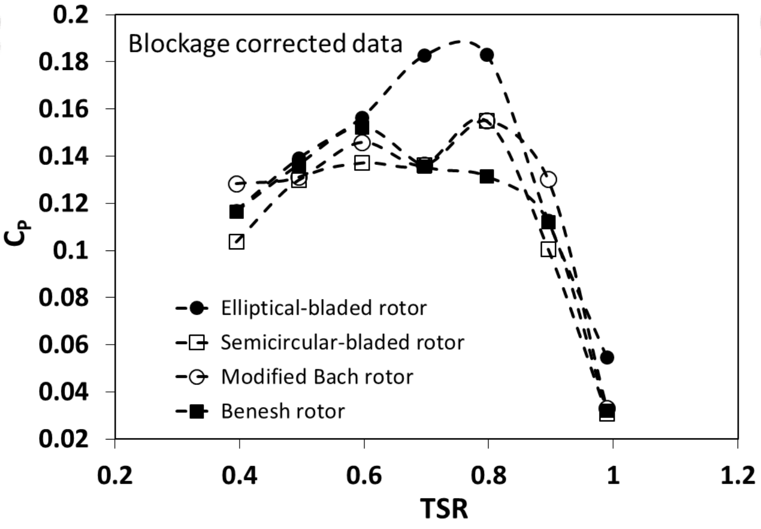

(b)* C_p vs *TSR

Figure 7.14: Blocakge corrected performance coefficients obtained from WTTs

7.7 Effect of Vent-augmentation Techniques

From the wind tunnel experiments without the blockage correction, the vented elliptical-bladed rotor shows a C_{pmax} = 0.15 at *TSR* = 0.5 and *AR* = 0.7, while the non-vented rotor shows C_{pmax}= 0.14 at the same *TSR.* The variation of C_T and C_P with *TSR* are shown in Figures 7.15 and 7.16. The experiments are also carried out for the conventional semicircular-bladed rotor to have a direct comparison and this reported a C_{pmax} of 0.12 at the same *AR* and *TSR*.

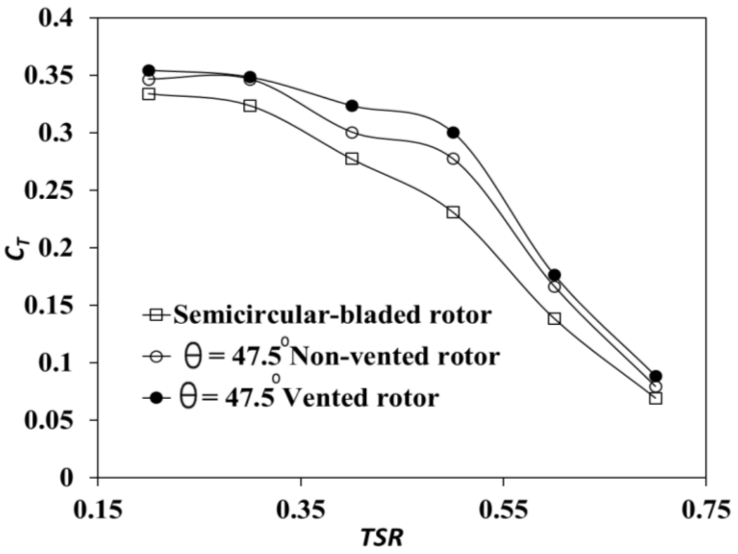

Figure 7.15: Variation of C_T with *TSR* for the tested rotors

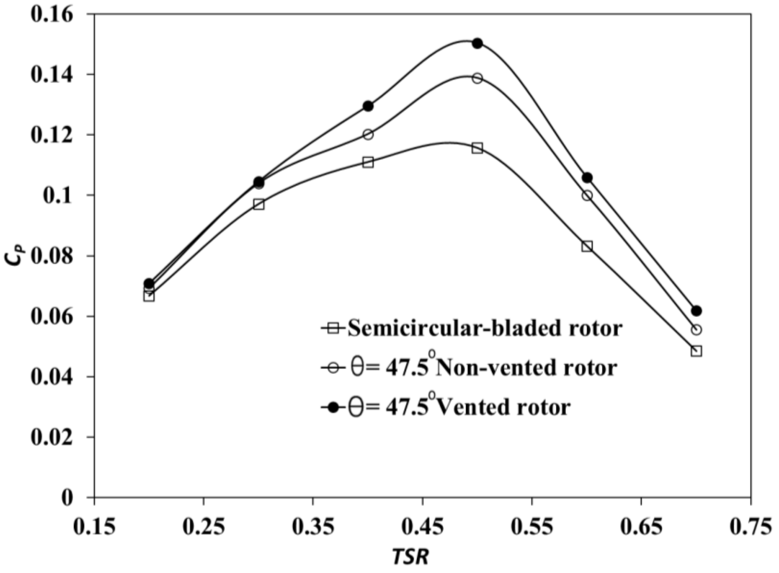

Figure 7.16: Variation of C_P with *TSR* for the tested rotors

With the inclusion of blockage correction, the vented elliptical-bladed rotor in the present investigation shows a C_{pmax} = 0.146 at *TSR* = 0.49, while the non-vented rotor shows C_{pmax} = 0.134 at the same *TSR.* These variations are shown in Figures 7.17 and 7.18. The conventional semicircular-bladed rotor shows a C_{pmax} of 0.115 at *TSR* = 0.49. Hence, there is a performance improvement of 9% in the vented elliptical-bladed rotor in comparison to the non-vented rotor.

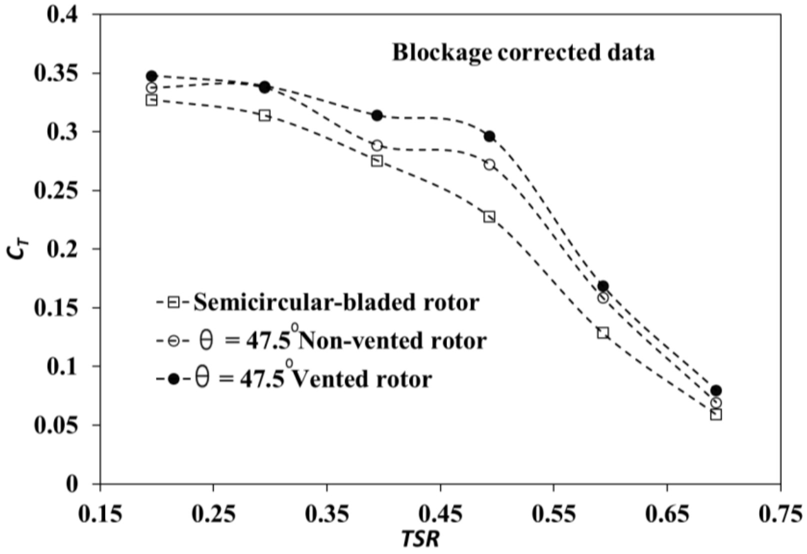

Figure 7.17: Blockage corrected C_T vs *TSR* of various tested rotor blades

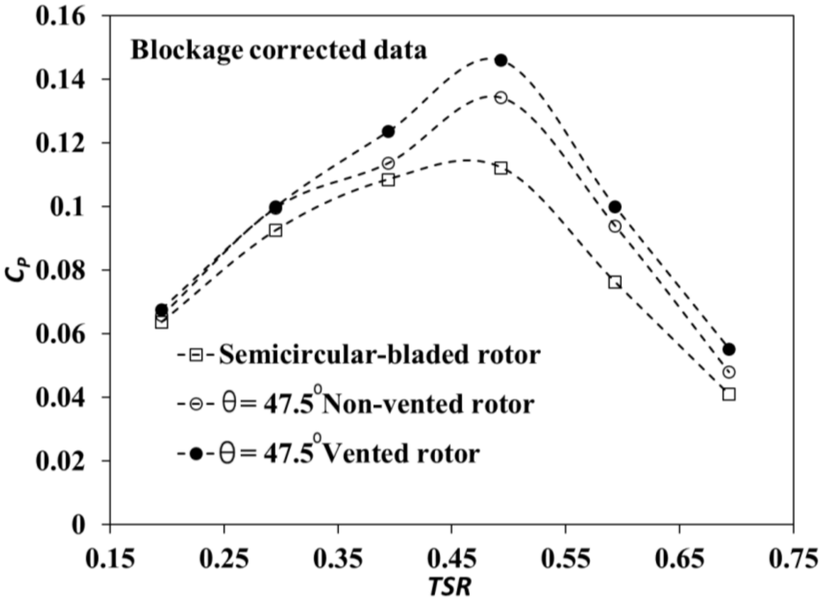

Figure 7.18: Blockage corrected C_P vs *TSR* of various tested rotor blades

7.8 Concluding Remarks

From the wind tunnel experiments, the peak C_P for the elliptical-bladed and semicircular-bladed rotors are found to be 0.19 and 0.15 at *TSR* = 0.7 and *AR* = 1.09; whereas the peak C_P for Benesh and modified Bach rotors are found to be 0.16 at *TSR* = 0.6 and 0.8, respectively.

Thus, the elliptical-bladed rotor shows an improvement of C_P by 27% as compared to the semicircular-bladed rotor at AR = 1.09. With the inclusion of blockage correction, the C_{pmax} is found to be 0.185 for elliptical-bladed rotor at AR = 1.09, while for the semicircular bladed rotor is found to be 0.146 at the same AR. The wind tunnel experiments are also conducted for the vented elliptical-bladed rotor. The results show that the C_{Pmax} for the vented and non-vented elliptical-bladed rotors to be 0.15 and 0.14 at AR = 0.7. The C_{pmax} for the conventional semicircular-bladed rotor is found to 0.12 at the same AR. In all the cases, the C_{pmax} is found be maximum at TSR = 0.5. Hence, there is a performance improvement of 7.2% in vented elliptical-bladed rotor than the non-vented rotor. Further, the vented elliptical-bladed rotor shows an improvement of 25% than the conventional semicircular-bladed rotor. Again, the non-vented elliptical-bladed rotor shows an improvement of 17% than the conventional semicircular-bladed rotor.

CHAPTER –8

Optimization Technique on Savonius Rotor

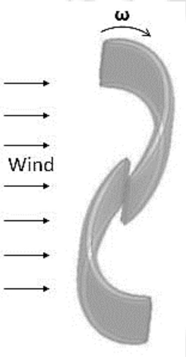

Chapter Outline

Overview

Optimization is a method for finding and identifying the best candidate from a group of substitutes without having to openly enumerate and assess all the possible alternatives. In the optimization process, one cycle of design process is realized in five stages such as generation, evaluation, selection, crossover and mutation. In the present investigation, the multi-objective genetic algorithm (MOGA) has been implemented in 2D the elliptical and semicircular profiles using ANSYS direct optimization technique. The MOGA is used to minimize the incoming velocity with the objective to maximize the C_T *and* C_L *and hence the* C_P *of the profile. From the MOGA, the minimum incoming velocity is found to be 5.91 at the maximum* $C_P = 0.35$ *in elliptical profile. Whereas, in case of semicircular profile, the minimum incoming velocity is found to be 6.06 m/s at the maximum* $C_P = 0.28$.

8.1 Introduction

Optimization is a technique for finding and recognizing the best contender from a group of alternatives, without having to openly count and evaluate all probable alternatives. In optimization process, one cycle of design process is realized in five stages. After the genetic algorithm (GA) takes as starting values the design variables and constants received from the user, it produces design parameters (genes) based on standard genetic procedure (generation, evaluation, selection, crossover, mutation). These produced genes are automatically transformed into geometric solid model inside the Design Modular and then they are meshed in the mechanical modular, according to the given criteria. Later, through ANSYS Fluent module, boundary conditions are implemented, and results are recorded in the file. The optimized results obtained from the genetic algorithm are compared with the results obtained from the 2D unsteady simulations at the identical conditions.

8.2 Multi-Objective Genetic Algorithm

The present multi-objective genetic algorithm (MOGA) is performed using direct optimization technique of ANSYS Design Modular. The MOGA is applied for 2D elliptical profile with the intention is to minimize the incoming velocity and to maximize the torque and lift coefficients (C_T and C_L). The details of the MOGA procedure and its various parameters are discussed in this section.

Number of Initial Samples: in general, the minimum recommended number of initial samples is 10 times the number of input parameters, larger the initial sample set, better the chances of finding the input parameter space that contains the best solutions. In the present MOGA optimization the number of initial samples have been taken as 100. However, it is evident that this number must be >1.

The maximum allowable pareto percentage is an important parameter in MOGA. A percentage which represents the ratio of the number of desired pareto points to samples per iteration. When this percentage is reached, the optimization is converged. In the present MOGA investigation the maximum allowable pareto percentage is chosen as 70%. Also, the convergence stability percentage is a percentage which characterizes the stability of the population, based on its mean and standard deviation. It allows to minimize the number of iterations performed while still reaching the desired level of stability. When this percentage is reached, the optimization is converged. In the present investigation the convergence stability percentage is chosen to be 2%.

Maximum Number of Iterations: the maximum possible number of iterations the algorithm executes. If this number is reached without the optimization having reached convergence, iteration will stop. This also provides an idea of the maximum possible number of function evaluations that are needed for the full cycle, as well as the maximum possible time it may take to run the optimization. In the present MOGA, the maximum number of iterations is taken as 20 (ANSYS Inc, 2015). The convergence criteria for the MOGA is shown in Figure 8.1.

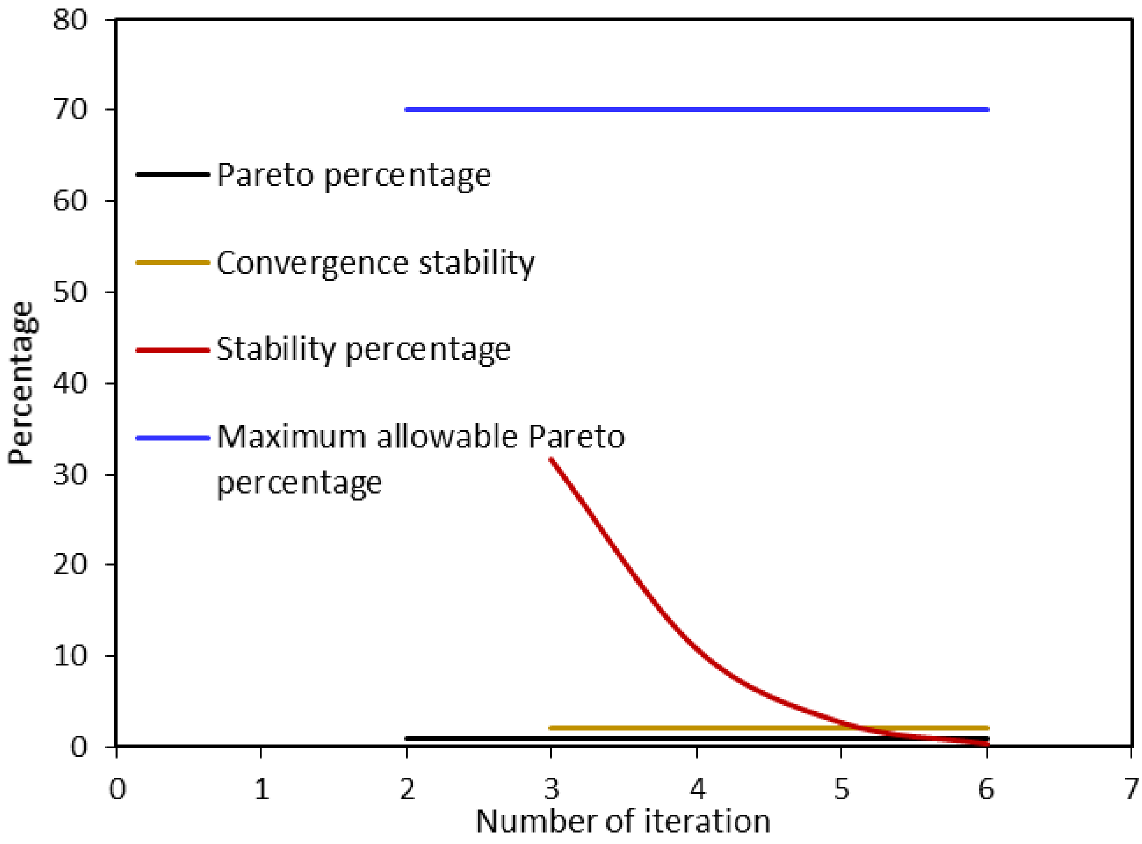

Figure 8.1: Convergence criteria of the multi-objective genetic algorithm

Mutation Probability: It permit to specify the probability of applying a mutation on a design configuration. The value must be from 0 and 1. A larger value specifies a more random algorithm; if the value is 1, the algorithm develops a pure random search. Generally, a low probability of mutation (<0.2) is suggested. However, in the present MOGA mutation probability is chosen to be 0.01.

Crossover Probability: It is the probability by which parent solutions are recombined to produce the offspring solutions. Crossover probability must be between 0 and 1. A lesser value specifies a more stable population and a faster (but less accurate) solution; if the value is 0, then the parents are copied straight to the new population. In the present MOGA the crossover probability is chosen to be 0.98.

The flow chart of the various steps performed during a MOGA is shown in Figure 8.2.

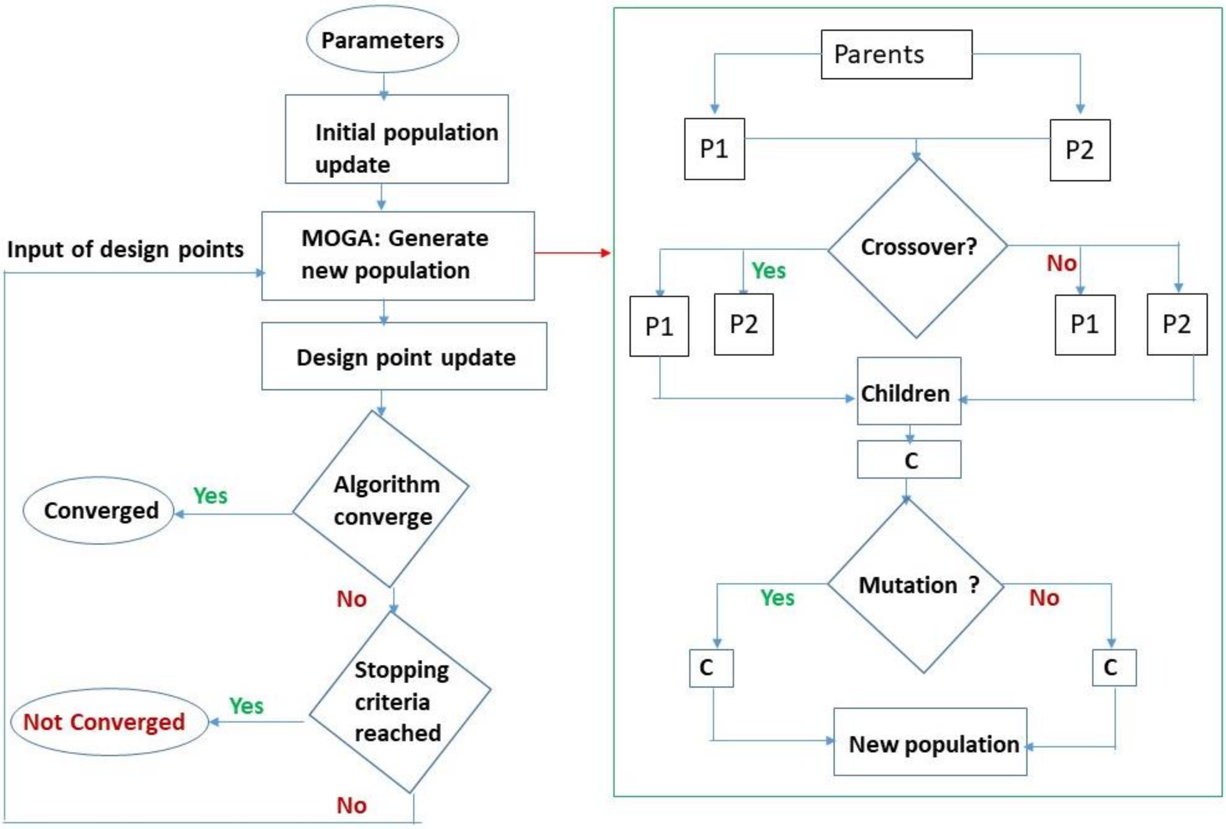

Figure 8.2. Flow chart for the multi objective genetic algorithm (ANSYS Inc, 2015)

8.3 Analysis of the Outcomes of MOGA

The genetic algorithm is an optimization tool that mimics natural selection and genetics. In the present investigation, multi-objective genetic algorithm (MOGA) has been carried out with the objective is to minimize the incoming velocity and to maximize the torque and lift coefficients of the elliptical and semicircular profiles for the given incoming velocity of 6.2 m/s. The genetic algorithm has been performed using ANSYS 17.1 direct optimization technique for the 2D geometric model of elliptical and semicircular profiles. The results obtained from the MOGA is shown in Figs 8.3 through 8.8. From Figs 8.3 through 8.5 shows that the initially there is a fluctuation in the C_T, velocity and C_L of the rotor, however, when the number iterations are reached to 300, the C_T, velocity and C_L is become almost steady state for the elliptical profile. In case of semicircular profile, the C_T become almost steady state when the number of iterations is reached to 400. From the MOGA, at TSR = 0.80, the elliptical profile shows that the C_P = 0.35 at V = 5.91 m/s. For the semicircular profile, the C_P = 0.28 at V = 6.06 m/s. However, from the unsteady numerical simulation for the elliptical profile, the C_P = 0.34 at V= 6.2 m/s and for the semicircular profile C_P = 0.27 at V = 6.2 m/s. The average C_L for the elliptical and semicircular profiles is found to be 0.89 and 0.93. However, from the 2D unsteady simulation the average C_L for the elliptical and semicircular profiles is found to be 0.95 and 0.96, respectively. The comparison of various results obtained from the MOGA and 2D unsteady simulations are shown Table 8.1.

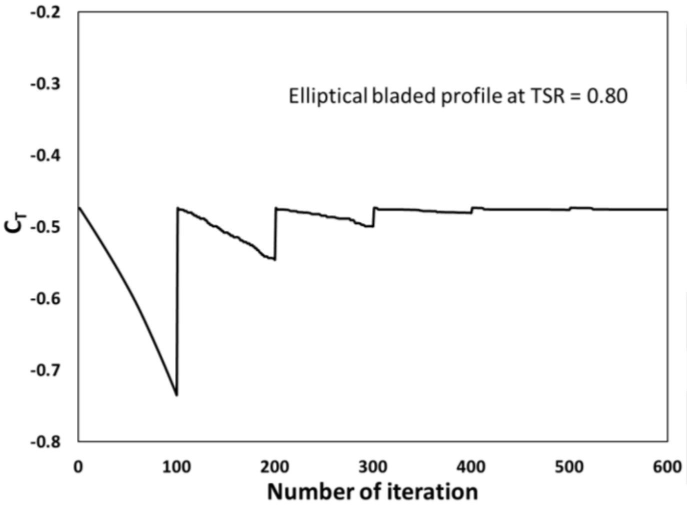

Figure 8.3: C_T vs number of iterations of the elliptical profile

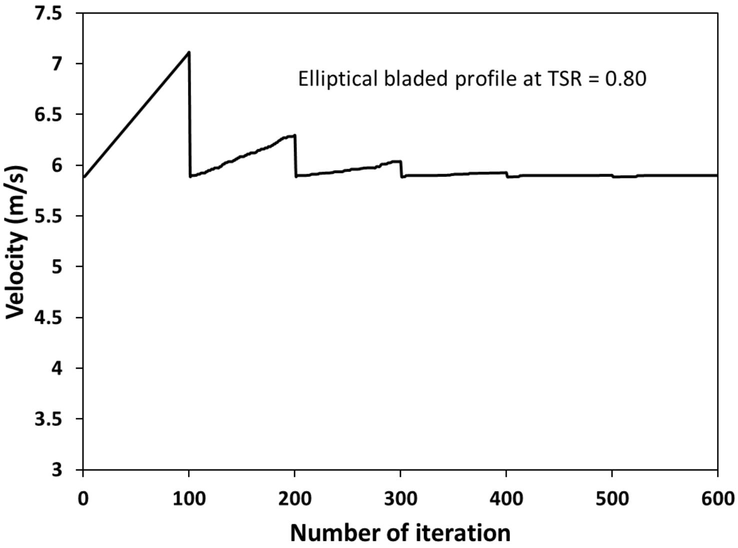

Figure 8.4: Velocity (m/s) vs number of iterations of the elliptical profile

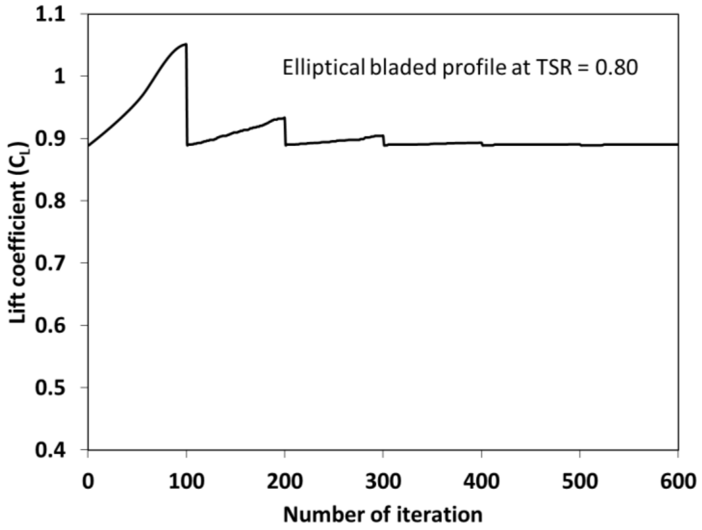

Figure 8.5: C_L vs number of iterations of the elliptical profile

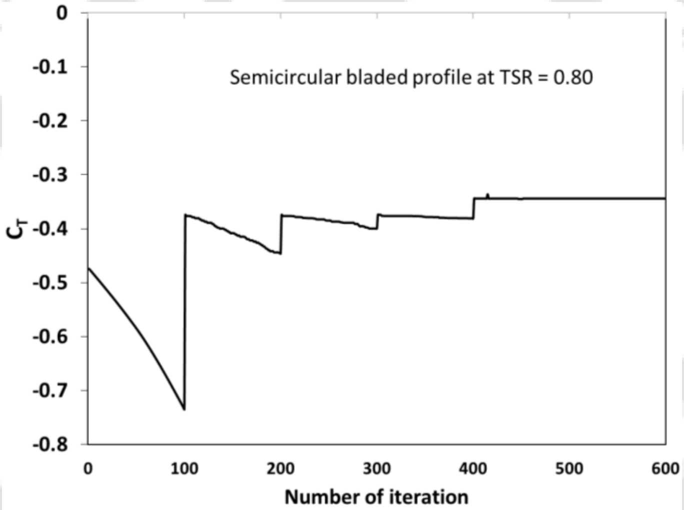

Figure 8.6: C_T vs number of iterations of the semicircular profile

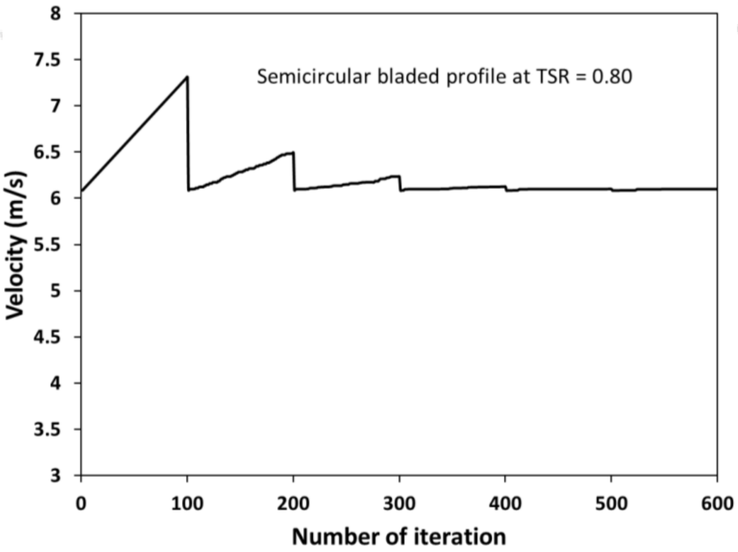

Figure 8.7: Velocity (m/s) vs number of iterations of the semicircular profile

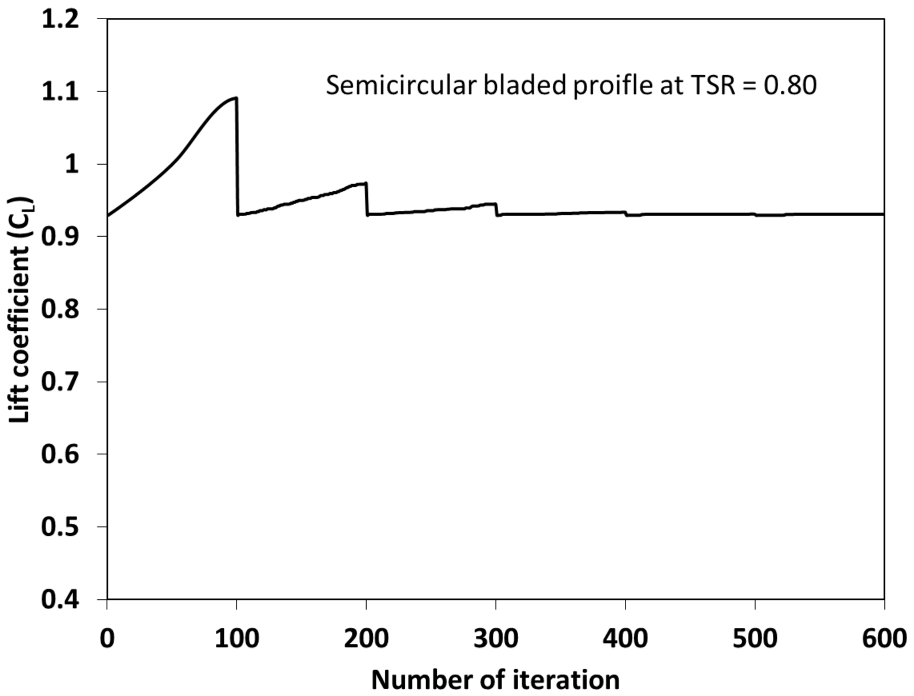

Figure 8.8: C_L vs number of iterations of the semicircular profile

Table 8.1: Performance comparison of MOGA and 2D unsteady simulations

	Velocity (m/s)	C_{Pmax}	C_{Lavg}	Velocity (m/s)	C_{Pmax}	C_{Lavg}
Profile	MOGA			2D unsteady simulations		
Elliptical	5.91	0.35	0.89	6.2	0.34	0.95
Semicircular	6.06	0.28	0.93	6.2	0.27	0.96

8.4 Concluding Remarks

The multi-objective genetic algorithm has been performed using ANSYS 17.1 direct optimization module. From the MOGA, at TSR = 0.80, the elliptical profile shows that the C_{Pmax} = 0.35 at V = 5.91 m/s. For the semicircular profile, the C_{Pmax} = 0.28 at V = 6.06 m/s. However, from the unsteady numerical simulation for the elliptical profile, the C_{Pmax} = 0.34 at V = 6.2 m/s and for the semicircular profile C_{Pmax} = 0.27 at V = 6.2 m/s. The average C_L for the elliptical and semicircular profiles is found to be 0.89 and 0.93. However, from the 2D unsteady simulation the average C_{Lavg} for the elliptical and semicircular profiles is found to be 0.95 and 0.96, respectively. Hence, the elliptical profile is found to be superior over the semicircular profile.

CHAPTER –9

Conclusions and Future Scope

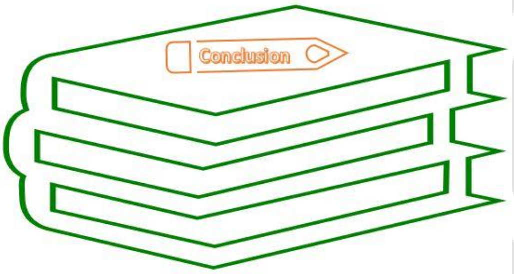

Chapter Outline

Overview

In the present investigation, an effort has been made to improve the aerodynamic performances of the drag-based Savonius rotor. Also, the flow behavior around the various profiles/rotors has been investigated. In this context, a series of 2D and 3D unsteady simulations as well as wind tunnel experiments are conducted. Furthermore, the vent-augmentation technique is also used with the newly developed elliptical profile. Finally, MOGA is implemented and investigated in 2D elliptical and semicircular profile. At the end, the application potential and the future scope of the present work are highlighted.

9.1 Contribution of the Present Work

The Savonius rotor, a class of vertical axis wind turbine can be a viable option for small-scale, low-cost off-grid energy conversion in certain cases of confined space and low wind speed region, where the other wind turbines cannot work efficiently. However, the existing design of rotor is yet a matter of research to make it more useful in such situations. In this context, the present study attempts to improve the performance of Savonius rotor by evolving a new elliptical-blade shape through a series of unsteady simulations and wind tunnel experiments.

To begin with, 2D unsteady simulations are carried out with using SST k-ω turbulence model to optimize the rotor blade profile. This analysis is followed by a series of 2D unsteady simulations on elliptical blade profile to optimize the overlap ratio, number of blade profile, effect of shaft and Reynolds number. Subsequently, 2D unsteady simulations are also carried out to investigate the lift and drag characteristic of various blade profile. Finally, 2D simulations are conducted for the vent augmented elliptical profile.

A new elliptical blade profile has been evolved through a series of unsteady simulations by varying the sectional cut angle of an ellipse. 3D unsteady simulations are carried out for elliptical profile to find its C_P and C_T. 3D unsteady simulations are also conducted to investigate the drag and lift characteristics of elliptical-bladed rotor. Finally, Wind tunnel tests are conducted on the newly developed elliptical-bladed rotor followed by its comparative analysis with the semicircular bladed rotor.

Although, 2D calculations are not good enough, these can only be useful for rapid comparison, evaluations and estimations of different blade shapes, geometric and aerodynamic parameters. The elliptical rotor blades (with and without vents) show a clearly improved performance (25% and 17%) over semicircular blades. Thus, the vent augmentation technique can be recommended because of its simpler design, easier manufacturing effort and lesser cost. As stated earlier, the 3D unsteady results are under predicted since the third dimension (height of the rotor) of the rotor is assumed to be infinite in 2D unsteady simulations. Furthermore, in 3D simulations, the tip vortices can induce a complex 3D vortex flow thereby reducing the overall C_D and C_L in comparison to the 2D simulation results. Apart from this, owing to various losses occurred in experimentation (such as frictions between the bearings, instrumental error and others) the C_P is likely to be lesser than the numerical results. The MOGA can be a useful tool to investigate the various geometric and aerodynamic parameters for the elliptical-bladed rotor.

The key findings of the present investigation are summarized in the subsequent sections.

9.1.1 2D unsteady simulations

A series of 2D unsteady simulations are carried out to study the performance and flow characteristics of various profiles. The influence of overlap ratio on the performance, the effect of number of rotor blade, influence of shaft, analysis of drag and lift, and effect of vents are studied for $V = 6.2$ *m/s.* The results are summarized in the following key points:

- ✓ The elliptical-profile shows a peak C_P of 0.34 at *TSR* = 0.8; whereas the semicircular, Benesh and modified Bach profiles show a peak C_P of 0.27, 0.29 and 0.30, respectively at the same *TSR.*
- ✓ During the complete cycle of Savonius rotor, various types of flow phenomena such as free stream flow, Coanda type flow, returning flow, stagnation, separation, and vortices formation are observed.
- ✓ Among the investigated overlap ratios (*OR* = 0.0 to 0.30), the maximum C_P was found at *OR*=0.15
- ✓ The maximum C_P is observed in case of 2-bladed system. The vortices formed behind the returning blades of 3-and 4-bladed systems reduced the rotor performance due to the generation of negative torque.

- ✓ From the 2D unsteady simulations, the C_{Dmax} for elliptical-profile is found to be 2.43 at α = 84° and 266° respectively; however, for the semicircular profile, C_{Dmax} is 2.07 corresponding α =91° and 270°. Hence, there is an improvement in C_{Dmax} of 17.4% in elliptical profile than the semicircular profile. It is also predicted that the C_{Lmax} is 2.05 and 1.96 at α = 23° and 210°, respectively for the elliptical profile; while C_{Lmax} is 1.85 and 1.84 in semicircular profile at α = 23° and 203°. Hence, there is 10.8% and 6.5% higher C_{Lmax} in the elliptical profile than the semicircular profile.

- ✓ The average C_D of modified Bach, Benesh and semicircular profiles are found to be 1.41, 1.25 and 1.35, respectively. Hence, in modified Bach profile, there is an improvement of C_D by 4.5% than the semicircular profiles. However, in case of C_L, the modified Bach profile has shown inferior values as compared to the others. The C_{Lavg} are found to be 0.95, 1.32, 0.96 for the modified Bach, Benesh, and semicircular profiles, respectively.

- ✓ From the unsteady simulations, the vented elliptical profile with $\theta = 47.5^0$ shows a C_{Pmax} of 0.35, whereas the non-vented elliptical and semicircular profiles indicate the highest C_{Pmax} of 0.34 and 0.27, respectively. The peak performance for all the cases is obtained at $TSR = 0.8$. Thus, a performance gain of 30% is obtained with the vented elliptical profile over the semicircular one.

- ✓ The low-pressure zone is also observed at the convex side of the advancing profile that helps in creating the pressure difference leading to the rotation of rotor. It is observed that such pressure difference is higher in the elliptical profile than the semicircular profile. This results a higher C_D in the elliptical profile, and consequently, a higher C_P.

9.1.2 3D unsteady simulations

The 3D unsteady simulations are carried out on the vented and non-vented elliptical-bladed Savonius rotor to estimate its performance parameters. The results obtained are compared to the semicircular bladed rotor at the identical conditions. The 3D unsteady simulations are also conducted to investigate the lift and drag characteristic of elliptical and semicircular bladed rotor.

- ✓ From the 3D, unsteady simulation at a wind speed of $V = 6.2$ m/s, the aspect ratio of the elliptical-bladed rotor is maintained at $AR = 0.7$. The vented rotor shows a $C_{pmax} = 0.14$ at $TSR = 0.8$, while the non-vented rotor shows $C_{pmax} = 0.13$ at the same *TSR.*

- ✓ An improved velocity region at the downstream of the blades is obtained for non-vented elliptical-bladed rotor than semicircular bladed rotor. Also, the unsteady flow analysis indicates a better velocity field with a lesser chance of flow separation for the elliptical blades.

- ✓ The Coanda effect, and hence, the increased contribution of the lift force on elliptical-bladed rotor is expected to increase the power output of the turbine.

- ✓ The adverse effect of pressure on the returning blade is prominent on the semicircular bladed rotor. However, it is much lesser in case of elliptical-bladed rotor.

- ✓ The average C_D is found to be 1.31 and 1.26 for the elliptical and the semicircular bladed rotor, respectively. The C_{Dmax} is found to be 2.19 and 2.19 at α =70° and 249°, respectively for the elliptical-bladed rotor, while, for the semicircular-bladed rotor, the C_{Dmax} is found to be 1.83 and 1.85 at α = 64° and 244°. The average C_L is found to be 0.48 and 0.55 for the elliptical and the semicircular bladed rotor, respectively. The C_{Lmax} for the elliptical-bladed rotor is found to be 1.46 and 1.43 at α = 32° and 211° respectively, and for the semicircular bladed rotor is 1.27 and 1.24 at same α.

- ✓ It is found that the vortices formed behind the returning semicircular-bladed rotor reduces its average C_D and as a result the C_T and C_P are found lesser as compared to the elliptical-bladed rotor. It is also observed that the tip losses are lesser in elliptical-bladed rotor than the semicircular-bladed rotor. This make the elliptical-bladed rotor to have higher C_D than the semicircular-bladed rotor.

9.1.3 Experimental investigations

Wind tunnel experiments are conducted on the non-vented and elliptical-bladed rotors. The tests are also conducted for semicircular bladed to have a direct comparison. The experiments are conducted to validate the obtained numerical results.

- ✓ Wind tunnel experiments are conducted for newly developed elliptical, modified Bach, Benesh and semicircular bladed AR = 1.09 to investigate blades and peak C_P is found in newly developed elliptical-bladed rotor than the other rotor blades.

- ✓ The wind tunnel tests show the peak C_P of 0.19 and 0.15 for elliptical-bladed and semicircular-bladed rotors, respectively at TSR = 0.7 and AR = 1.09, while the peak C_P for Benesh and modified Bach is found to be 0.16 at TSR = 0.6 and 0.8, respectively. Hence, there is an improvement of C_P by 27% in elliptical-bladed rotor than the semicircular-bladed rotor.

- ✓ From the wind tunnel experiments without the blockage correction, the vented elliptical-bladed rotor shows a C_{pmax} = 0.15 at *TSR* = 0.5, while the non-vented rotor shows C_{pmax}= 0.14 at the same *TSR.* The experiments are also carried out for the conventional semicircular-bladed rotor to have a direct comparison and this reported a C_{pmax} of 0.12 at *TSR* = 0.5.

- ✓ Considering the blockage correction factor, the wind tunnel experiments show C_{pmax} for the vented and non-vented elliptical-bladed rotors to be 0.146 and 0.134 at *AR* = 0.7. The C_{pmax} for the conventional semicircular-bladed rotor is found to 0.115. In all the cases, the C_{pmax} is found at *TSR* = 0.49.

- ✓ Hence, there is a performance improvement of 7.2% in vented elliptical-bladed rotor than the non-vented rotor. Further, the vented elliptical-bladed rotor shows an improvement of 25% than the conventional semicircular-bladed rotor. Again, the non-vented elliptical-bladed rotor shows an improvement of 17% over the conventional semicircular-bladed rotor.

9.1.4 MOGA findings

- ✓ The MOGA has been performed using ANSYS multi-physics solver with direct optimization technique. From the MOGA, the optimum velocity has been found to be 5.91 m/s and 6.06 for the elliptical and semicircular profiles, respectively.

- ✓ From the MOGA, the C_L for the elliptical and semicircular profiles are found to be 0.89 and 0.93, respectively.

9.2 Application Potential

The Savonius rotor is very simple in design, hence it can effortlessly be fabricated and maintained at a low cost. The cut-in speed for this rotor is also quite low. The Savonius rotor is generally insensitive to the wind flow directions, and therefore, are quite suitable for the specific locations of flexible wind directions. Furthermore, the vertical rotational axis allows them to be positioned in multiple numbers in a confined space. These rotors when provided with an energy storage system can be a quite beneficial at the top of buildings or communication towers or at hilly locations for distributed small-scale electricity production.

The Savonius rotors are also used in pumping water in irrigation. For these purposes the vent-augmented elliptical profile can be used as it has lesser complexity to design. Recently, a combination of drag-based Savonius rotor and lift-based Darrieus rotor has been suggested to improve the starting characteristics of Savonius rotor (Roy, 2014).

9.3 Scopes for Future Work

- ✓ Several augmentation techniques such as deflector, curtains, conveyor-deflector and nozzle can be implemented in the newly developed elliptical profile to improve its performance further. Thus, a simulation study followed by wind tunnel experiments can be carried out for the newly developed elliptical-bladed rotor with various augmentation techniques.

- ✓ Throughout the wind tunnel tests, it has been observed that at a wind speed below 3 m/s, the self-starting ability is lesser. Thus, an investigation can be performed on the newly developed elliptical-bladed rotor with light blade materials to make it more beneficial at quite low wind speeds.

- ✓ The lift based Darrieus-rotors have a reasonably higher performance due to their low solidity factor and high influence of lift forces. Nevertheless, their starting capability is much inferior to that of Savonius rotor. The newly developed elliptical-bladed profile can also be a useful device for a combined Savonius-Darrieus rotor.

- ✓ In the present numerical investigation unstructured grids were used to perform the simulations. The structured grids can also be studied further to have a more accurate analysis of the flow behavior around the newly developed elliptical-bladed profile.

- ✓ RANS modelling is known to be inaccurate in complex flow situations and this approach is gradually being replaced with advanced turbulence modelling approaches such as large eddy simulation (LES) and direct numerical simulation (DNS). These modelling could be used for the Savonius rotor for better accuracy.

- ✓ In the present analysis, multi-objective genetic algorithm has been used in ANSYS. Some other optimization techniques could be used to optimize the various parameters of the elliptical-bladed Savonius rotor.

REFERENCES

Abraham, J. P., Plourde, B. D., Mowry, G. S., Minkowycz, W. J., and **Sparrow, E. M**., 2012. Summary of Savonius wind turbine development and future applications for small-scale power generation. Journal of Renewable and Sustainable Energy, 4, pp. 042703-1-042703-21

Akwa, J. V., Alves Da Silva Junior, G., and **Petry, A. P.,** 2012. Discussion on the verification of the overlap ratio influence on performance coefficients of a Savonius wind rotor using computational fluid dynamics. Renewable Energy, 38, pp. 141–149.

Akwa, J. V., Vielmo, H. A., and **Petry, A. P.,** 2012. A review on the performance of Savonius wind turbines. Renewable Sustainable Energy Reviews, 16, pp. 3054–3064.

Alexander, A. J., and **Holownia, B. P**., 1978. Wind tunnel tests on a Savonius rotor. Journal of Industrial Aerodynamics, 3, pp. 343–351.

Alaimo, A., Esposito, A., Milazzo, A., Orlando, C., and **Trentacosti, F.**, 2013. Slotted blades Savonius wind turbine analysis by CFD. Energies , 6, pp. 6335-6351

Alakashi, A. M., and **Basuno, I. B.**, 2014. Comparison between structured and unstructured grid generation on two dimensional flows based on Finite Volume Method (FVM). International Journal of Mining, Metallurgy & Mechanical Engineering (IJMMME), vol. 2, Issue 2, pp. 97–103.

Aldoss, T., 1984. Savonius rotor using swinging blades as an augmentation system. Wind Engineering. 8, pp. 214–220.

Aldoss T., and **Najjar, Y**., 1985. Further development of the swinging-blade Savonius rotor. Wind Engineering. 9, pp. 165–170.

Alom, N., Kolaprathi, S. C., Gadde, S. C., and **Saha, U. K**., 2016. Aerodynamic design optimization of elliptical-bladed Savonius-style wind turbine by numerical simulations. Paper No. OMAE2016-55095, ASME 35th International Conference on Ocean, Offshore and Arctic Engineering, June 19–24, Busan, South Korea.

Altan, B. D., and **Atilgan, M**., 2010. The use of a curtain design to increase the performance level of a Savonius wind rotors. Renewable Energy, 35, pp. 821–829.

Altan, B. D., and **Atilgan, M.**, 2008. An experimental and numerical study on the improvement of the performance of Savonius wind rotor. Energy Conversion and Management, 49, pp. 3425–3432.

Amano, R. S., 2017. Review of wind turbine research in 21st century. ASME Journal of Solar Energy Engineering, 139(5), pp. 50801.

ANSYS Inc, 2009. ANSYS Fluent Theory Guide 12.0.

ANSYS Inc, 2015. ANSYS Fluent Theory Guide 12.0.

Banerjee, A., Roy, S., Mukherjee, P., and **Saha, U. K**., 2014. Unsteady flow analysis around an elliptic-bladed Savonius-style wind turbine. Paper No. GTINDIA2014-8141, ASME 2014 Gas Turbine India Conference, December 15-17, New Delhi, India

Benesh, A. H., 1988. Wind turbine system using a vertical axis Savonius type rotor. in U.S. patent US5494407 A (November 15).

Benesh, A. H., 1989. Wind turbine system using a Savonius type rotor. U.S. patent 4838757 (July 10).

Benesh, A. H., 1992. The Benesh wind turbine. in Eleventh ASME Wind Energy Symposium.

Bach, G., 1931. Untersuchungen uber Savonius-Rotoren und verwandte Stromungsmaschinen. Forsch. Geb. Ingenieurwes. 2(6), pp. 218–231.

CEA Report, 2018. http://www.cea.nic.in/reports/monthly/installedcapacity/2018/installed capacity-02.pdf.

Chauvin, A. and **Benghrib, D**., 1989. Drag and lift coefficients evolution of a Savonius rotor. Experiments in Fluids; 8(1-2), pp. 118-20.

Chan, C. M., Bai, H. L., and **He, D. Q.**, 2018. Blade shape optimization of the Savonius wind turbine using a genetic algorithm. Applied Energy, 213, pp. 148–157

Chong, W. T., Pan, K. C., Poh, S. C., Fazlizan, A., Oon, C. S., Badarudin, A., and **Nik-ghazali, N.**, 2013. Performance investigation of a power augmented vertical axis wind turbine for urban high-rise application. Renewable Energy, 51, pp. 388–397.

D'Alessandro, V., Montelpare, S., Ricci, R., and **Secchiaroli, A**., 2010. Unsteady aerodynamics of a Savonius wind rotor: A new computational approach for the simulation of energy performance. Energy, 35, pp. 3349–3363.

Damak, A., Driss, Z., and **Abid, M. S.,** 2013. Experimental investigation of helical Savonius rotor with a twist of 180^0. Renewable Energy, 52, pp. 136–142.

Damak, A., Driss, Z., and **Abid, M. S**., 2018, "Optimization of the helical Savonius rotor through wind tunnel experiments," Journal of Wind Engineering & Industrial Aerodynamics, 174 (December 2017), pp. 80–93.

Driss, Z., Mlayeh, O., Driss, D., Maaloul, M., and **Abid, M. S**., 2014. Numerical simulation and experimental validation of the turbulent flow around a small incurved Savonius wind rotor. Energy, 74, pp. 506–517.

Dobrev, I., and **Massouh, F**., 2011. CFD and PIV investigation of unsteady flow through Savonius wind turbine. Energy Procedia, 6, pp. 711–720.

Ducoin, A., Shadloo, M. S., and **Roy, S.**, 2017. Direct numerical simulation of flow instabilities over Savonius style wind turbine blades. Renewable Energy, 105, pp. 374–385.

El-Askary, W. A., Nasef, M. H., AbdEL-hamid, A. A., and **Gad, H. E**., 2015. Harvesting wind energy for improving performance of Savonius rotor. Journal of Wind Engineering & Industrial Aerodynamics, 139, pp. 8–15.

Emmanuel, B., and **Jun, W**., 2011. Numerical study of a six-bladed Savonius wind turbine. ASME Journal of Solar Energy Engineering, 133, pp. 44503.

Faizal, M, Ahmed, M. R., and **Lee, Y. H**. 2010. On utilizing the orbital motion in water waves to drive a Savonius rotor. Renewable Energy, 35, pp.164–169

Frikha, S., Driss, Z., Ayadi, E., Masmoudi, Z., and **Abid, M. S**., 2016. Numerical and experimental characterization of multi-stage Savonius rotors. Energy 114, pp. 382–404.

Fujisawa, N., 1996. Velocity measurements and numerical calculations of flow fields in and around Savonius rotors. Journal of Wind Engineering & Industrial Aerodynamics ,59, pp. 39–50.

Fujisawa, N., 1992. On the torque mechanism of Savonius rotors. Journal of Wind Engineering & Industrial Aerodynamics, 40, pp. 277–292.

Fujisawa, N., and **Gotoh, F**., 1994. Experimental study on the aerodynamic performance of a Savonius rotor. ASME Journal Solar Energy Engineering, 116, pp. 148–152.

Fujisawa, N., Ishimatsu, K., and **Kage, K.**, 1995. A comparative study of Navier-Stokes calculations and experiments for the Savonius rotor. ASME Journal Solar Energy Engineering 117, pp. 344.

Gareth, C., and **Mishra, R.,** 2011. Computational flow field analysis of a Vertical Axis Wind Turbine. In: International Conference on Renewable Energies and Power Quality (ICREPQ'11), April 13-15, Las Palmas de Gran Canaria, Spain.

Golecha, K., Eldho, T. I., and **Prabhu, S. V.**, 2011. Influence of the deflector plate on the performance of modified Savonius water turbine. Appled Energy, 88, pp. 3207–3217.

Grinspan, A. S., 2002. Development of a low speed wind tunnel and testing of Savonius wind turbine rotor with twisted blades. M. Tech Thesis, Department of Mechanical Engineering, IIT Guwahati, India.

Grinspan, A. S., Saha, U. K., and **Mahanta, P.**, 2004. Experimental investigation of twisted bladed savonius wind turbine rotor. RERIC International Energy Journal, 5, pp. 1–9

Gupta, A. K., 2015. Efficient wind energy conversion: Evolution to modern design. ASME Journal of Energy Resourse Technology, 137, pp. 51201.

Gupta, R., Biswas, A., and **Sharma, K. K.,** 2008. Comparative study of a three-bucket Savonius rotor with a combined three-bucket Savonius-three-bladed Darrieus rotor. Renewable Energy, 33, pp. 1974–1981.

Gerardo, G., and **Molfino, R.**, 2014.From Savonius to Bronzinus: a comparison among vertical wind turbines. Energy Procedia, 50, pp. 10–18.

Global Wind Energy Outlook 2016, GWEC.

Hayashi, T., Li, Y., and **Hara, Y.,** 2005. Wind tunnel tests on a different phase three-stage Savonius rotor. JSME International Journal, Ser. B 48, pp. 9–16.

Howell, R., Qin, N., Edwards, J., and **Durrani, N.,** 2010. Wind tunnel and numerical study of a small vertical axis wind turbine. Renewable Energy, 35, pp. 412–422.

H**olman, J. P**., 2004. Experimental Methods for Engineers. Tata McGraw Hill, New Delhi, India.

Huda, M. D., Selim, M. A., Sadrul, Islam, A. K. M., and **Islam, M. Q**., 1992. The performance of an S-shaped Savonius rotor with a deflecting plate. RERIC International Energy Journal. 14(1), pp. 25-32

Hu, Y., Tong, Z., and **Wang, S.**, 2009. A new type of VAWT and blade optimization. Int. Technol. Innov. Conf. 2009 (ITIC 2009), pp. 14–14.

Irabu, K., and **Roy, J. N.,** 2011. Study of direct force measurement and characteristics on blades of Savonius rotor at static state. Experimental Thermal and Fluid Science, 35, pp. 653–659

Irabu, K., and **Roy, J. N**., 2007. Characteristics of wind power on Savonius rotor using a guide-box tunnel. Experimental Thermal and Fluid Science, 32, pp. 580–586.

Jian, C., Kumbernuss, J., Linhua, Z., Lin, L., and **Hongxing, Y**., 2012. Influence of phase-shift and overlap ratio on Savonius wind turbine’s performance. ASME Journal of Solar Energy Engineering, 134, pp. 11016.

Jaohindy, P., McTavish, S., Garde, F. and **Bastide, A.,** 2013. An analysis of the transient forces acting on Savonius rotors with different aspect ratios. Renewable Energy, 55, pp. 286-295.

Jeon, K. S., Jeong, J. I., Pan, J. K., and **Ryu, K. W**., 2015. Effects of end plates with various shapes and sizes on helical Savonius wind turbines. Renewable Energy, 79, pp. 167-176.

Kacprzak, K., Liskiewicz, G., and **Sobczak, K.**, 2013. Numerical investigation of conventional and modified Savonius wind turbines. Renewable Energy, 60, pp. 578–585.

Kamoji, M. A., Kedare, S. B., and **Prabhu, S. V**., 2009. Performance tests on helical Savonius rotors. Renewable Energy, 34, pp. 521–529.

Khan, J. R., Bashar, M. M., Rahman, M., Bashar, M. M., Rahman, M., and **Khan, J**., 2013. Computational studies on the flow field of various shapes-bladed vertical axis Savonius turbine in static condition. Paper No. IMECE2013-65081, ASME International Mechanical Engineering Congress and Exposition, November 5-9, San Diego, CA, USA

Kianifar, A., Anbarsooz, M., and **Javadi, M.,** 2010. Blade curve influences on performance of Savonius rotors: Experimental and numerical, Paper No. FEDSM-ICNMM2010-30919, ASME 3rd Joint US-European Fluids Engineering Summer Meeting, August 1-5, Montreal, Canada.

Kline, S. J., 1985. The purposes of uncertainty analysis. ASME Journal of Fluids Engineering, 107(2), pp. 153-160.

Karthikeyan, T., Samad, A., and **Badhurshah, R**., 2013. Review of air turbines for wave energy conversion, International Conference on Renewable Energy and Sustainable Energy, December 5-6, Coimbatore, India.

Le, T-Q, Lee, K-S., Park, J-S., and **Ko, J-H**. 2014. Flow-driven rotor simulation of vertical axis tidal turbines: A comparison of helical and straight blades, International Journal of Naval Architecture and Ocean Engineering, 6:257-268.

Lee, S., 1997. Unsteady aerodynamic force prediction on a square cylinder using k-ε turbulence models. Journal of Wind Engineering & Industrial Aerodynamics, 68, pp. 79–90

Menet, J. L., 2004. A double-step Savonius rotor for local production of electricity: A design study. Renewable Energy, 29, pp. 1843–1862.

Menter, F. R., **1994**. Two-equation eddy-viscosity turbulence models for engineering applications, AIAA Journal, Vol. 32, No. 8, pp. 1598–1605.

Modi, V., and **Fernando, M.**, 1989. On the performance of the Savonius wind turbine. Journal of Wind Engineering & Industrial Aerodynamics, 111, pp. 71–81.

Modi, V. J., and **Fernando, M. S. U. K.,** 1993. Unsteady aerodynamics and wake of the Savonius wind turbine: A numerical study. Journal of Wind Engineering & Industrial Aerodynamics, 46–47, pp. 811–816.

Modi, V. J., Roth, N. J., and **Fernando, M. S. U. K.**, 1984. Optimum-configuration studies and prototype design of a wind-energy-operated irrigation system. Journal of Wind Engineering & Industrial Aerodynamics, 16, pp. 85–96.

Mohamed, M. H., Janiga, G., Pap, E., and **Thévenin, D.**, 2011. Optimal blade shape of a modified Savonius turbine using an obstacle shielding the returning blade. Energy Conversion and Management, 52, pp. 236–242.

Mohamed, M. H., Janiga, G., Pap, E., and **Thévenin, D**., 2010. Optimization of Savonius turbines using an obstacle shielding the returning blade. Renewable Energy, 35, 2618-2626

Manwell, J. F., Mcgowan, J. G., and **Rogers, A. L.**, 2009. Wind energy explained: Theory, design and application. UK: John Wiley & Sons Limited.

Mari, M., Venturini, M., and **Beyene, A.**, 2017. A novel geometry for vertical axis wind turbines based on the savonius concept. ASME Journal of Energy Resources Technology, 139(6), pp. 1–9.

Mojola, O. O., 1985. On the aerodynamic design of the Savonius windmill rotor. Journal of Wind Engineering & Industrial Aerodynamics, 21, pp. 223–231.

Mohammadi, M., Lakestani, M., and **Mohamed, M. H**., 2018. Intelligent parameter optimization of Savonius rotor using Artificial Neural Network and Genetic Algorithm. Energy, 143, pp. 56-68

Moffat, R. J., 1982. Contributions to the theory of single-sample uncertainty analysis. ASME Journal of Fluids Engineering, 104, pp. 250-258.

Morcos, S. M., Khalafallah, M. G., and **Heikel, H. A.**, 1981. The effect of shielding on the aerodynamic performance of Savonius wind turbines. in: Proceedings of the 16th Intersoc. Energy Convers. Eng. Conf., Atlanta, GA, August 9-14, 2037-2040

Müller, G., Jentsch, M. F., and **Stoddart, E.**, 2009. Vertical axis resistance type wind turbines for use in buildings. Renewable Energy, 34(5), pp. 1407–1412.

Nasef, M. H., El-Askary, W. A., AbdEL-hamid, A. A., and **Gad, H. E.**, 2013. Evaluation of Savonius rotor performance: Static and dynamic studies. Journal of Wind Engineering & Industrial Aerodynamics, 123, pp. 1–11.

Newman, 1974. Measurements on Savonius rotor with variable gap. in Proceeding of Sherbrook University Symposium on Wind Energy, Sherbrook Canada.

Neto, J. X. V., Junior, E. J. G., Moreno, S. R., Ayala, H. V. H., Mariani, V. C., and **Coelho, L. S**., 2018. Wind turbine blade geometry design based on multi-objective optimization using metaheuristics. Energy, 162, pp. 645-658

Ogawa, T., 1984. Theoretical study on the flow about Savonius rotor. ASME Journal of Fluids Engineering, 106, pp. 85–91.

Ogawa, T., Yoshida, H., and **Yokota, Y.**, 1989. Development of rotational speed control systems for a Savonius-type wind turbine. ASME Journal of Fluids Engineering, 111, pp. 53-58.

Paraschivoiu, I., 2002. Wind turbine design: with emphasis on Darrieus concept, Presses inter Polytechnique, Canada.

Plourde, B., Abraham, J., Mowry, G., and **Minkowycz, W.**, 2012. Simulations of three-dimensional vertical-axis turbines for communications applications. Wind Engineering, 36, pp. 443–454.

Promdee, C., and **Photong, C.,** 2016. Effects of wind angles and wind speeds on voltage generation of Savonius wind turbine with double wind tunnels. Procedia Computer Science, 86, pp. 401–404

Pope, K., Rodrigues, V., Doyle, R., Tsopelas, A., Gravelsins, R., Naterer, G. F., and **Tsang, E.**, 2010. Effects of stator vanes on power coefficients of a zephyr vertical axis wind turbine. Renewable Energy, 35, pp. 1043–1051

Prabhukhot, P. R., and **Prabhukhot, A. R**., 2017. Computer analysis of S822 aerofoil section for blades of small wind turbines at low wind speed. ASME Journal of Solar Energy Engineering, Vol. 139 (5), p. 051008-1

Rajkumar, M. J., and **Saha, U. K.,** 2006. Valve-aided twisted Savonius rotor. Wind Engineering, 30, pp. 243–254.

Rajkumar, M. J., 2004. Experimental investigation and flow simulation of Savonius rotor. M. Tech. Thesis, Department of Mechanical Engineering, IIT Guwahati, India.

Ramadan, A., Yousef, K., Said, M., and **Mohamed, M. H**., 2018. Shape optimization and experimental validation of a drag vertical axis wind turbine. Energy,151, pp. 839-853.

Reupke, P., and **Probert, S. D.**, 1991. Slatted-blade Savonius wind-rotors. Applied Energy, 40, pp. 65–75.

Ricci, R., Romagnoli, R., Montelpare, S., and **Vitali, D**., 2016. Experimental study on a Savonius wind rotor for street lighting systems. Applied Energy, 161, pp. 143–152.

Roy, S., and **Ducoin, A.,** 2016. Unsteady analysis on the instantaneous forces and moment arms acting on a novel Savonius-style wind turbine. Energy Conversion Management, 121, pp. 281–296.

Roy, S., 2014. Aerodynamic performance evaluation of a novel Savonius-style wind turbine through unsteady simulations and wind tunnel experiments. PhD thesis, Department of Mechanical Engineering, IIT Guwahati, India

Roy, S., Mukherjee, P., and **Saha, U. K.**, 2014. Aerodynamic performance evaluation of novel Savonius-style wind turbine under oriented jet. Paper No. GTINDIA2014-8152, ASME 2014 Gas Turbine India Conference, December 15-17, New Delhi, India.

Roy, S., and **Saha, U. K.,** 2015. Wind tunnel experiments of a newly developed two-bladed Savonius-style wind turbine. Applied Energy, 137, pp. 117–125.

Roy, S., and **Saha, U. K.,** 2014. An adapted blockage factor correlation approach in wind tunnel experiments of a Savonius-style wind turbine. Energy Conversion Management, 86, pp. 418–427.

Roy, S., and **Saha, U. K.,** 2013. Review of experimental investigations into the design, performance and optimization of the Savonius rotor. Proc. Inst. Mech. Eng. Part A-Journal Power and Energy, 227, pp. 528–542.

Roy, S., and **Saha, U. K.**, 2013. Computational study to assess the influence of overlap ratio on static torque characteristics of a vertical axis wind turbine. Procedia Engineering, 51, pp. 694–702.

Roy, S., and **Saha, U. K**., 2013. Investigation on the effect of aspect ratio into the performance of Savonius rotor. Paper No. GTINDIA2013-3729, ASME Gas Turbine India Conference, December 5-6, Bangalore, India

Roy, S., and **Saha, U. K.**, 2013. Numerical investigation to assess an optimal blade profile for the drag based vertical axis wind turbine. Paper No. IMECE2013-64001, ASME International Mechanical Engineering Congress & Exposition, November 15-21, 2013, San Diego, CA, USA.

Ross, I., and **Altman**, A., 2011. Wind tunnel blockage corrections: Review and application to Savonius vertical-axis wind turbines. Journal of Wind Engineering & Industrial Aerodynamics, 99(5), pp. 523–538.

Rahai, H., and **Hefazi, H.**, 2005. Development of optimum design configuration and performance for vertical axis wind turbine. Feasibility Analysis and Final EISG Report (California Energy Commission).

Sargolzaei, J., and **Kianifar, A.,** 2010. Neuro–fuzzy modeling tools for estimation of torque in Savonius rotor wind turbine. Advances in Engineering Software, 41, pp. 619–626

Saha, U. K., and **Rajkumar, M. J.**, 2006. On the performance analysis of Savonius rotor with twisted blades. Renewable Energy, 31, pp. 1776–1788.

Saha, U. K., Thotla, S., and **Maity, D.,** 2008. Optimum design configuration of Savonius rotor through wind tunnel experiments. Journal of Wind Engineering & Industrial Aerodynamics, 96, pp. 1359–1375.

Savonius, S. J., 1930. The S-rotor and its applications. Mechanical Engineering 1931;53(5):333-38

Sharma, S., and **Sharma, R. K**., 2017. CFD investigation to quantify the effect of layered multiple miniature blades on the performance of Savonius rotor. Energy Conversion and Management, 144, pp. 275–285.

Sharma, S., and **Sharma, R. K**., 2016. Performance improvement of Savonius rotor using multiple quarter blades - A CFD investigation. Energy Conversion and Management, 127, pp. 43–54.

Shaughnessy, B. M., and **Probert, S. D.,** 1992. Partially-blocked Savonius rotor. Applied Energy, 43, pp. 239–249.

Sheldahl, R. E., Feltz, L. V., and **Blackwell, B. F.**, 1978. Wind tunnel performance data for two- and three-bucket Savonius rotors. Energy, 2, pp. 160–164.

Shikha, Bhatti, T. S., and **Kothari, D. P.**, 2003. Wind energy conversion systems as a distributed source of generation. ASCE Journal of Energy Engineering. 129, pp. 69–80.

Shahzad, A., Asim, T., Mishra, R., and **Paris, A.**, 2013. Performance of a Vertical Axis Wind Turbine under Accelerating and Decelerating Flows, Procedia CIRP, 11, pp. 311 – 316

Singh, R. K., and **Ahmed, M. R.**, 2013. Blade design and performance testing of a small wind turbine rotor for low wind speed applications. Renewable Energy, 50, pp. 812-819

Song, C., Zheng, Y., Zhao, Z., Zhang, Y., Li, C., and **Jiang, H**., 2015. Investigation of meshing strategies and turbulence models of computational fluid dynamics simulations of vertical axis wind turbines. Journal of Renewable and Sustainable Energy, 7, pp. 0–19.

Song, L., Yang, Z.-X., Deng, R.-T., and **Yang, X.-G.,** 2013. Performance and structure optimization for a new type of vertical axis wind turbine, in: Proceedings of the IEEE2013 International Conference on Advanced Mechatronic Systems. pp. 687–692.

Simonds, M. H., and **Bodek, A**., 1964. Performance test of a Savonius rotor (Brace Research Institute. McGill University, Quebec, Canada.

Sahim, K., Santoso, D., and **Radentan, A.**, 2013. Performance of Combined Water Turbine with Semi elliptic Section of the Savonius Rotor. Hindawi Publishing Corporation International Journal of Rotating Machinery Volume 2013, Article ID 985943, 5 pages

Sivasegaram, S., and **Sivapalan, S**., 1983. Augmentation of power in slow-running vertical-axis wind rotors using multiple vanes. Wind Engineering, Vol. 7, No. 1, pp. 12–19.

Tartuferi, M., Alessandro, V. D., Montelpare, S., and **Ricci, R.,** 2015. Enhancement of Savonius wind rotor aerodynamic performance : a computational study of new blade shapes and curtain systems. Energy, 79, pp. 371–384.

Tian, W., Mao, Z., An, X., Zhang, B., and **Wen, H.,** 2017**.** Numerical study of energy recovery from the wakes of moving vehicles on highways by using a vertical axis wind turbine. Energy, 141, pp. 715–728.

Thotla, S,. 2006. Optimum design configuration of Savonius rotor through wind tunnel testing. M. Tech. Thesis, Department of Mechanical Engineering, IIT Guwahati, India.

Ushiyama, I., Nagai, H., and **Mino, M.**, 1982. The optimum design configurations of Savonius wind turbines. In: Proceedings of the 17th intersociety energy conversion engineering conference (IECEC '82), Los Angeles, California, August 8–12, Vol. 4, pp. 2096–2101.

Ushiyama, I., and **Nagai, H.**, 1988. Optimum design configurations and performance of Savonius rotors. Wind Engineering, 12(1), pp. 59–75.

White, F. M., 2011. Fluid mechanics. New York, USA: McGraw-Hills.

WWEA 2019. World wind energy association.

Wong, K. H., Chong, W. T., Sukiman, N. L., Poh, S. C., Shiah, Y-C., and **Wang, C-T**., 2017. Performance enhancements on vertical axis wind turbines using flow augmentation systems: A review. Renewable and Sustainable Energy Reviews, 73, pp. 904–21.

Zhao, Z., Zheng, Y., Xu, X., Liu, W., and **Hu, G.,** 2009. Research on the Improvement of the Performance of Savonius Rotor Based on Numerical Study. in: Proceedings of the International Conference on Sustainable Power Generation and supply. pp. 1–6.

Zhang, B., Song, B., Mao, Z., and **Tian, W.**, 2017. A novel wake energy reuse method to optimize the layout for Savonius-type vertical axis wind turbines. Energy, 121, pp. 341–355.

Zhou, T., and **Rempfer, D**., 2013. Numerical study of detailed flow field and performance of Savonius wind turbines. Renewable Energy, 51, pp. 373–381.

Zhou, Q., Xu, Z., Cheng, S., Huang, Y., and **Xiao, J.**, 2018. Innovative Savonius rotors evolved by genetic algorithm based on 2D-DCT encoding. Soft Computing.

Xu, G and **Sankar, L. N.**, 2000. Computational study of horizontal axis wind turbines. ASME Journal of Solar Energy Engineering, 122, pp. 35-39.

Appendix

As flow around the Savonius rotor is fully turbulent, so the Reynolds decomposition can be applied in the incompressible RANS equations are listed below (Song et al., 2015).

$$\frac{\partial \bar{u}_j}{\partial x_j} = 0 \qquad \text{A.1}$$

$$\frac{\partial \bar{u}_i}{\partial t} + \bar{u}_j \frac{\partial \bar{u}_i}{\partial x_j} = -\frac{1}{\rho}\frac{\partial \bar{p}}{\partial x_i} + \frac{\partial}{\partial x_j}\left(\nu \frac{\partial \bar{u}_i}{\partial x_j}\right) + \frac{1}{\rho}\frac{\partial\left(-\rho \overline{u_i' u_j'}\right)}{\partial x_j} + \overline{f_i} \qquad \text{A.2}$$

Where, t is the time, ρ is the density of fluid, u is the velocity, x_i and x_j are the Cartesian coordinate components, i and j can take values of 1, 2, and 3 in order to take three dimensions into account, p is the pressure, ν is the kinematic viscosity, and f_i is the body force per unit volume. However, the body force (f_i) in the present investigation is neglected.

The $-\rho \overline{u_i' u_j'}$ generally known as Reynolds stress.

A. Shear-stress transport (SST) *k-ω* model

The shear stress transport (SST) *k-ω* model was developed by Menter (1994) to efficiently blend the robust and precise formulation of the *k-ω* model in the near wall region with free-stream independence of the *k-ϵ* model in the far field. To attain this, the *k-ϵ* model is transformed into a *k-ω* formulation. The SST *k-ω* model is analogous to standard *k-ω* model, though it includes the following improvements:

- The standard *k-ω* model and transformed *k-ϵ* model are both multiplied by a blending function and both are added together. The blending function is intended to be one in the near wall region, which triggers the standard *k-ω* model, and zero away from the surface, which triggers the transformed *k-ϵ* model.
- The SST *k-ω* model includes a damped cross diffusion derivative term in the *ω* equation.
- The definition of the turbulent viscosity is modified to account for the transport of the turbulent shear stress.
- The modeling constants are different.

These features make the SST *k-ω* model more precise and dependable for a wider class of flows (e.g., flow over airfoils, shock waves, rotating flows etc.) than the standard *k-ω* model.

B. Transport equations for the standard *k-ω* model

The SST *k-ω* model has a similar form to the standard *k-ω* model turbulence kinetic energy, *k*, and the specific dissipation rate, *ω*, are found from the following transport equations:

$$\frac{\partial}{\partial t}(\rho k)+\frac{\partial}{\partial x_i}(\rho k u_i)=\frac{\partial}{\partial x_j}\left(\Gamma_k \frac{\partial k}{\partial x_j}\right)+\tilde{G}_k-Y_k \quad \text{(A.3)}$$

and

$$\frac{\partial}{\partial t}(\rho \omega)+\frac{\partial}{\partial x_i}(\rho \omega u_i)=\frac{\partial}{\partial x_j}\left(\Gamma_\omega \frac{\partial \omega}{\partial x_j}\right)+G_\omega-Y_\omega+D_\omega \quad \text{(A.4)}$$

where, D_ω represents the cross-diffusion term. G_k is the generation of turbulence kinetic energy due to mean velocity gradients. G_ω is the generation of ω. Y_k and Y_ω are the dissipation of k and ω due to turbulence.

However, the turbulent viscosity, μ_t, the turbulent Prandtl numbers, σ_k and σ_ω are computed as follows:

$$\mu_t=\frac{\rho k}{\omega}\frac{1}{\max\left[\frac{1}{\alpha^*},\frac{SF_2}{\alpha_1\omega}\right]} \quad \text{(A.5)}$$

Where, *S* is the strain rate magnitude and

$$\sigma_k=\frac{1}{\left(F_1/\sigma_{k,1}\right)+\left(\left(1-F_1\right)/\sigma_{k,2}\right)} \quad \text{(A.6)}$$

$$\sigma_\omega=\frac{1}{\left(F_1/\sigma_{\omega,1}\right)+\left(\left(1-F_1\right)/\sigma_{\omega,2}\right)} \quad \text{(A.7)}$$

The blending functions, F_1 and F_1 are given by:

$$F_1 = \tanh\left(\Phi_1{}^4\right) \tag{A.8}$$

$$\Phi_1 = \min\left[\max\left(\frac{\sqrt{k}}{0.09\omega y}, \frac{500\mu}{\rho y^2 \omega}\right), \frac{4\rho k}{\sigma_{\omega,2} D_\omega^+ y^2}\right] \tag{A.9}$$

$$D_\omega^+ = \max\left[2\rho \frac{1}{\sigma_{\omega,2}} \frac{1}{\omega} \frac{\partial k}{\partial x_j} \frac{\partial \omega}{\partial x_j}, 10^{-10}\right] \tag{A.10}$$

$$F_2 = \tanh\left(\Phi_2{}^2\right) \tag{A.11}$$

$$\Phi_2 = \max\left[2\frac{\sqrt{k}}{0.09\omega y}, \frac{500\mu}{\rho y^2 \omega}\right] \tag{A.12}$$

where, y is the distance to the next surface,

$\alpha_1 = 0.31$, $\sigma_{k,1} = 1.176$, $\sigma_{k,2} = 1$, $\sigma_{\omega,1} = 2$, $\sigma_{\omega,2} = 1.168$,

$$Y_k = \rho \beta_i \omega^2 \tag{A.13}$$

Instead of having a constant value of β_i, in this model it is given by:

$$\beta_i = F_1 \beta_{i,1} + (1 - F_1)\beta_{i,2} \tag{A.14}$$

where, $\beta_{i,1} = 0.075$, $\beta_{i,2} = 0.0828$

The cross-diffusion term D_ω is given by:

$$D_\omega = 2(1 - F_1)\rho\sigma_{\omega,2} \frac{1}{\omega} \frac{\partial k}{\partial x_j} \frac{\partial \omega}{\partial x_j} \tag{A.15}$$

LIST OF PUBLICATIONS

Journals

1. Alom, N., and Saha, U. K., 2019. Examining the aerodynamic drag and lift characteristics of a newly developed elliptical- bladed Savonius rotor, ASME Journal of Energy Resources Technology, Vol. 141, No. 5, p. 051201.
2. Alom, N., and Saha, U. K., 2019. Evolution and progress in the development of Savonius wind turbine rotor blade profiles and shapes, ASME Journal of Solar Energy Engineering, Vol. 141, No.3, p. 030801.
3. Alom, N., and Saha, U. K., 2019. Influence of blade profiles on Savonius rotor performance: Numerical simulation and experimental validation, Energy Conversion and Management, Vol. 186, pp: 267-277
4. Alom, N., and Saha, U. K., 2019. Drag and lift characteristics of a novel elliptical-bladed Savonius rotor with vent augmenters, ASME Journal of Solar Energy Engineering, Vol. 141, No. 5, p. 051007.
5. Alom, N., and Saha, U. K., 2018. Four decades of research into the augmentation techniques of Savonius wind turbine rotor, ASME Journal of Energy Resources Technology, Vol. 140, No. 5, p. 050801.
6. Alom, N., and Saha, U. K., 2018. Performance analysis of a vent-augmented elliptical-bladed Savonius rotor by numerical simulation and wind tunnel experiments, Energy, Vol. 152, pp: 277-290.
7. Alom, N., Borah, B., and Saha, U. K., 2018. An insight into the drag and lift characteristics of modified Bach and Benesh profiles of Savonius rotor, Energy Procedia, Vol. 144, pp: 50-56.

Conferences

8. Alom N, and Saha U. K., 2019. Determining the optimal location of vent augmenters in an elliptical-bladed Savonius rotor, Paper No. GTIndia2019-2344, ASME Gas Turbine India Conference, December 05 – 06, Chennai, India (Accepted).
9. Alom N, Das R, and Saha U. K., 2019. Optimization of aerodynamic parameters of an elliptical-Bladed Savonius wind rotor using multi-objective genetic algorithm, Paper No. GTIndia2019-2346, ASME Gas Turbine India Conference, December 05 – 06, Chennai, India (Accepted).
10. Alom, N., Kumar, N., and Saha, U. K., 2018. Analyzing the effect of shaft and end-plates of a newly developed elliptical-bladed Savonius rotor from wind tunnel tests, Paper No. OMAE2019-95570, ASME 38th International Conference on Ocean, Offshore and Arctic Engineering, June 9-14, 2019, Glasgow, Scotland, UK.
11. Alom, N., Borah, B., and Saha, U. K., 2018. An insight into the drag and lift characteristics of modified Bach and Benesh profiles of Savonius rotor, 4th International Symposium on Hydrogen Energy, Renewable Energy and Materials (HEREM), *June 13–14, Bangkok, Thailand.*
12. Alom, N., and Saha, U. K., 2017. Arriving at the optimum overlap ratio for an elliptical-bladed Savonius rotor, Paper No. GT2017-64137, ASME Turbo Expo, June 26–30, Charlotte, North Carolina, USA.
13. Alom, N., Kumar, N., and Saha, U. K., 2017. Aerodynamic performance of an elliptical-bladed Savonius rotor under the influence of number of blades and shaft, Paper No. GTIndia2017-4554, ASME Gas Turbine India Conference, December 7–8, Bangalore, India.
14. Alom, N., and Saha, U.K., 2016. Numerical optimization of semicircular-bladed Savonius rotor using vent augmenters, Asian Congress on Gas Turbines 2016, November 14-16, IIT Bombay, Mumbai, India.